Stony Brook University

Structural Characterization of Gas Adsorption in Metal Organic Frameworks

A Dissertation Presented

by

Anna Monika Plonka

to

The Graduate School

in Partial Fulfillment of the

Requirements

for the Degree of

Doctor of Philosophy

in

Geosciences

Stony Brook University

May 2015

Stony Brook University

The Graduate School

Anna Monika Plonka

We, the dissertation committee for the above candidate for the

Doctor of Philosophy degree, hereby recommend

acceptance of this dissertation.

John B. Parise, Ph. D. – Dissertation Advisor
Distinguished Professor, Department of Chemistry & Geosciences, Stony Brook University

Brian Phillips, Ph. D. – Chairperson of Defense
Professor, Department of Geosciences, Stony Brook University

Lars Ehm, Ph. D.
Research Associate Professor, Department of Geosciences, Stony Brook University

Deanne Rogers, Ph. D.
Assistant Professor, Department of Geosciences, Stony Brook University

Chris Cahill, Ph. D. – Outside Member
Professor of Chemistry, Department of Chemistry, George Washington University

This dissertation is accepted by the Graduate School

Charles Taber
Dean of the Graduate School

Abstract of the Dissertation

Structural Characterization of Gas Adsorption in Metal Organic Frameworks

by

Anna Monika Plonka

Doctor of Philosophy

in

Geosciences

Stony Brook University

2015

Selective adsorption and sequestration of carbon dioxide from sources of anthropogenic emissions is important to mitigate the growing level of the atmospheric CO_2. Solid state adsorbents, such as metal organic frameworks (MOFs), are proposed as an alternative to the currently used toxic and corrosive alkanolamine solutions. The aim of this work was to understand the interactions between adsorbed gases and a pore surface of crystalline MOFs at a molecular level, and identify the connection between geometry and gas selectivity.

In contrast to current trends in the design of MOFs, we described the unique mechanism responsible for a high CO_2/N_2 adsorption selectivity in a Ca-based MOF: Ca(sdb), (sdb: 4,4'-sulfonyldibenzoate), even in the presence of water in the gas stream. Single crystal XRD experiments of gas-loaded samples revealed that the v-shaped linker provides a "π-pocket" formed by two phenyl rings, and that CO_2 locate between the rings, resulting in a high heat of adsorption. To determine the gas adsorption performance *in situ* in the presence of water, we used X-ray Diffraction (XRD) simultaneously with differential scanning calorimetry (XRD-DSC). The XRD-DSC technique allows measurements of heat flow that provide enthalpy of

adsorption, while at the same time XRD allows evaluation of structural responses during MOF activation and gas adsorption. We also used XRD-DSC to determine the performance of Cd(sdb), the Cd-based analogue of Ca(sdb): Cd(sdb) shows a high selectivity for CO_2 over N_2. *In situ* vacuum-swing XRD-DSC allowed us to determine the heat of adsorption values of the adsorbate; results of these studies were consistent with the π–CO_2 interaction as the origin of the selectivity.

The newly described "π-pocket" is a potential site for a selective adsorption of gases other than CO_2. Hydrocarbon gases (C_2H_n), such as ethane, ethylene and acetylene, were adsorbed on Ca(sdb) and on another Ca-based MOF: Ca(tcpb) [tcpb: 1,2,4,5-tetrakis(4-carboxyphenyl)benzene] with a high measured energy of interaction. Structural data suggest that C_2H_n interact with the organic linkers within the MOF frameworks through C-H$\cdots\pi$ and C-H$\cdots$O interactions. The knowledge acquired here can promote systematic synthetic searches for novel materials that can serve as selective solid-state adsorbents.

Finally, the formation of Ca-based Metal Organic Frameworks was studied using different structural isomers of pyridinedicarboxylic acid. Nine MOF materials were synthesized and structurally analyzed. The atomic arrangements in the crystal structure of resultant MOFs are based on a variety of the inorganic structural motifs, ranging from isolated polyhedra to infinite chains, a layer or a 3-D connectivity, depending on the linker geometry and the synthetic condition.

Table of Contents

List of Abbreviations

APS	Advanced Photon Source
atz	3-amino-1,2,4-triazole
bdc	1,4-benzenedicarboxylate
BET	Brunauer-Emmett-Teller
bpdc	4,4’-biphenyldicarboxylate
bpee	1,2-bipyriylethylene
btc	1,3,5-benzenetricarboxylate
CCS	Carbon Capture and Storage
CO_2eq	carbon dioxide equivalents
dabco	1,4-diazabicyclo(2.2.2)octane
DEF	diethylformamide
DFT	Density Functional Theory
DMF	dimethylformamide
dobdc	2,5-dihydroxyterephtalate
DSC	differential scanning calorimetry
DSLF	Dual-site Langmuir-Freundlich
ECP	effective core potential
ESP	electrostatic potential
EtOH	ethanol
etz	3,5-diethyl-1,2,4-triazole
GCMC	Grand Canonical Monte Carlo
HKUST	Hong Kong University of Science and Technology
HKUST-1	$Cu_3(btc)_2$
H_2pdc	pyridinedicarboxylic acid
H_2(sdb)	4,4'-sulfonyldibenzoic acid
H_2(tcpb)	1,2,4,5-tetrakis(4-carboxyphenyl)benzene acid
IAST	Ideal Adsorbed Solution Theory
IPCC	Intergovermental Panel on Climate Change

IR	infra-red
L	tetrakis-3,5-bis[(4carboxy)phenyl]phenyl porphine
LJ	Lennard-Jones
MAF	metal azolate framework
MAF-2	Cu(etz)
MeOH	methanol
MIL	Materials Institute of Lavoisier
MIL-47	V(O)(bdc)
MIL-53-Cr	Cr(OH)(bdc)
MOF	metal organic framework
MOF-5	$Zn_4O(bdc)_3$
Ni-MOF-74	Ni_2(dobdc)
ox	oxalate
PAF	porous aromatic framework
pdc	pyridinedicarboxylate
phim	benzimidazole
PXRD	powder X-ray diffraction
pyz	pyrazine
pzdc	pyrazine 2,3-dicarboxylate
RH	relative humidity
RPM	Rutgers Porous Material
RPM-3-Zn	$Zn_2(bpdc)_2$(bpee)
RT	room temperature
SCXRD	single crystal X-ray diffraction
sdb	4,4’-sulfonyldibenzoate
SBU	secondary-building units
tcpb	1,2,4,5-tetrakis(4-carboxyphenyl)benzene
TGA	thermogravimetric analysis
UFF	universal force field
UNLPF	University of Nebraska- Lincoln Porous Framework
UNLPF-2	$Co_2(CO_2)$(CoL)(H_2O)

VDW	van der Waals
XRD	X-ray diffraction
ZIF	zeolitic imidazole framework
ZIF-7	$Zn(phim)_2$

List of Figures

List of Tables

Acknowledgments

I would like to express my gratitude to all the people who helped me throughout this work. First and foremost I thank my academic advisor Prof. John Parise for his continuous support and guidance. His great scientific curiosity was always truly inspiring, working with him allowed me to accomplish more than I thought possible. I am also grateful to all my committee members, whose helpful suggestions made this dissertation better: Prof. Brian Phillips, Prof. Lars Ehm, Prof. Deanne Rogers and Prof. Christopher Cahill.

I owe a special thanks to Debasis Banerjee, my former group member and my friend, who introduced me to Metal Organic Frameworks and their synthesis, and with whom I collaborated extensively over the past years. Much of my work would not be possible without the contribution of many collaborators and beamline scientists: Zhijuan Zhang, Hao Wang, Jing Li, Hongijan Jin, Nancy Goroff, Przemek Dera, Andrey Yakovenko, Gregory Halder, Yu-Sheng Chen, Simon Teat, Paul Forster, Nour Nijem, and Yves Chabal.

I would like to thank all the past and present Parise Group members: Xianyin Chen, William Woerner, Lena Lazareva, Paul Calderone, Wenqian Xu, Quddus Nizami, Richard Harrington, Lauren Borkowski, Alex Sinclair, Jesse John, Alwin James, Naveen Dharmagunawardhane. Even if not involved directly in my research their presence, support and advices helped me a lot throughout the years.

I want to also thank my friends and family for their support and encouragement. I owe special gratitude to my parents, my mother who always believed in me and supported my dreams, even the seemingly impossible ones. And also my father who was the first one to show me how amazing the world is and inspired me to dedicate my career to science. Finally I thank

my husband, Marcin, for his love and especially for his incredible patience. He not only was with me and supported me through most difficult times, but also, through the dedication to his work, reminded me every day what it means to truly love science.

This work was funded by the U.S. Department of Energy (DOE), Office of Science, Office of Basic Energy Sciences, under contract number DE-FG02-09ER46650 and by the National Science Foundation (NSF) through grant DMR-0800415. Crystal structures were determined using the Stony Brook University single-crystal diffractometer, obtained through the support of the NSF (grant number CHE-0840483) and in ChemMatCars (Sector 15), Advanced Photon Source (APS), principally supported by the National Science Foundation/Department of Energy (NSF/CHE-0822838). Use of APS was supported by the U.S. Department of Energy, Office of Science, Office of Basic Energy Sciences under contract number DE-AC02-06CH11357. Powder XRD work was done using the diffractometer obtained through the support of NASA (grant number MFRP07-0022).

Publications

1. **Plonka, A. M.**; Banerjee, D.; Parise, J. B., Poly [(μ4-adamantane-1, 3-dicarboxylato-κ5O1: O1′: O3, O3′: O3′)(μ3-adamantane-1, 3-dicarboxylato-κ5O1, O1′: O3, O3′: O3′) dimagnesium]: a layered coordination polymer. *Acta Cryst. Sect. C* **2011,** *67* (11), 335-337.

2. **Plonka, A. M.**; Banerjee, D.; Parise, J. B., Effect of Ligand Structural Isomerism in Formation of Calcium Coordination Networks. *Cryst. Growth Des.* **2012,** *12* (5), 2460-2467.

3. **Plonka, A. M.**; Dera, P.; Irmen, P.; Rivers, M. L.; Ehm, L.; Parise, J. B., β-diopside, a new ultrahigh-pressure polymorph of $CaMgSi_2O_6$with six-coordinated silicon. *Geophys. Res. Lett.* **2012,** *39* (24).

4. Banerjee, D.; Zhang, Z.; **Plonka, A. M.**; Li, J.; Parise, J. B., A Calcium Coordination Framework Having Permanent Porosity and High CO_2/N_2 Selectivity. *Cryst. Growth Des.* **2012,** *12* (5), 2162-2165.

5. Chen, X.; **Plonka, A. M.**; Banerjee, D.; Parise, J. B., Synthesis, Structures and Photoluminescence Properties of a Series of Alkaline Earth Metal-Based Coordination Networks Synthesized Using Thiophene-Based Linkers. *Cryst. Growth Des*. **2012,** *13* (1), 326-332.

6. **Plonka, A. M**.; Banerjee, D.; Woerner, W. R.; Zhang, Z.; Nijem, N.; Chabal, Y. J.; Li, J.; Parise, J. B., Mechanism of Carbon Dioxide Adsorption in a Highly Selective Coordination Network Supported by Direct Structural Evidence. *Angew. Chem. Int. Ed.* **2013,** *52* (6), 1692-1695.

7. **Plonka, A. M.**; Banerjee, D.; Woerner, W. R.; Zhang, Z.; Li, J.; Parise, J. B., Effect of ligand geometry on selective gas-adsorption: the case of a microporous cadmium metal organic framework with a V-shaped linker. *Chem. Commun.* **2013,** *49* (63), 7055-7057.

8. Banerjee, D.; **Plonka, A. M.**; Kim, S. J.; Xu, W.; Parise, J. B., Synthesis, structural characterization and high pressure phase transitions of monolithium hydronium sulfate. *J. Solid State Chem.* **2013,** *197*, 181-185.

9. Calderone, P. J.; Banerjee, D.; **Plonka, A. M.**; Kim, S. J.; Parise, J. B., Temperature dependent structure formation and photoluminescence studies of a series of magnesium-based coordination networks. *Inorg. Chim. Acta* **2013,** *394*, 452-458.

10. Calderone, P. J.; **Plonka, A. M.**; Banerjee, D.; Nizami, Q. A.; Parise, J. B., Lanthanide metal-organic frameworks based on a thiophenedicarboxylate linker: Characterization and luminescence. *Solid State Sci.* **2013,** *15*, 36-41.

11. Jin, H.; **Plonka, A. M.**; Parise, J. B.; Goroff, N. S., Pressure induced topochemical polymerization of diiodobutadiyne: a single-crystal-to-single-crystal transformation. *CrystEngComm* **2013,** *15* (16), 3106-3110.

12. Arnold, J. A.; Glotch, T. D.; **Plonka, A. M.**, Mid-infrared optical constants of clinopyroxene and orthoclase derived from oriented single-crystal reflectance spectra. *Am. Mineral.* **2014,** *99* (10), 1942-1955.

Chapter 1

Introduction

1.1 Carbon sequestration

The development of an efficient, inexpensive and easy to implement adsorber systems for the removal of carbon dioxide from sources of anthropogenic emission is one of the grand challenges faced by modern science and engineering. The level of CO_2 is constantly monitored due to its implication in global warming and increasing concerns of continuous use of fossil fuel combustion as a main energy source. The level of atmospheric CO_2 continues to grow and in March 2015 it reached a concentration of 403.1 ppm, which is the highest value recorded in recent history (Fig. 1.1).[1] In the last 800 thousand years, the bounds generally do not exceed 300 from the oscillatory mean (Fig. 1.2) supporting the argument that the recently observed increase of CO_2 indeed is of anthropogenic origin.[2]

Global emission of greenhouse gases is increasing at the fastest rate ever, despite development and implementation of mitigation technologies. In the decade 2000 – 2010 annual emission was increasing by 10 Gt carbon dioxide equivalents (CO_2eq) per year.[2] Among other processes leading to greenhouse gases production, the burning of fossil fuels contributes to over 60% of the total global emission (Fig. 1.3).[2] The majority of emitted CO_2 comes from energy generation – in USA almost 70% of electricity in 2014 was obtained from plants burning coal and natural gas (Fig. 1.4).[3] Globally the burning of fossil fuels provides over 86% of energy, and this amount is projected to increase due to economic growth particularly in developing nations.[2] The Intergovernmental Panel on Climate Change (IPCC) reported in 2013 that based on the

concentration growth rate of CO_2 the average global temperature will increase from 3.7 to 4.8 ºC by the year 2100.[2]

The central strategies developed for stabilizing the amount of atmospheric CO_2 are based on carbon capture and storage (CCS) of CO_2 emitted from fuel plants and natural gas wells.[4] The majority of emitted CO_2 arises from coal and gas combustion, motivating the development of new energy sources, and stimulating research into engineering solutions that would drastically reduce the emission by capturing CO_2 from currently operating plants.[5] The estimation shows that fuel plant equipped with CCS technology will reduce the CO_2 emission by 80-90%.[4] CCS is a three-step process: 1) CO_2 capture and separation 2) transportation and 3) permanent storage.[4] Of three basic options for CO_2 capture – post-combustion, pre-combustion or oxy-fuel combustion, an efficient and selective post-combustion capture is of particular interest because it could be readily implemented, whereas pre-combustion and oxy-fuel combustion require development and installation of new technologies, and replacement of currently operating power plants.[4] After successful CO_2 capture large amounts of gas need to be stored permanently as the quantity will most likely exceed possible demands of chemical industry, where CO_2 may be used as a feedstock.[4] The basic strategies for CO_2 storage include injecting compressed gas into depleted gas and oil reservoirs, saline or brine aquifers or into ocean water below 1000 m.[5]

The technology of CO_2 capture and separation is facing many challenges. Typical flue gas stream contains N_2:H_2O:CO_2 ratios of 6.2:1:1 (by weight) and up to 15% of CO_2 by volume at pressures of ~1bar.[2] Selective capture of CO_2 at such a low concentration, from gas flow containing other components that may compete with CO_2 during sorption processes, requires development of new materials. The retrieval of CO_2 from flue gas mainly requires N_2/CO_2 separation as N_2 is the predominant component in the gas stream (Fig.1.5). Such separation is

especially difficult in the presence of water, because water can strongly compete with CO_2 during sorption processes. Similarly, "sour" natural gas sources typically contain over 40% of CO_2; unlike separations from flue streams, which are typically at about 1 atm pressure, separation technologies of selective removal of CO_2 from natural gas streams must operate at high pressures.[6]

Current post-combustion capture and gas purification technologies utilize chemisorption in aqueous alkanolamine solutions, which are highly efficient in CO_2 removal but require significant energy for regeneration. The CO_2-amine bond formed during absorption needs to be cleaved for the regeneraiton of the sorbent.[7] The energy cost is elevated even more due to high heat capacity of water, which comprises approximatelly 70% of the solution and needs to be heated for the sorbent regeneration.[5] Furthermore, alkanolamine solutions are toxic and corrosive what limits their apllications on the larger scale.[7] Hence the use of dry solid state sorbents such as zeolites, activated carbon and more recently Metal Organic Frameworks (MOFs) are proposed as alternatives especially in combination with pressure swing processes.[5, 8] Zeolites or moleular sieves are porous aluminosilicate materials wich are highly efficient for CO_2/N_2 separation in dry conditions, but they become saturated with water, what over time leads to significant reduction of CO_2 sorption capacitity.[9] Activated carbon, which is an amorphous porous solid prepared by pyrolysis of reisins containing carbon, has a much lower CO_2 affinity when compared to zeolites or MOFs, due to uniformly distributed electric potential without strong adsorption sites, leading further to low CO_2/N_2 selectivity.[8d]

Rather than relying solely on tuning the pore diameters of microporous materials to select between gases based in size (the kinetic diameters of CO_2, CH_4, H_2O and N_2 are 3.30, 3.76, 2.65, 3.64 Å, respectively) selective separation must rely on differences in electronic properties such

as quadrupole moment and polarizability.[5] The affinity towards CO_2 is one of the major parameters requiring optimization with the major trade-offs being between the high sorbent-CO_2 interaction energy, which favors selectivity but comes with the high energy cost required for material regeneration.[5] On the other hand low CO_2-affinity diminishes sorption efficiency despite cost-effective regeneration.[5] Also, the optimal CO_2 sorbent must be stable over many adsorption-desorption cycles to be to utilized during the whole lifetime of the plant.[5] Finally, the adsorbent must have sufficiently high surface area, leading to high CO_2 gravimetric uptake to lower the volume of the sorbent bed.[5]

For natural gas purification CO_2 and light hydrocarbons are removed from methane in order to reduce CO_2-induced pipeline corrosion and produce high-purity gases for energy and other industrial applications.[10] The purified methane obtained from natural gas is the cleaner alternative to gasoline or diesel automobile fuels, producing less CO_2 during burning.[11] Furthermore natural gas is the main source of ethane, after methane it is the second largest component with the volume percent ranging from 0.7 to 6.8.[12] Ethane is the main feedstock for ethylene production, which in turn serves as the primary building block of polyethylene-based materials.[13] Currently CO_2 and light hydrocarbon fractions of natural gas are separated through the cryogenic distillation, which is energy intensive; separation using solid state adsorbents capable of operating in higher temperatures is proposed as a more economical alternative.[14] Indeed several classes of porous solid state materials have been tested for industrially important gaseous hydrocarbon separation (e.g. C_2, C_3, C_4) with encouraging results. Zeolites 5A and 13X can be used for the propylene/propane separation as reported by Järvelin and Fair.[15] Linear and branched hydrocarbon mixtures such as n-butane/i-butane or xylene isomers can be separated with MFI-type zeolites, with the reported selectivity between 20-60 for n-butane and over 600

for xylene.[16] Silver exchanged porous aromatic framework PAF-1-SO_3H effectively separates C_2 hydrocarbons as reported by Ma and coworkers.[17]

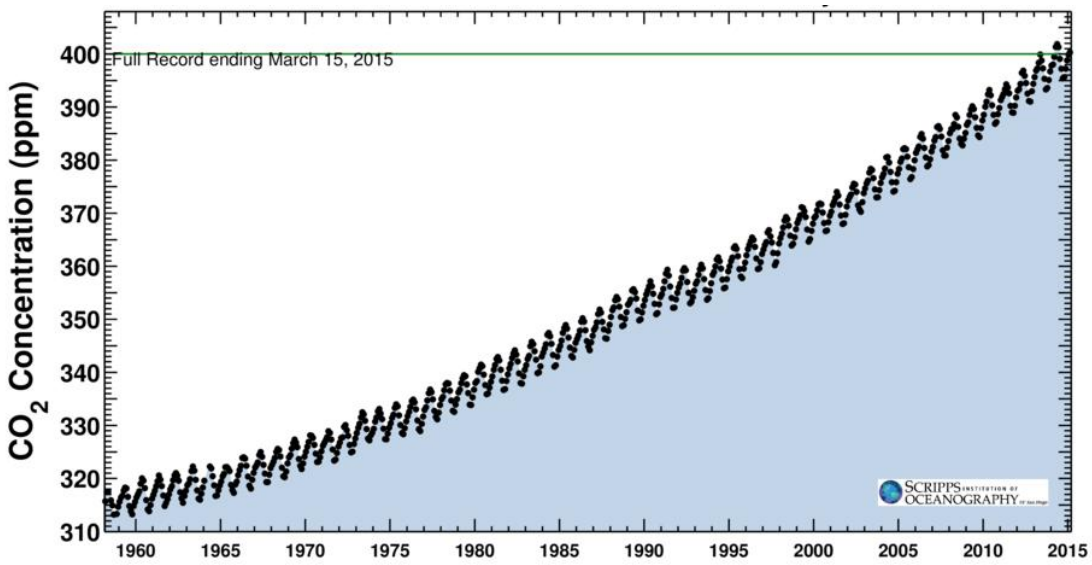

Figure 1.1 Carbon dioxide concentration measured at Mauna Loa Observatory, latest CO_2 reading as of March 15 2015 is 403.10 ppm.[1]

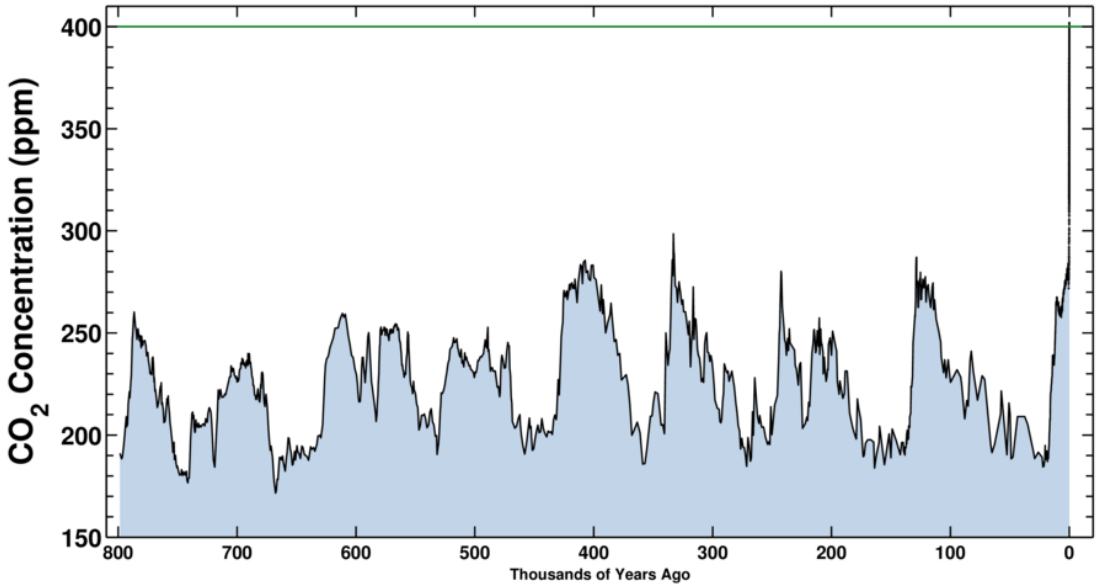

Figure 1.2 Atmospheric CO_2 concentration in last 800 thousand years, the levels before 1958 acquired form ice core data, after 1958 from Mauna Loa Observatory. Green line indicates 400 ppm level, which was reached in early 2015.[1]

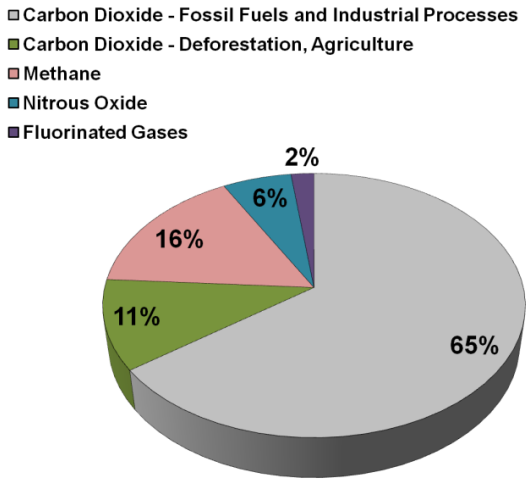

Figure 1.3 Sources of global anthropogenic greenhouse gases emission in 2010. Approximately 76% of the total emission comes from CO_2 gas.[2]

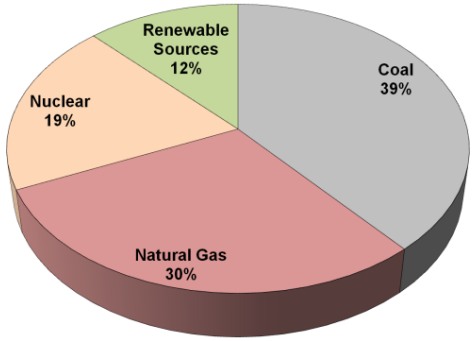

Figure 1.4 Electricity generation by energy source in USA 2014.[3]

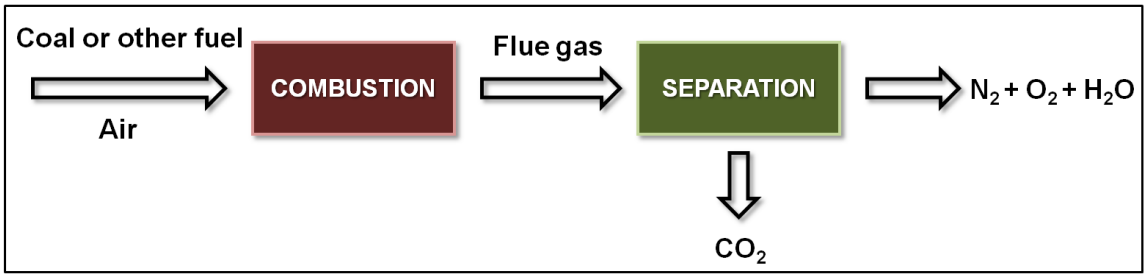

Figure 1.5 Schematic diagram of the post-combustion carbon capture. The sequestration process requires mainly CO_2/N_2 separation in the presence of water.

1.2 Metal Organic Frameworks for Gas Adsorption and Separation

Metal Organic Frameworks (MOFs) are a new class of porous materials that exhibit adsorption properties comparable or superior to commercially important materials such as aluminosilicate zeolites. There are reports of MOFs having higher surface areas per gram than any other porous material.[18] At a high pressure, a container filled with certain MOFs of ultra-high surface area is able to store nearly ten times more CO_2 than an empty container alone.[19]

The generic structure of a MOF is derived from metal nodes formed by single ions or metal clusters which are connected by organic ligands to form infinite networks (Fig. 1.6).[18a] MOFs possess great structural and chemical diversity and are easily modified to allow for tuning of material properties for a specific function. Their diversity, utility and ease of synthesis lead to the tremendous explosion in the number of MOF structures reported to date.[20] MOFs are proposed as an alternative in various gas adsorption and separation processes including CO_2 removal from flue gas or from natural gas for its purification.[5-6] Their great chemical diversity and high surface areas also suggest other industrial applications including gas storage, drug delivery, catalysis, sensing, proton conduction and artificial photosynthesis.[21]

Due to their hybrid organic-inorganic nature, and the possibility of functionalizing metal centers and ligands (Fig.1.6), MOFs can be more easily modified and optimized to suit specific applications to higher extent than other porous materials such as aluminosilicate zeolites. Most MOFs are synthesized under mild conditions allowing for better control over the synthesis and retrieval of metastable phases.[22] Even though the resultant structure mainly depends on the metal and linker used, the reaction temperature, solvent and rate of the crystal growth can also influence the structure type produced.[21a] The type of solvent used for synthesis can completely

change the resulting network topology and this is rationalized by hypothesizing that solvent molecules may act as templates to form porous networks of the specific pore sizes and dimensions.[21a] Furthermore, organic ligands can be easily synthesized or modified for the MOF of desired topology and functional groups within pore space (Fig. 1.7).[22] Finally, the structure of MOF can be modified post-synthesis, via the addition or exchange of functional groups, linkers or metal nodes exchange, and encapsulation of metal nanoparticles within the pores.[23] Among the diverse range of porous MOFs reported so far, those containing biocompatible metals like calcium and magnesium are of special interest. The low toxicity and Earth abundance of Ca- and Mg-based MOFs, relative to first-row transitional metals or lanthanide metals based MOF analogues may be especially beneficial in potential industrial applications.[24]

Strategies used to produce MOFs with CO_2 separation properties competitive with those of commercially established aluminosilicate zeolites, include pore surface modification with strongly polarizing functional groups such as amines, and desolvating metal centers to produce under coordinated sites suitable for the CO_2 sorption.[5, 25] The strong adsorption sites such as amine groups or open metals, offer higher enthalpy of CO_2 adsorption and increased CO_2/N_2 selectivity. In the amine-functionalized materials the selectivity toward CO_2 adsorption is especially high, but the additional functional groups lower the effective pore surface area and so the total uptake capacity.[26] Strong interaction with polarizing functional groups as well as with open metal sites presents other drawbacks, including an increase in material regeneration cost.[5] Furthermore, small amounts of water in the gas stream can significantly affect the CO_2 adsorption properties in zeolites and MOFs with open metal sites, since the exposed cation will be immediately coordinated by water molecules, preventing CO_2 from interacting with the adsorption sites.[27] The lack of CO_2 adsorption in the presence of humidity severely limits the

utility of materials functionalized with under-coordinated metal centers for the CO_2 removal from flue gas. Strategies complimentary to relying on under-coordinated metal centers for producing gas-selective MOFs are therefore sought. One such strategy might be to design frameworks that contain adsorption sites within the organic linker that selectively bind gases rather than water, with moderate binding energy so as to facilitate easy regeneration.[28]

Experimental gas sorption studies of MOFs usually focus on gas isotherms measurments that, while providing the necessary information on the overall gas uptake and framework behavior upon gas loading, yield limited information on the mechanism of gas adsorption. Understanding the key atom-atom interactions responsible for a high gas selectivity provides a means to discriminate between possible materials for industrial applications, like CO_2 sequestration or natural gas purification. Determining the key guest-host interactions is also vital to the development of reliable inter-atomic potentials necessary for simulating adsorption behavior. For zeolite molecular sieves this approach allows routine prediction of adsorption behavior.[29] Repeating this success for crystalline MOFs requires high quality X-ray diffraction data to facilitate precise characterization of sorption sites, and to augment the still limited number of the structural reports of CO_2 adsorbed on porous hybrid materials. [25, 30]

One of the earliest crystallographic studies on CO_2-loaded MOF was performed on the flexible MIL-53-Cr [MIL: Materials Institute of Lavoisier; Cr(OH)(bdc); bdc: 1,4-benzenedicarboxylate]. The synchrotron *in situ* powder X-ray diffraction experiment allowed the description of the breathing behavior of MIL-53-Cr upon the gas loading and identified strong adsorption sites responsible for the high CO_2-network affinity.[31] Further, Vaidhyanathan *et al.* performed an *in situ* single crystal X-ray diffraction study of amine functionalized zinc-based MOF [$Zn_2(atz)_2(ox)$; atz: 3-amino-1,2,4-triazole, ox: oxalate]. The study provided direct

experimental proof that CO_2 interacts with amine functional groups within MOF framework, through a weak interaction in a physisorptive manner. In the gas-loaded $Zn_2(atz)_2(ox)$, CO_2 molecules are located in two distinct crystallographic sites; one interacting with the amine, while the other is placed within two oxalate ligands.[30e] CO_2 interacting with open metal sites was observed in Ni-MOF-74 [Ni_2(dobdc); dobdc = 2,5-dihydroxyterephtalate] by Blom and coworkers. They performed high resolution powder X-ray diffraction experiment and observed short $Ni^{\cdots}CO_2$ distances (2.29 Å), supporting the claim that the polarizing nature of Ni is responsible for the high CO_2 heat of adsorption (Fig. 1.8). More recently, Johnson *et al.* reported a direct observation of CO_2 molecules trapped in a pre-designed porphyrinic UNLPF-2 [UNLPF: University of Nebraska- Lincoln Porous Framework; $Co_2(CO_2)(CoL)(H_2O)$; L: tetrakis-3,5-bis[(4carboxy)phenyl]phenyl porphine] from single crystal X-ray diffraction. UNLPF-2 was synthesized using the octatopic porphyrin linker providing optimal distance between open metal sites and forming CO_2-specific molecular traps.[25]

Apart from CO_2 capture, MOF-based solid state adsorbents can be utilized for various types of hydrocarbon separation.[13] For example, ZIF-7 and RPM-3-Zn [ZIF: Zeolitic Imidazole Framework, $Zn(phim)_2$; phim: benzimidazole, RPM: Rutgers Porous Material; $Zn_2(bpdc)_2(bpee)$; bpdc: 4,4'-biphenyldicarboxylate, bpee: 1,2-bipyriylethylene] can separate C_2-C_4 hydrocarbons, due to the gate opening effect, appearing at different pressures for smaller and larger molecules.[32] MOF-5 [$Zn_4O(bdc)_3$] was reported to separate methane from n-butane, and linear from branched alkanes.[33] HKUST-1 [HKUST: Hong Kong University of Science and Technology; $Cu_3(btc)_2$; btc: 1,3,5-benzenetricarboxylate] separates o-, m- and p-xylenes, as reported from the study of gas chromatography in capillary columns.[34]

There are limited amount of reports describing structures of MOFs loaded with hydrocarbon gases.[30d] Long and coworkers recently reported the neutron diffraction study on C_2-C_3 hydrocarbon adsorption on Fe-MOF-74, which selectively adsorbs olefins over paraffins. The selectivity originates in the stronger interaction between unsaturated than saturated hydrocarbons with bare Fe(II) sites, as determined from the distances between adsorbate and the open metal site.[35] Kitagawa and coworkers used the *in-situ* synchrotron X-ray diffraction technique to discover the structural reasons for a high uptake of acetylene, and they located sorption sites for acetylene in a small pore MOF – $Cu_2(pzdc)_2(pyz)$ [pzdc = pyrazine 2,3-dicarboxylate, pyz = pyrazine] (Fig. 1.8).[36] Further, MIL-47 [V(O)(bdc)] and MIL-53-Cr can separate xylene isomers, with MIL-47 displaying higher values of selectivity due to the entropic effect.[37] The structure of xylene-loaded MIL-47 was determined with the Rietveld refinement using the synchrotron X-ray powder diffraction data.[37]

Single crystal X-ray diffraction was used to characterize adsorption mechanisms of C_1-C_2 hydrocarbons in several MOFs, but only a very limited number of those studies are reported to date.[30d] Kim and coworkers characterized the methane adsorption mechanism in $Zn_2(bdc)_2(dabco)$ [bdc = 1,4-benzenedicarboxylate, dabco = 1,4-diazabicyclo(2.2.2)octane], as well as the acetylene adsorption on Mg and Mn formates.[38] The adsorption sites of various gases, including methane and acetylene in a $Sc_2(bdc)_3$ framework were reported by Miller *et al.*[19] Finally, Zhang and Chen reported acetylene and carbon dioxide adsorption mechanism in MAF-2 (MAF: metal azolate framework; Cu(etz); Hetz: 3,5-diethyl-1,2,4-triazole), with a maximum acetylene uptake some 40 times higher than for acetylene in a gas cylinder at 1.0 – 1.5 bar, due to the optimal geometry of the framework pores.[39]

In conclusion, application of porous MOFs presents opportunities for CO_2 sequestration or hydrocarbon separation as currently used alakolamine solutions and zeolites suffer from high toxicity and water sensitivity, respectively. MOFs, especially those based on Earth abundant metals, offer many advantages, including low toxicity, extremely high surface areas and ease of modifications and tailoring for specific uses. In order to ascertain their utility, further research is needed to produce tailor-made, inexpensive, industrially applicable MOFs. Structural studies of the gas binding sites within MOF pore space contribute to our understanding of the specific interactions responsible for enhanced adsorption and selectivity, and can assist with new synthetic targets for various gas separation processes.

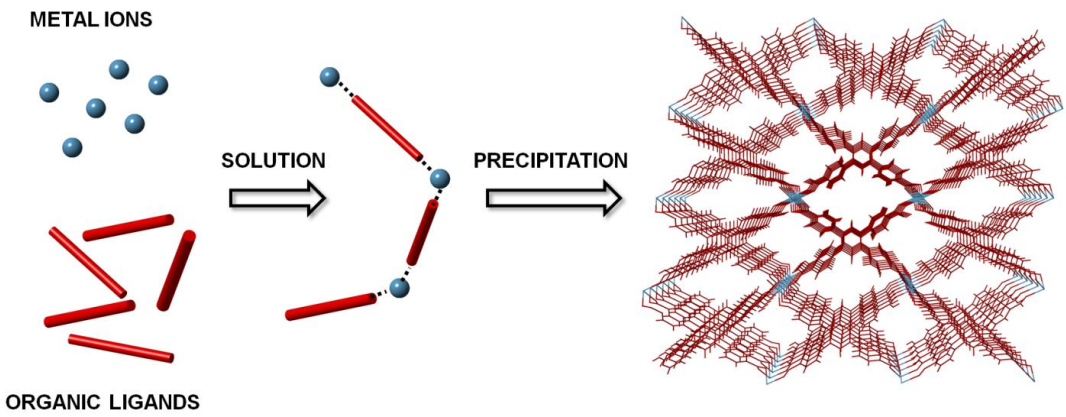

Figure 1.6 Formation of MOFs; metal ions and linkers are binding in the solution forming infinite structures

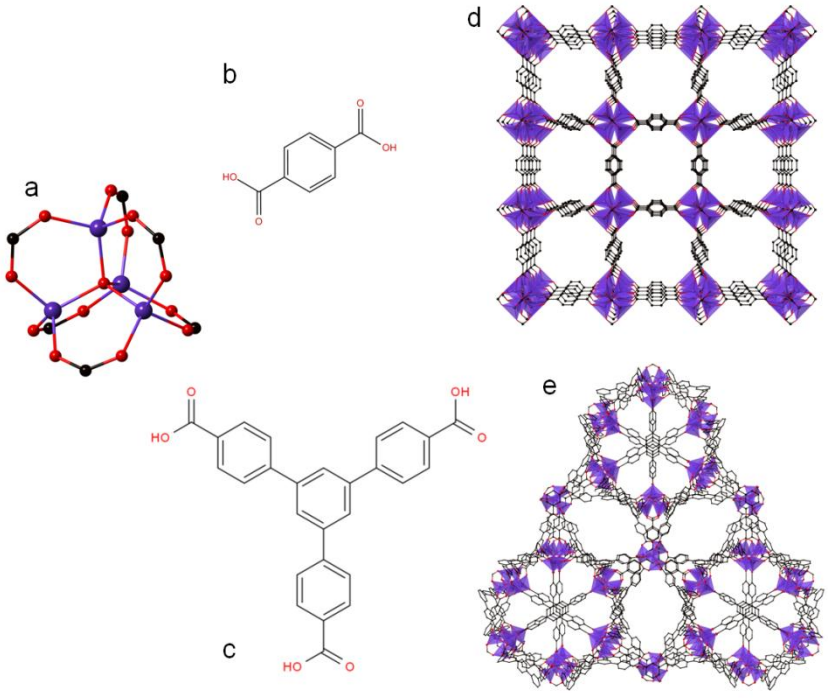

Figure 1.7 Example of how resultant MOF topology depends on the linker. (a) $[Zn_4O]$ cluster appearing in both structures (b) ligand used in synthesis of MOF-5 and (c) MOF-177. (d) Structure of MOF-5, (e) structure of MOF-177. Purple spheres and polyhedra represent Zn, black – carbon and red – oxygen. Hydrogen atoms omitted for clarity.

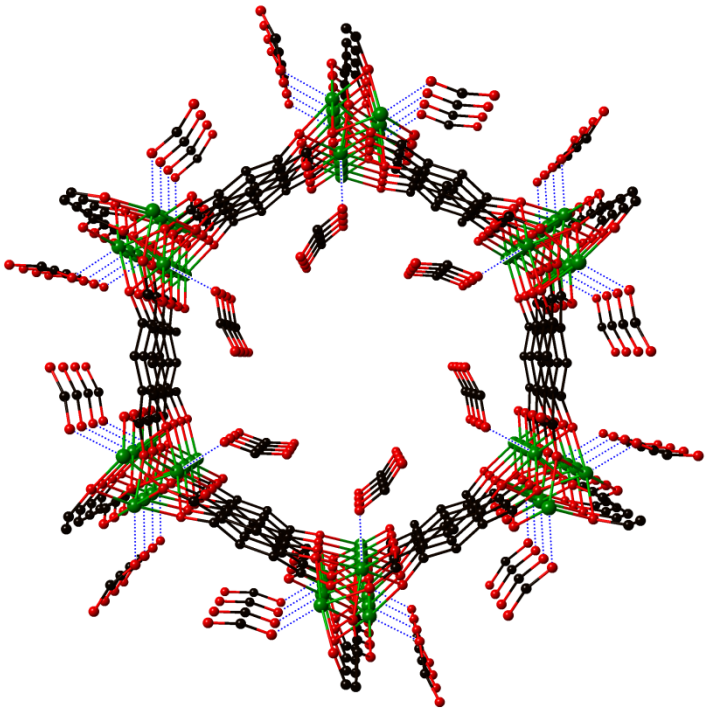

Figure 1.8 Structure of Ni-MOF-74 after loading with CO_2. Green spheres represent Ni, black – carbon and red – oxygen. Hydrogen atoms omitted for clarity.[30a]

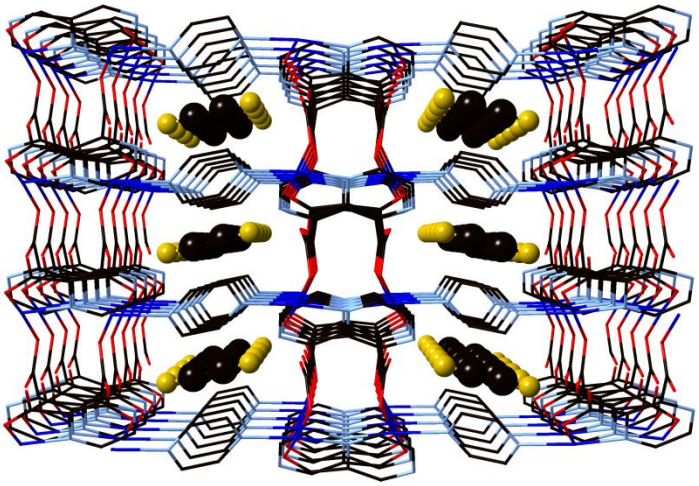

Figure 1.9 Crystallographic structure of $Cu_2(pzdc)_2(pyz)$ after loading with C_2H_2. Navy blue wire represent Cu, light blue – N, black – carbon and red – oxygen, yellow sphere – hydrogen. Hydrogen atoms from the framework omitted for clarity.[36]

Chapter 2

Experimental Methods

2.1 Synthesis of Metal Organic Frameworks

All MOF materials described herein were synthesized with solvothermal methods. Usually, solvothermal synthesis of MOFs is conducted with water or organic solvents at the temperatures above 100°C. Such temperatures exceed boiling points of the majority of solvents, so the synthesis is conducted using autoclaves as 'pressure-vessels'. Teflon-lined stainless steel Parr® Autoclaves, used herein, can be utilized for the synthesis up to 250°C and approximately 150 bar. Examples of solvents used for the MOF synthesis include ethanol, water, methanol, dimethylformamide (DMF), diethylformamide (DEF), benzene, cyclohexane etc. or mixtures of them. The use of organic solvent/water mixture for the synthesis can improve the solubility of the reactants, as often the metal salt is soluble in water, and the organic ligand is soluble in organic solvent.[40] It is also postulated that the mixture of solvents is advantageous for the growth of the large crystals necessary for the crystal structure determination.[40]

A typical synthesis for MOFs in this thesis involves mixing of appropriate metal salts and organic linkers with either pure or mixture of solvents, followed by mixing the resultant slurry for 1-4 hours to achieve a homogenous solution. The solution was then heated in Teflon-lined stainless steel Parr® Autoclaves for 2-5 days. The solvents used for this work include ethanol, methanol, DMF, water and their mixtures. The as synthesized materials were filtered, washed with ethanol or DMF, while still on the filter paper, and then air dried.

2.2 Thermogravimetric Analysis

Thermogravimetric analysis (TGA) is a technique where the sample is placed in a controlled atmosphere and heated with the constant rate, to measure the change of mass as a function of the temperature or time.[41] A shape of the TGA curve reveals various information about the material, including but not limited to the materials' thermal stability, essential for industrial applications, or the purity of the sample. In the case of MOFs containing solvent molecules within the pores, the TGA curve shows several weight loss steps, where first steps correspond to the removal of the solvent (activation) and the final step indicates decomposition of the material. TGA experiments are crucial for the gas adsorption studies in porous MOFs, as they provide information on the temperature necessary for the activation of the material. The activation temperature depends on the topology of the framework, nature of the solvent and the strength of the guest-network interaction. Dense MOFs with no guest molecules display only final weight-loss step, where the framework decomposes due to the removal of organic linkers.

TGA traces for materials described below were collected using a Netzsch 449C Jupiter instrument. The instrument operates in the temperature range from room temperature (RT) to 1500 °C and is equipped with a microbalance of ± 0.01 mg accuracy. Before data collection a background curve is measured with an empty alumina crucible. Next, approximately 10 mg of the sample is placed into the alumina crucible, which is then heated to 750 °C at a rate of 10 °C /min in a N_2 atmosphere. The weight of the sample is monitored throughout the experiment.

2.3 Differential Scanning Calorimetry

Differential scanning calorimetry (DSC) is an analytical technique that measures the difference of heat required for the increase of the sample temperature, with respect to a known standard, as a function of temperature. The sample and the reference are kept at the same temperature which is increased with the constant rate. The technique allows for the detection of exothermic or endothermic phase transitions such as melting, crystallization or glass transitions.[41] Measuring the difference of a heat flow between the sample and the reference provides an estimate of the amount of heat adsorbed or released during such transitions. DSC can also be used as a method to measure the enthalpy of gas adsorption on porous MOFs (see 2.6).

The result of the DSC experiment is a curve of the heat flow versus temperature and time. Positive or negative peaks correspond to exothermic or endothermic reactions, respectively, and the integration of the peak provides the enthalpy of such reactions. The enthalpy of the reaction ($-\Delta H$) can be expressed as:

$$-\Delta H = C \times A \qquad (2.1)$$

where A is the area under the peak and C is the calorimetric constant. The constant varies with different instruments and needs to be measured with a standard material possessing a well-known enthalpy of transition.[41]

DSC data of materials described herein were collected using a Netzsch 449C Jupiter instrument as accompanying datasets to the TGA analysis. The DSC method was also used in conjunction with simultaneous observation of the XRD pattern in order to estimate heats of adsorption of CO_2, N_2 and hydrocarbon gases, along with structural changes occurring during that adsorption, using a Rigaku® Ultima IV diffractometer equipped with a DSC stage (see 2.6).

2.4 Gas Adsorption Measurments

2.4.1 Gas Isotherms

Gas adsorption isotherms were collected at Rutgers University in the laboratory of Prof. Jing Li.

Gas adsorption is defined as the addition of atoms, ions or molecules from a gas medium onto a surface of solid or fluid.[42] In contrast to absorption, where adducts enter the bulk phase, adsorption appears in an interfacial layer. Adsorption can be further divided into two categories depending on the nature of the adsorbate-adsorbent interaction: chemisorption and physisorption.[21a] Chemisorption occurs when the atoms on the surface form chemical bonding with a sorbent. Physisorption, on the other hand, is characterized by weak van der Waals adsorbate-adsorbent interactions; physisorption does not involve a major change in the electronic structure of interacting species. Chemisorption is limited to a single layer on the surface, while physisoprtion can be accompanied with the multilayer adsorption, which may change with temperature.

The gas adsorption studies of the materials described herein were performed with a volumetric gas sorption analyzer (Autosorb-1-MP, Quantachrome Instruments) with the ultra-high purity gases (99.999%). Initially, approximately 100 mg of the sample was activated at an elevated temperature, under vacuum, for 12 hours, and the weight was measured before and after activation to ensure the full solvent removal. After cooling, isotherms were collected at three different temperatures in the pressures up to 1 bar. The activation step was repeated for the same sample between each run.

2.4.2 Surface Area

Porous materials are classified based on their pore sizes dimensions, including the size of the window leading to the pore, into three categories: 1) macroporous (pore window dimaterer > 500 Å), 2) mesoporous (pore window diameter 20 -500 Å) and 3) microporous (pore window diameter < 20 Å).[21a] Of the MOFs reported as showing reversible gas uptake, the majority are microporous. Further, microporous materials can be divided into supermicroporous and ultramicroporous, with pore window sizes 7-20 Å and < 7 Å, respectively.[21a]

The adsorption mechanisms in MOFs cannot be represented by a Langmuir theory, as it applies to homogenous surfaces with monolayer adsorption.[21a] The pores surface in MOFs is heterogeneous with specific adsorption sites within metal nodes or organic linkers.[21a] At low pressures the strongest adsorption sites are occupied first, and the weaker sites occupied later at higher pressure.[21a] In the case of materials with pores of different sizes, smaller pores are occupied preferentially at lower pressure and larger pores are filled later.[21a] For the estimation of a MOF surface area Langmuir theory may not provide accurate results, due to localized adsorption on ultramicroporous MOFs and multilayer adsorption on supermicroporous MOFs.[21a]

The surface area of MOFs is usually measured with a N_2 adsorption, applying the Brunauer-Emmett-Teller (BET) theory.[43] The theory allows determining the surface area of the material, based on the amount of gas adsorbed at a given pressure.[43] The concept of the BET theory expands the Langmuir theory from single layer molecular adsorption, to molecular adsorption on multiple layers, where adsorption on each layer follows the Langmuir theory. The BET theory assumes that 1) the adsorption involves only specific strong sites, 2) the outer molecule layer is in equilibrium with the gas, 3) there are no lateral interactions within the

adsorbed layers, 4) at a saturation pressure a number of adsorbed layers is infinite, 5) the desorption is controlled kinetically.[44] BET is widely used for the surface area measurments, due to its simplicity and ease of implementation.

In this work, the surface area of the materials was characterized using a Quantochrome Nova 2200e Surface Area Analyzer instrument. Before the analysis, samples were activated under vacuum by heating overnight, which removes water or other solvent molecules present in the pores of a native, as-synthesized materials. The desolvation temperature was determined from TGA of the respective compounds. After the solvent removal, materials were weighted to confirm full evacuation of the pores. For the analysis, samples were cooled to -196 °C in liquid nitrogen, and a sample tube was filled with N_2 gas with a known reference pressure. The surface area and the pore volume were calculated from the decrease in pressure, arising from the N_2 diffusion within the pore space.

2.4.3 Heat of Adsorption

Isosteric heat of adsorption (Q_{st}) is the interaction energy between a gas molecule and a MOF framework. Q_{st} can be calculated from the gas adsorption isotherms, collected at two different temperatures, by fitting the isotherms to the Langmuir-Freundlich equation, or virial equation.[21a] Those calculations deliver the heat of adsorption as a function of adsorbed amount of gas, even though they do not provide information on the localization and the number of gas adsorption sites. The zero-coverage isosteric heat corresponds to the interaction energy between the gas molecule and the strongest adsorption site within the MOF framework.[21a]

Other method for estimating Q_{st} of the adsorbed gas is a direct measurement with differential scanning calorimetry (see 2.6).

2.4.4 Ideal Adsorbed Solution Theory

IAST calculations were performed by Zhijuan Zhang and Hao Wang at Rutgers University.

An ideal adsorbed solution theory (IAST), developed by Myers and Prausnitz,[45] is used to simulate the competitive loading of a gas mixture on a material, based on adsorption isotherms of individual components.[46] IAST is widely used to calculate a gas adsorption selectivity in porous materials such as MOFs.[46] The IAST model assumes that 1) all adsorbates have the same surface area available; 2) the multi-component mixture is an ideal solution, meaning that the strength of interaction between molecules of each component is equal at constant temperature and pressure; 3) the adsorbent is inert.

The relation between mole fraction of the adsorbed phase (x_i) and the mole fraction of the bulk gaseous phase (y_i) of the component *i* at a given pressure (p) is:

$$p \times y_i = p_i^0(\pi^*)x_i \qquad (2.2)$$

where p_i^0 is the pressure of component *i* and π^* is the spreading pressure of the gas mixture. π^* is described by:

$$\pi^* = \int_0^{p_i^0} \frac{q_i}{p} dp \qquad (2.3)$$

where *qi* is the adsorbed amount of component *i* under pressure *p* obtained via single component isotherm.

At equilibrium the spreading pressure of each component is the same:

$$\pi_i^* = \pi_j^* \ (i \neq j) \qquad (2.4)$$

The adsorption selectivity ($S_{i/j}$) of component *i* over *j* is defined as:

$$S_{i/j} = \frac{x_i / x_j}{y_i / y_j} \qquad (2.5)$$

To perform the IAST calculations, an adsorption model is needed in order to fit a discrete set of adsorption data from single-component isotherms with a continuous function.[46] In this work we used a Dual-site Langmuir-Freundlich (DSLF) model for the fitting of the adsorption isotherms. There is no limitation on the adsorption model used, but DSLF is found to fit the isotherms in the most precise manner.[47]

The DSLF model can be expressed as follows:

$$N = N_1^{max} \times \frac{b_1 p^{1/n_1}}{1 + b_1 p^{1/n_1}} + N_2^{max} \times \frac{b_2 p^{1/n_2}}{1 + b_2 p^{1/n_2}} \qquad (2.6)$$

Here, p is the pressure of the bulk gas at equilibrium with the adsorbed phase, N is the adsorbed amount per mass of the adsorbent, N_1^{max} and N_2^{max} are the saturation capacities of sites 1 and 2, respectively; b_1 and b_2 are the affinity coefficients of sites 1 and 2, and n_1 and n_2 represent the deviations from an ideal homogeneous surface.

2.5 Powder Diffraction

The diffraction data of gas-loaded MOFs can be collected from single crystal or powdered samples; the two techniques are complementary. However, single crystal X-ray diffraction method requires high quality single crystals, which for some materials cannot be obtained. Also, long data collection times, some 8 or more hours per sample per temperature on a

laboratory instrument, require that the gas loaded sample is in the equilibrium conditions. Powder diffraction data provide less information, but the data collection time is also much shorter (approximately 30 min on the laboratory instrument), which allows for determination of structural changes that the flexible framework may undergo upon gas adsorption/desorption.

The diffraction maxima appear when a subset of crystallites is in an orientation that satisfies Bragg's law:

$$\lambda = 2d_{hkl} \sin\theta_{\eta\kappa\lambda} \qquad (2.7)$$

where, λ is a wavelength of the incident wave, $\theta_{\eta\kappa\lambda}$ is a scattering angle, and d_{hkl} is an interplanar distance for the planes with Miller index *hkl* in the crystal structure of the material. On the diffraction pattern the intensity of scattered X-ray is plotted versus 2θ.

In this work PXRD data were collected in order to determine the structural changes of MOFs upon the gas adsorption and desorption. PXRD was also used to determine the purity of the as-synthesized samples and for the phase analysis after solvent-exchange reactions. Data were collected using a Rigaku® Ultima-IV diffractometer equipped with Cu Kα (λ = 1.5405 Å) radiation. The diffractometer is configured in Bragg-Brentano parfocusing geometry where the incident beam and take-off geometry are fixed at the θ/θ configuration. X-rays were generated at 40KV and 44mA.

2.6 XRD-DSC

Simultaneous measurement of powder XRD and differential scanning calorimetry (DSC) under either static or dynamically varied relative humidity (RH), temperature, and gas, is a particularly powerful technique for gas adsorption studies in MOFs. In one loading of the sample, we follow structural changes upon activation, and effects of gas, gas-mixtures, temperature, RH – varied serially or in combination – on the structure and thermal response.[48]

The *in situ* XRD-DSC experiments were performed with the laboratory instrument Rigaku® Ultima-IV equipped with XRD-DSC stage (Fig. 2.1). The XRD-DSC stage allows for simultaneous collection of XRD and DSC data under a controlled atmosphere. A humidity generator (Rigaku® HUM-1) was used to control the humidity of the atmosphere during data collection. The DSC measurements were performed using 10-30 mg of sample in an aluminum crucible, with the equal amount of Al_2O_3 in the reference crucible.

In this work, two types of XRD-DSD experiments were performed – vacuum-swing and gas-swing experiments – using a custom made gas adsorption system (Fig. 1.2). During vacuum-swing experiments the atmosphere over the sample is cycled between gas and vacuum. When the atmosphere is changed from vacuum to gas, an exothermic effect is observed on the DSC curve. The area of the peak corresponds to the heat released from gas adsorption, and it allows for direct measurments of the enthalpy ($-\Delta H$; kJ/mol_{MOF}), which in turn can be used to calculate isosteric heat of adsorption (Q_{st}; kJ/mol_{GAS}) through the relation:

$$-\Delta H = Q_{st} \times n_i \qquad (2.8)$$

where n_i corresponds to the moles of the adsorbed gas and is determined with gas isotherms measurments.

Vacuum-swing experiments can be performed with different pressure steps. In a typical experiment 1 atm of gas is introduced in one step, which allows determination of the differential enthalpy between the empty pore and the gas-loaded MOF at ambient conditions (1 atm gas, RT). In the case of flexible compounds it is beneficial to increase the gas pressure in multiple steps, allowing reconstruction of the enthalpy of the gas adsorption before and after a phase transition. The interpretation of the PXRD data collected at different pressure steps also shows the structural changes accompanying the phase transition.

In a second type of XRD-DSC experiments, the atmosphere of the sample is changed between different gases. Here, we cycled CO_2/N_2 gases to qualitatively characterize the CO_2/N_2 selectivity of MOFs in dry and humid conditions. Gas-displacements that are exothermic indicate a preference for the displacing gas, and those that are endothermic indicate a preference of the framework for the gas being displaced. The area under the exothermic peak corresponds to a difference between CO_2 adsorption and N_2 adsorption enthalpy. Through the introduction of humidity in the gas flow we can also determine how effectively CO_2 competes with water at the strong adsorption sites.

Before vacuum and gas-swing experiments the sample was activated *in situ* on the XRD-DSC, and held at elevated temperature for 5-12 hours, to ensure a full evacuation of the pores. After the activation the sample was cooled to the room temperature. For the 1-step vacuum-swing experiment the chamber was pressurized to 1 atm of gas over the course of 10 seconds. After 2-30 minutes, when the DSC signal returned to the baseline, the chamber was evacuated to vacuum again over the course of 10 seconds. A total of 3-10 cycles were completed. In the case of the multiple-step vacuum-swing, gas pressure was increased in ~0.1 bar steps up to 1 bar, and then decreased to 0 bar (vacuum) also in ~0.1 steps.

In the gas-swing experiment the activated sample was exposed to the N_2 atmosphere at a constant flow rate of 50 ml/min, until the DSC signal returned to the baseline, and then the atmosphere was switched to CO_2 and held in CO_2 for an hour. Changes were made every hour for 12 hours. CO_2/N_2 gas-swing experiments were performed in 3%, 30% and 75-80% RH.

2.7 Single Crystal X-ray Diffraction

The most informative technique for directly obtaining structural information regarding CO_2 or other gases bound to the pore surfaces of MOFs is via single crystal diffraction studies (SCXRD).[30d] Here, the activated crystal is loaded with gas, diffraction data are collected and structural refinements are subsequently performed in order to reveal the location of the adsorbed gas molecules. SCXRD allows for direct structure solution and very accurate refinements, including gas molecules occupancy and positional disorder. Single crystal diffraction is also a necessary tool for the structure determination of most new, as-synthesized MOFs. Powder XRD usually does not provide sufficiently high data-to-parameter ratio for the structure solution of materials with complex topologies such as MOFs.[30d]

Single crystal diffraction method relies on the measurments of position and intensity of thousands reflections from one representative crystal. The crystal chosen for SCXRD experiment is preferably single, although modern methods of data analysis allow for modeling of twinning to some extent. Structure factor for each hkl reflection can be assigned using the equation:

$$F_{hkl} = \sum_i f_i \, exp[2\pi(hx_i + ky_i + lz_i)] \quad (2.9)$$

where f_i corresponds to a scattering factor of the atom i and x_i y_i and z_i are the fractional coordinates of the atom i.

Further, the electron distribution in the crystal can be represented as a three dimensional Fourier series:

$$\rho(x,y,z) = \frac{1}{V}\sum_{h}\sum_{k}\sum_{l} F_{hkl} \exp\,[-2\,\pi i(h_x + k_y + l_z)]$$

(2.10)

where $\rho(x,y,z)$corresponds to the electron density at fractional coordinates *x y z* and *V* is a unit cell volume. After determining the F_{hkl} structure factors, the positions of the atoms within the unit cell can be deduced by calculating the electron density distribution.

The measured intensity of the reflection I_{hkl} corresponds to the structure factor F_{hkl} through the following:

$$I_{hkl} \propto {F_{hkl}}^2 \qquad (2.11)$$

Because the structure factors are proportional to square root of measured intensity, the phase information is lost. There are several methods of structure solution designed to overcome this phase problem. In this work a direct method was used for all the structure solutions using the SHELXS software.[49] In the direct method all phases are derived *ab initio* from the measured intensities. The phase calculation is performed statistically by using a random set of starting phase values.

After initial solution of the crystal structure positions of the atoms and their displacement is optimized with a least-square refinement. The displacement of the atom around their equilibrium positions is preferably refined anisotropically, as an ellipsoid described by six parameters.

The quality of the structure refinement can be judged with the R_1 factor defined by:

$$R_1 = \frac{\sum|F_{obs} - F_{calc}|}{\sum|F_{obs}|} \qquad (2.12)$$

where F_{obs} correspond to experimentally measured structure factors and F_{calc} are structure factors calculated from the current model. Ideally R_1 approaches zero, once no more differences exist.

In this work, crystal structures of the as-synthesized, activated and gas-loaded compounds were refined using the SHELXTL software.[49-50] All of the non-hydrogen atoms were refined anisotropically. Hydrogen atoms were added to the structure model using geometrical constraints. The position for the adsorbed gas molecules were located in the Fourier difference maps, calculated with the WingX suite.[51] The occupancy of the atoms in gas molecules was refined. Finally, most of the bond lengths within adsorbed gas molecules were restrained to standard values.[52]

Materials used for the single crystal diffraction studies of gas adsorption herein do not contain open metal sites within pore space. Further, the pores remain empty after activation, even in the presence of air and humidity, as analysis of single crystal diffraction data did not reveal any significant residual electron density remaining inside the channels of activated samples after exposure to air. The lack of open metal sites and water adsorption from the air allowed for loading the crystal with gases *ex situ*. After activation under vacuum, crystals were briefly exposed to air (<1min) before placing them in the gas atmosphere for gas loading.

For the CO_2 loading the activated sample was placed together with pieces of solid CO_2 into a 37ml Teflon bottle sealed with Parafilm®. Because the bottle was sealed with sublimating dry ice inside, the pressure of CO_2 reached level above 1 atm. The Parafilm® seal was thick enough to contain the pressure but some expansion of the film was observed. After an hour the bottle was open with the dry ice still present inside, and Paratone® oil was poured to coat CO_2-loaded crystals (Fig. 2.3). Then the crystals were analyzed under an optical microscope, fitted with polarizing optics. Those crystals showing sharp extinction when rotated under crossed

polars were judged to be of good quality; subsequent structure analysis was carried out on a subset of these crystals.

For hydrocarbon loading activated single crystals were placed in a three-neck flask with hydrocarbon gas flowing over sample to maintain the pressure of 1 atm of the gas (Fig 2.4). The sample was kept under the flowing gas for 2-5 hours to ensure a full loading. Further, crystals were coated with Paratone® oil to retain the adsorbed gases within the pores, while keeping the gas flow to maintain 1 atm conditions.

Laboratory single crystal data for freshly synthesized, activated and gas-loaded crystals were collected using a four-circle kappa Oxford Gemini diffractometer, equipped with an Atlas detector and Mo Kα and Cu Kα X-ray sources (λ = 0.71073 Å and 1.54184 Å, respectively), with 1° ω scans, at approximately 100 K. The raw intensity data were collected, integrated and corrected for absorption effects using CrysAlis PRO software.[53]

In the case of compounds that do not form large crystals (<100μm), laboratory single diffractometers do not provide sufficiently high X-ray intensity for structure characterization. We used the X-ray diffraction setup at Advance Photon Source (APS) for studies of microcrystalline compounds. Synchrotron sources offer exceptionally high brightness, tunability and low divergence of X-ray beam, presenting the opportunity to study crystals as small as ~ 5μm. In comparison to laboratory diffractometers, synchrotron radiation is ten orders of magnitude brighter. Reflections for compounds were collected at 100 K using a three-circle Bruker D8 diffractometer, equipped with an APEX II detector, with the X-ray wavelength λ = 0.41328 Å, using 0.5° φ scans at APS ChemMatCars (sector 15) beamline. The raw intensity data were collected, integrated and corrected for absorption effects with the Apex II software suite.[54]

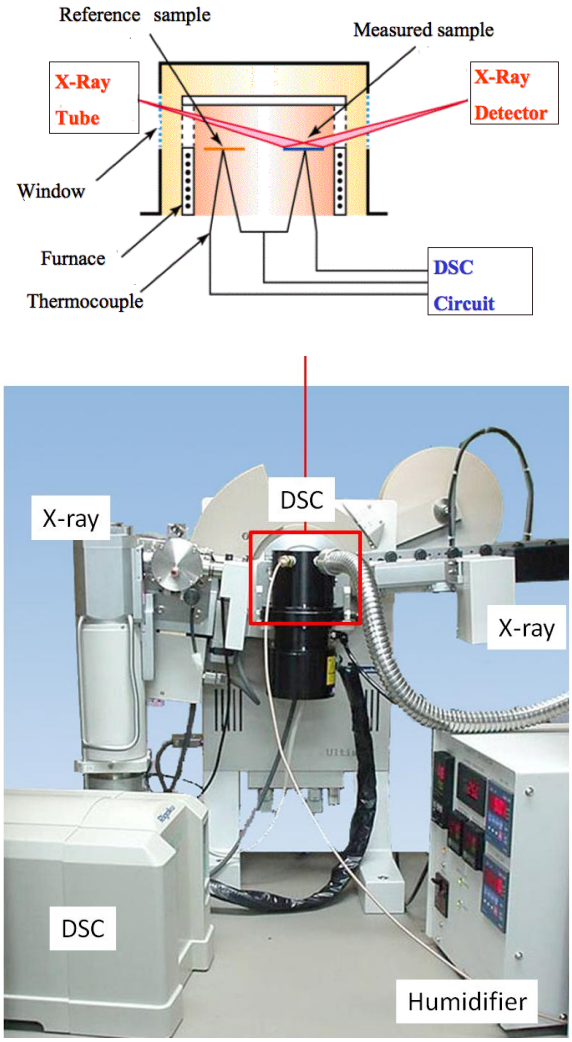

Figure 2.1 (top) Schematic diagram of the sample chamber in the XRD-DSC unit shown (bottom) mounted on a Rigaku® diffractometer. The temperature on a reference sample and a measured sample is monitored with thermocouples. The X-ray beam is focused on the measured sample. The heat flow difference between the reference and the measured sample is followed, and diffraction data from the measured sample are collected throughout the experiment. The XRD-DSC unit is connected to gas and vacuum lines, allowing for changes in the gas atmosphere and pressure. The humidifier is used to control the humidity of the chamber (3%-80% RH).

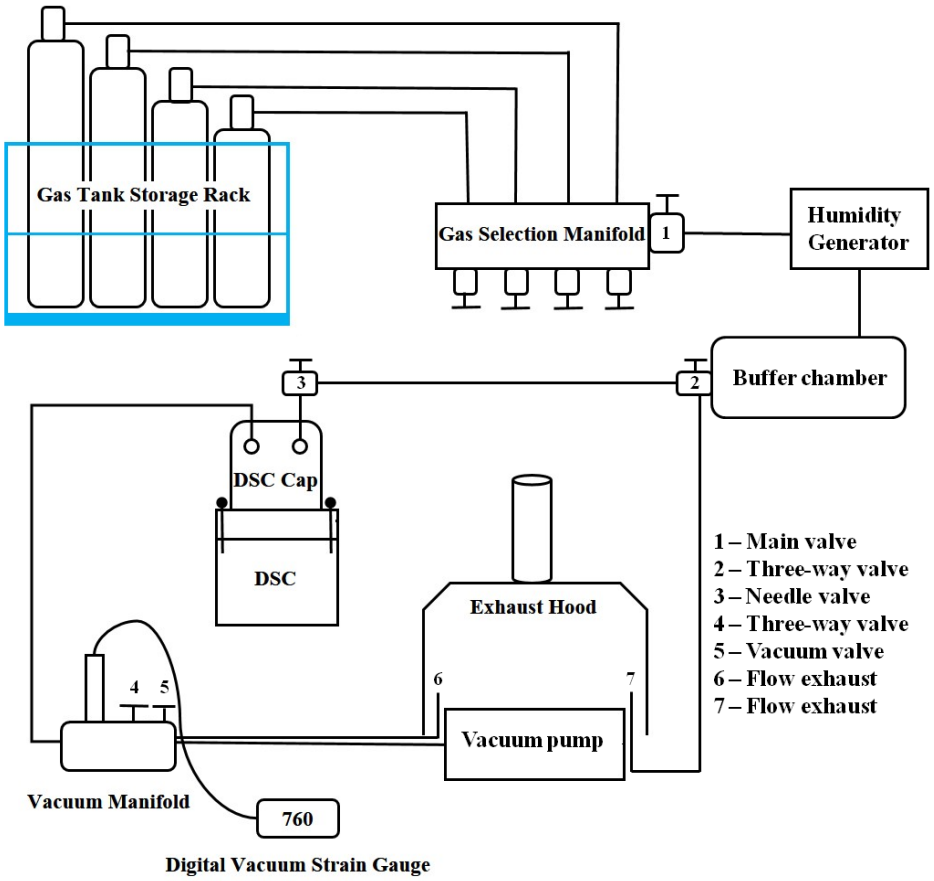

Figure 2.2 Schematic diagram of the vacuum-/gas-swing apparatus connected to the XRD-DSC unit (courtesy of W.R. Woerner, modified). DSC chamber contains a base (DSC on the figure) and a DSC cap. The cap can be removed in order to place a sample inside the DSC chamber. After placing the sample and a reference inside, the cap is placed back on the unit. In and out gas lines are connected to the cap. A gas selection manifold allows change between gases during the gas-swing experiment. Main valve (1) is used to close the gas flow before gas enters lines directly connected to the DSC unit (safety valve). A humidity generator controls the humidity in the DSC chamber (0%-80% RH). A buffer chamber is used to stabilize the RH of the flowing gas. When gas is changed, a three-way valve (2) is open towards a flow exhaust (7) until the RH of the flowing gas stabilizes on a desired level. During the vacuum-swing experiment a needle valve (3) is used to precisely control the pressure in the DSC chamber, when changing from a vacuum to a gas atmosphere. Pressure is measured with a digital vacuum strain gauge. A vacuum manifold contains the strain gauge, a three-way valve (4) and a vacuum valve (5). The three way valve allows change from a vacuum line used in vacuum-swing experiments to a flow exhaust line (6) used in gas-swing experiments. The vacuum valve (5) opens the line to vacuum pump.

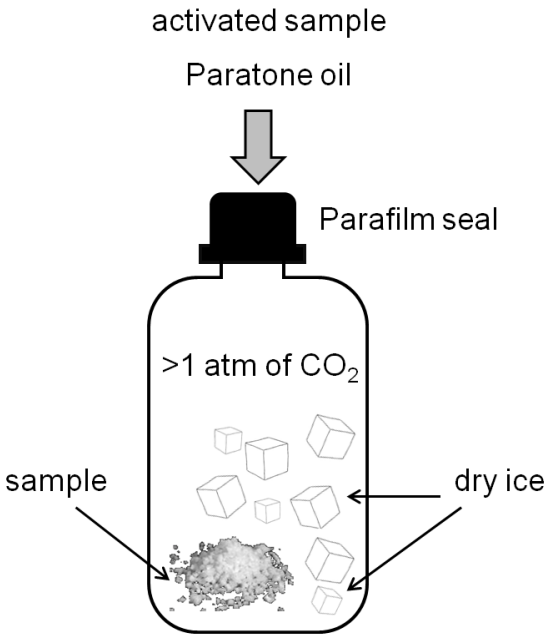

Figure 2.3 Schematic diagram of the CO_2 loading procedure prior to performing the single crystal XRD experiment.

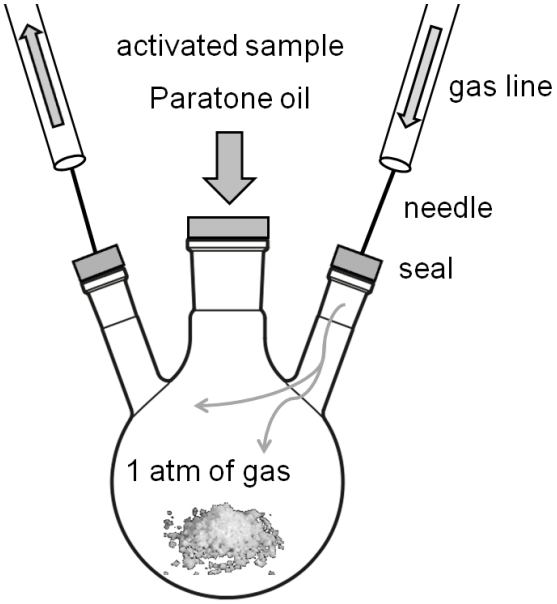

Figure 2.4 Schematic diagram of the hydrocarbon gases loading procedure prior to performing the single crystal XRD experiment.

Chapter 3

Mechanism of Carbon Dioxide Adsorption on a Highly Selective Ca-based Metal Organic Framework from Direct Structural Evidence

The content of this chapter is published in

Plonka, A. M.; Banerjee, D.; Woerner, W. R.; Zhang, Z.; Nijem, N.; Chabal, Y. J.; Li, J.; Parise, J. B.

Angew. Chem. Int. Ed. **2013,** *52* (6), 1692-1695.

3.1 Abstract

Much current work focuses on the design of functionalized metal organic frameworks (MOFs) that selectively adsorb CO_2.[5] While interactions between CO_2 molecules and the π clouds of aromatic linkers in MOFs under ambient conditions have been explored theoretically, to date only a few structural reports provide evidences of such interactions.[30d] Here we provide direct structural insight into CO_2-π interactions in a porous calcium-based MOF. The direct evidence is based on results from single crystal X-ray diffraction methods, and is supported by powder diffraction coupled with differential scanning calorimetry (XRD-DSC), *in-situ* IR/Raman and molecular simulation data. We postulate that such interactions are responsible for the high CO_2/N_2 sorption selectivity (45-85), even in the presence of high relative humidity (RH). Our data suggest that the key interaction responsible for such selectivity, the room temperature stability and the relative insensitivity to RH of the CO_2-MOF adduct, is between two phenyl rings of the linker in the MOF and the molecular quadrupole of CO_2. The specific geometry of the linker molecule results in a 'pocket' where carbon from the CO_2 molecule is placed between two centroids of the aromatic ring leading to high heat of adsorption (Q_{st} = 31 kJ/mol). Our

experimental confirmation of this variation on theoretically postulated interactions between CO_2 and phenyl will promote the search for other MOFs containing phenyl-ring pockets.

3.2 Introduction

Ca(sdb) (sdb: sulfonyldibenzoate) is a recently reported porous MOF with high CO_2/N_2 selectivity.[55] At 0.15 bar of CO_2 and 0.85 bar of N_2, a typical composition of flue gas mixture from power plants, the selectivity is in the range of 48 – 85 at 298 K. **Ca(sdb)** shows a reversible uptake of CO_2 of 5.75 wt% at 273K and 1 bar pressure and 4.37 wt% at room temperature, with heats of adsorption for CO_2 and N_2 of 31 kJ/mol_{GAS} and 19 kJ/mol_{GAS}, respectively. The as-synthesized compound contains uncoordinated water molecules and is easily activated for gas sorption by heating to 290 °C in vacuum; remarkably the activated framework does not reabsorb water, even if exposed to RH > 85%. The structure of the compound is based on CaO_6 octahedral chains, interconnected by organic linkers, resulting in infinite, diamond-shaped channels with ca. 5.9 Å × 5.8 Å in free diameter, built by double layer of phenyl rings, running in the [010] crystallographic direction (Fig. 3.1). The structure contains neither open metal sites, nor additional functionalities generally associated with sites for selective CO_2 sorption in the current literature,[5] raising questions of the structural origin for **Ca(sdb)'s** selectivity.

In this work we employ the single crystal X-ray diffraction technique to solve the crystal structure of a **Ca(sdb):CO_2** adduct at 110K and room temperature. In combination with powder X-ray diffraction (PXRD), Raman and IR spectroscopy, theoretical calculations and real time XRD-DSC, the CO_2 gas adosorption mechanism in **Ca(sdb)** is accurately described. We find that the unique architecture of the sdb linkers is responsible for the strong affinity for CO_2.

3.3 Experimental Section

3.3.1 Synthesis and Activation of Ca(sdb)·nH$_2$O

Compound **Ca(sdb)·nH$_2$O** was synthesized via solvothermal method. Starting materials include 4,4'-sulfonyldibenzoic acid (H_2sdb, $C_{14}SO_6H_{10}$, 98%, Sigma-Aldrich), calcium chloride ($CaCl_2$, 96% Acros-Organics) and ethanol (95%, Fisher-Scientific) and were used without further purification. A mixture of 0.0006 moles of Ca salt ($CaCl_2$, 0.074 g) and 0.0006 moles of H_2sdb acid (0.198 g) was dissolved in 10 g of ethanol (molar ration of metal salt/linker/solvent 1:1:380) and stirred for 3 hours to achieve homogeneity. The solution was placed in an oven in 180°C and held at 180°C for 4 days. Products of the reaction were the colorless, prism-shaped crystals, which after recovering from the reaction were filtered and washed with ethanol (yield: 50% based on Ca, ~0.100 g). The water in the pores of as-synthesized **Ca(sdb)·nH$_2$O** was delivered from 95% ethanol or from $CaCl_2$ reactant contained as adsorbed moisture. For the removal of water **Ca(sdb)·H$_2$O** was activated in vacuum at 290 °C overnight.[55] The resulting material was crystalline and free of impurities, as determined from powder XRD. During vacuum heating the compound transformed to the activated phase.[55]

3.3.2 Single Crystal XRD with Adsorbed CO_2

For the CO_2 loading procedure and single crystal diffraction details see the chapter 2.7, SCXRD was performed with Oxford Gemini diffractometer, λ = 0.71073 Å at 110K and RT.

The crystal structure of **Ca(sdb)·$(CO_2)_{0.32}$** was solved using direct methods (SHELXS).[49] Calcium and oxygen atoms were located first followed by determination of carbon atom positions from Fourier difference maps. All of the non-hydrogen atoms were refined anisotropically. Hydrogen atoms were added to the structure model using geometrical constraints (HFIX command for hydrogen atoms on aromatic C rings). The position for the CO_2 molecule was located in Fourier difference maps.[51] The occupancy of the atoms in CO_2 was refined to 32%. The C-O bond length was restrained to 1.16(1) Å. A summary of some important crystallographic details can be found in Table 3.1.

3.3.3 XRD-DSC

For the details of gas-swing and vacuum-swing procedure see the chapter 2.6.

Two different stages were used during data collection, an XRD-DSC stage and a low/medium temperature stage. The XRD-DSC stage allows for simultaneous collection of XRD and DSC data under a controlled atmosphere. The DSC measurements were performed using 9.6 mg of sample in an aluminum crucible with an equal amount of Al_2O_3 in the reference crucible. The XRD patterns (Fig. 3.6) were collected using the low/medium temperature Rigaku® stage. The low/medium temperature stage allows for a controlled atmosphere in the same manner as the

XRD-DSC stage but the use of a gram of sample as opposed to ~10 mg in the XRD-DSC stage provides higher quality XRD patterns.

Sample was first activated *in situ* at 290 °C under vacuum for 8 hours. For the vacuum-swing experiment a total of 10 cycles were completed. The gas-swing experiments were performed in 3% and 75% RH at room temperature (RT). The changes were made every hour for 12 hours.

3.3.4 Raman/IR Spectroscopy

Raman/IR experiments were performed by Nour Nijem at University of Texas-Dallas.

Raman spectroscopy measurements were performed using a solid state 532 nm laser. The sample was loaded into a Linkam FTIR600 cooling/heating stage, and the sample was heated to 290°C in N_2 purge for activation. A laser power of 10% (0.113-1.23 mW) was used to avoid sample degradation under the laser beam during the Raman measurements.

Infra-red (IR) absorption spectroscopy measurements were performed in transmission mode at room temperature using a liquid N_2 cooled Mercury Cadmium Telluride (MCT-A) detector. A small amount of **Ca(sdb)** ~5 mg was pressed onto a KBr support and mounted into a high temperature, high pressure cell (Specac product P/N 5850c) and heated overnight at 290^{o}C in dynamic vacuum for activation.

3.4 Theoretical Calculations

Theoretical calculations were performed by Zhijuan Zhang at Rutgers University.

3.4.1 Force Fields

Force fields play an important role in molecular simulations, and the adsorption behavior of CO_2 is extremely sensitive to the gradient of the electrostatic field inside the pores of a MOF structure. In this work, van der Waals (VDW) interactions between the framework and adsorbates were treated with a 12-6 Lennard-Jones (LJ) potential (see Eq. 3.1).[56] The cross-interaction parameters between different atoms were calculated using the Lorentz-Berthelot mixing rules (see Eqs 3.2 and 3.3).[57]

$$u_{LJ} = 4\varepsilon_{ij}\left[\left(\frac{\sigma_{ij}}{r_{ij}}\right)^{12} - \left(\frac{\sigma_{ij}}{r_{ij}}\right)^{6}\right] \qquad (3.1)$$

$$\sigma_{ij} = \frac{1}{2}(\sigma_i + \sigma_j) \qquad (3.2)$$

$$\varepsilon_{ij} = \sqrt{\varepsilon_i \varepsilon_j} \qquad (3.3)$$

where ε_{ij} is the depth of the potential well between atom *i* and *j*. σ_{ij} is the finite distance between atom *i* and *j* at which the inter-atom potential is zero. r_{ij} is the distance between the atoms.

Lennard-Jones (LJ) parameters for **Ca(sdb)** atoms were taken from the all-atom universal force field (UFF) and are presented in Table 3.5. The cutoff radii for **Ca(sdb)** were set to be 5.6 Å. CO_2 was modeled as a three-site rigid molecule, and its intrinsic quadrupole moment as described by a partial charge model. The partial charges on C and O atoms were q_C = 0.576e and q_O = -0.288e, respectively. The C-O bond length was 1.16 Å, and bond angle ∠OCO was 180°.

3.4.2 Density Functional Theory (DFT) Calculations

Many studies have demonstrated that it is very important to take the CO_2-MOF electrostatic interactions into account because of the large quadruple moment of the CO_2 molecule. In this work, the atomic charges of framework atoms were calculated from density functional theory (DFT) on the basis of the fragmental clusters cleaved from the unit cell of **Ca(sdb)** structure as illustrated in Figure 3.10. To maintain a correct hybridization, all the dangling bonds on the fragmented clusters were terminated by $–CH_3$. The electrostatic potential (ESP) charges were used as the atomic partial charges, and the ChelpG method was adopted.[58] To that purpose, the density functional theory computations used the Lee-Yang-Parr correlation functional (B3LYP) were carried out with the Gaussian 03 electronic structure package.[59] And the basis set LANL2DZ was used for atom Ca, while 6-31+G* was used for the rest of the atoms.[60] For heavy atoms, effective core potential (ECP) is often chosen in *ab inito* calculations to reduce the amount of necessary computation, and LANL2DZ is a collection of double-ξ basis sets. The calculated results of atomic partial charges are listed in Table 3.6.

3.4.3 Grand Canonical Monte Carlo Methodology

Grand Canonical Monte Carlo (GCMC) simulations at a fixed adsorbate chemical potential μ, volume V, and temperature T were carried out for the adsorption of CO_2 at 100 K and 298 K. Because the chemical potentials of adsorbates in the adsorbed and bulk phase are identical at thermodynamic equilibrium, GCMC simulation allows one to directly relate the chemical potentials of the adsorbates in both phases and has been widely used for the simulation of adsorption. In this work, the simulations box represents 2×2×2 unit cells was adopted for

Ca(sdb). At least 20 million trials were used in the single-component and mixture simulations. Among these trials, the first half was used for equilibration, and the last half was used to calculate the ensemble averages. The **Ca(sdb)** framework was assumed to be rigid, and the potential energy between adsorbate atoms and frameworks was pre-tabulated.

3.5 Results and Discussion

3.5.1 Structural Description of Ca(sdb)·$(CO_2)_{0.32}$

Prior to collection of single crystal XRD data, activated crystals of **Ca(sdb)** were exposed to CO_2 in a closed container, followed by retrieval after coating in Paratone® oil (see Fig. 2.3). The CO_2 is retained within the channels for at least a week as judged from separate experiments. Room temperature data were collected just after the retrieval of one crystal, while low T data were collected from a different crystal after a week of storing it in oil. The location of CO_2 molecules is in agreement in both cases, suggestive of a strong interaction between sorption sites and the framework, and that the gas adduct is stable over time. This long-term retention allowed the location of gas adsorption sites within the framework from calculations of Fourier difference maps (Fig. 3.2). The structure model derived from the dataset collected at 110 K will be used for discussions of the structural features responsible for CO_2 selectivity (Fig. 3.3, Tables 3.2-3.4).

The main observed interaction between the CO_2 molecule and the pore surface of **Ca(sdb)** appears to be between the delocalized π-aromatic system of both phenyl rings of the linker and the molecular quadrupole of CO_2 (Fig. 3.4). The specific geometry of the sulfonyldibenzoate results in a ‘pocket’ where carbon from the CO_2 molecule is placed between

two centroids of the aromatic ring, with the average distance of 3.81 Å (Fig. 3.4). The molecule is oriented approximately parallel to both phenyl rings, keeping oxygen atoms as far as possible from their centroids, at averaged distances of 3.66 Å (O1C) and 4.26 Å (O2C) (Fig. 3.3). This configuration keeps both oxygen atoms relatively close to two hydrogen atoms, with the average distances of 3.89 Å and 3.85 Å for O1C and O2C, respectively. The CO_2 molecule adopts two possible positions approximately in the middle of the channel, binding to one of the linkers, which are averaged in diffraction data, thus maintaining the $P2_1/n$ space group of the structure (Fig. 3.5). The occupancy of the CO_2 molecule was refined to be 32% and it shows no spatial disorder.

The distance and parallel configuration of the aromatic ring and CO_2 molecule observed in **Ca(sdb)** is in good agreement with theoretical studies reported on single phenyl rings.[61] However, the calculated heat of adsorption for CO_2 in **Ca(sdb)** (>30 kJ/mole)[55] is significantly higher than the predicted 5.6 kJ/mol for benzene $\cdots$ CO_2 molecular complex. This higher interaction energy is most probably the result of simultaneous interactions with two rings, coupled with the influence of additional hydrogen atoms and possibly an overall effect of the small pores, which allows for weak interaction with the other linker. Structural data show that the selective adsorption of CO_2 over N_2 is displayed by the **Ca(sdb)** due to the large quadrupole moment of CO_2 (43.0×10^{-27} esu^{-1} cm^{-1}) compared to that of N_2 (15.2×10^{-27} esu^{-1} cm^{-1}).

3.5.2 XRD-DSC

Our observation that the activated form of **Ca(sdb)** does not readsorb water from the atmosphere, and adsorbs CO_2 strongly enough to allow for structure determination, suggested

that it may retain selectivity to high RH. XRD-DSC is a very effective means of correlating thermal signatures and a structural response of sorption. We observed the XRD-DSC signatures for CO_2 adsorption at 2% and 75% RH during a gas-swing adsorption experiment. During the experiment the atmosphere was alternated between flowing N_2 and CO_2 in several cycles allowing the system to equilibrate after each change. The DSC signal was recorded simultaneously with powder XRD scans (Fig.3.6), and the results show that the crystallinity and the performance of CO_2 adsorption is not diminished over at least five cycles in either dry (2% RH) or humid (75% RH) conditions (Fig. 3.6). Measurements in both dry and humid conditions show very strong exothermic effects after changing the atmosphere from N_2 to CO_2, proving that CO_2 competes very effectively with water for sorption at the phenyl pockets (Fig. 3.8). Powder diffraction patterns recorded after equilibration in the CO_2 atmosphere reveal that there is no major structural change in **Ca(sdb)** when CO_2 is introduced, but that the low angle peaks **10$\bar{1}$**, **002** and **101** reproducibly decrease in comparison to the rest of the pattern suggesting that CO_2 occupies space within the pore, consistent with the proposed CO_2 adsorption mechanism (Fig. 3.7).

For the exact calorimetric measurements we additionally performed a vacuum-swing process for both CO_2 and N_2 gases. The measured enthalpy of adsorption was 10.22(8) kJ/mol_{MOF} and 0.78(3) kJ/mol_{MOF} for CO_2 and N_2, respectively (Fig. 3.9). At 1 atm pressure and room temperature, the wt% of CO_2 and N_2 absorbed is 4.5 and 0.3, with Q_{st} values of 30 kJ/mol_{GAS} and 22 kJ/mol_{GAS}, respectively.[55] This yields a calculated enthalpy of adsorption of 0.811 kJ/mol_{MOF} for N_2 and 10.56 kJ/mol_{MOF} for CO_2. The measured and calculated values are in very good agreement, which confirms the vacuum-swing DSC measurements provide valid

results useful for judging activity of the compound for gas adsorption, and can be applied as a screening technique to other compounds and gases as well.

3.5.3 Grand Canonical Monte Carlo (GCMC) Simulations

For the GCMC simulations, carried out by Zhijuan Zhang at Rutgers University, snapshots of the structure of **Ca(sdb)** with adsorbed CO_2 were collected and analyzed. Four snapshots for the adsorption of CO_2 in **Ca(sdb)** at 1 atm and 298 K are given as an example in Figure 3.11. The final calculated results confirm that CO_2 preferentially locates next to the phenyl rings and utilize the 'pocket' of the linker, with an average shorter C-centroid distance of 3.03 Å and longer one of 3.80 Å. Interestingly, calculations for adsorption at loadings of one molecule per mole (initial conditions: 1 atm pressure of CO_2 in room temperature), rather than the 0.32 molecules per mole for the refined experimental model, show that CO_2 molecules influence each other's position through quadrupolar interaction, and equilibrate to orientations approximately perpendicular to one another.

3.5.4 IR and Raman Spectroscopy

The results from Infra-red (IR) and Raman spectroscopy experiments, carried out by Nour Nijem at University of Texas-Dallas, further confirm that the main CO_2 sorption site is within the organic linker. *In situ* Raman spectroscopy measurements performed at 1 atm pressure of CO_2, show only one additional Raman mode, as compared to the absorption modes of the **Ca(sdb)** itself, observed at 1378 cm^{-1} (approximately -11 cm^{-1} red shifted from the symmetric

stretch mode of CO_2 at 1388 cm^{-1}) (Fig. 3.12). This mode is consistent with CO_2 adsorbed on the organic linkers.[62]

IR absorption spectroscopy measurements of CO_2 adsorption as a function of pressure (100 mTorr-6 Torr) at low loadings reveal several IR absorption modes corresponding to the asymmetric stretch mode of CO_2, with different intensity, indicating the presence of several adsorption sites (Fig. 3.13). The red shifted IR absorption modes at 2334 and 2344 cm^{-1} can be assigned to CO_2 interacting through its carbon with the organic linkers.[62] The IR absorption mode at 2350 cm^{-1} (~1 cm^{-1} blue shifted from the unperturbed CO_2 stretch mode at 2349 cm^{-1}) can be assigned to adsorbed CO_2 interacting with the Ca^{2+} ion consistent with an interaction of CO_2 through one of its oxygen atoms.[63] The difference in IR intensity of these modes reflects the much smaller number of the molecules interacting with Ca^{2+} ions as compared to the organic linkers.

3.6 Conclusions

In conclusion, a molecular-level understanding of the nature of interactions between adsorbed gas and pore surface is vital to an exploration and attempts at rational development of gas-selective nanoporous solids. It requires the high quality XRD data to precisely identify sorption sites, and to augment the still limited number of the structural reports of CO_2 adsorbed on porous MOFs. Most reports focus on the interaction between CO_2 and under-coordinated cations or additional functionalities inside the framework.[5, 30d] In this context our study describing CO_2-phenyl ring interactaion in an alkaline-metal containing MOF is unique and can fill the gap in our understanding of CO_2 sorption in porous materials.

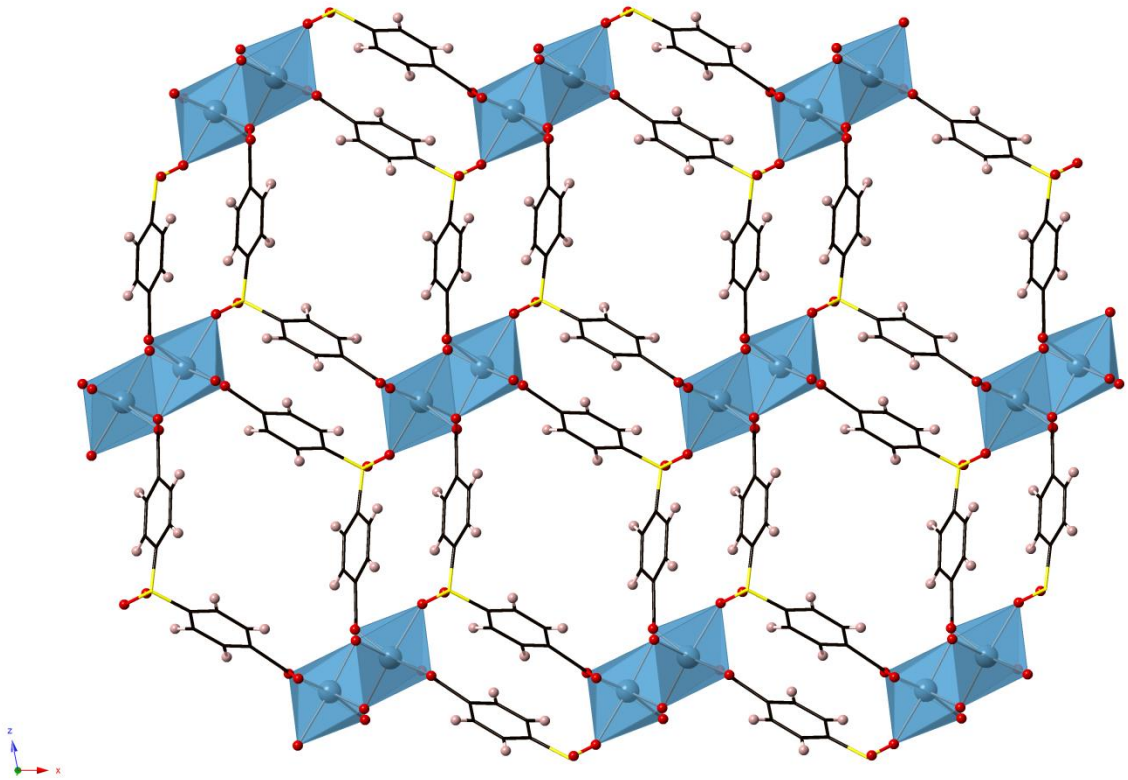

Figure 3.1 Polyhedral representation of the structure of **Ca(sdb).** Blue octahedra represent calcium, black wire – carbon, red spheres - oxygen, yellow – sulfur, pink – hydrogen.

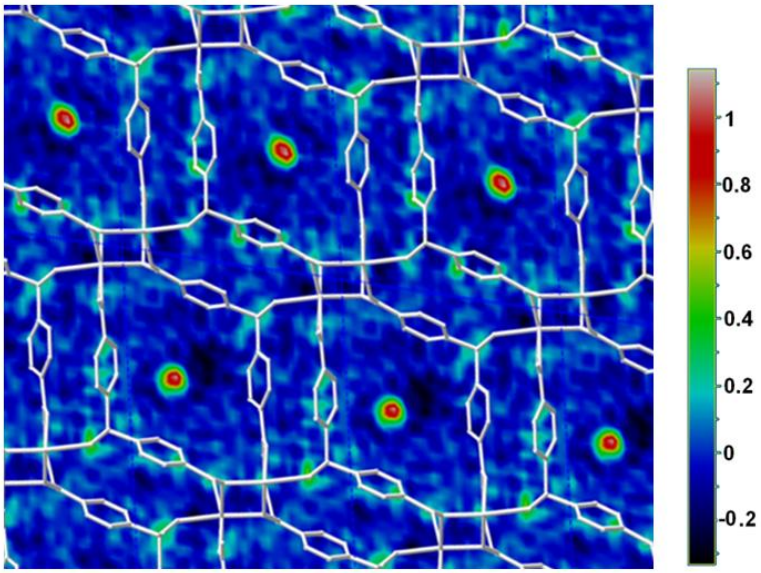

Figure 3.2 The difference electron density map ($\bar{e}/Å^3$) from data collected at 110K calculated before assigning CO_2, showing the carbon dioxide inside the channel (oxygen atoms are above and below the plane), white wire represents the superimposed structure of the **Ca(sdb)** framework.

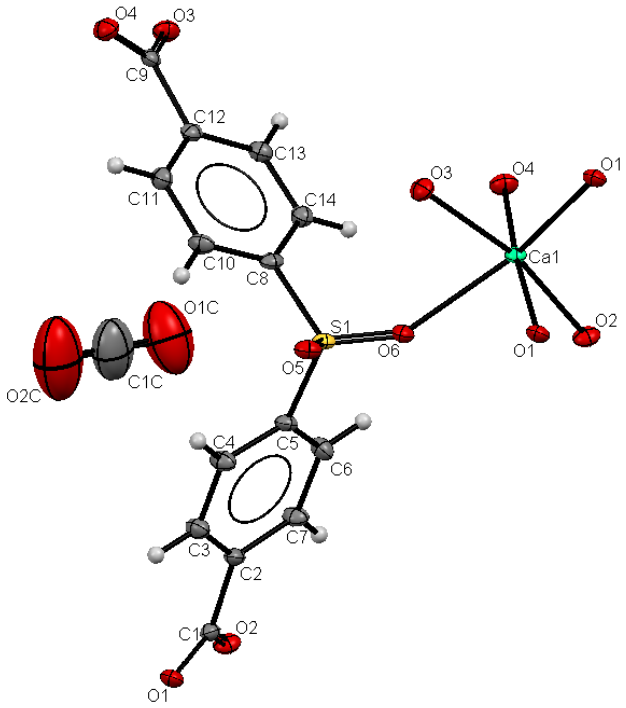

Figure 3.3 Thermal ellipsoid plot of the refined model **Ca(sdb)·$(CO_2)_{0.32}$** from data collected at 110K, the ellipsoids are drawn at the 50% probability level.

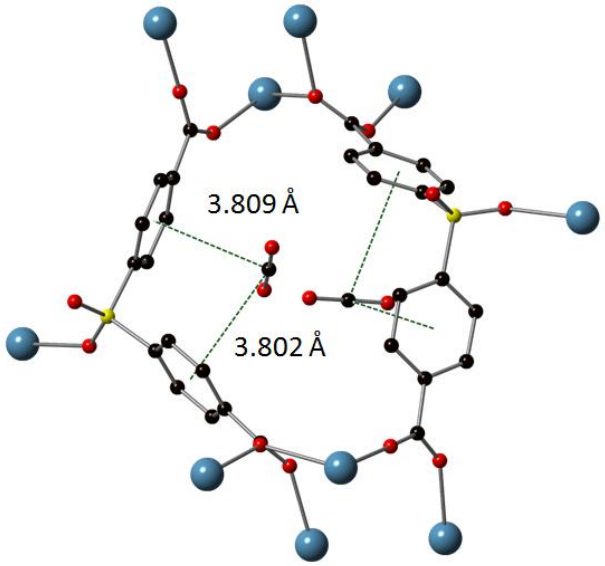

Figure 3.4 Local environment of the adsorbed CO_2 molecule at 110 K. Dashed lines represent phenyl ··· CO_2 π-quadrupole interactions. The CO_2 molecule occupies two equivalent positions, with 32% occupancy on each.

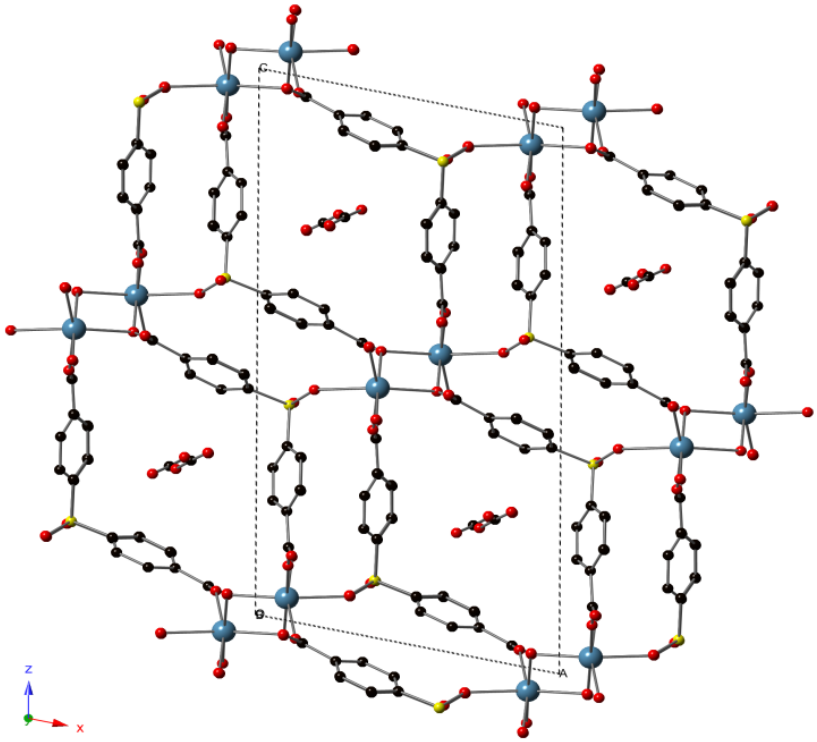

Figure 3.5 Packing along [010] showing the location of CO_2 at 110 K; blue spheres represent calcium, red: oxygen, black: carbon and yellow: sulfur. Hydrogen atoms are omitted for clarity.

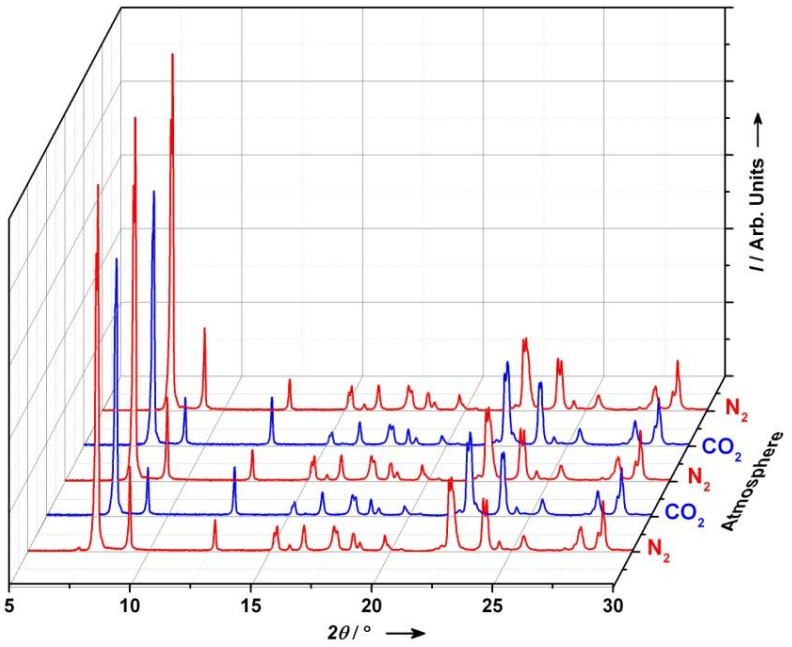

Figure 3.6 Gas-swing experiment for CO_2 loading on **Ca(sdb)** at 298 K. Background subtracted XRD patterns at 2% relative humidity showing the change in relative intensities under the different conditions, confirming that CO_2 is adsorbing inside the channels.

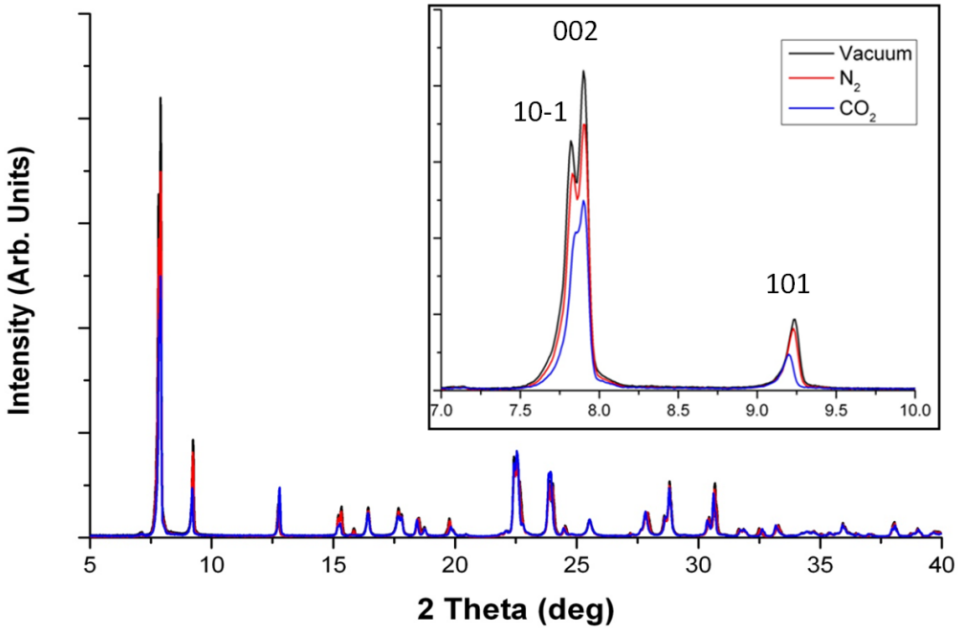

Figure 3.7 Overlaid XRD patterns (background subtracted) at 2% relative humidity showing the change in relative intensities under the different conditions at 298 K. The most sensitive low angle peaks **$10\bar{1}$**, **002**, and **101** are shown in insert.

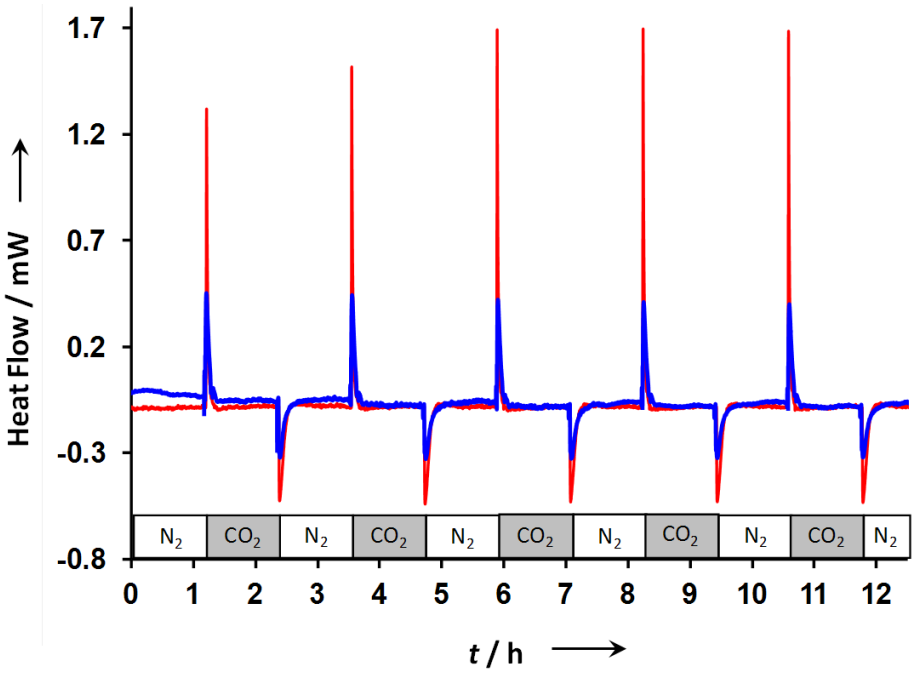

Figure 3.8 Gas-swing experiment for CO_2 loading on **Ca(sdb)**. Strong exothermic and endothermic effects for experiment performed in 2% relative humidity (red) and 75% relative humidity (blue) at 298 K.

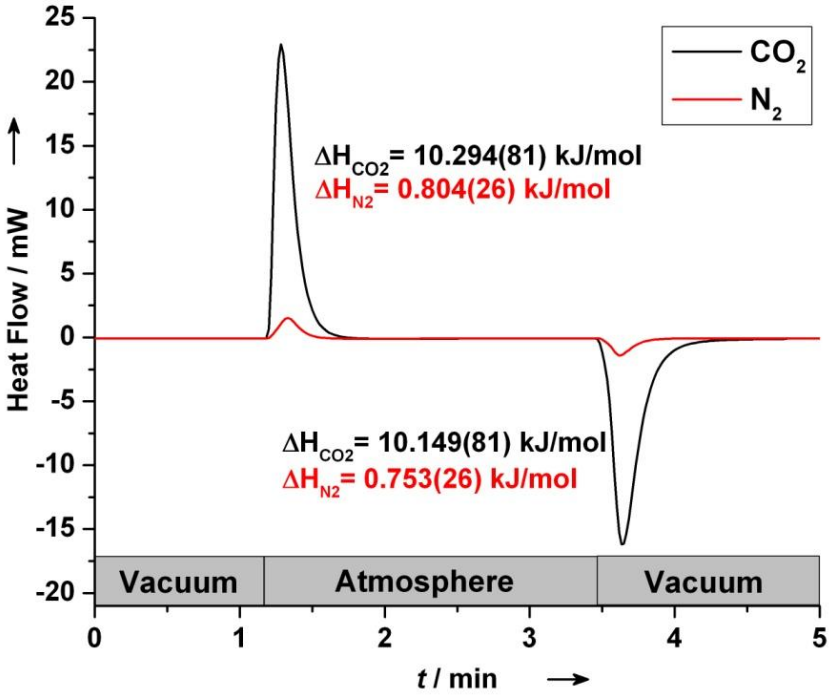

Figure 3.9 Vacuum-swing adsorption DSC data for 1 cycle of CO_2 and N_2 loading/unloading on **Ca(sdb)** at 298 K.

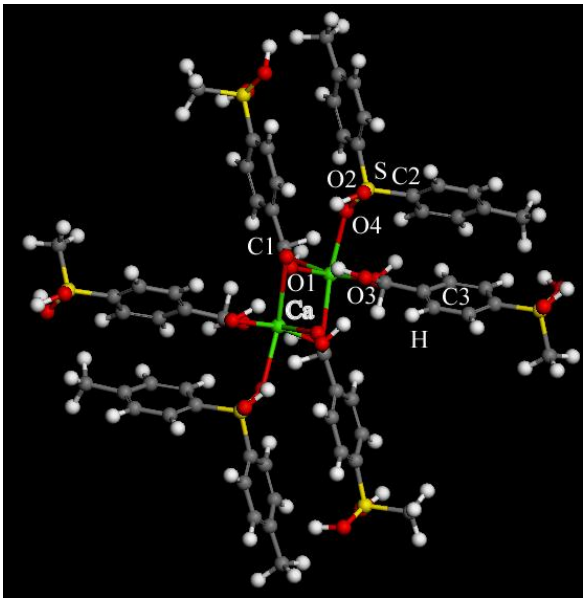

Figure 3.10 Fragmented clusters used in the B3LYP/6-31+G* calculations for **Ca(sdb)**. To maintain the correct hybridization, the dangling bonds on the fragmented clusters were terminated by $-CH_3$.

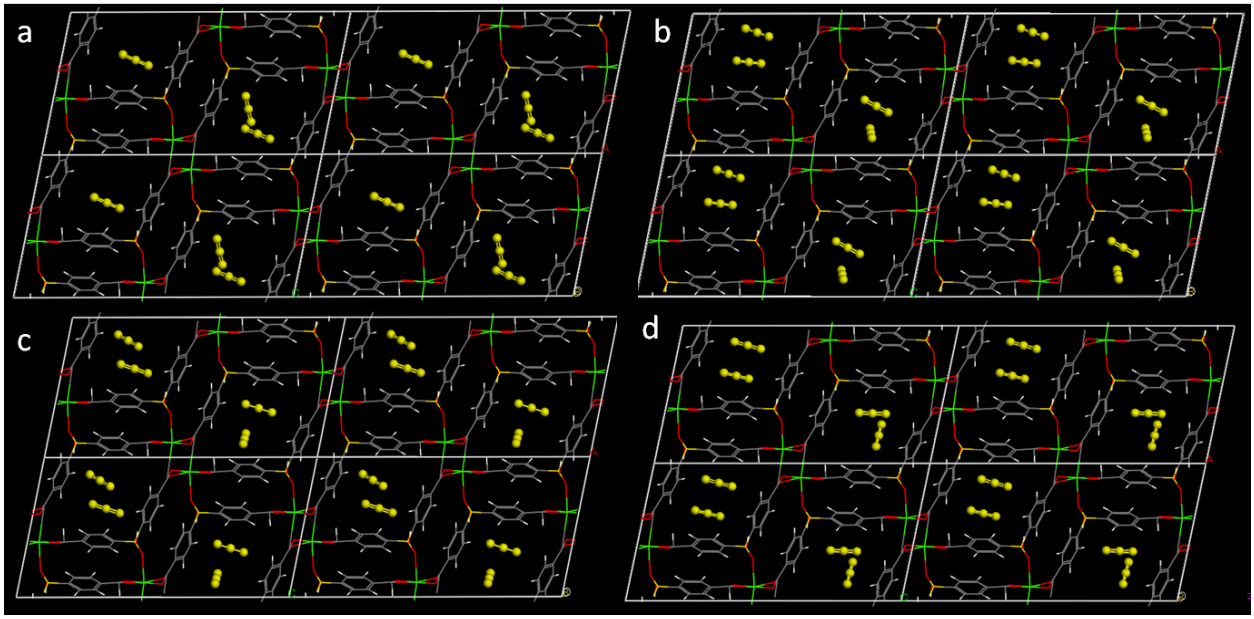

Figure 3.11 Snapshots of the calculated structure of **Ca(sdb)** with adsorbed carbon dioxide (yellow) along the [010] at 1 atm and 298 K. (a) with 10000 equilibration steps; (b) with 100000 equilibration steps; (c) with 10000000 equilibration steps; (d) final equilibration status.

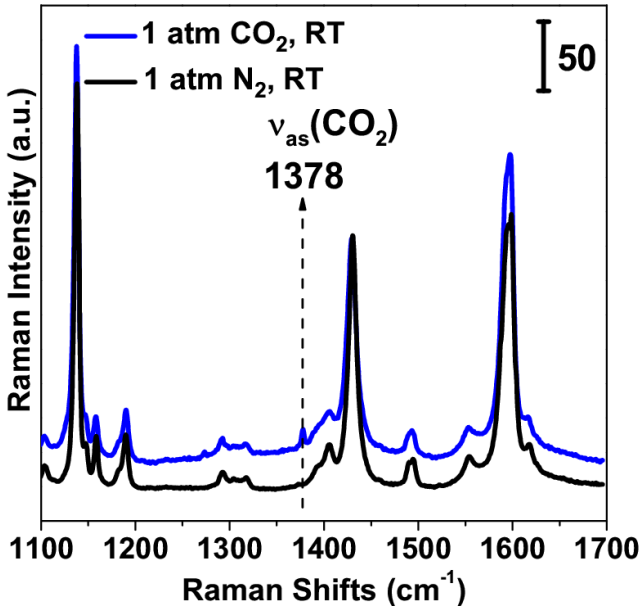

Figure 3.12 Raman spectra of **Ca(sdb)** in 1 atm of N_2 (black spectrum) and under 1 atm of CO_2 (blue spectrum).

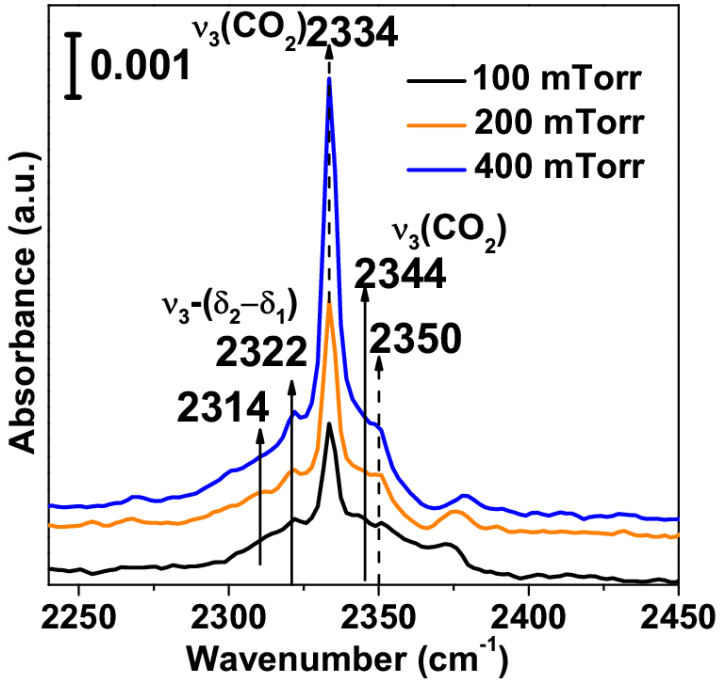

Figure 3.13 IR absorption spectra of CO_2 adsorbed on **Ca(sdb)** as a function of pressure at room temperature, show IR absorption bands corresponding to the asymmetric stretch mode of CO_2 and the combination bands of the two non-degenerate bending modes and the asymmetric stretch mode.

Table 3.1: Crystallographic data and structural refinement details of **$Ca(sdb)(CO_2)_{0.32}$**

Empirical formula	$CaC_{14.32}H_8O_{6.64}S$
Formula weight	358.57
Collection Temperature (K)	110
Wavelength (Å)	0.71073
Space Group	***P*** $2_1/n$
a (Å)	11.8831(8)
b (Å)	5.5418(3)
c (Å)	22.6515(15)
β (°)	101.607(7)
Volume ($Å^3$)	1461.18(16)
Z	4
Calculated Density (g/cm^3)	1.630
Absorption coefficient (mm^{-1})	0.604
F(000)	732.6
Crystal size (mm)	0.15 × 0.10 × 0.05
θ range of data collection (°)	3.79 - 26.37
Index range	$-14 \leq h \leq 14$,
	$-6 \leq k \leq 6$
	$-28 \leq l \leq 28$
Total reflection	14836
Independent reflection	2970
R_{int}	0.0352
Completeness to θ_{max}	99.7 %
Goodness of fit	1.084
Data/ Restraints/parameter	2970 / 3 / 228
R_1(*on* F_o, $I>2\sigma(I)$)	0.0396
wR_2 (*on* F_o^2, *all data*)	0.1061

Table 3.2: Atomic coordinates ($\times 10^4$) and equivalent isotropic displacement parameters (U_{eq}; $Å^2 \times 10^3$) for **$Ca(sdb)(CO_2)_{0.32}$**

	x	y	z	U_{eq}
Ca(1)	13977(1)	2347(1)	9579(1)	11(1)
S(1)	11071(1)	242(1)	8953(1)	13(1)
O(2)	6316(1)	4834(3)	9703(1)	17(1)
O(5)	11206(1)	-2326(3)	9018(1)	17(1)
O(6)	11899(1)	1828(3)	9321(1)	16(1)
O(3)	11179(2)	4614(3)	6199(1)	18(1)
O(1)	5927(1)	918(3)	9730(1)	16(1)
O(4)	11065(2)	663(3)	6009(1)	20(1)
C(9)	11081(2)	2457(4)	6343(1)	13(1)
C(1)	6559(2)	2671(4)	9642(1)	13(1)
C(4)	8828(2)	-661(4)	8995(1)	17(1)
C(10)	10543(2)	-689(4)	7753(1)	16(1)
C(14)	11459(2)	3159(4)	8042(1)	16(1)
C(8)	11014(2)	974(4)	8189(1)	14(1)
C(3)	7798(2)	-119(4)	9164(1)	17(1)
C(13)	11443(2)	3646(4)	7436(1)	15(1)
C(12)	11007(2)	1967(4)	6994(1)	14(1)
C(2)	7653(2)	2084(4)	9431(1)	14(1)
C(11)	10554(2)	-192(4)	7152(1)	17(1)
C(5)	9713(2)	1018(4)	9107(1)	14(1)
C(6)	9575(2)	3255(4)	9354(1)	17(1)
C(7)	8533(2)	3778(4)	9516(1)	17(1)
O(1C)	6595(12)	9550(20)	7213(7)	111(7)
C(1C)	7135(17)	7900(30)	7415(8)	86(6)
O(2C)	7647(14)	6220(20)	7619(7)	142(10)

Table 3.3: Anisotropic displacement parameters ($Å^2 \times 10^3$) for **Ca(sdb)$(CO_2)_{0.32}$**

	U^{11}	U^{22}	U^{33}	U^{23}	U^{13}	U^{12}
Ca(1)	11(1)	12(1)	12(1)	0(1)	5(1)	2(1)
S(1)	12(1)	16(1)	14(1)	1(1)	7(1)	1(1)
O(2)	19(1)	17(1)	17(1)	-1(1)	8(1)	6(1)
O(5)	17(1)	18(1)	18(1)	2(1)	9(1)	2(1)
O(6)	12(1)	23(1)	15(1)	-1(1)	6(1)	0(1)
O(3)	21(1)	17(1)	17(1)	5(1)	6(1)	0(1)
O(1)	13(1)	20(1)	16(1)	1(1)	6(1)	-3(1)
O(4)	23(1)	19(1)	18(1)	-4(1)	8(1)	-2(1)
C(9)	9(1)	16(1)	15(1)	1(1)	4(1)	0(1)
C(1)	12(1)	17(1)	10(1)	1(1)	3(1)	1(1)
C(4)	17(1)	14(1)	22(1)	-2(1)	9(1)	0(1)
C(10)	18(1)	13(1)	20(1)	2(1)	9(1)	-1(1)
C(14)	14(1)	17(1)	17(1)	-1(1)	4(1)	-1(1)
C(8)	12(1)	17(1)	15(1)	2(1)	7(1)	4(1)
C(3)	17(1)	16(1)	21(1)	-2(1)	8(1)	-3(1)
C(13)	14(1)	14(1)	19(1)	1(1)	6(1)	1(1)
C(12)	11(1)	19(1)	14(1)	0(1)	5(1)	2(1)
C(2)	11(1)	20(1)	12(1)	2(1)	5(1)	1(1)
C(11)	17(1)	16(1)	18(1)	-3(1)	5(1)	-2(1)
C(5)	12(1)	17(1)	14(1)	2(1)	6(1)	1(1)
C(6)	13(1)	17(1)	22(1)	-1(1)	5(1)	-1(1)
C(7)	17(1)	16(1)	20(1)	-2(1)	9(1)	1(1)
O(1C)	84(11)	81(10)	151(15)	-7(9)	-18(9)	-2(8)
C(1C)	85(13)	80(12)	76(12)	-19(9)	-22(10)	10(10)
O(2C)	136(15)	120(15)	137(15)	-24(10)	-50(10)	16(11)

Table 3.4: Selected bond lengths for **Ca(sdb)(CO_2)$_{0.32}$**

Bond	Bond length (Å)
Ca(1)-O(4)#1	2.2645(16)
Ca(1)-O(3)#2	2.3027(16)
Ca(1)-O(2)#3	2.3312(16)
Ca(1)-O(1)#4	2.3806(16)
Ca(1)-O(1)#5	2.4071(16)
Ca(1)-O(6)	2.4384(16)
O(1C)-C(1C)	1.157(11)
O(1C)-O(2C)#9	1.294(17)
C(1C)-O(2C)	1.157(12)

Symmetry transformations used to generate equivalent atoms:

#1 -x+5/2,y+1/2,-z+3/2
#2 -x+5/2,y-1/2,-z+3/2
#3 -x+2,-y+1,-z+2
#4 -x+2,-y,-z+2
#5 x+1,y,z
#6 -x+3/2,y+1/2,-z+3/2

Table 3.5: LJ potential parameters for the atoms of **Ca(sdb)**.

Elements	σ (Å)	ε/k_B (K)
Ca	2.98	78.5
S	3.595	137.890
C	3.431	52.841
O	3.118	30.195
H	2.571	22.143

Table 3.6: Atomic partial charges in the fragmented cluster of **Ca(sdb)** in Figure 3.9 (unit of electron volt, ev).

Atoms	Charges (ev)
C(1)	+0.712
C(2)	-0.249
C(3)	-0.184
O(1)	-0.557
O(2)	-0.305
O(3)	-0.668
O(4)	+0.708
H	+0.140
S	+0.525
Ca	+0.917

Chapter 4

Effect of Ligand Geometry on Selective Gas Adsorption: the Case of Microporous Cadmium Metal Organic Framework with a V-shaped Linker

The content of this chapter is published in

Plonka, A. M.; Banerjee, D.; Woerner, W. R.; Zhang, Z.; Li, J.; Parise, J. B. *Chem. Commun* **2013,** *49* (63), 7055-7057.

4.1 Abstract

Herein we report synthesis and structural characterization of a novel microporous cadmium metal organic framework, **Cd(sdb)**, based on Cd metal centers and v-shaped sulfonyldibenzoate ligands. **Cd(sdb)** was synthesized with a solvothermal method and characterized with a single crystal X-ray diffraction method. The material crystallizes in a *Cc* space group with the unit cell parameters of: a = 13.3382(4), b = 21.4986(7), c = 10.1527(6) and β = 95.000(1). Structurally, **Cd(sdb)** forms a three dimensional framework with 1-D sinusoidal channels. **Cd(sdb)** selectively adsorbs CO_2 over N_2 with the CO_2/N_2 selectivity of approximately 25 in ideal flue gas conditions, as determined with gas adsorption measurments and IAST calculations. The selectivity is attributed to CO_2 molecules interacting with phenyl rings of a v-shaped linker as estimated by the *in-situ* XRD-DSC study. The **Cd(sdb)** CO_2/N_2 selectivity is considerably lower than for **Ca(sdb)** in the same conditions (45).

4.2 Introduction

Current trends in the design of MOFs for selective CO_2 adsorption emphasize under-coordinated metal centers, which provide high energy of CO_2 adsorption but also are sensitive to water present in a gas stream. In contrast, we have recently discovered a unique mechanism responsible for the high CO_2/N_2 adsorption selectivity in a porous calcium based metal organic framework **Ca(sdb)**, even in the presence of a high relative humidity (RH).[48] The V-shaped sdb linker provides a "π-pocket" formed by two phenyl rings and CO_2 is positioned at an equal distance to both rings, resulting in a high heat of adsorption: Q_{st} = 31 kJ/mol$_{MOF}$. This unique result – that the linker geometry is responsible for the CO_2 adsorption at high RH – spurred our search for other sdb-based frameworks that might also possess this property. We were particularly interested in obtaining a cadmium analog of **Ca(sdb)** to investigate how changing the metal node influences the CO_2 affinity of the framework, as the Ca^{2+} and Cd^{2+} ions are known for an easy substitution for one another in the crystal lattice, due to their almost identical size and identical charge. We were able to synthesize a novel, sdb-based MOF with unusual topology, based on the sdb linker and Cd metal center [**Cd(sdb)·nH$_2$O**], which has similar gas adsorption properties to the previously reported **Ca(sdb)**, but with a different Cd-sdb connectivity.

4.3 Experimental Section

4.3.1 Synthesis of Cd(sdb)·nH$_2$O

Cadmium sulfonyldibenzoate [**Cd(sdb)·nH$_2$O**] was synthesized under solvothermal conditions. Starting materials include cadmium nitrate tetrahydrate [Cd(NO$_3$)$_2$·4H$_2$O, 98%, Aldrich], 4,4'-sulfonyldibenzoic acid [H$_2$(sdb), 98%,Sigma-Aldrich] and ethanol (95%, Fisher-Scientific) and were used without purification.

A mixture of 0.001 moles of Cd(NO$_3$)$_2$·4H$_2$O (0.310 g) and 0.001 moles of H$_2$(sdb) (0.296 g) were dissolved in 12 grams of ethanol and stirred for 2 hours to achieve homogeneity. The resultant solution was heated at 180°C for 4 days. Colorless needle shaped crystals were recovered as products and washed with ethanol (yield ~60%, 0.320g). Water molecules occupying the pores come from the 95% ethanol solvent and from the Cd(NO$_3$)$_2$ reactant.

4.3.2 Single Crystal X-ray Diffraction

Reflections for **Cd(sdb)·nH$_2$O** were collected at APS ChemMatCars (sector 15) beamline at 100 K (see the chapter 2.7).

The structure of **Cd(sdb)·nH$_2$O** was solved using direct methods (SHELXS) and a structural model was refined with SHELXTL (Tables 4.3-4.4).[49-50] Cadmium and sulfur atoms were located first, followed by the determination of other atom (O, C) positions from the Fourier difference map, with all the non-hydrogen atoms belonging to the framework refined anisotropically (Fig. 4.3). Hydrogen atoms were added in the structure using geometrical constraints (HFIX command). Oxygen atoms from water molecules were refined isotropically

and their occupancy was also refined. Hydrogen atoms from the water molecules were not localized. The summary of crystallographic data and structural refinement details can be found in Tables 4.1-4.4.

Bulk sample identification and a phase purity determination were performed using powder X-ray diffraction. Data were collected using a Scintag Pad-X diffractometer equipped with Cu Kα radiation (λ = 1.5405 Å) within a range of 5° ≤ 2θ ≤ 40° (step size: 0.02°, counting time: 1s/step). A comparison of observed and calculated powder X-ray diffraction patterns for **Cd(sdb)·nH$_2$O** confirmed phase purity (Fig. 4.4).

4.3.3. Dual Site Langmuir-Freundlich Model for CO_2 and N_2 Adsorption Isotherms

Gas isotherms, DSLF model and IAST calculations were performed by Zhijuan Zhang at Rutgers University.

For the details on gas adsorption procedures see the chapter 2.4.

Single-component CO_2 and N_2 adsorption isotherms were fitted with a DSLF model to enable the application of IAST in simulating the performance of **Cd(sdb)** under a mixed component gas. Fitting parameters of DSLF equation as well as the correlation coefficients (R2) are listed in Table 4.5. Experimental and fitted isotherms for CO_2 and N_2 at 298 K are depicted in Figures 4.10-4.13.

4.3.4 XRD-DSC

For the details of gas-swing and vacuum-swing procedures see the chapter 2.6.

DSC measurements were performed using 10.5 mg of **Cd(sdb)** in an aluminum crucible with an equal amount of Al_2O_3 in the reference crucible.

Sample was first activated *in situ* at 210°C under vacuum for 2 hours. For the vacuum-swing experiment a total of 10 cycles were completed. Gas-swing experiments were performed at 30% and 80% RH. The 30% RH atmosphere was changed between CO_2 and N_2 over the course of 48 hours. The first exothermic peak shows that **Cd(sdb)** is still operating at its full capacity (dry enthalpy of $CO_2 - N_2$ = 9.086 kJ/mol$_{MOF}$ - 0.770 kJ/mol$_{MOF}$ = 8.316 kJ/mol$_{MOF}$) but after 24 hours drops to 5.7(5) kJ/mol$_{MOF}$, which is 69% of its initial enthalpy. Under the 30% RH conditions, **Cd(sdb)** is active for the gas adsorption but at a reduced capacity of 69% (Fig. 4.15).

Similar experiment was performed at 80% RH and DSC data show that **Cd(sdb)** can no longer perform an atmosphere swing (Fig. 4.16).

4.4 Results and Discussion

4.4.1 Structural Description of Cd(sdb)·nH$_2$O

Cd(sdb)·nH$_2$O is a three dimensional framework with channels similar to **Ca(sdb)**. The sdb V-shaped linker builds walls of the channels, providing the accessible sorption sides of "π-pockets". However, in spite of the similar ionic radii of Ca^{2+} and Cd^{2+}, the two frameworks are not isostructural. While the structures are related, that of **Cd(sdb)·nH$_2$O** contains sinusoidal channels rather than straight ones (Fig. 4.1). The crystallographically unique cadmium metal center adopts distorted trigonal prism coordination, with five carboxyl and one sulfonyl oxygen atoms, forming edge-sharing dimers. Those dimers are connected by carboxyl and sulfonyl

groups to form chains in the [001] direction (Fig. 4.2). There are two unique sulfur atoms, both located on a two-fold axis, so that the halves of sdb linkers are generated by a symmetry operation (Fig. 4.3). The sdb linker adopts two different coordination modes, each coordinates to six cadmium atoms but only a S1 sulfonyl group coordinates to the metal, while the S2 sulfonyl is uncoordinated.

4.4.2 Gas Adsorption Studies

Channels in the structure of **Cd(sdb)·nH$_2$O** contain disordered water molecules, which can be easily removed by heating at 200°C in vacuum [**Cd(sdb)**] as determined from the TGA (Fig. 4.5). A permanent porosity of **Cd(sdb)** was confirmed by pore characterization and gas-adsorption studies. **Cd(sdb)** exhibits a BET surface area of approximately 100 m^2/g, which is slightly lower than the calcium analogue.

Cd(sdb) was tested for gas adsorption by Zhijuan Zhang at Rutgers University. N_2 adsorption isotherms at 77 K and RT display a type-I sorption behavior, typical for a microporous material (Fig. 4.6). **Cd(sdb)** exhibits a moderate H_2 uptake of 0.3 wt% at 77 K and 1 atm (Fig. 4.7). Further, the activated material was tested for the CO_2 adsorption at different temperatures. **Cd(sdb)** shows reversible uptake of 4.25 wt% and 3.5 wt% at 273K and 298K under 1 atm, respectively (Fig. 4.8). Isosteric heats of the CO_2 adsorption at low loadings (0-0.5 wt%) are about 26-28 kJ/mol_{GAS} (Fig. 4.9). The values of Q_{st} (CO_2) are comparable to our previously reported **Ca(sdb)** framework, but lower than those of the members of the M-MOF-74 series (M = Co, Ni, Mg), because of the presence of open metal sites in the activated framework in the latter case, while **Cd(sdb)** posses no open metal sites.[64] An Ideal Adsorbed Solution

Theory (IAST) was employed by Zhijuan Zhang to estimate the CO_2 adsorption selectivity of **Cd(sdb),** and the results are shown in Figures 4.10-4.12. At 0.15 bar of CO_2 and 0.85 bar of N_2, a typical composition of flue gas mixture from power plants, the selectivity is around 25 (Fig. 4.13), lower than that of the **Ca(sdb)** material which has value of 45.

4.4.3 XRD-DSC

The XRD-DSC method allows for experimental measurement of gas sorption enthalpy and qualitative determination of gas selectivity, while simultaneously giving information about ongoing structural changes.[48] First, the sample was thermally activated *in situ* and then the atmosphere was cycled between vacuum and CO_2 or N_2 to measure a differential enthalpy between empty and gas occupied pores. The measured enthalpy of adsorption was 9.1(1) kJ/mol_{MOF} for CO_2 and 0.77(4) kJ/mol_{MOF} for N_2 (Fig. 4.14). The CO_2 enthalpy of adsorption calculated from the isotherm values at RT and 1 atm (Q_{st} = 26.69 kJ/mol_{GAS}; CO_2 wt% = 3.58) is 9.171 kJ/mol_{MOF}, which is in excellent agreement with the measured value. We were not able to calculate Q_{st} of N_2 using the Virial method because data had a low signal to noise discrimination, due to the small amount of the gas adsorbed. However, we were able to estimate the Q_{st} value based on the DSC method, proving that this new protocol is highly valuable in gas sorption studies. The enthalpy of N_2 was measured at 0.77(4) kJ/mol_{MOF} using DSC, while the isotherm studies determined the N_2 uptake to be 0.28 wt% at 1 atm. We calculated the Q_{st} of nitrogen adsorption to be 17.9(9) kJ/mol_{GAS}, which is significantly lower in comparison to the CO_2 adsorption.

Furthermore, we tested the adsorption enthalpies of the activated material as a function of exposure to gases with 30% and 80% RH. It was determined from gas-swings under 30% RH conditions that **Cd(sdb)** remains active for the CO_2 adsorption but at a reduced capacity of approximately 69% (Fig. 4.15). DSC data show the enthalpy of the gas-swing decreases to steady state of 5.7(5) kJ/mol_{MOF} after 24 hours of exposure to the 30% RH atmosphere. Further, results of 80% RH experiment indicate that **Cd(sdb**) can no longer perform the gas-swing as no exothermic effect was observed during N_2/CO_2 swing (Fig. 4.16).

Powder diffraction patterns recorded after equilibration in a dry CO_2 atmosphere reveal that there is no major structural change in **Cd(sdb)** when CO_2 is introduced, but that the low angle (**110)** reflection intensity decreases with respect to higher angle peaks, suggesting that CO_2 occupies the channels (Figs. 4.17-4.18). The low angle (high d-spacing) peaks provide sensitivity to chemical heterogeneities within the structure; in porous materials the scattering contrast is easily seen when the pores are alternatively filled and emptied. In this case, occupancy by CO_2 gives subtle – and clearly reproducible – changes in the low angle peaks.

The results of XRD-DSC support the hypothesis that sorption on the 'π-pocket' is responsible for the CO_2/N_2 selectivity as seen in the case of **Ca(sdb)**.

4.5 Conclusions

In summary, a new microporous cadmium based metal organic framework has been synthesized and structurally characterized. The material exhibits selective CO_2 adsorption over N_2 of approximately 25 under post-combustion flue gas conditions as calculated with the IAST theory. The CO_2/N_2 selectivity of **Cd(sdb)** is lower for Ca analogue in the same conditions (45).

The complementary *in-situ* vacuum-swing XRD-DSC study confirms the heat of adsorption values for the adsorbate, with a validation of π-CO_2 interaction for the origin of selectivity.

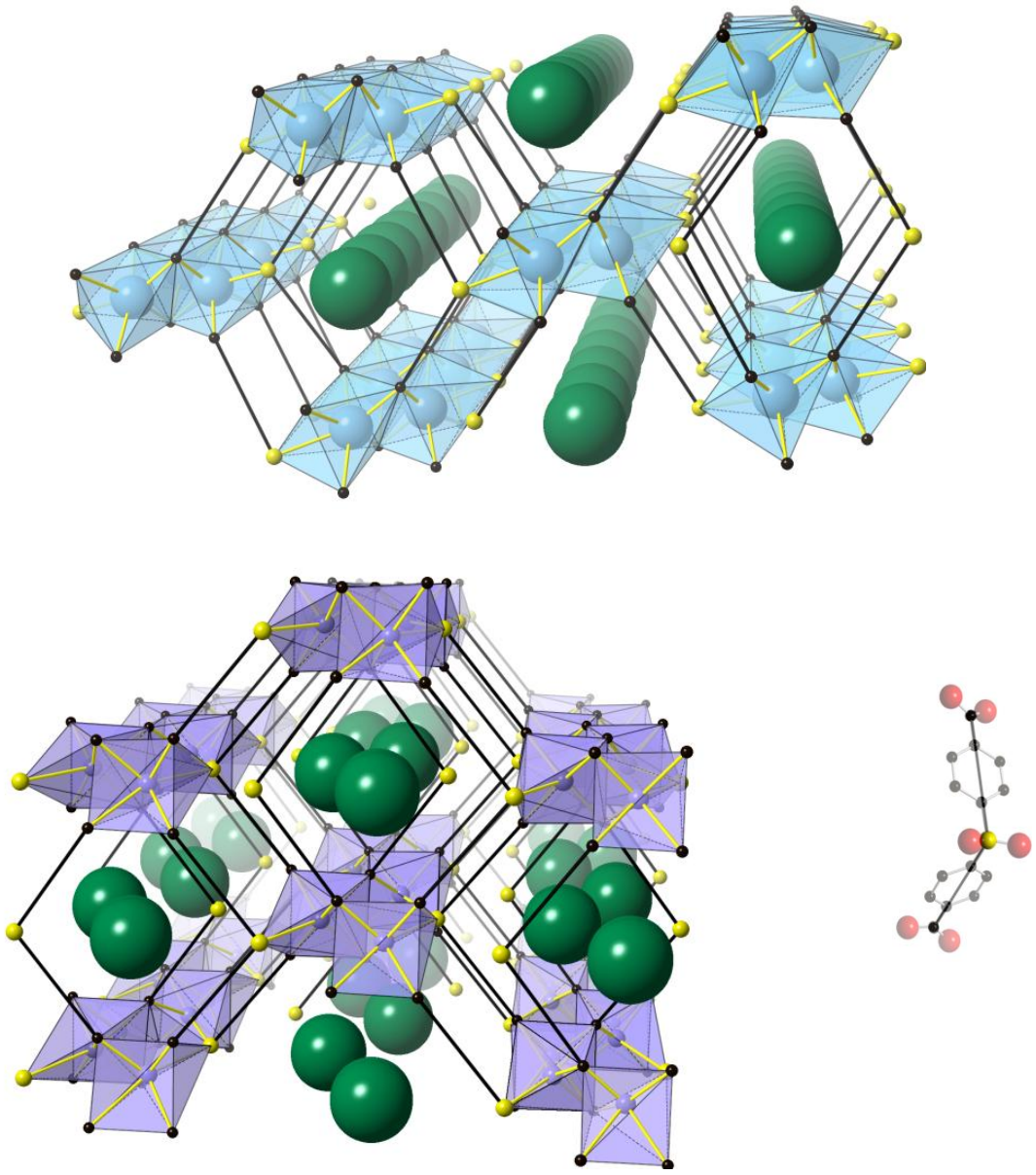

Figure 4.1 Comparison of the straight and sinusoidal channels in **Ca-** (top) and **Cd(sdb)** (bottom), respectively. The large spheres are guides to the eye to emphasize the shapes of the 1-D channels running approximately away from the viewer. Purple polyhedra represent Cd, blue – Ca. Yellow spheres represent sulfonyl moieties and the black spheres represent carboxyl groups.

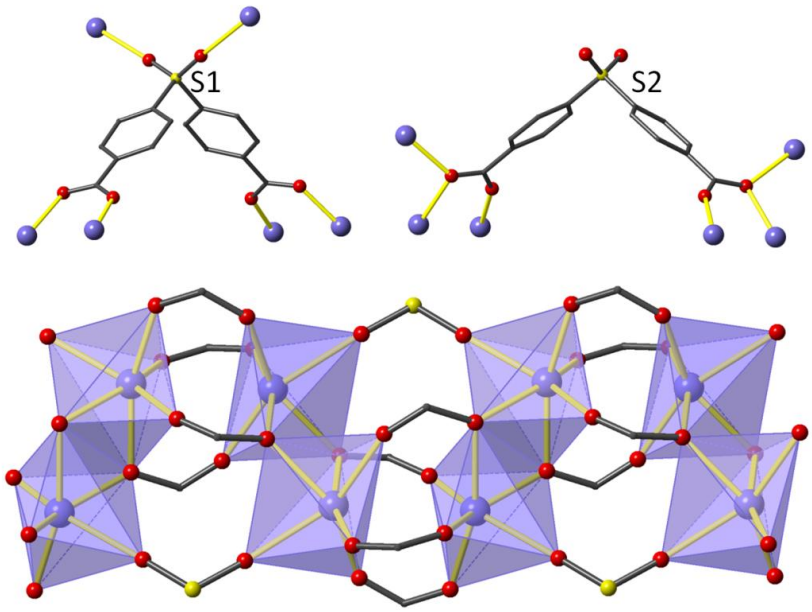

Figure 4.2 Coordination of sulfonyl moieties and the inorganic connectivity in **Cd(sdb)·nH$_2$O**. Purple polyhedra represent Cd, black wire – C, yellow spheres – S and red spheres – O.

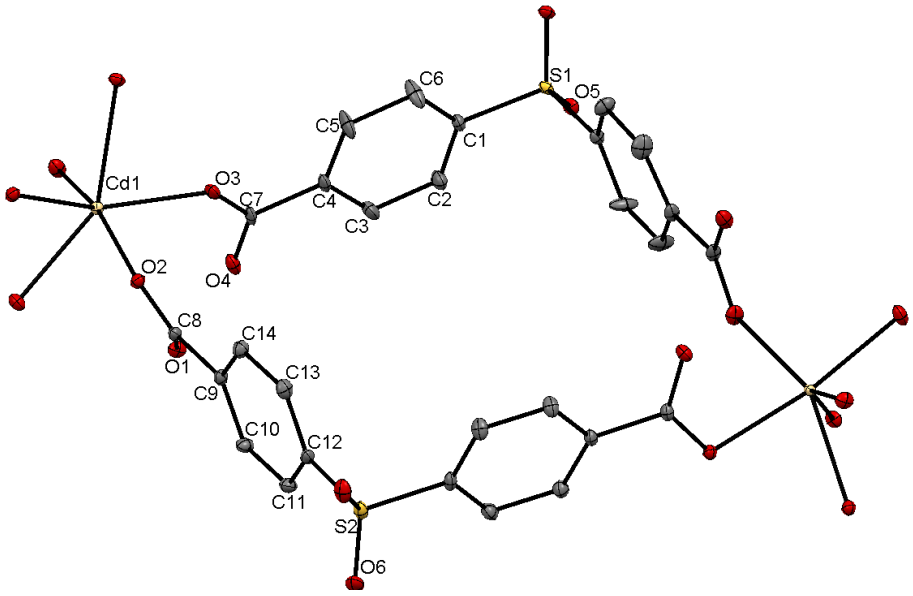

Figure 4.3 Thermal ellipsoid view of **Cd(sdb)·nH$_2$O** at 100K, illustrating the numbering scheme. Ellipsoids are shown at the 50% probability level. Hydrogen atoms and solvent water atoms are omitted for clarity. Symmetry related atoms are shown to complete the coordination sphere of the metal centers and linkers.

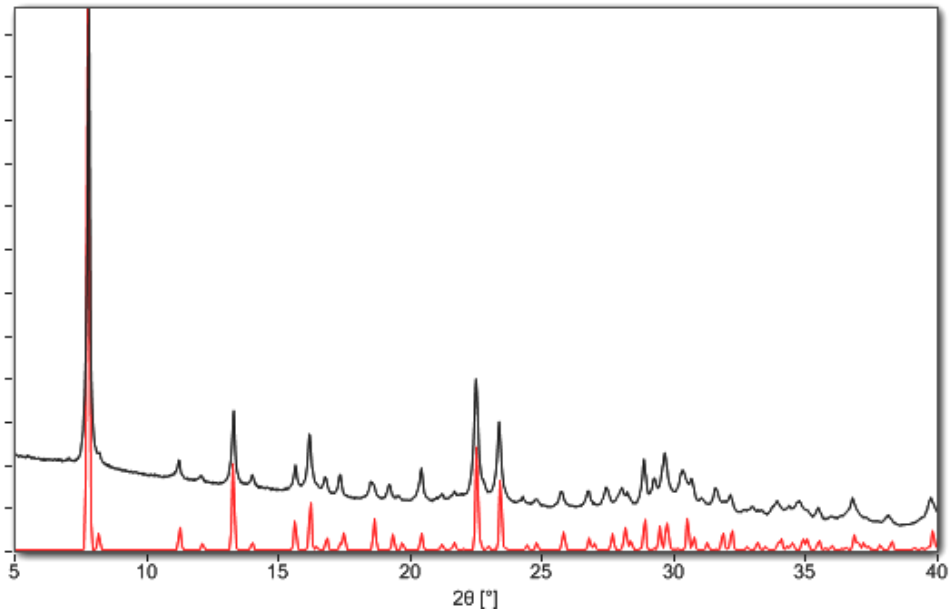

Figure 4.4 Simulated (red) and experimental (black) powder XRD patterns of **Cd(sdb)·nH$_2$O**.

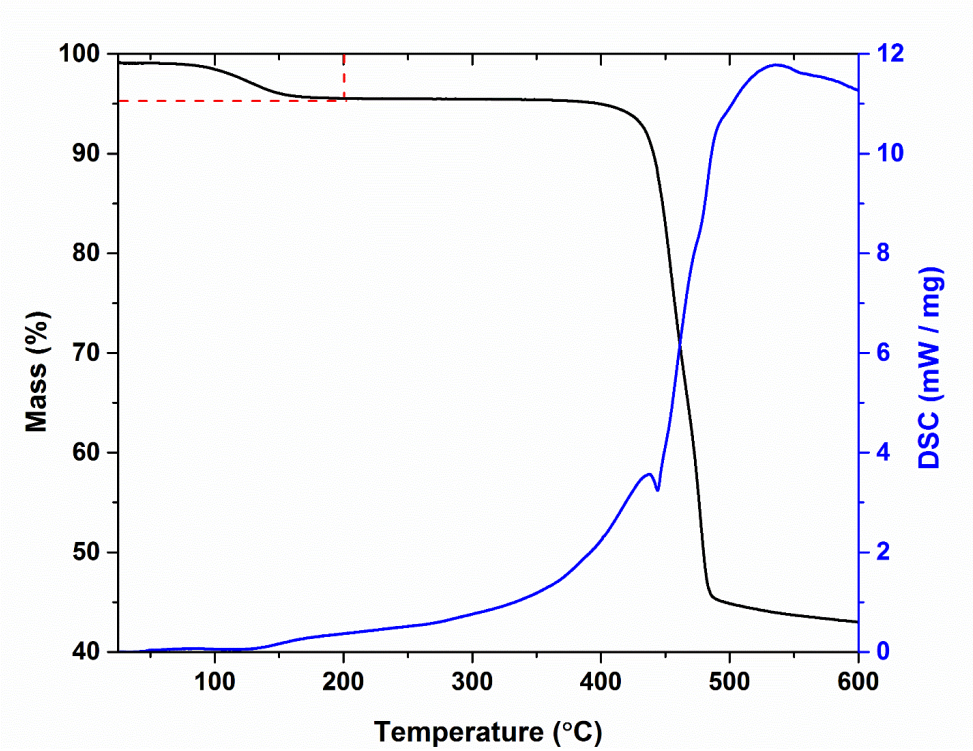

Figure 4.5 TGA-DSC data collected during the heating of **Cd(sdb)·nH$_2$O**. The first weight loss event amounts to a ~5% weight loss and is finished by 200°C.

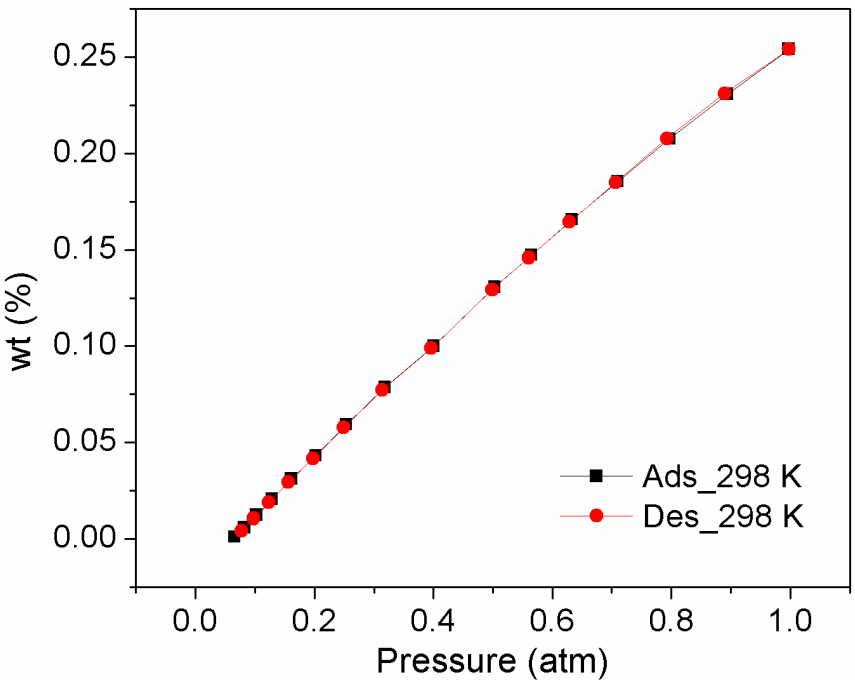

Figure 4.6 N_2 adsorption-desorption isotherm on **Cd(sdb)** at room temperature.

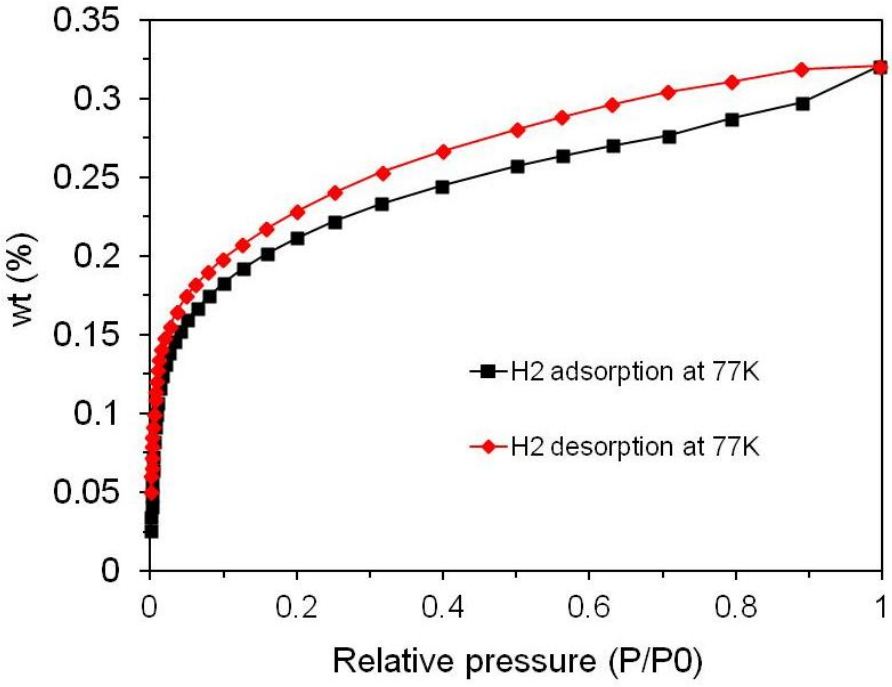

Figure 4.7 H_2 adsorption-desorption isotherm on **Cd(sdb)** at 77 K.

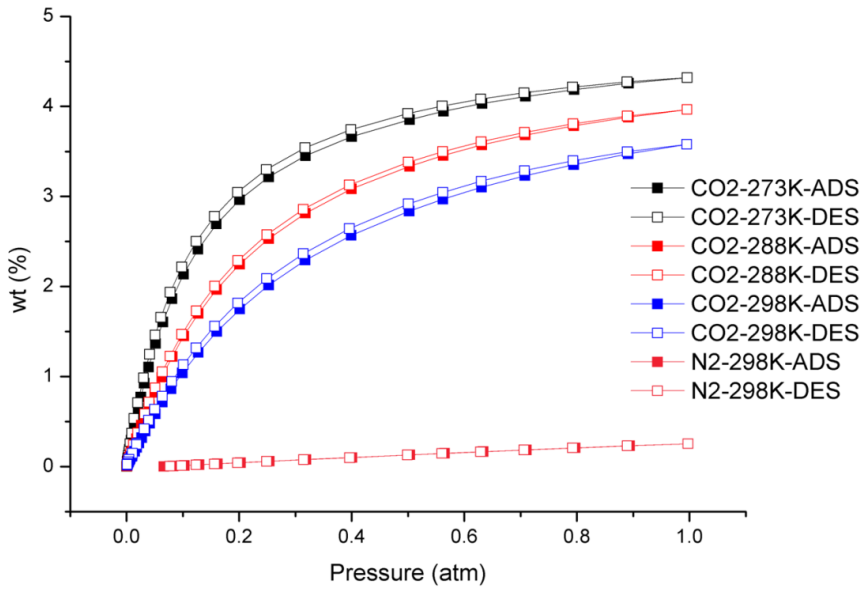

Figure 4.8 CO_2 and N_2 adsorption-desorption isotherms on **Cd(sdb)** at 3 different temperatures for CO_2 and RT for N_2.

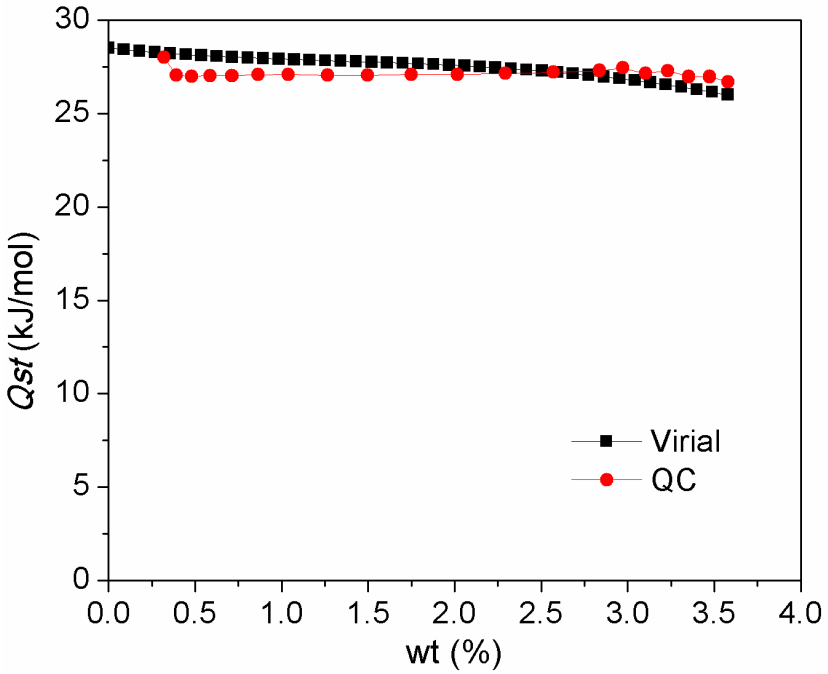

Figure 4.9 Q_{st} of CO_2 adsorption on **Cd(sdb)** calculated by Virial and QC method.[65]

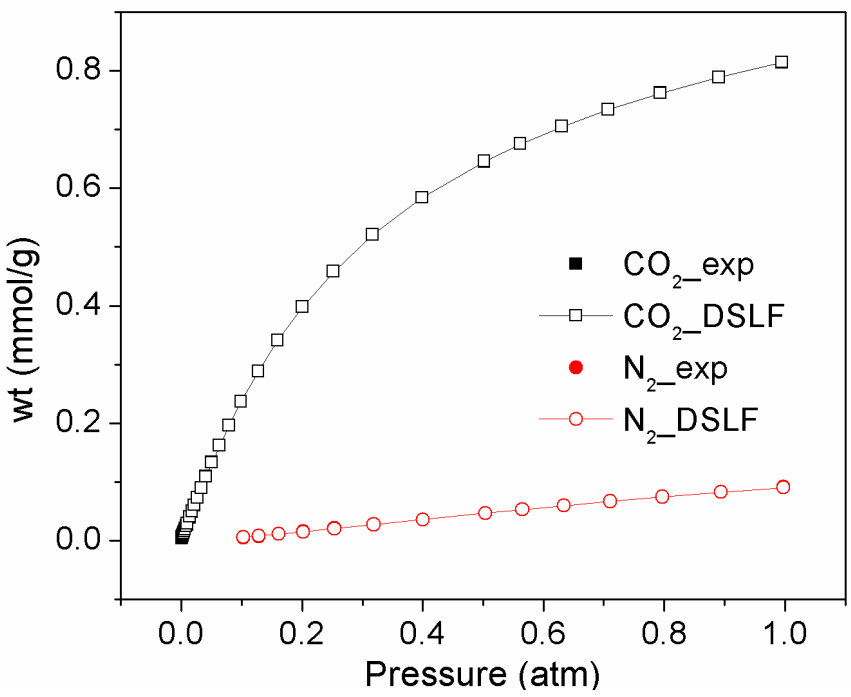

Figure 4.10 Experimental and fitted isotherms for CO_2 and N_2 at 298 K for **Cd(sdb)**.

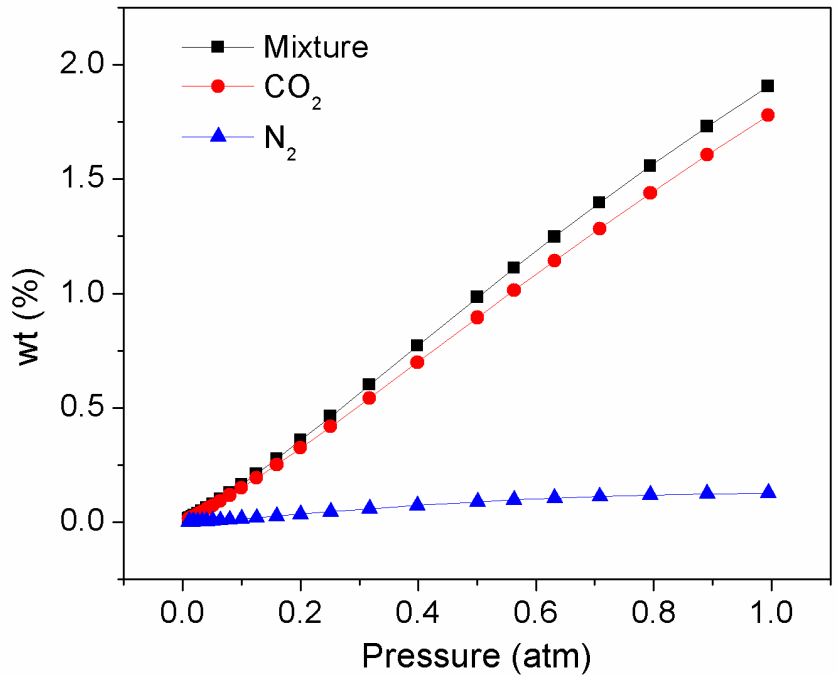

Figure 4.11 IAST predicted isotherms of a binary mixture of CO_2 and N_2 (CO_2:N_2 = 15:85) at 298 K as a function of the total pressure for **Cd(sdb)**.

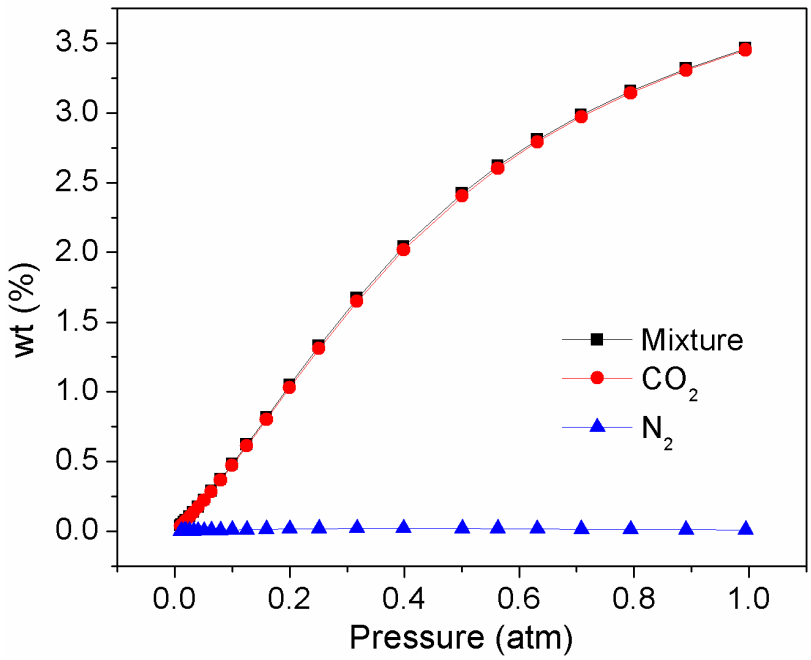

Figure 4.12 IAST predicted isotherms of a binary mixture of CO_2 and N_2 (CO_2:N_2 = 10:90) at 298 K as a function of the total pressure for **Cd(sdb)**.

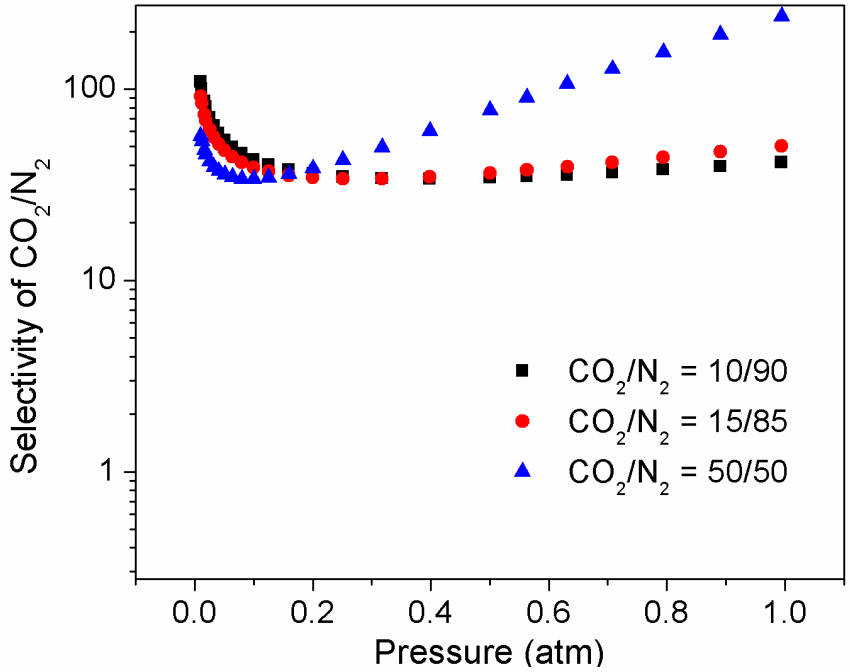

Figure 4.13 A room temperature CO_2/N_2 selectivity calculated with the IAST method for three CO_2 concentrations (CO_2/N_2: 10:90, 15:85 and 20:80) in the CO_2-N_2 binary mixtures for **Cd(sdb)**.

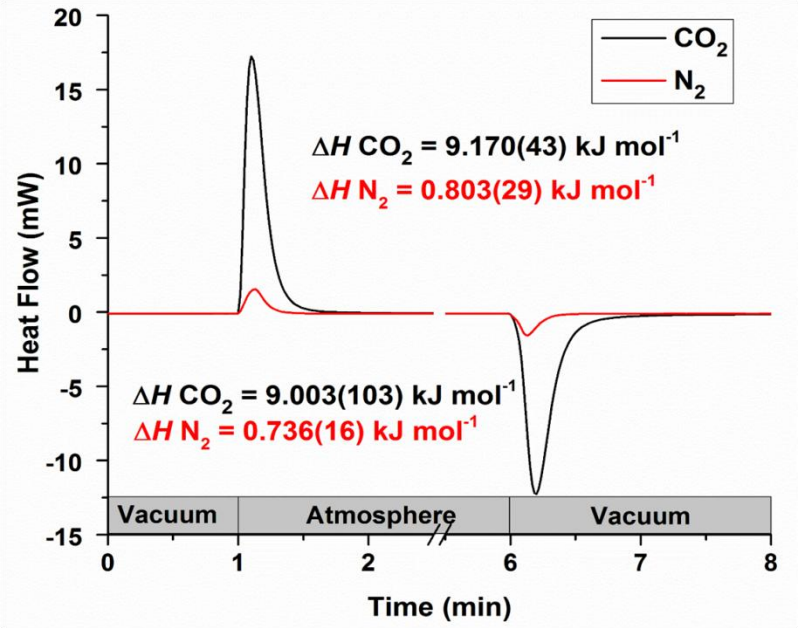

Figure 4.14 DSC signals of **Cd(sdb)** during vacuum-swing events to nitrogen and carbon dioxide atmospheres at 2% RH.

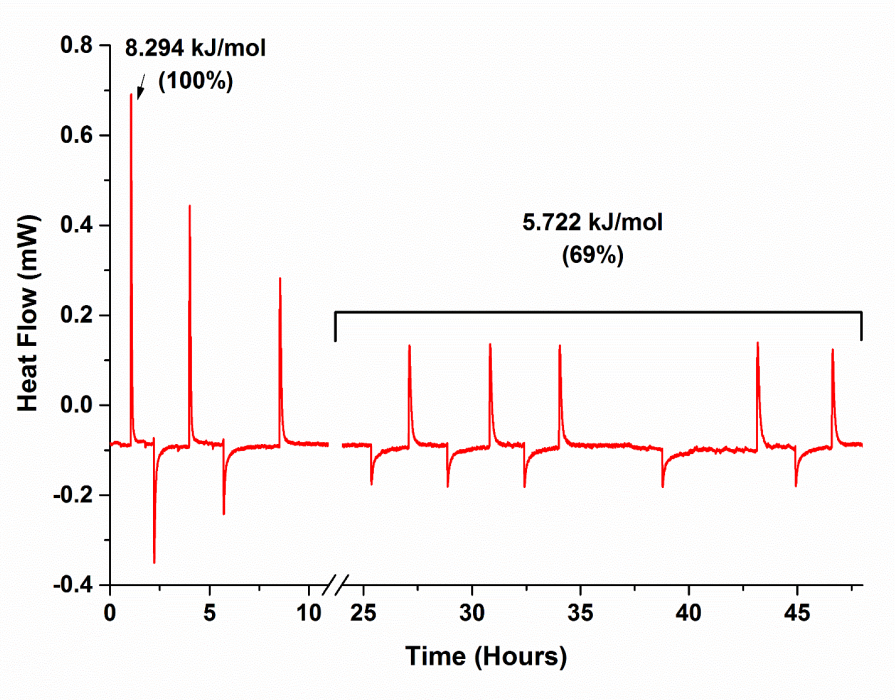

Figure 4.15 DSC data of **Cd(sdb)** during atmosphere swings between CO_2 and N_2 at 30% RH, the 8.294 kJ/mol value correspond to differential enthalpy between CO_2 and N_2 gas sorption.

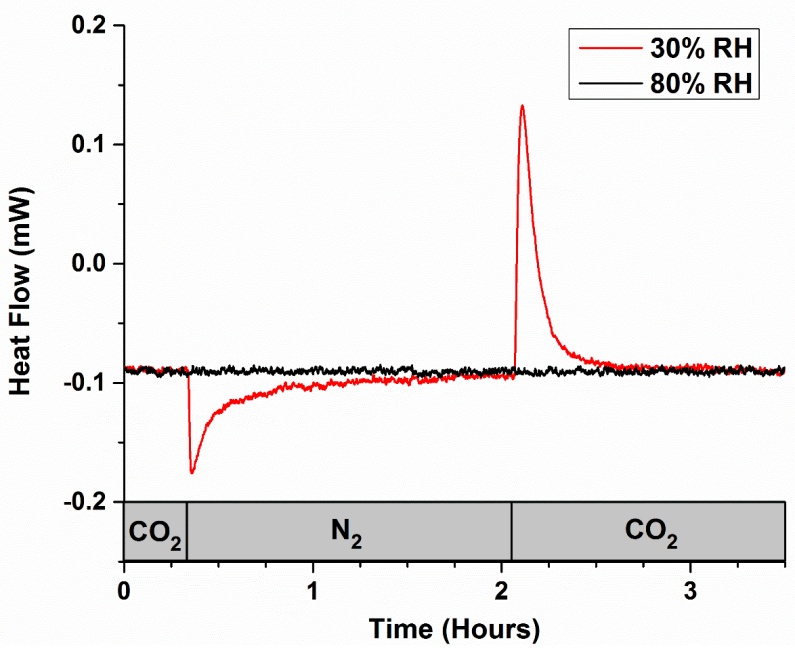

Figure 4.16 DSC data of **Cd(sdb)** during an atmosphere swing cycle from CO_2 to N_2 back to CO_2 at 30% RH (red) and 80% RH (black).

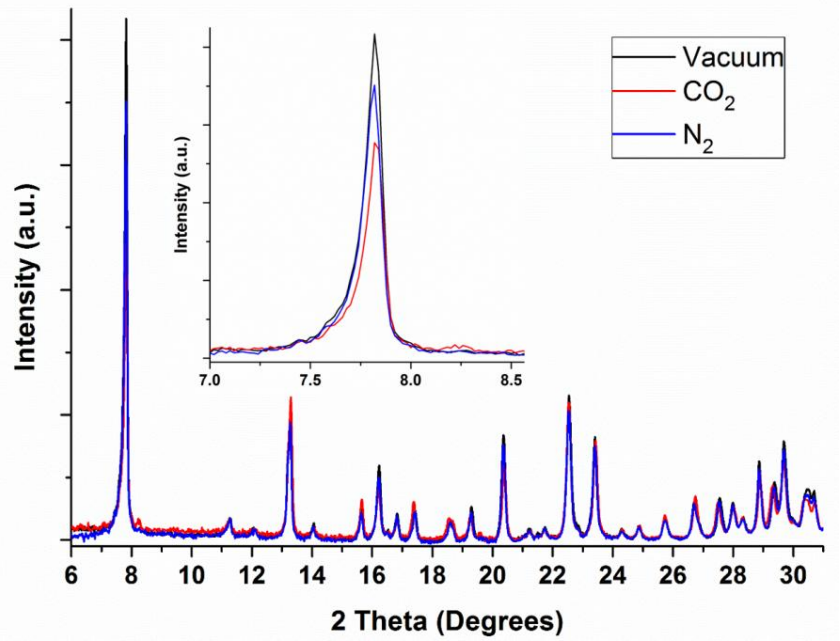

Figure 4.17 XRD patterns of **Cd(sdb)** in vacuum (black), nitrogen (blue), and carbon dioxide (red) atmospheres. The XRD patterns show the relative intensities of some reflections change while the most notable change is the intensity of the low angle (**110**) reflection at ~7.85° 2 theta.

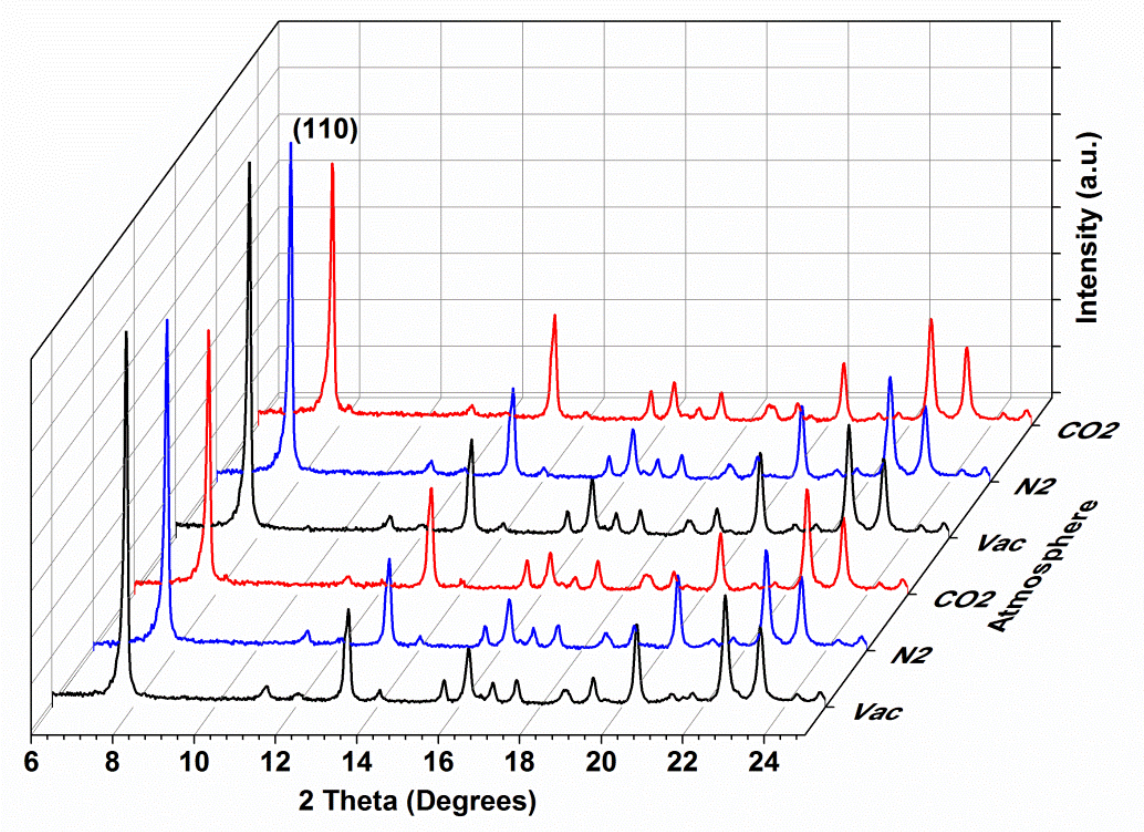

Figure 4.18 Gas-swing experiments for the CO_2 loading on the activated **Cd(sdb)** at 2% RH, 298 K showing change in relative intensities of low angle peaks.

Table 4.1: Crystallographic data and structural refinement details of **Cd(sdb)·nH$_2$O**.

Empirical formula	$CdC_{14}H_8SO_{7.44}$
Formula weight	439.66
Space Group	C 2/c
a (Å)	13.3382(4)
b (Å)	21.4986(7)
c (Å)	10.1527(6)
β (°)	95.000(1)
Volume (Å^3)	2900.2(2)
Z	8
Collection Temperature (K)	100
Wavelength (Å)	0.41328
Absorption coefficient (mm^{-1})	2.011
Crystal size (mm)	0.08 × 0.02 × 0.02
Index range	$-18 \leq h \leq 19$
	$0 \leq k \leq 30$
	$-10 \leq l \leq 14$
Measured reflection	6850
Independent reflection	4342
Reflections with $I > 2s(I)$	3853
R_{int}	0.031
Data /Restraints /parameter	4342/0/230
R ($F^2 > 2\sigma(F^2)$	0.055
wR (F^2)	0.162
S	1.22

Table 4.2: Atomic coordinates ($\times 10^4$) and equivalent isotropic displacement parameters (U_{eq}, $Å^2 \times 10^3$) for **Cd(sdb)·nH$_2$O**.

	x	y	z	U_{eq}
C(1)	1033(4)	7198(3)	7546(6)	14(1)
C(4)	2599(5)	8031(3)	7541(7)	17(1)
C(2)	1367(9)	7365(5)	6357(11)	22(2)
C(3)	2156(9)	7798(5)	6382(12)	26(3)
C(5)	2215(10)	7859(7)	8749(13)	29(3)
C(6)	1424(10)	7436(6)	8752(12)	29(3)
C(2')	1713(17)	7145(11)	6600(20)	11(4)
C(3')	2514(16)	7563(10)	6620(20)	10(4)
C(5')	1950(20)	8092(16)	8460(30)	27(6)
C(6')	1130(20)	7691(15)	8480(30)	24(6)
C(7)	3466(4)	8475(3)	7522(7)	17(1)
C(8)	3628(4)	10173(3)	8044(6)	13(1)
C(9)	2726(4)	10593(3)	7927(6)	14(1)
C(10)	2384(5)	10820(3)	6681(7)	18(1)
C(11)	1540(5)	11201(3)	6559(7)	19(1)
C(12)	1051(4)	11346(3)	7678(7)	16(1)
C(13)	1382(5)	11117(3)	8916(7)	19(1)
C(14)	2227(5)	10737(3)	9033(7)	18(1)
Cd(1)	5155(1)	9270(1)	9195(1)	9(1)
O(1)	3851(3)	9906(2)	7035(5)	16(1)
O(2)	4100(3)	10095(2)	9191(4)	13(1)
O(1W)	-240(50)	9630(30)	8060(60)	290(50)
O(3)	3789(3)	8710(2)	8607(5)	18(1)
O(2W)	0	8980(50)	7500	320(70)
O(4)	3802(4)	8568(2)	6406(5)	20(1)
O(5)	46(3)	6338(2)	8725(5)	14(1)
O(6)	45(4)	12183(2)	6280(6)	23(1)
S(1)	0	6685(1)	7500	11(1)
S(2)	0	11850(1)	7500	17(1)
O(3W)	360(40)	9450(20)	9150(50)	100(20)

Table 4.3: Anisotropic displacement parameters ($Å^2 \times 10^3$) for **Cd(sdb)·nH$_2$O.**

	U^{11}	U^{22}	U^{33}	U^{23}	U^{13}	U^{12}
C(1)	11(2)	11(2)	19(3)	-1(2)	4(2)	-2(2)
C(4)	11(2)	10(2)	29(3)	0(2)	2(2)	-3(2)
C(2)	21(5)	21(5)	25(5)	0(4)	1(4)	-9(4)
C(3)	22(5)	22(5)	35(6)	9(4)	5(4)	-8(4)
C(5)	26(6)	30(7)	32(6)	-14(5)	10(5)	-19(5)
C(6)	33(6)	34(7)	22(5)	-16(5)	17(5)	-20(6)
C(7)	10(2)	9(2)	31(4)	-1(2)	1(2)	-4(2)
C(8)	10(2)	12(2)	17(3)	3(2)	2(2)	1(2)
C(9)	10(2)	13(3)	19(3)	1(2)	2(2)	1(2)
C(10)	16(3)	21(3)	17(3)	6(2)	5(2)	3(2)
C(11)	17(3)	20(3)	20(3)	8(2)	4(2)	2(2)
C(12)	10(2)	12(3)	24(3)	4(2)	0(2)	1(2)
C(13)	16(3)	18(3)	23(3)	-3(2)	6(2)	1(2)
C(14)	15(3)	18(3)	20(3)	0(2)	2(2)	1(2)
Cd(1)	9(1)	8(1)	11(1)	-1(1)	1(1)	1(1)
O(1)	17(2)	14(2)	18(2)	-1(2)	4(2)	4(2)
O(2)	13(2)	12(2)	14(2)	0(2)	-1(2)	1(2)
O(3)	16(2)	12(2)	26(2)	5(2)	2(2)	-4(2)
O(4)	15(2)	13(2)	32(3)	-2(2)	7(2)	-3(2)
O(5)	17(2)	10(2)	16(2)	4(2)	2(2)	1(2)
O(6)	19(2)	16(2)	34(3)	9(2)	2(2)	1(2)
S(1)	12(1)	8(1)	13(1)	0	3(1)	0
S(2)	12(1)	11(1)	28(1)	0	2(1)	0

Table 4.4: Selected bond lengths and angles for **Cd(sdb)·nH$_2$O**.

Bond	(Å)
Cd(1)-O(4)#1	2.175(5)
Cd(1)-O(3)	2.220(5)
Cd(1)-O(2)	2.264(4)
Cd(1)-O(2)#2	2.293(4)
Cd(1)-O(1)#1	2.341(5)
Cd(1)-O(5)#3	2.518(4)
Angle	**(°)**
O(4)#1-Cd(1)-O(3)	94.54(19)
O(4)#1-Cd(1)-O(2)	162.85(18)
O(3)-Cd(1)-O(2)	85.92(16)
O(4)#1-Cd(1)-O(2)#2	111.43(18)
O(3)-Cd(1)-O(2)#2	144.01(18)
O(2)-Cd(1)-O(2)#2	76.41(17)
O(4)#1-Cd(1)-O(1)#1	81.37(17)
O(3)-Cd(1)-O(1)#1	131.53(17)
O(2)-Cd(1)-O(1)#1	85.51(16)
O(2)#2-Cd(1)-O(1)#1	78.60(16)
O(4)#1-Cd(1)-O(5)#3	89.60(17)
O(3)-Cd(1)-O(5)#3	78.42(16)
O(2)-Cd(1)-O(5)#3	107.24(15)
O(2)#2-Cd(1)-O(5)#3	77.34(15)
O(1)#1-Cd(1)-O(5)#3	149.06(16)

Symmetry transformations used to generate equivalent atoms:

#1 -x+1,y,-z+3/2

#2 -x+1,-y+2,-z+2

#3 -x+1/2,-y+3/2,-z+2

Table 4.5: Equation parameters for the DSLF isotherm model for CO_2 and N_2 adsorption on **Cd(sdb)**

Adsorbates	N_1^{max} (mmol/g)	b_1 (kPa^{-1})	n_1	N_2^{max} (mmol/g)	b_2 (kPa^{-1})	n_2	R^2
CO_2	0.92	0.025	0.92	17.18	0.00034	1.67	0.9999
N_2	0	0.00016	3.93	0.20	0.00099	0.68	0.9991

Chapter 5

Molecular Traps for Light Hydrocarbons – Understanding the Sorption of Ethane, Ethylene and Acetylene in two novel Ca-based MOFs

5.1 Abstract

Herein, we report the mechanism of ethane, ethylene and acetylene adsorption on two microporous metal organic frameworks. The proposed adsorption mechanism is consistent with observations from a number of techniques including single crystal X-ray diffraction (XRD), *in situ* XRD-DSC and gas isotherm measurments. The two calcium-based materials, **Ca(sdb)** and **Ca(tcpb),** form microporous three-dimensional frameworks surrounding one-dimensional channels. After removal of the solvent water both **Ca(sdb)** and **Ca(tcpb)** remain porous, and do not saturate with water vapor from the air. Pore geometries of both **Ca(sdb)** and **Ca(tcpb)** provide multiple adsorption sites for hydrocarbon molecules trough C-H$^{\cdots}\pi$ and C-H$^{\cdots}$O interactions, similarly to interactions in the molecular and protein crystals. Both materials show selective adsorption of C_2 hydrocarbon gases – ethane, ethylene and actylene (C_2H_n) over methane as determined from IAST calculations, with C_2H_6/CH_4 selectivity as high as 74 in **Ca(sdb).**

5.2 Introduction

The separation of hydrocarbon gases using solid state adsorbents is proposed as an alternative to the expensive and energy intensive process of cryogenic distillation.[14] A critical component for the rational designing of efficient adsorbents, requires a detailed molecular level understanding of the mechanism responsible for the gas adsorption, and any associated selectivity towards particular gases, in existing materials.[30d] The effective separation of light hydrocarbon gases (C_1-C_2) is important for the petroleum industry and influences the price and availability of plastics, used routinely in our daily lives.[13]

We have recently described permanently porous sdb-based MOF with interesting gas-uptake properties. Herein, we report the hydrocarbon adsorption mechanism of **Ca(sdb)** and of a novel material - **Ca(tcpb)** [tcpb: 1,2,4,5-tetrakis(4-carboxyphenyl)benzene] and their associated C_2/C_1 selectivity determined from the ideal adsorbed solution theory (IAST) calculations. Since the examples related to the C_2H_n-framework interaction determined by single crystal diffraction method are scarce, the detailed structural insights gained here will help design further gas-selective solids of this type.

For the detailed description of **Ca(sdb)** structure see the chapter 3.

Ca(tcpb) is a novel material that we recently reported, which has a surface area of 195 m^2/g and exhibits a high Xe/Kr selectivity of about 10 at 298 K.[66] Structurally, **Ca(tcpb)** is based on isolated CaO_6 octahedra, connected by half-deprotonated tcpb linkers into a three-dimensional framework, with diamond-shaped one-dimensional channels, running in a [001] direction (Fig. 5.1). **Ca(tcpb)** has a permanent porosity of 25.6% (PLATON[67]) and it contains two types of crystallographically different channels (type I and II). The channels have walls built with phenyl

rings, and additionally the channels of the type II contain polar -OH groups. Both the phenyl rings and oxygen atoms serve as strong adsorption sites for C_2H_n molecules. Similarly to **Ca(sdb)**, after removal of the native solvent water, **Ca(tcpb)** does not saturate with the water vapor from the atmosphere as evident from TGA and SCXRD experiments.[66]

5.3 Experimental Section

5.3.1 Synthesis and Activation

For the synthesis and activation procedures for **Ca(sdb)·nH$_2$O** see the chapter 3.3.1.

Ca(tcpb)·nH$_2$O was synthesized by Xianyin Chen under solvothermal conditions. Starting materials include calcium chloride ($CaCl_2$, 96%, Acros-Organics), 1,2,4,5-Tetrakis(4-carboxyphenyl)benzene acid [H_2(tcpb), Sigma Aldrich, 98%] and ethanol (95%, Fisher Scientific) and were used without further purification. A mixture of 0.027g (0.25 mmoles) of $CaCl_2$ and 0.03g (0.05 mmoles) of H_2(tcpb) was dissolved in 12 grams of ethanol and stirred for 2 hours to achieve homogeneity. The resultant solution was heated at 373 K for 3 days in the oven. Colorless prism-shaped crystals were recovered as a product and washed with ethanol. The yield was ~50%, 0.02g. The as-synthesized **Ca(tcpb)·nH$_2$O** contains uncoordinated, disordered water molecules inside the channels. The water molecules come from the 95% ethanol solvent and the adsorbed moisture on the $CaCl_2$ reactant.

For the activation (see the chapter 2.2) **Ca(tcpb)·nH$_2$O** was heated to 513 K and held in vacuum for 5 hours.[66]

5.3.2 Single Crystal XRD with Adsorbed Hydrocarbon Gases

For details on hydrocarbon gas loading and single crystal diffraction see the chapter 2.7

For the gas loading, activated crystals of **Ca(sdb)** and **Ca(tcpb)** were placed in a three-neck flask with ethane, ethylene or acetylene flowing into the flask, and kept for 2 hours. Further the crystals were coated with the Paratone® oil, while keeping the gas flowing to maintain 1 bar conditions (see the chapter 2.7).

The crystals of the C_2H_n-loaded **Ca(sdb)** and **Ca(tcpb)** suitable for the single crystal X-ray diffraction were selected from the bulk using polarizing microscope to determine crystal quality. Reflections for the compounds **Ca(sdb):C_2H_2**, **Ca(sdb):C_2H_4**, **Ca(tcpb):C_2H_2** and **Ca(tcpb):C_2H_4** were collected with 1°ω-scans at 100 K using a four-circle kappa Oxford Gemini diffractometer (λ= 0.71073/1.54184Å). Reflections for **Ca(sdb):C_2H_6** and **Ca(tcpb):C_2H_6** were collected at 100 K at APS ChemMatCars (sector 15) beamline (see the chapter 2.7).

The structures of gas-loaded **Ca(sdb)** and **Ca(tcpb)** were solved with direct methods using SHELXS-97 and refined with full-matrix least squares on F^2 with SHELXL-97 (Tables 5.1-5.14). [49-50] During the structure solution atoms from the MOF framework were located first and refined with anisotropic displacement parameters. Hydrogen atoms were added to aromatic rings using geometrical constrains (HFIX command). After obtaining a satisfactory model of the framework, Fourier difference maps were calculated to locate the adsorbed gas molecules. All gas molecules were located from the strong electron density peaks and refined with anisotropic displacement parameters. The occupancy of the C atoms from the adsorbed gases was also refined. The C-C distances in the hydrocarbon molecules were restrained to 1.20(1) Å, 1.30(1) Å and 1.47(1) Å for acetylene, ethylene and ethane, respectively. Hydrogen atoms on the

hydrocarbon molecules were added with geometrical constrains, in most cases the H atoms were visible on the electron density maps.

5.3.3 Gas Adsorption

Gas isotherm measurments, DSLF model and IAST calculations were performed by Hao Wang at Rutgers University.

For the details on gas adsorption procedures see the chapter 1.4.

Ca(sdb) and **Ca(tcpb)** were tested by Hao Wang for the C_1-C_2 hydrocarbon gases adsorption at 273/278 K, 288 K, 298 K and pressures up to 1 bar (Figs. 5.2-5.3). Additionally, the adsorption of propane, propylene and n-butane was measured by Hao Wang for **Ca(tcpb)** and results are shown in Figure 5.5. The differential enthalpy of adsorption ($-\Delta H$, kJ/mol_{MOF}) was measured with XRD-DSC method, via vacuum-swing experimental procedure (Figs. 5.2-5.3, 5.5) for C_1-C_2 in **Ca(sdb)** and C_1-nC_4 in **Ca(tcpb)**. Isosteric heat of adsorption values (Q_{st}, kJ/mol_{GAS}) were obtained through the relation $Q_{st} = H/n_i$, where n_i corresponds to the adsorbed moles of the gas (Table 5.15). Furthermore, Q_{st} for C_1-nC_4 was calculated for **Ca(tcpb)** with the Virial method, and the values of Q_{st} obtained with DSC and Virial methods are in a good agreement (Table 5.16).

The single-component hydrocarbon gases adsorption isotherms were fitted with the DSLF model to enable the application of IAST in simulating the performance of **Ca(sdb)** and **Ca(tcpb)** under a mixed component gas.

5.3.4 XRD-DSC

For the details of vacuum-swing procedure see the chapter 2.6.

Powder X-ray diffraction (PXRD) patterns were collected within a range $5° \leq 2\theta \leq 37°$ (step size: 0.02°, counting time: 2s/step). The DSC measurements were performed using 9 – 10.5 mg of the sample in an aluminum crucible with an equal amount of Al_2O_3 in the reference crucible. Vacuum-swing measurments on **Ca(sdb)** and **Ca(tcpb)** were conducted to determine the differential enthalpy between empty and gas-loaded materials at 298 K and 1 atm. **Ca(sdb)** was tested for the adsorption of C_1-C_2 hydrocarbons and **Ca(tcpb)** for the adsorption of C_1-nC_4 hydrocarbons.

Samples were activated first at 563 K [**Ca(sdb)**] or 523 K [**Ca(tcpb)**] under vacuum on the XRD-DSC stage and held at the activation temperature for 5 to 10 h, then cooled to RT. Further, the chamber was pressurized to 1 bar of hydrocarbon gas over the course of 15 seconds. After 120 minutes for **Ca(sdb)** or 10 minutes for **Ca(tcpb)**, when the DSC signal returned to the baseline, the chamber was evacuated to vacuum over the course of 15 seconds. In the case of **Ca(sdb)** the strong interaction between the adsorbate and the framework leads to an incomplete removal under experimental vacuum conditions, during the second swing the exotherm was only reaching to the values ~85% of the first exotherm. As a result the reported enthalpies were calculated based on the averages of the first exotherms of three different samples. In the case of **Ca(tcpb)** gas can be removed fully with vacuum, and a total of 6 to 8 cycles of vacuum-swing was completed.

5.4 Results and Discussion

5.4.1 Gas Adsorption Isotherms, Enthalpy of Adsorption and Selectivity.

Ca(sdb) shows a moderate adsorption of C_2H_n at 298 K; uptakes of 29.5, 30.0 and 25.6 cm^3/g were measured for ethane, ethylene and acetylene, respectively. Methane is adsorbed at a lower amount than C_2H_n with the uptake of 18.85 cm^3/g at 1 bar, 298 K (Fig. 5.2). The main difference between the adsorption of methane and C_2H_n is apparent when looking at the low pressure region of the isotherm. **Ca(sdb)** is saturated with C_2H_n at a very low pressure; for example, the ethane uptake of 27.3 cm^3/g at 0.1 bar is equal to over 90% of the total uptake at 1 bar. For comparison, methane adsorption at 0.1 bar (0.91 cm^3/g) is equivalent to less than 5% of the total uptake at 1 bar, and is more than 30 times lower than the ethane uptake at this pressure. Q_{st} of C_1-C_2 hydrocarbons in **Ca(sdb)** is relatively high,[14, 35] with the moderate differences between methane and C_2H_n (Table 5.15). The difference in adsorption behavior and heats of adsorption between methane and C_2H_n could be explained by the higher electrostatic and dispersion interactions with the pore surface, and thus higher affinity of **Ca(sdb)** towards C_2 gases compared to small methane.[14] The gas adsorption selectivity calculated with the IAST method shows the C_2H_6/CH_4 selectivity of 74, C_2H_4/CH_4 of 73 and C_2H_2/CH_4 of 33 (Fig. 5.4). The C_2H_4/CH_4 and C_2H_2/CH_4 selectivity for **Ca(sdb)** are lower than those of the Fe-MOF-74 (700 and 200, respectively), because of the presence of open metal sites in the activated framework in the latter case, while **Ca(sdb)** posses no open metal sites.[35] However, the 74 C_2H_6/CH_4 selectivity is more than 3 times higher than for Fe-MOF-74 (20).[35]

Ca(tcpb) uptake of C_2H_n is more than 2 times higher than in the case of **Ca(sdb)** at 298 K and 1 bar, and the difference in maximum uptake between methane and C_2H_n is more prominent than for **Ca(sdb)**. **Ca(tcpb)** adsorbs 17.3 cm^3/g of methane at 298 K and 64.7, 59.8 and 62.2 cm^3/g of acetylene, ethylene and ethane, respectively. The maximum uptake of C_2H_n in **Ca(tcpb)** at 1 bar, 298K is lower than for prototypical MOFs such as Fe-MOF-74, or MOF-5 but considerably higher than those of other porous materials extensively studied for hydrocarbon adsorption like ZIF-7 or RPM-3-Zn.[13, 32, 68] The Q_{st} values for C_1-C_2 hydrocarbons adsorbed on **Ca(tcpb)** are lower than in the case of the **Ca(sdb)** material (Table 5.15). The calculated C_2/C_1 selectivity in **Ca(tcpb)** are 26, for C_2H_6/CH_4, 16 for C_2H_4/CH_4 and 18 for C_2H_2/CH_4 (Fig. 5.4), also lower than those calculated for **Ca(sdb)** and Fe-MOF-74.[35]

As in **Ca(sdb)** the only presumed interaction between gas molecules and the pore space is C-H$\cdots\pi$, it is expected that the Q_{st} values will decrease with the C-C bond saturation.[69] Indeed acetylene displays the highest energy of interaction of the three gases with the Q_{st} of 41.5(4) kJ/mol_{GAS}. However, the Q_{st} values of ethylene and ethane are quite similar to each other (36.3(7) vs. 35.0(5) kJ/mol_{GAS}), suggesting that there is no significant influence of the C-C double bond on the adsorbent-adsorbate interaction. In **Ca(tcpb)** all C_2H_n display even more similar values of Q_{st}, with 30.3(2) kJ/mol_{GAS}, 29.2(1) kJ/mol_{GAS} and 32.3(1) kJ/mol_{GAS} for ethane, ethylene and acetylene, respectively. However, we can see that ethane interacts with the pore surface with the highest energy of the three, in spite of the full saturation of the C-C bond, normally leading to the lower adsorbent-adsorbate energy.[69a] The C_2H_n Q_{st} values for adsorption both in **Ca(sdb)** and **Ca(tcpb)** suggest that the size of the molecule and the number of the H-pore surface interactions play a more important role on the resultant energy of adsorption than the saturation of the C-C bond.

Ca(tcpb) was further tested for the adsorption of heavier C_3-nC_4 hydrocarbon gases (Fig. 5.5). When looking on the gas adsorption of C_1-C_4 alkanes in **Ca(tcpb)** we can see that the adsorption follows the general trends observed for porous MOFs such as MOF-5.[33b, 70] **Ca(tcpb)** saturates with longer alkanes at lower pressures, and the heavier gas generally displays a lower capacity than the lighter counterpart (Fig. 5.5). The measured -ΔH is dependant both on the Q_{st} and the gas uptake, and we can see that the -ΔH measured during butane adsorption is smaller than for propane, due to the smaller butane uptake (Fig. 5.5). Q_{st} becomes higher with an increase in the chain length due to the enhanced electrostatic and dispersion interactions between the adsorbed gases and the pore surfaces (Figs. 5.6-5.7).[71] In mixtures the longer chains are preferred over the smaller ones until the point of the maximum selectivity, when the entropic cost of the long chain ordering affects the energy gained from the adsorption.[14]

5.4.2 Structural Description of Ca(sdb):C_2H_n and Ca(tcpb):C_2H_n

We solved the crystal structures of the C_2H_n-loaded **Ca(sdb)** and **Ca(tcpb)** from single crystal diffraction data. Representative examples of the electron density map obtained from the diffraction data showing the adsorbed gas molecule, and the displacement ellipsoid plot of **Ca(tcpb)** are shown in the Figure 5.9. The refined occupancies of the gases are in average within less than 10% from the values obtained with gas-adsorption experiments, confirming the validity of the gas-loading technique (Table 5.17). The main presumed adsorbate-host interactions in **Ca(sdb)** and **Ca(tcpb)** are the C-H$\cdots\pi$ and C-H$\cdots$O, with the latter appearing only in the channels of the type II in **Ca(tcpb)**. Such interactions play a significant role in the molecular crystals packing, protein folding and molecular recognition.[69, 71]

Analysis of the structural data of **Ca(sdb):C_2H_n** collected at 100 K revealed that upon the loading with C_2H_n, the sdb linkers rotated back to a parallel configuration observed in the as-synthesized material. Adsorbates locate on the inversion center at the center of the pore. In the each structure half of the C_2H_n molecule is within the asymmetric unit and the second half is generated by the symmetry operation. Distances between the hydrogen atoms of the C_2H_n molecules and neighboring phenyl ring centroids are within 3.07(4) – 3.36(4) Å. The distance between adsorbate molecules along the channel is equivalent to lattice parameter *b*: 5.556(1) Å (Fig. 5.10). The parallel orientation of the linkers provides the optimal geometry for the hydrocarbon molecules, forming cages of four phenyl rings (Figs. 5.12 - 5.14). Ethylene molecule is oriented so that each of the H atoms is pointing towards the closest phenyl ring with the average distance of 3.15(9) Å. Ethane and acetylene gases locate in similar way, with the average C-H$^{\cdots}\pi$ distances of 3.4(1) and 3.23(8) Å, respectively. Acetylene and ethylene molecules display a two-fold disorder; ethane shows no spatial disorder (Figs. 5.12 - 5.14).

In **Ca(tcpb)**, gas adsorption sites differ between channels of the type I and II. In the type I channels, the only presumed interaction is between the hydrogen atoms of the adsorbates and the π clouds of the organic linkers. The adsorbates locate within less than 4 Å distance to two or four phenyl rings at a time. The shortest C-H$^{\cdots}$ π lengths, measured as distances between the H atom and the phenyl centroid, are 3.11(2), 3.09(2) and 3.10(2) Å for acetylene, ethylene and ethane, respectively (Figs. 5.14 - 5.16). All three adsorbates can be located unambiguously from the electron density maps and all three, except acetylene in the channels of type II, show no spatial disorder. Gases were especially well ordered in the type II channels, where hydrogen atoms could be located directly from electron density maps. As the pore surface is decorated with multiple oxygen atoms including the -OH groups within 4 Å from the center of the pore, it

provides strong adsorption sites for the adsorbates through the presumed C-H···O interaction (Figs. 5.14 - 5.16). The shortest C-H···O distances are: 3.10(2), 2.44(2) and 2.79(2) Å for acetylene, ethylene and ethane, respectively.

5.4.3 XRD-DSC

DSC experiments were used to measure -ΔH and further calculate Q_{st} of the hydrocarbon gases in **Ca(sdb)** and **Ca(tcpb)** with the gas-swing procedure, and the results are shown in the Table 5.15.

In situ PXRD diffraction patterns of **Ca(sdb)** and **Ca(tcpb)** confirm the adsorption mechanisms determined with the single crystal diffraction. Upon gas loading, low angle peaks decrease with respect to higher angle reflections, consistent with the gas molecules occupying the pore space (Fig. 5.18). Further, **Ca(tcpb)** shows an increasing lattice change with the size of adsorbates as evident from the shifting of peaks' positions in the PXRD patterns. A lattice dimension *a* increases and an α angle decreases from 5.1011(3) Å and 83.132(5)° in the activated sample to 5.2195(2) Å and 82.533(1)° in the **Ca(tcpb):C_2H_6**, as determined from single crystal data and consistent with PXRD observations (Figs. 5.18 – 5.20). The *a* parameter is equivalent to the distance between adsorbed gas molecules along the pore. *In situ* PXRD data collected at 298 K from C_3-nC_4 gas-loaded **Ca(tcpb)** show further increasing change between activated and gas-loaded material with increasing length of hydrocarbon chain, suggesting that **Ca(tcpb)** framework is flexible and can accommodate larger molecules (Figs. 5.21-5.24).

5.5 Conclusions

We characterized adsorption mechanisms of ethane, ethylene and acetylene in two microporous Ca-based metal organic frameworks, **Ca(sdb)** and **Ca(tcpb)**. Both materials are selective towards C_2H_n hydrocarbons over methane with the maximum C_2/C_1 selectivity of 74 for C_2H_6/CH_4 in **Ca(sdb)**. Crystal structure of the gas-loaded **Ca(sdb)** shows that the framework behaves like a trap towards the C_2 hydrocarbons. The pore geometry in **Ca(sdb)** is optimal for the small C_2H_n molecules, as each of the pore segments is built with four phenyl rings, providing strong adsorption sites through C-H$^{\cdots}\pi$ interactions. **Ca(tcpb)** contains two types of channels, in the first type only phenyl rings are accessible as adsorption sites for hydrocarbon molecules, while the second type contains multiple O atoms in the close proximity to the center of the pore. The adsorbate-adsorbent interaction in **Ca(tcpb)** appears to be similar to the **Ca(sdb)** case, except in the channels where additional polarizing -OH groups and oxygen atoms serve as strong adsorption sites for C_2H_n, through the C-H$^{\cdots}$O interaction. Those single crystal data are confirmed by the experimental gas adsorption and the XRD-DSC studies. *In situ* XRD-DSC results further suggest that **Ca(tcpb)** displays some network flexibility, which allows accommodating all the C_1-nC_4 hydrocarbon gases inside the pore space.

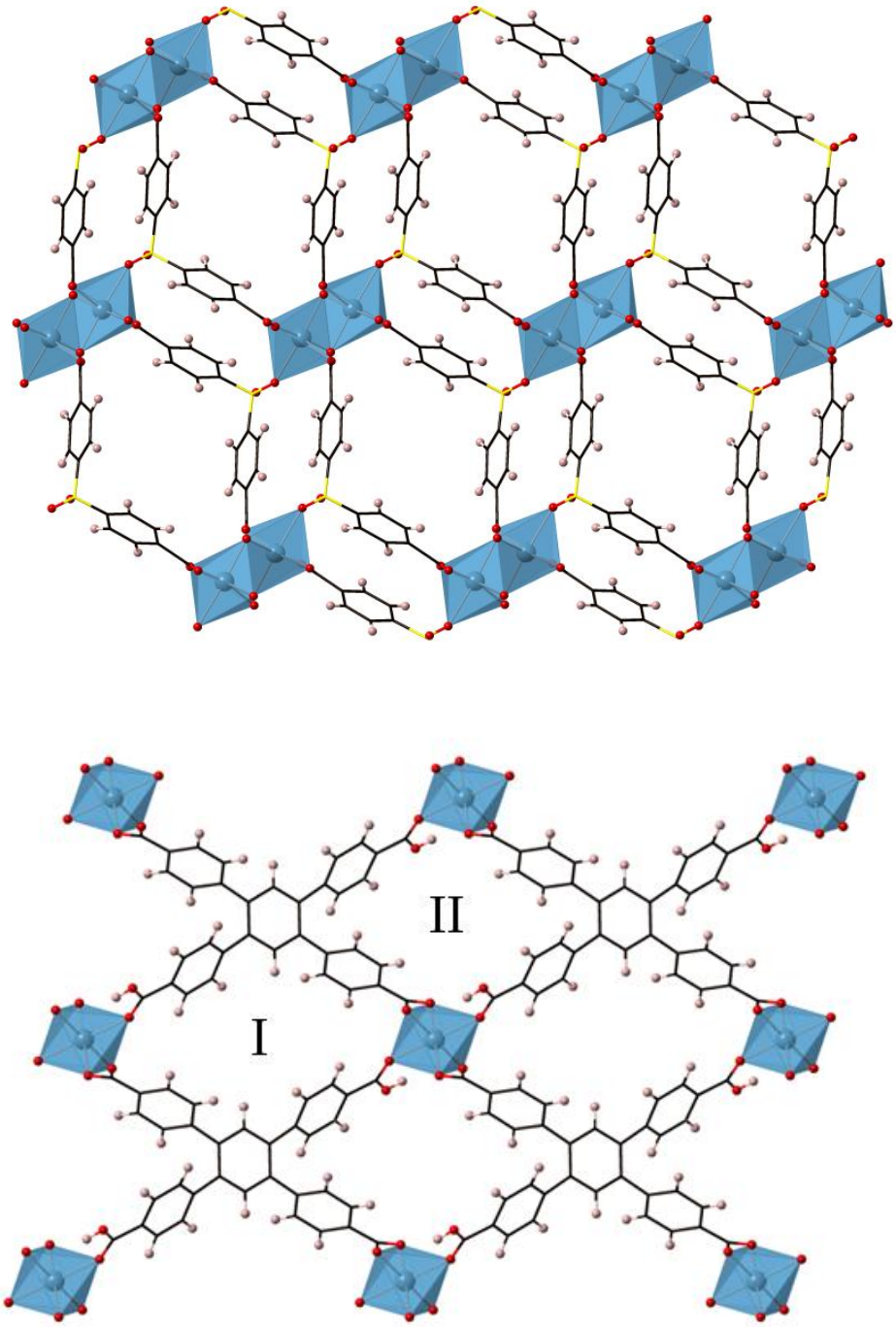

Figure 5.1 Polyhedral representation of (top) **Ca(sdb)** and (bottom) **Ca(tcpb)** structures, as seen in [010] and [100], respectively. **Ca(tcpb)** displays two crystallographically different types of channels, designated on the figure as I and II. Blue polyhedra represent Ca, red spheres – O, black wire – C, yellow wire – S and pink spheres – H.

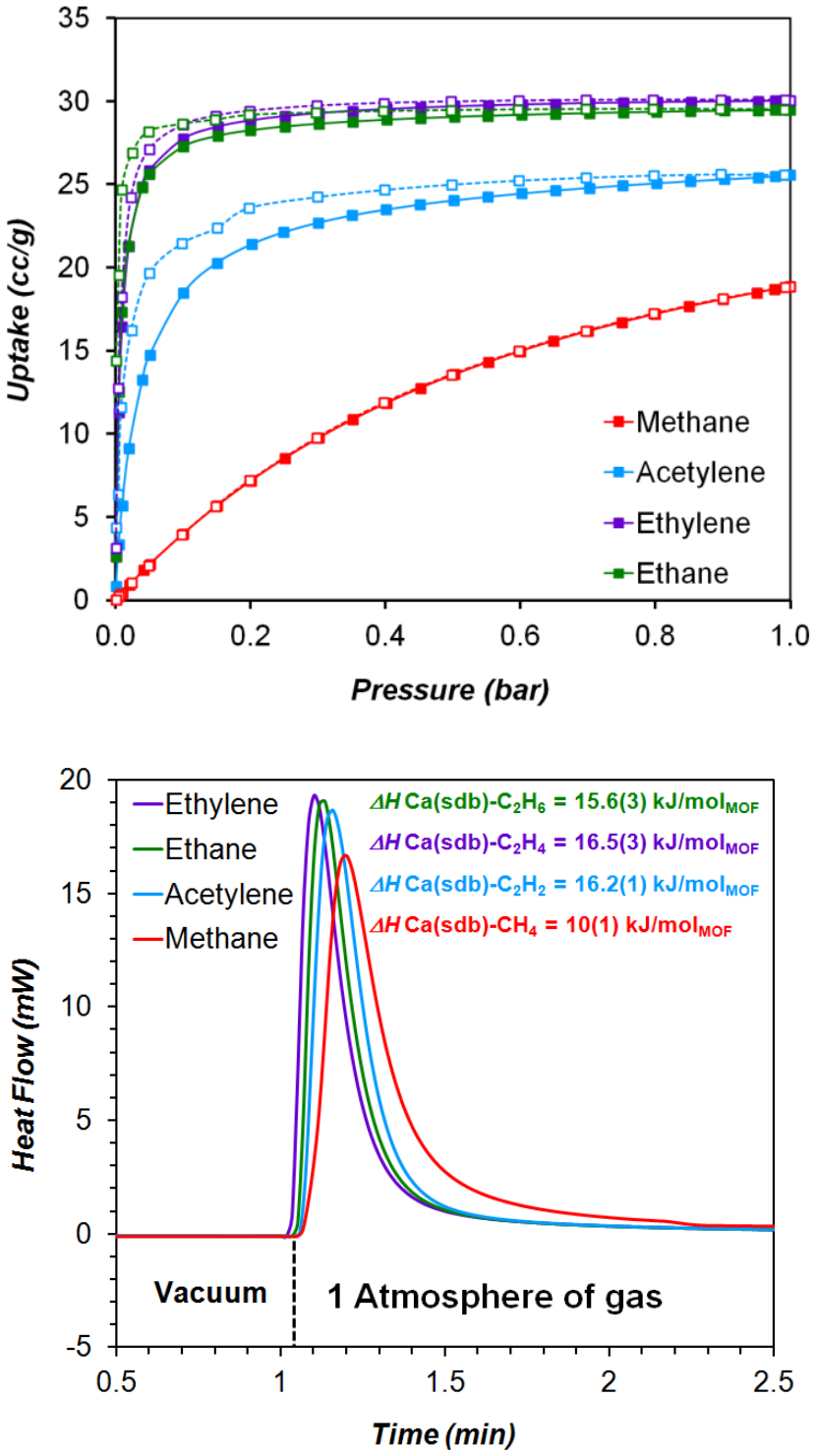

Figure 5.2 Top: C_1-C_2 hydrocarbon isotherms at 298 K for **Ca(sdb)**; bottom: DSC signals measured upon loading activated **Ca(sdb)** with C_1-C_2 gases.

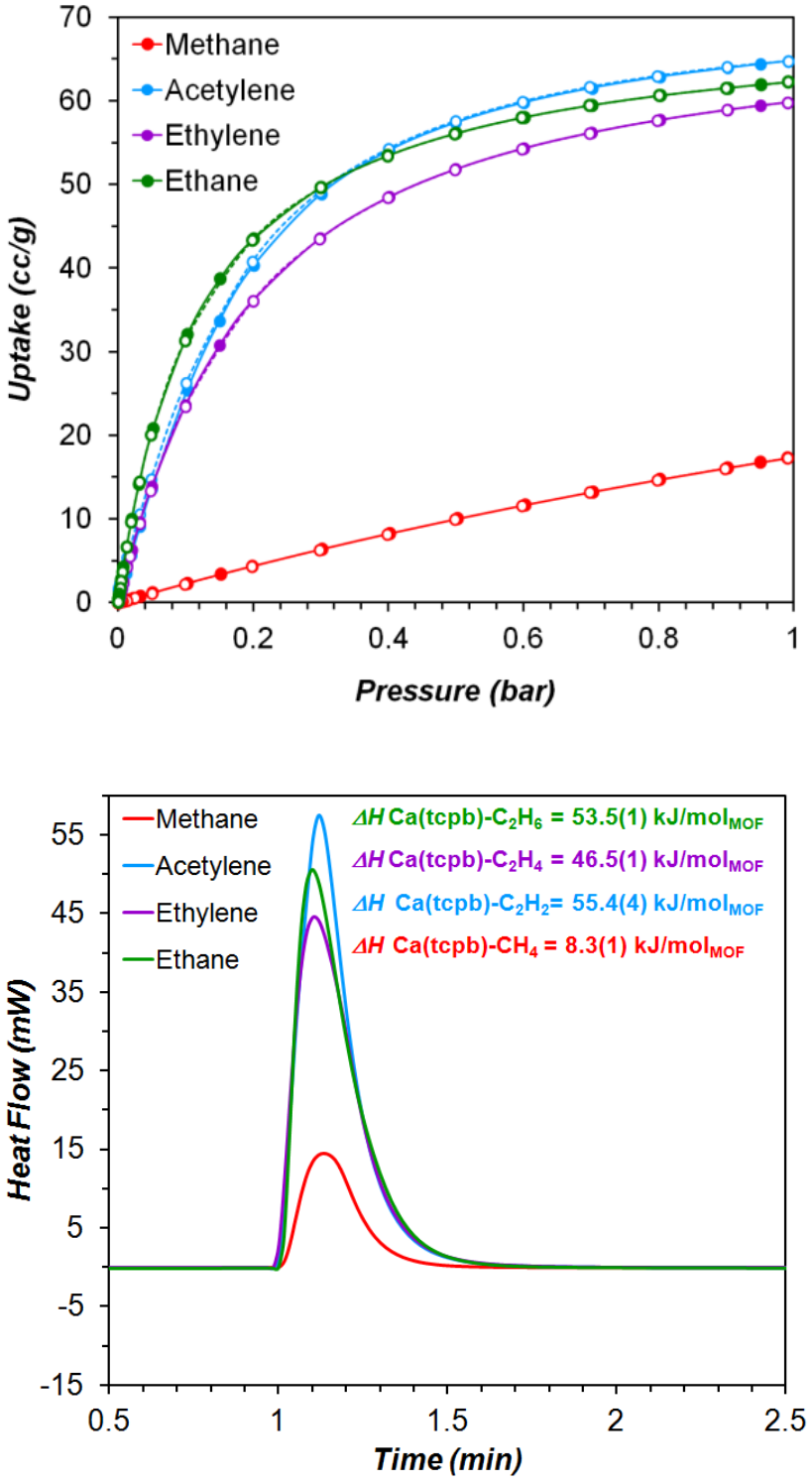

Figure 5.3 Top: C_1-C_2 hydrocarbon isotherms at 298 K for **Ca(tcpb)**; bottom: DSC signals measured upon loading activated **Ca(tcpb)** with C_1-C_2 gases.

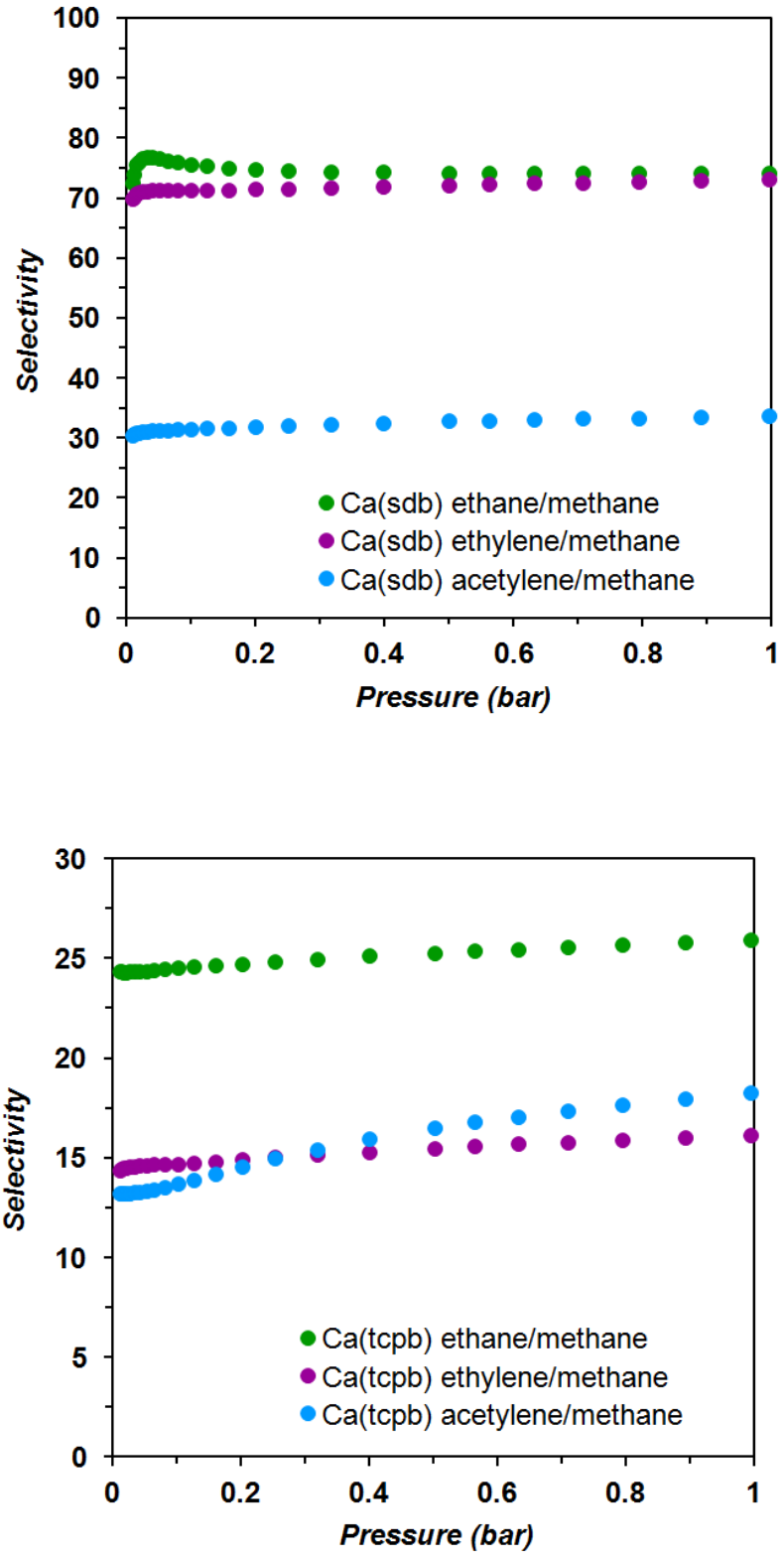

Figure 5.4 C_2H_n/CH_4 selectivity at 298 for (top) **Ca(sdb)** and (bottom) **Ca(tcpb)**.

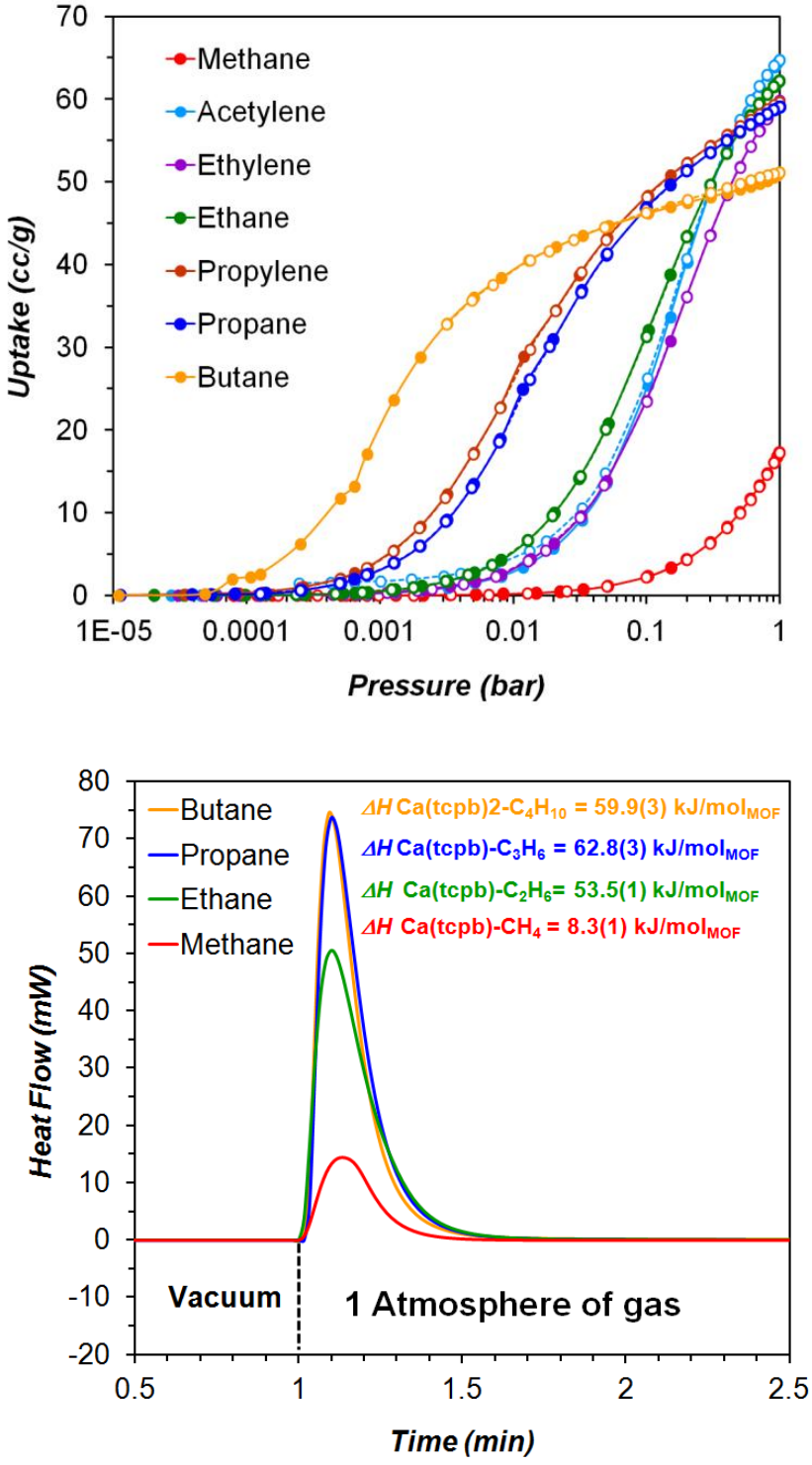

Figure 5.5 Top**:** C_1-nC_4 hydrocarbons isotherms at 298 K for **Ca(tcpb)**; bottom: DSC signals measured upon loading activated **Ca(tcpb)** with C_1-nC_4 alkanes.

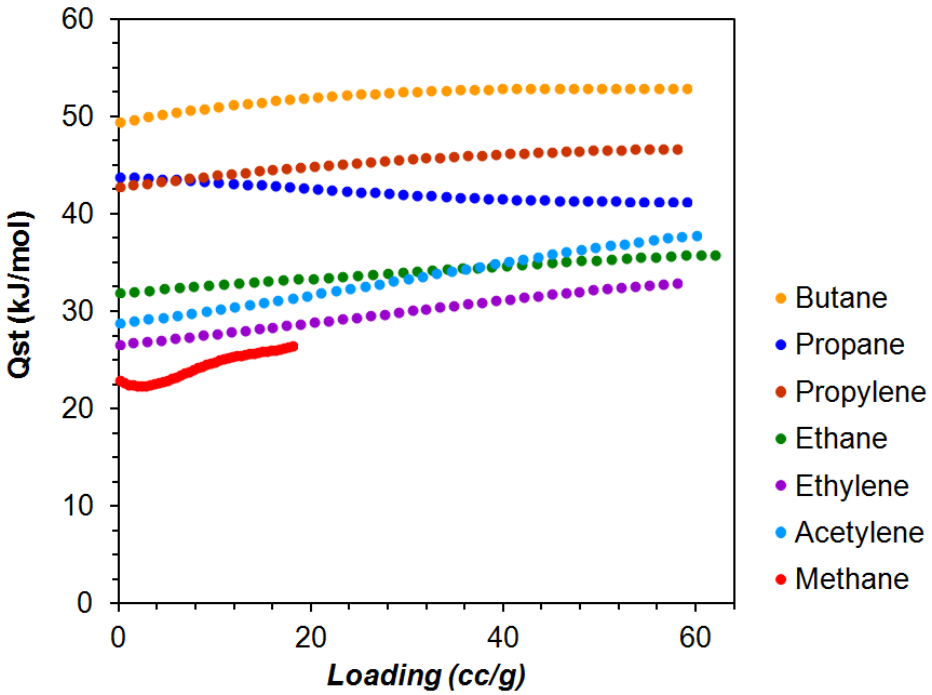

Figure 5.6 Isosteric heat of adsorption of C_1-nC_4 gases on **Ca(tcpb)** calculated with Virial method.

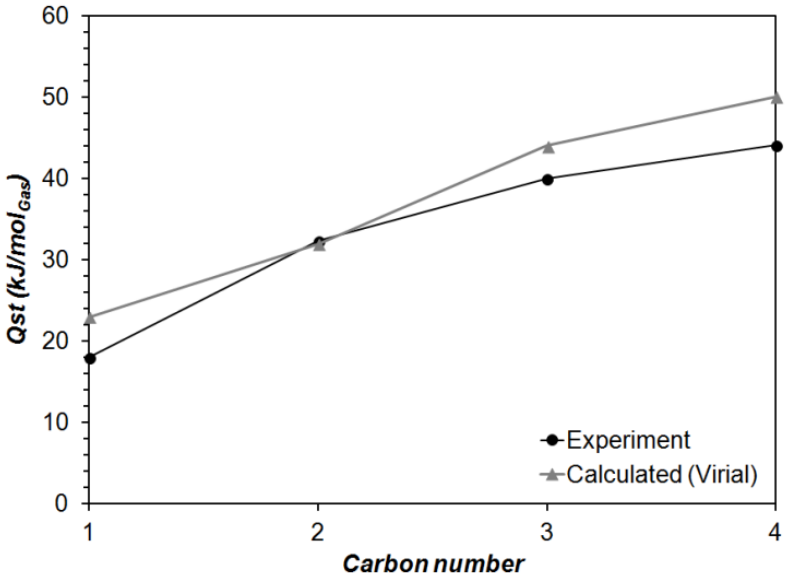

Figure 5.7 Trends in experimental and calculated Q_{st} of C_1-nC_4 alkanes adsorbed on **Ca(tcpb)** as a function of carbon number.

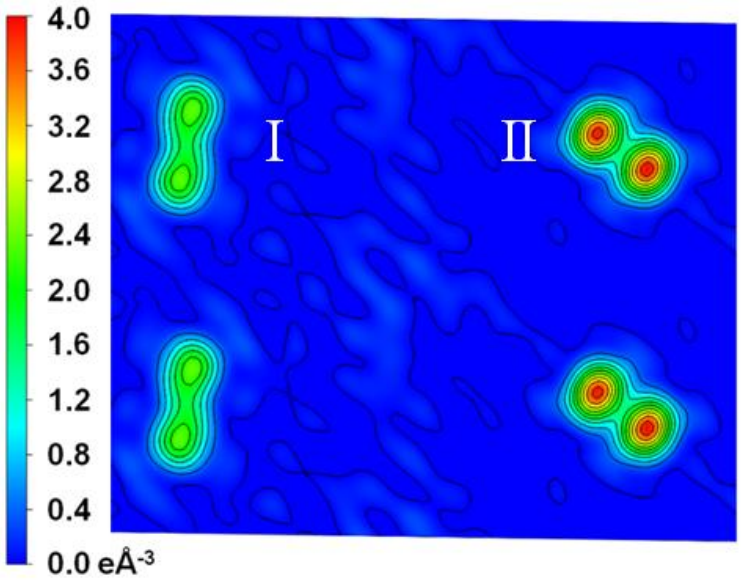

Figure 5.8 Differential Fourier electron density map of **Ca(tcpb):C_2H_4** before assigning ethylene atoms, localized electron density on the left side indicate ethylene molecules in the channel of the type I, on the right side – the channel of the type II.

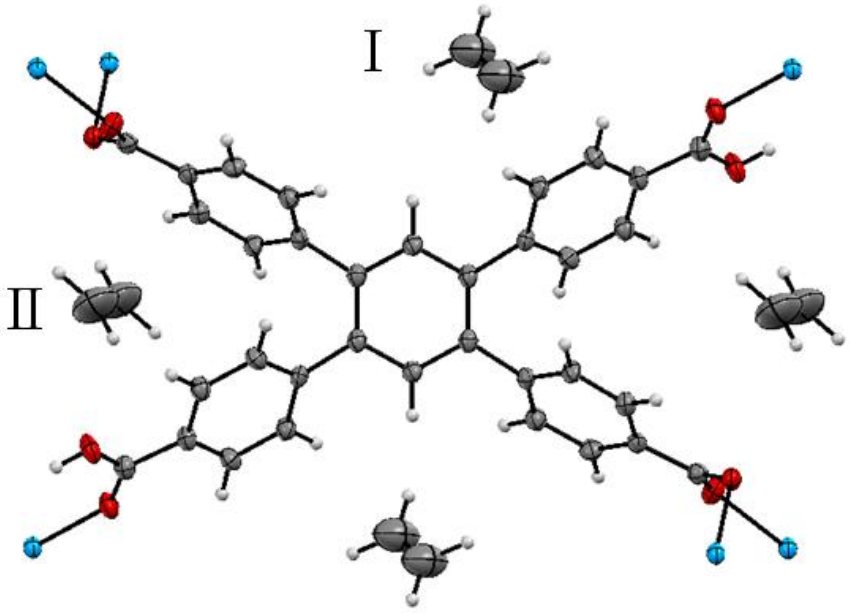

Figure 5.9 Refined **Ca(tcpb):C_2H_4** structure, atoms drawn at a 50% probability level.

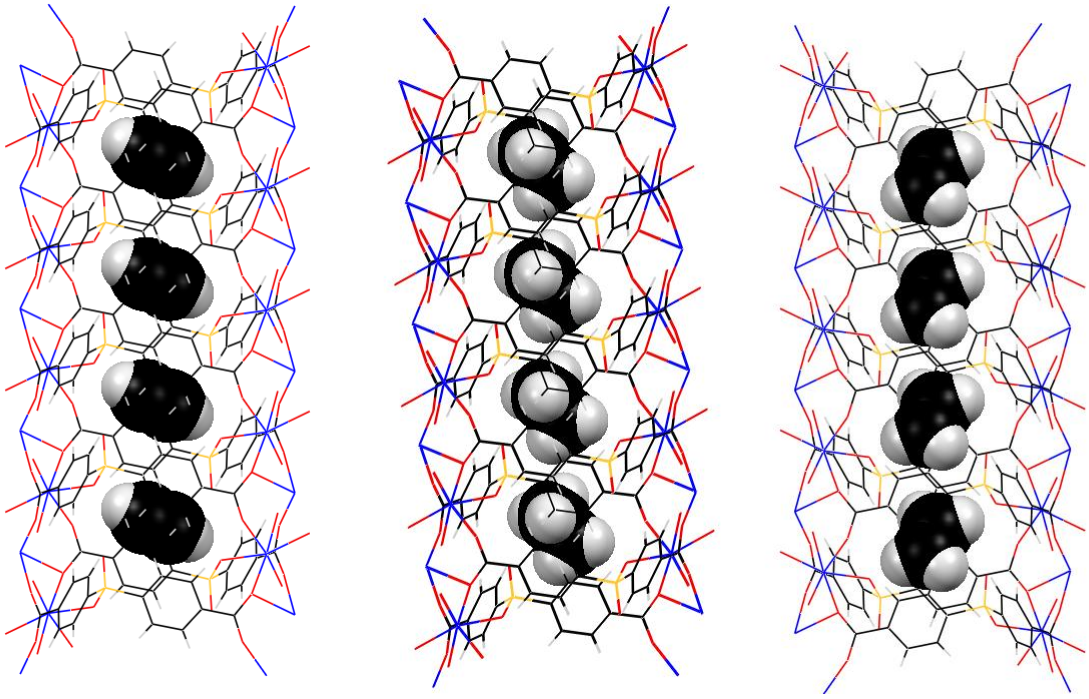

Figure 5.10 Packing of the C_2H_n gases along the channels of **Ca(sdb)**

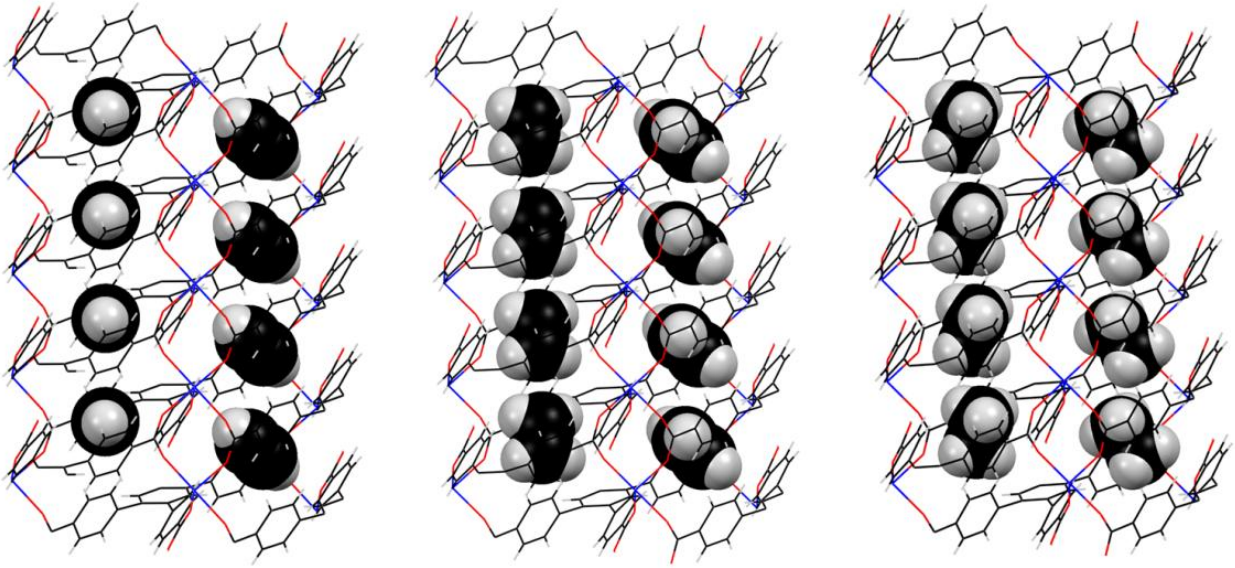

Figure 5.11 Packing of the C_2H_n gases along the channels of **Ca(tcpb).**

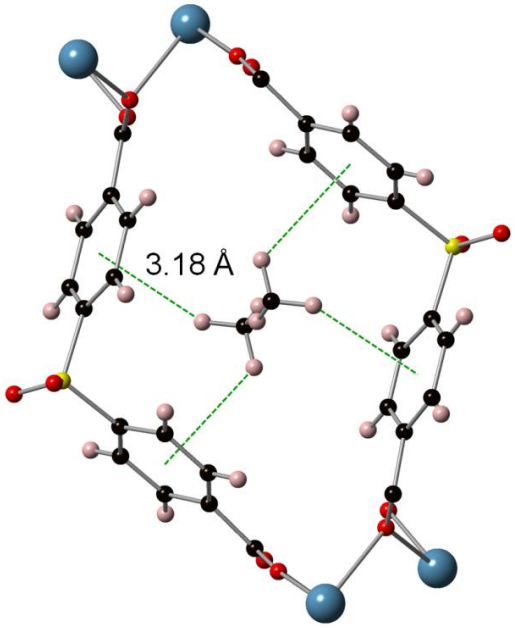

Figure 5.12 Ethane adsorption site in **Ca(sdb)**, the shortest gas-sorption site distances are shown, the gas molecule shows no spatial disorder.

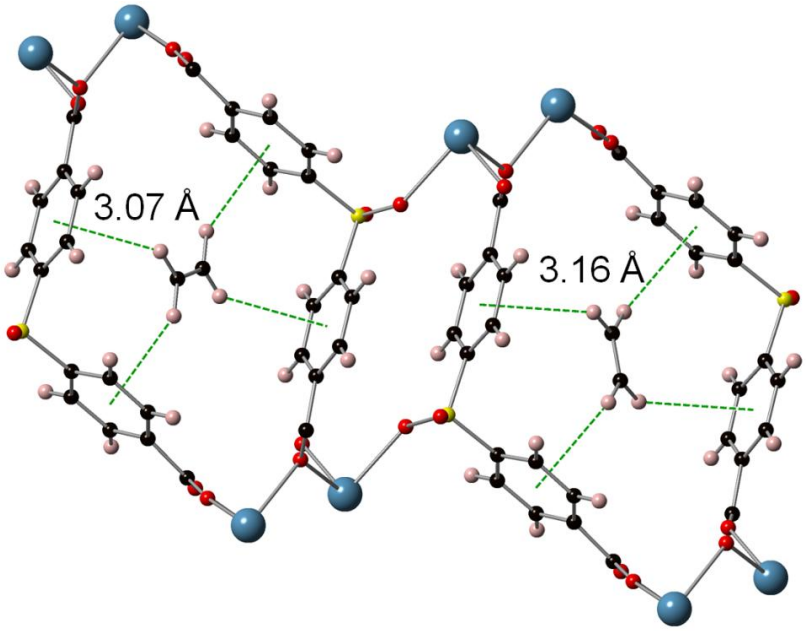

Figure 5.13 Ethylene adsorption sites in **Ca(sdb)**, the shortest gas-sorption site distances are shown, gas displays two-fold disorder, second orientation shown in a consecutive pore.

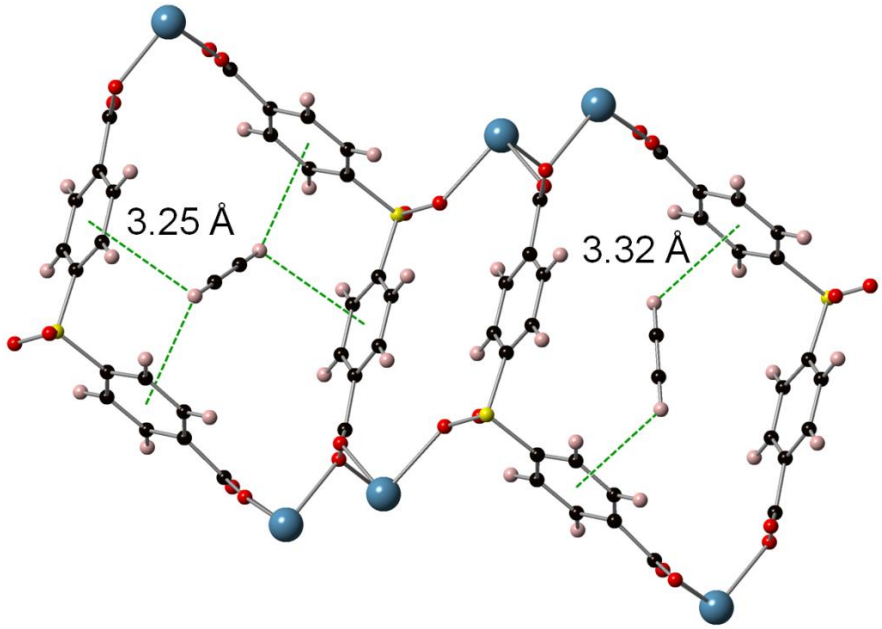

Figure 5.14 Acetylene adsorption sites in **Ca(sdb)**, the shortest gas-sorption site distances are shown, gas displays two-fold disorder, second orientation shown in a consecutive pore.

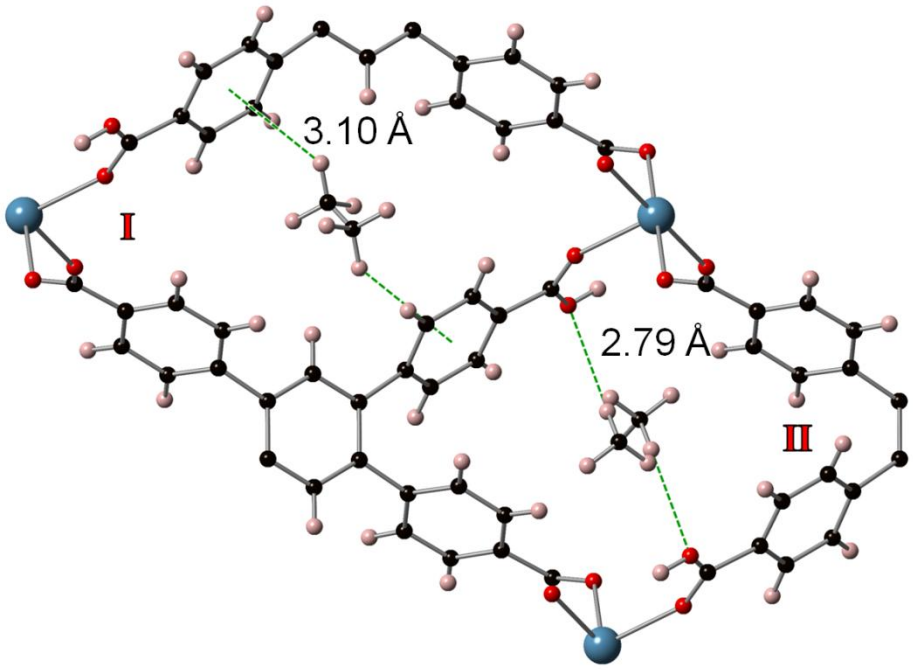

Figure 5.15 Ethane adsorption sites in **Ca(tcpb)**, the shortest gas-sorption site distances are shown, gas molecules show no spatial disorder, channels type I and II are marked red.

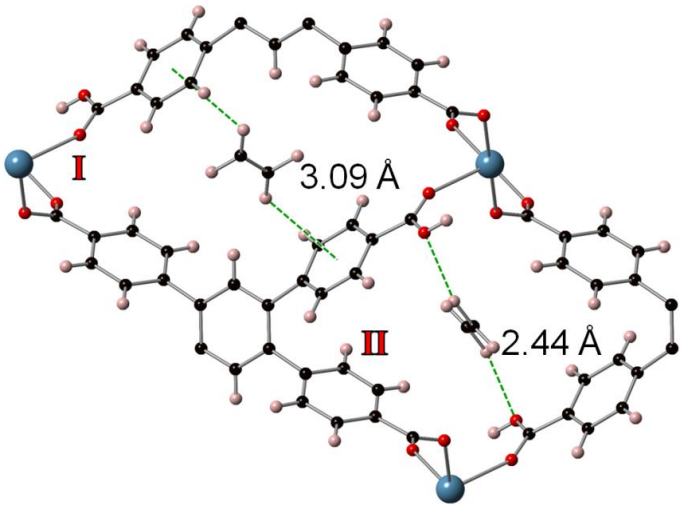

Figure 5.16 Ethylene adsorption sites in **Ca(tcpb)**, the shortest gas-sorption site distances are shown, gas molecules show no spatial disorder, channels type I and II are marked red.

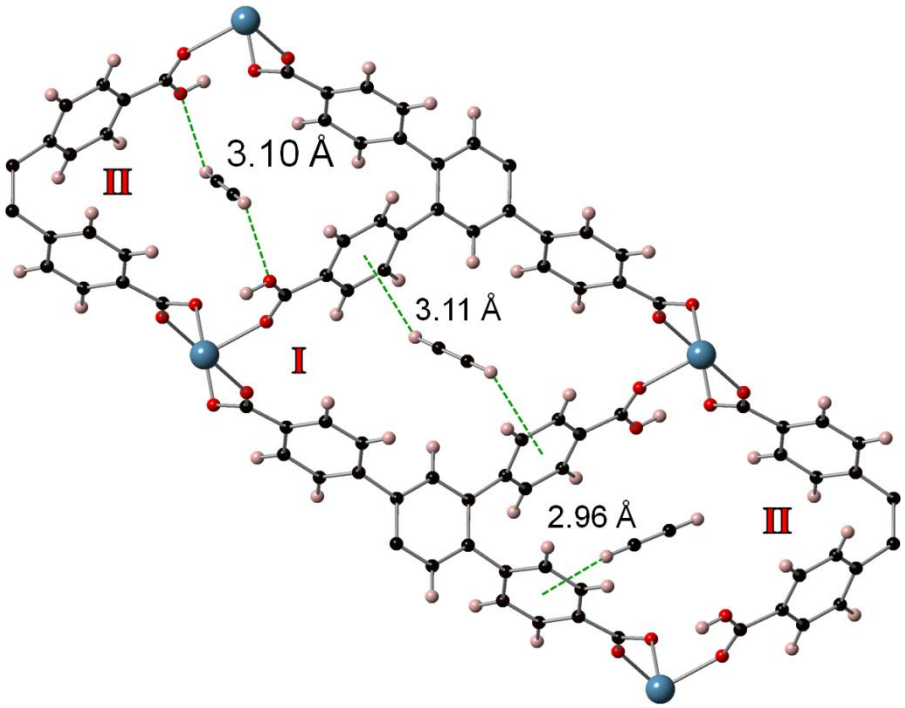

Figure 5.17 Acetylene adsorption sites in **Ca(tcpb)**, the shortest gas-sorption site distances are shown, in the pore of the type I gas molecules show no spatial disorder, in the pore of the type II gas is disordered over two positions, channels type I and II are marked red.

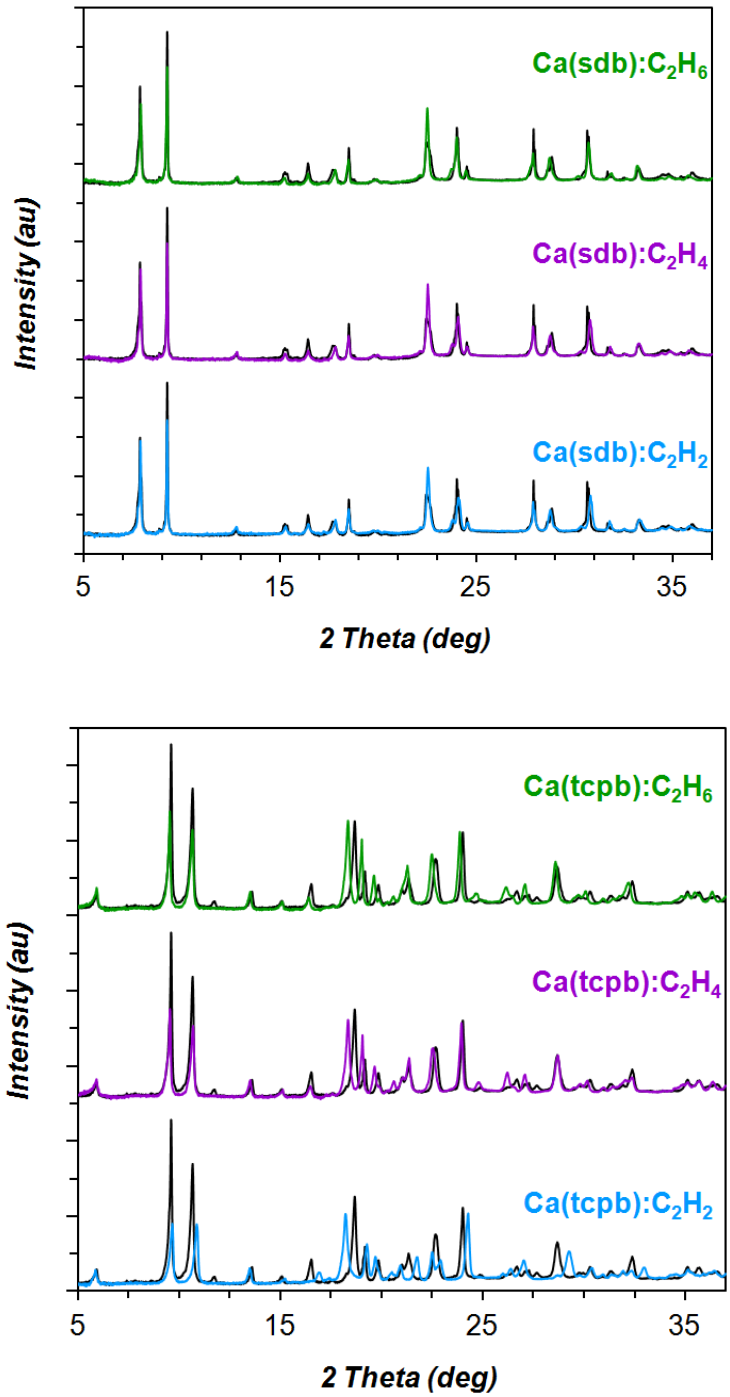

Figure 5.18 *In situ* PXRD patterns of (top) **Ca(sdb):C_2H_n** and (bottom) **Ca(tcpb):C_2H_n** collected at 1 atm pressure of C_2 hydrocarbons. Black patterns represent activated samples.

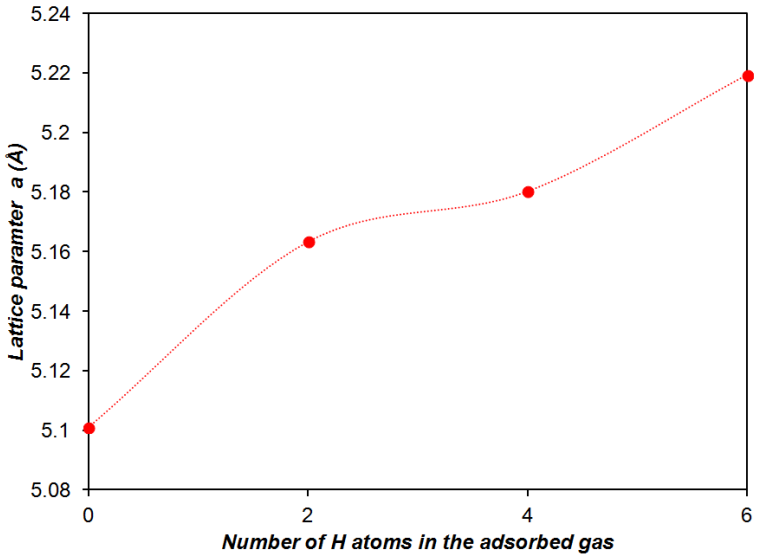

Figure 5.19 The development of the **Ca(tcpb)** lattice parameter *a* with the number of H atoms of the adsorbed hydrocarbon gas from single crystal diffraction data. Line added to guide the eye. Value for the activated sample (0 on the x axis) after Chen et al.[66]

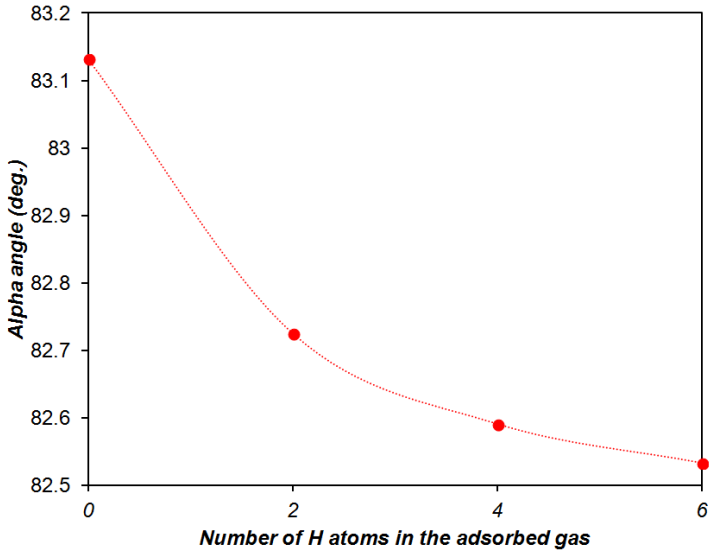

Figure 5.20 The development of the **Ca(tcpb)** lattice angle α with the size and number of H atoms of the adsorbed hydrocarbon gas. Line added to guide the eye. Value for the activated sample (0 on x axis) after Chen et al.[66]

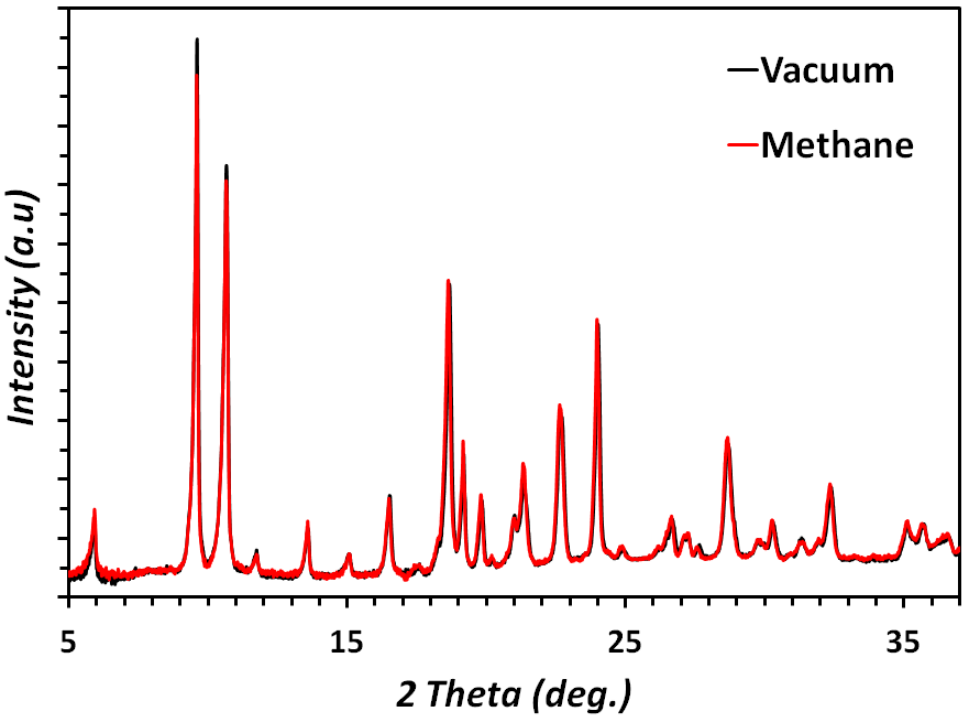

Figure 5.21 *In situ* PXRD patterns of activated and methane-loaded **Ca(tcpb)**.

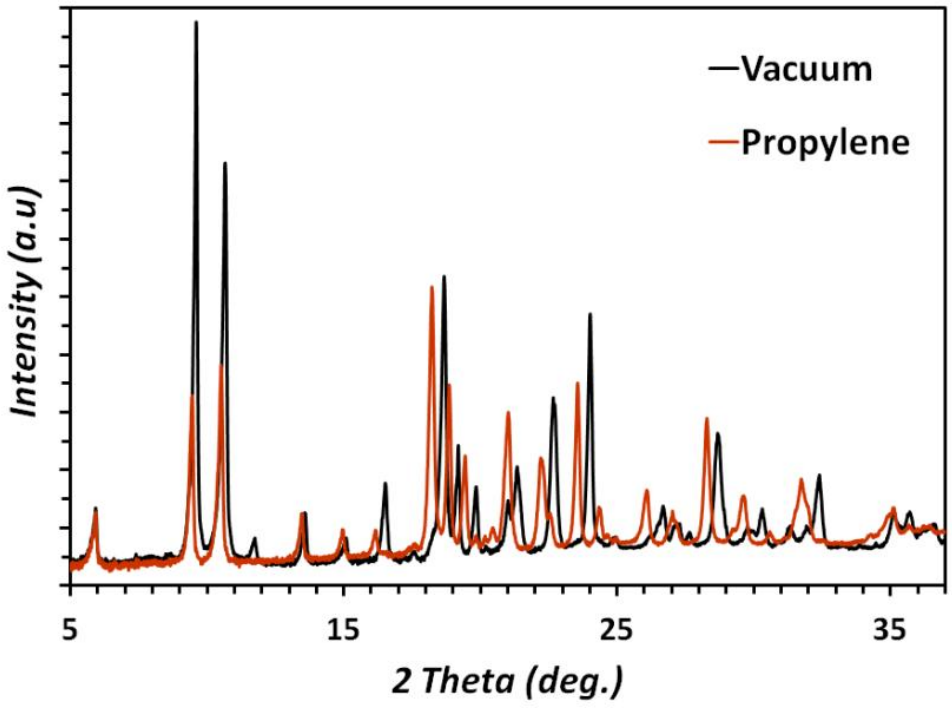

Figure 5.22 *In situ* PXRD patterns of activated and propylene-loaded **Ca(tcpb)**.

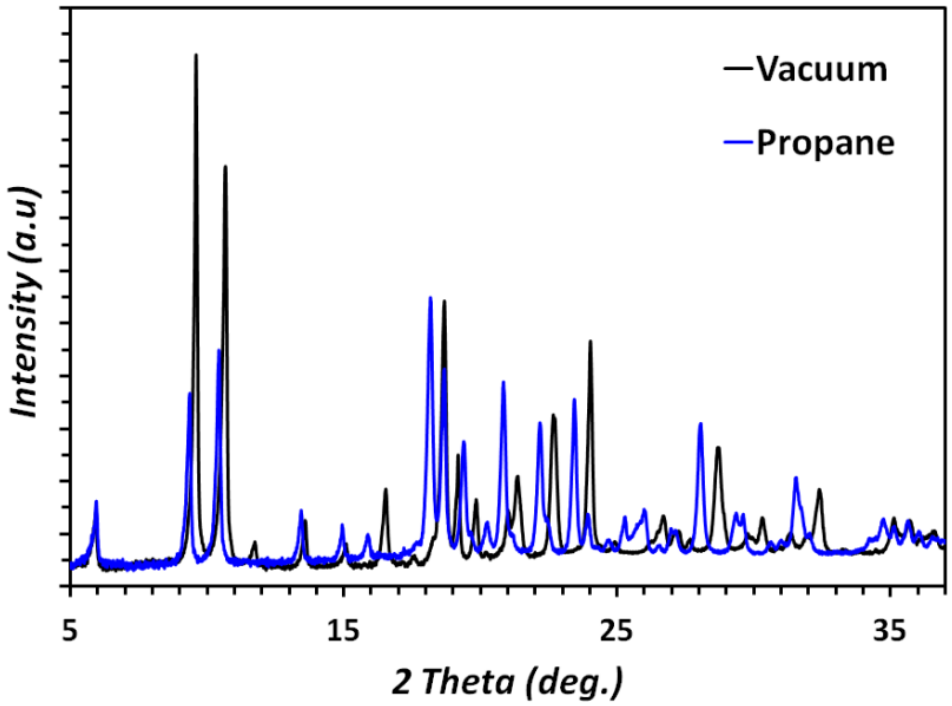

Figure 5.23 *In situ* PXRD patterns of activated and propane-loaded **Ca(tcpb)**.

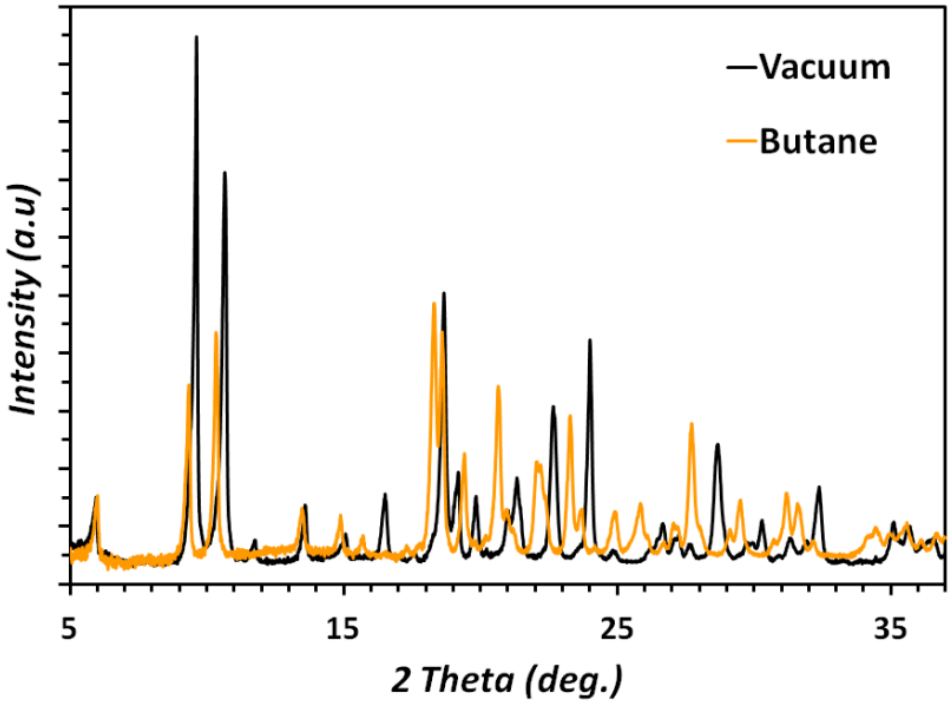

Figure 5.24 *In situ* PXRD patterns of activated and butane-loaded **Ca(tcpb)**.

Table 5.1: Crystal data and structure refinement parameters for **Ca(sdb):C_2H_n**

Sample	**Ca(sdb):C_2H_2**	**Ca(sdb):C_2H_4**	**Ca(sdb):C_2H_6**
Empirical formula	$Ca(C_{14}H_8SO_6)\cdot(C_2H_2)_{0.35}$	$Ca(C_{14}H_8SO_6)\cdot(C_2H_4)_{0.34}$	$Ca(C_{14}H_8SO_6)\cdot(C_2H_6)_{0.43}$
Formula weight	353.33	353.88	357.27
T (K)	100(2)	100(2)	100(2)
Wavelength (Å)	1.54184	0.71073	0.41328
Space Group	$P2_1/n$	$P2_1/n$	$P2_1/n$
a (Å)	11.6583(3)	11.5955(3)	11.6667(11)
b (Å)	5.5671(1)	5.5581(1)	5.5586(5)
c (Å)	22.9110(6)	22.9548(5)	22.935(2)
α (°)	90	90	90
β (°)	100.901(2)	101.062(3)	101.011(3)
γ (°)	90	90	90
Volume ($Å^3$)	1460.16(6)	1451.93(6)	1460.0(2)
$Density_{calc}$ (g/cm^3)	1.607	1.619	1.625
Mu (mm^{-1})	5.320	0.604	0.144
Reflections, unique	9878	23013	9452
Reflections [$I>2\sigma(I)$]	3081	4416	2212
R_{int}	0.0341	0.0374	0.0639
Completeness to θ_{max}	0.992	0.998	0.888
F(000)	723.3	725.8	735.0
Goodness of fit	1.106	1.053	1.082
Data/restraints/parameter	3081/20/219	4416/18/213	2212/31/210
R_1[$I>2\sigma(I)$]	0.0446	0.0346	0.0998
wR_2 [all data]	0.1221	0.0905	0.2532

Table 5.2: Crystal data and structure refinement parameters for **Ca(tcpb):C_2H_n**

Sample	**Ca(tcpb):C_2H_2**	**Ca(tcpb):C_2H_4**	**Ca(tcpb):C_2H_6**
Empirical formula	$Ca(C_{34}H_{20}O_8)\cdot(C_2H_2)_{1.76}$	$Ca(C_{34}H_{20}O_8)\cdot(C_2H_4)_{1.47}$	$Ca(C_{34}H_{20}O_8)\cdot(C_2H_6)_{1.58}$
Formula weight	642.17	637.68	644.08
T (K)	100(2)	100(2)	100(2)
Wavelength (Å)	0.71073	1.54184	0.41328
Space Group	*P* -1	*P* -1	*P* -1
a (Å)	5.1634(2)	5.1803(3)	5.2195(2)
b (Å)	10.5518(5)	10.6508(5)	10.5691(5)
c (Å)	15.4849(7)	15.2914(6)	15.3604(7)
α (°)	82.725(4)	82.591(4)	82.533(1)
β (°)	87.233(4)	85.945(4)	86.657(1)
γ (°)	83.782(4)	82.739(4)	83.000(1)
Volume ($Å^3$)	831.44(6)	828.67(7)	833.14(6)
$Density_{calc}$ (g/cm^3)	1.283	1.278	1.284
Mu (mm^{-1})	0.240	2.060	0.067
Reflections, unique	24429	10168	4214
Reflections [$I>2\sigma(I)$]	4128	2888	2019
R_{int}	0.0643	0.0560	0.0213
Completeness to θ_{max}	0.993	0.953	0.710
F(000)	332.5	331.4	336.4
Goodness of fit	1.037	1.070	1.208
Data/restraints/parameter	4128/1/235	2888/ 11/ 221	2019/ 2/ 218
R_1[$I>2\sigma(I)$]	0.0464	0.0530	0.0384
wR_2 [all data]	0.1244	0.1260	0.1298

Table 5.3: Atomic coordinates ($\times 10^4$) and equivalent isotropic displacement parameters (U_{eq}; $Å^2 \times 10^3$) for **Ca(sdb):C_2H_2**.

	x	y	z	U_{eq}
O(6)	4942(2)	1920(4)	1291(1)	16(1)
O(5)	4136(2)	-2220(4)	1097(1)	17(1)
C(8)	3514(3)	1087(6)	299(1)	14(1)
C(5)	2789(3)	1082(6)	1414(1)	14(1)
C(1A)	-30(140)	4600(300)	240(30)	210(20)
C(2A)	290(80)	4200(130)	130(50)	190(20)
Ca(1)	6370(1)	2432(1)	2214(1)	12(1)
S(1)	3969(1)	342(1)	1060(1)	13(1)
O(2)	2597(2)	857(4)	-1911(1)	15(1)
O(1)	2635(2)	4770(4)	-1723(1)	16(1)
O(4)	-123(2)	4760(4)	2470(1)	17(1)
O(3)	-413(2)	808(4)	2560(1)	19(1)
C(7)	1879(3)	3764(5)	2001(1)	14(1)
C(4)	1898(3)	-587(6)	1397(1)	17(1)
C(13)	3806(3)	3322(6)	100(1)	16(1)
C(2)	997(3)	2082(6)	2007(1)	14(1)
C(11)	2967(3)	2087(6)	-900(1)	13(1)
C(10)	2648(3)	-115(6)	-692(1)	18(1)
C(6)	2799(3)	3266(6)	1706(1)	15(1)
C(12)	3524(3)	3808(6)	-506(1)	17(1)
C(9)	2913(3)	-611(6)	-82(1)	17(1)
C(14)	2734(2)	2621(5)	-1555(1)	13(1)
C(3)	1007(3)	-95(6)	1706(1)	17(1)
C(1)	70(3)	2589(5)	2377(1)	14(1)

Table 5.4: Anisotropic displacement parameters ($Å^2 \times 10^3$) for **Ca(sdb):C_2H_2**

	U^{11}	U^{22}	U^{33}	U^{23}	U^{13}	U^{12}
O(6)	18(1)	15(1)	14(1)	-1(1)	4(1)	-1(1)
O(5)	24(1)	16(1)	12(1)	1(1)	5(1)	1(1)
C(8)	19(1)	16(2)	7(1)	-1(1)	5(1)	1(1)
C(5)	19(1)	15(1)	9(1)	3(1)	3(1)	2(1)
C(1A)	150(50)	140(40)	310(50)	60(30)	-50(40)	-20(30)
C(2A)	120(40)	130(30)	300(50)	60(30)	-30(30)	20(20)
Ca(1)	16(1)	10(1)	10(1)	0(1)	4(1)	-1(1)
S(1)	17(1)	12(1)	10(1)	0(1)	4(1)	1(1)
O(2)	19(1)	16(1)	10(1)	-2(1)	3(1)	0(1)
O(1)	20(1)	14(1)	14(1)	3(1)	5(1)	1(1)
O(4)	19(1)	15(1)	18(1)	-2(1)	6(1)	2(1)
O(3)	22(1)	15(1)	21(1)	-1(1)	9(1)	-3(1)
C(7)	22(2)	12(1)	7(1)	1(1)	2(1)	1(1)
C(4)	23(2)	12(1)	16(2)	-2(1)	5(1)	1(1)
C(13)	22(1)	13(1)	14(2)	-3(1)	3(1)	-2(1)
C(2)	17(1)	14(2)	10(1)	1(1)	3(1)	2(1)
C(11)	16(1)	13(1)	11(1)	-1(1)	4(1)	1(1)
C(10)	25(2)	14(2)	14(2)	-2(1)	3(1)	-3(1)
C(6)	19(1)	13(1)	12(1)	-1(1)	2(1)	-2(1)
C(12)	23(2)	14(2)	15(2)	1(1)	5(1)	-1(1)
C(9)	26(2)	13(1)	13(2)	2(1)	4(1)	-3(1)
C(14)	14(1)	13(1)	12(2)	1(1)	5(1)	0(1)
C(3)	19(1)	15(2)	16(2)	-1(1)	3(1)	-3(1)
C(1)	17(1)	14(1)	10(1)	-1(1)	2(1)	0(1)

Table 5.5: Atomic coordinates ($\times 10^4$) and equivalent isotropic displacement parameters (U_{eq}; $Å^2 \times 10^3$) for **Ca(sdb):C_2H_4**.

	x	y	z	U_{eq}
O(2)	7373(1)	4786(2)	6723(1)	14(1)
C(14)	7278(1)	2633(3)	6556(1)	11(1)
Ca(1)	3632(1)	2422(1)	2792(1)	9(1)
S(1)	6043(1)	334(1)	3947(1)	10(1)
O(3)	10116(1)	4744(2)	2521(1)	15(1)
O(1)	7410(1)	866(2)	6911(1)	13(1)
O(6)	5060(1)	1911(2)	3716(1)	13(1)
O(4)	10405(1)	793(2)	2432(1)	16(1)
O(5)	5875(1)	-2233(2)	3911(1)	13(1)
C(11)	7047(1)	2102(3)	5902(1)	11(1)
C(12)	7374(1)	-105(3)	5694(1)	14(1)
C(5)	7216(1)	1073(3)	3595(1)	11(1)
C(8)	6503(1)	1088(3)	4704(1)	11(1)
C(2)	9007(1)	2069(3)	2990(1)	11(1)
C(3)	9006(1)	-104(3)	3295(1)	14(1)
C(4)	8117(1)	-599(3)	3606(1)	14(1)
C(9)	6203(1)	3323(3)	4903(1)	14(1)
C(7)	8122(1)	3750(3)	3004(1)	12(1)
C(13)	7109(1)	-612(3)	5090(1)	14(1)
C(1)	9929(1)	2577(3)	2620(1)	11(1)
C(6)	7210(1)	3264(3)	3299(1)	13(1)
C(10)	6485(1)	3821(3)	5506(1)	14(1)
C(1E)	9702(1)	4053(3)	4911(1)	90(9)
C(2E)	9903(1)	5082(3)	5264(1)	113(11)

Table 5.6: Anisotropic displacement parameters ($Å^2 \times 10^3$) for **Ca(sdb):C_2H_4**

	U^{11}	U^{22}	U^{33}	U^{23}	U^{13}	U^{12}
O(2)	17(1)	12(1)	13(1)	-5(1)	5(1)	-2(1)
C(14)	11(1)	13(1)	9(1)	0(1)	2(1)	0(1)
Ca(1)	13(1)	8(1)	8(1)	0(1)	2(1)	1(1)
S(1)	14(1)	10(1)	7(1)	0(1)	3(1)	-1(1)
O(3)	18(1)	11(1)	17(1)	2(1)	6(1)	-2(1)
O(1)	16(1)	14(1)	9(1)	2(1)	2(1)	0(1)
O(6)	13(1)	16(1)	9(1)	1(1)	2(1)	2(1)
O(4)	19(1)	13(1)	17(1)	0(1)	6(1)	3(1)
O(5)	20(1)	11(1)	10(1)	0(1)	4(1)	-2(1)
C(11)	14(1)	12(1)	8(1)	0(1)	2(1)	-1(1)
C(12)	20(1)	12(1)	10(1)	1(1)	2(1)	4(1)
C(5)	14(1)	11(1)	8(1)	-1(1)	3(1)	0(1)
C(8)	14(1)	12(1)	8(1)	1(1)	2(1)	0(1)
C(2)	13(1)	11(1)	10(1)	-1(1)	2(1)	-1(1)
C(3)	15(1)	12(1)	14(1)	1(1)	4(1)	2(1)
C(4)	18(1)	10(1)	13(1)	2(1)	4(1)	2(1)
C(9)	19(1)	11(1)	11(1)	1(1)	2(1)	2(1)
C(7)	16(1)	9(1)	12(1)	1(1)	3(1)	0(1)
C(13)	21(1)	11(1)	11(1)	-1(1)	3(1)	3(1)
C(1)	12(1)	12(1)	10(1)	1(1)	2(1)	0(1)
C(6)	15(1)	11(1)	13(1)	0(1)	3(1)	1(1)
C(10)	19(1)	10(1)	12(1)	-1(1)	4(1)	1(1)
C(1E)	90(11)	74(9)	110(20)	-6(8)	30(9)	-30(8)
C(2E)	98(13)	130(20)	111(13)	22(14)	22(12)	35(15)

Table 5.7: Atomic coordinates ($\times 10^4$) and equivalent isotropic displacement parameters (U_{eq}; $Å^2 \times 10^3$) for **Ca(sdb):C_2H_6**.

	x	y	z	U_{eq}
S(1)	3961(1)	346(3)	1060(1)	10(1)
O(3)	-131(4)	4756(8)	2471(2)	14(1)
O(1)	2595(4)	834(8)	-1903(2)	12(1)
O(4)	-412(4)	802(9)	2556(2)	16(1)
O(2)	2641(4)	4768(8)	-1727(2)	11(1)
O(5)	4127(4)	-2245(8)	1100(2)	11(1)
O(6)	4936(4)	1964(8)	1291(2)	12(1)
C(4)	1886(6)	-578(12)	1392(3)	11(1)
C(5)	2792(6)	1094(11)	1409(3)	11(2)
C(13)	2906(6)	-594(12)	-87(3)	12(1)
C(8)	3520(6)	1097(11)	290(3)	11(1)
C(6)	2781(6)	3294(12)	1705(3)	12(1)
C(9)	3806(6)	3352(12)	106(3)	14(2)
C(12)	2635(6)	-102(12)	-685(3)	12(1)
C(3)	1003(6)	-71(12)	1701(3)	12(2)
C(7)	1882(6)	3771(11)	1998(3)	11(2)
C(10)	3521(6)	3827(11)	-504(3)	11(1)
C(1E)	272(5)	3920(20)	153(10)	129(13)
C(14)	2738(5)	2606(9)	-1550(3)	3(1)
C(1)	61(5)	2562(9)	2372(3)	4(1)
C(2)	987(5)	2128(11)	2008(3)	7(1)
C(11)	2966(6)	2131(11)	-900(3)	7(1)
Ca(1)	6366(1)	2437(2)	2213(1)	3(1)

Table 5.8: Anisotropic displacement parameters ($Å^2 \times 10^3$) for **Ca(sdb):C_2H_6**

	U^{11}	U^{22}	U^{33}	U^{23}	U^{13}	U^{12}
S(1)	10(1)	13(1)	6(1)	0(1)	1(1)	0(1)
O(3)	16(2)	14(2)	13(2)	-5(2)	2(2)	7(2)
O(1)	8(2)	17(2)	12(2)	-7(2)	2(2)	-1(2)
O(4)	14(2)	20(2)	12(2)	2(2)	2(2)	-7(2)
O(2)	9(2)	13(2)	12(2)	7(2)	6(2)	3(2)
O(5)	10(2)	17(2)	7(2)	-2(2)	2(2)	2(2)
O(6)	11(1)	14(1)	10(1)	0(1)	2(1)	-1(1)
C(4)	10(3)	15(3)	9(3)	-1(2)	2(3)	-4(3)
C(5)	9(3)	13(3)	12(3)	3(2)	1(3)	4(2)
C(13)	9(3)	16(3)	14(3)	5(3)	5(3)	-2(3)
C(8)	9(3)	11(3)	12(3)	1(2)	-2(3)	6(2)
C(6)	7(3)	16(3)	14(3)	1(3)	5(3)	-2(3)
C(9)	12(3)	14(3)	12(3)	0(3)	-2(3)	-3(3)
C(12)	10(3)	15(3)	11(3)	-2(2)	3(3)	2(3)
C(3)	8(3)	12(3)	16(3)	1(2)	1(3)	-2(2)
C(7)	12(3)	13(3)	7(3)	-2(2)	-3(3)	-2(3)
C(10)	11(3)	13(3)	9(3)	1(2)	4(3)	1(3)
C(1E)	82(15)	76(14)	200(30)	30(15)	-60(16)	4(10)
C(14)	2(2)	3(2)	3(2)	0(1)	1(1)	0(1)
C(1)	4(2)	4(2)	3(2)	0(1)	0(1)	0(1)
C(2)	4(3)	12(3)	4(3)	3(2)	1(3)	3(2)
C(11)	6(2)	7(2)	6(2)	0(1)	1(1)	1(1)
Ca(1)	4(1)	3(1)	1(1)	-1(1)	1(1)	-1(1)

Table 5.9: Atomic coordinates ($\times 10^4$) and equivalent isotropic displacement parameters (U_{eq}; $Å^2 \times 10^3$) for **Ca(tcpb):C_2H_2**.

	x	y	z	U_{eq}
C(1A)	4415(14)	9802(6)	5303(5)	69(2)
C(1)	-184(3)	6320(2)	4896(1)	18(1)
C(2)	790(3)	5655(2)	5671(1)	17(1)
C(3)	964(3)	4299(2)	5776(1)	17(1)
C(11)	1632(3)	6386(2)	6356(1)	16(1)
C(12)	3936(4)	5991(2)	6791(1)	19(1)
C(13)	4577(4)	6600(2)	7481(1)	21(1)
C(14)	2931(4)	7627(2)	7744(1)	18(1)
C(16)	57(4)	7462(2)	6592(1)	20(1)
C(17)	3462(4)	8216(2)	8536(1)	19(1)
C(4)	1829(3)	3517(2)	6602(1)	17(1)
C(9)	4074(4)	2641(2)	6611(1)	21(1)
C(8)	4970(4)	1995(2)	7397(1)	21(1)
C(7)	3602(3)	2170(2)	8175(1)	16(1)
C(6)	1293(3)	2985(2)	8160(1)	19(1)
C(5)	442(3)	3662(2)	7382(1)	19(1)
C(10)	4648(3)	1545(2)	9030(1)	16(1)
O(2)	6989(2)	1128(1)	9057(1)	23(1)
O(1)	3052(2)	1502(1)	9694(1)	18(1)
O(3)	1872(3)	9006(1)	8837(1)	24(1)
O(4)	5719(3)	7805(1)	8868(1)	26(1)
Ca(1)	0	0	10000	15(1)
C(15)	691(4)	8075(2)	7285(1)	21(1)
C(2A)	6179(16)	4744(6)	9789(4)	49(2)
C(3A)	5987(15)	4312(8)	9118(5)	55(2)
C(4A)	8820(30)	4805(18)	10180(11)	162(9)

Table 5.10: Anisotropic displacement parameters ($Å^2 \times 10^3$) for **Ca(tcpb):C_2H_2**

	U^{11}	U^{22}	U^{33}	U^{23}	U^{13}	U^{12}
C(1A)	80(5)	52(4)	74(5)	-7(3)	10(4)	-5(3)
C(1)	19(1)	19(1)	15(1)	-3(1)	-4(1)	1(1)
C(2)	16(1)	21(1)	14(1)	-4(1)	-4(1)	0(1)
C(3)	17(1)	22(1)	13(1)	-3(1)	-4(1)	3(1)
C(11)	20(1)	20(1)	10(1)	-2(1)	-2(1)	-1(1)
C(12)	19(1)	23(1)	16(1)	-7(1)	-3(1)	1(1)
C(13)	19(1)	28(1)	17(1)	-6(1)	-6(1)	-1(1)
C(14)	19(1)	23(1)	13(1)	-5(1)	-3(1)	-2(1)
C(16)	20(1)	23(1)	16(1)	-3(1)	-7(1)	2(1)
C(17)	21(1)	23(1)	14(1)	-5(1)	-2(1)	-5(1)
C(4)	20(1)	19(1)	13(1)	-2(1)	-7(1)	-1(1)
C(9)	24(1)	25(1)	13(1)	-4(1)	-2(1)	3(1)
C(8)	20(1)	23(1)	18(1)	-2(1)	-3(1)	6(1)
C(7)	17(1)	18(1)	14(1)	-1(1)	-7(1)	-3(1)
C(6)	19(1)	23(1)	14(1)	-2(1)	-2(1)	0(1)
C(5)	16(1)	23(1)	17(1)	-1(1)	-5(1)	3(1)
C(10)	19(1)	16(1)	14(1)	-1(1)	-6(1)	-4(1)
O(2)	19(1)	29(1)	19(1)	6(1)	-6(1)	-1(1)
O(1)	20(1)	20(1)	13(1)	-2(1)	-5(1)	-3(1)
O(3)	26(1)	28(1)	18(1)	-11(1)	-3(1)	1(1)
O(4)	24(1)	37(1)	21(1)	-16(1)	-9(1)	1(1)
Ca(1)	15(1)	17(1)	12(1)	-2(1)	-4(1)	0(1)
C(15)	22(1)	23(1)	18(1)	-6(1)	-3(1)	4(1)
C(2A)	83(6)	29(3)	35(4)	-6(3)	21(4)	-11(3)
C(3A)	51(5)	58(5)	60(5)	-30(4)	-3(4)	-1(3)
C(4A)	190(20)	186(17)	132(15)	-93(13)	25(12)	-61(14)

Table 5.11: Atomic coordinates ($\times 10^4$) and equivalent isotropic displacement parameters (U_{eq}; $Å^2 \times 10^3$) for **Ca(tcpb):C_2H_4**.

	x	y	z	U_{eq}
C(1)	-182(5)	6306(3)	4876(2)	22(1)
C(2)	804(5)	5666(3)	5656(2)	22(1)
C(3)	973(6)	4323(3)	5788(2)	23(1)
C(4)	1855(6)	3558(3)	6626(2)	22(1)
C(5)	4111(6)	2694(3)	6631(2)	26(1)
C(6)	5001(6)	2054(3)	7419(2)	26(1)
C(7)	3600(6)	2232(3)	8214(2)	22(1)
C(8)	1280(6)	3052(3)	8207(2)	24(1)
C(9)	451(6)	3719(3)	7424(2)	23(1)
C(10)	4623(6)	1593(3)	9070(2)	24(1)
C(11)	1654(6)	6409(3)	6332(2)	21(1)
C(12)	3950(6)	6015(3)	6756(2)	26(1)
C(13)	4602(6)	6636(3)	7433(2)	26(1)
C(14)	2974(6)	7690(3)	7691(2)	24(1)
C(15)	745(6)	8131(3)	7236(2)	27(1)
C(16)	98(6)	7501(3)	6561(2)	25(1)
C(17)	3529(6)	8298(3)	8469(2)	26(1)
O(1)	2998(4)	1499(2)	9746(1)	24(1)
O(2)	6990(4)	1205(2)	9097(1)	30(1)
O(3)	1938(4)	9101(2)	8780(1)	29(1)
O(4)	5793(4)	7888(2)	8785(1)	32(1)
Ca(1)	0	0	10000	21(1)
C(1E)	4280(11)	9745(5)	5311(4)	84(3)
C(2E)	6249(10)	5000(8)	10065(6)	110(5)

Table 5.12: Anisotropic displacement parameters ($Å^2 \times 10^3$) for **Ca(tcpb):C_2H_4**

	U^{11}	U^{22}	U^{33}	U^{23}	U^{13}	U^{12}
C(1)	21(2)	23(1)	23(2)	-4(1)	-3(1)	1(1)
C(2)	18(2)	27(1)	21(1)	-5(1)	-3(1)	0(1)
C(3)	21(2)	27(1)	20(1)	-4(1)	-1(1)	-1(1)
C(4)	24(2)	24(1)	21(1)	-5(1)	-7(1)	-4(1)
C(5)	29(2)	29(2)	22(2)	-7(1)	-2(1)	0(1)
C(6)	24(2)	24(1)	29(2)	-4(1)	-3(1)	2(1)
C(7)	26(2)	23(1)	20(1)	-2(1)	-4(1)	-5(1)
C(8)	24(2)	28(2)	21(1)	-4(1)	-1(1)	-4(1)
C(9)	21(2)	25(1)	23(2)	-4(1)	-7(1)	3(1)
C(10)	24(2)	22(1)	27(2)	-4(1)	-5(1)	-4(1)
C(11)	23(2)	25(1)	15(1)	-1(1)	-3(1)	-2(1)
C(12)	29(2)	25(1)	24(2)	-7(1)	0(1)	-2(1)
C(13)	23(2)	30(2)	24(2)	-6(1)	-4(1)	0(1)
C(14)	24(2)	29(2)	21(2)	-7(1)	-1(1)	-3(1)
C(15)	31(2)	27(2)	22(2)	-8(1)	0(1)	-1(1)
C(16)	24(2)	29(2)	22(2)	-2(1)	-6(1)	0(1)
C(17)	27(2)	30(2)	22(2)	-4(1)	-1(1)	-4(1)
O(1)	26(1)	27(1)	20(1)	-3(1)	-3(1)	-4(1)
O(2)	28(1)	36(1)	25(1)	4(1)	-4(1)	-3(1)
O(3)	32(1)	34(1)	23(1)	-13(1)	-2(1)	1(1)
O(4)	27(1)	44(1)	29(1)	-19(1)	-8(1)	0(1)
Ca(1)	22(1)	24(1)	18(1)	-4(1)	-3(1)	-1(1)
C(1E)	101(6)	56(4)	92(5)	-10(3)	24(4)	-12(3)
C(2E)	170(13)	69(6)	90(7)	26(5)	-22(8)	-33(8)

Table 5.13: Atomic coordinates ($\times 10^4$) and equivalent isotropic displacement parameters (U_{eq}; $Å^2 \times 10^3$) for **Ca(tcpb):C_2H_6**.

	x	y	z	U_{eq}
C(1)	-188(4)	6320(2)	4879(1)	13(1)
C(2)	784(4)	5660(2)	5665(1)	12(1)
C(3)	960(4)	4316(2)	5784(1)	13(1)
C(4)	1833(4)	3541(2)	6623(1)	12(1)
C(5)	4071(4)	2670(2)	6634(1)	15(1)
C(6)	4975(4)	2031(2)	7425(1)	15(1)
C(7)	3601(4)	2220(2)	8211(1)	12(1)
C(8)	1294(4)	3034(2)	8199(1)	13(1)
C(9)	442(4)	3704(2)	7413(1)	13(1)
C(10)	4633(4)	1579(2)	9073(1)	12(1)
C(11)	1617(4)	6409(2)	6340(1)	12(1)
C(12)	3923(4)	6015(2)	6767(1)	14(1)
C(13)	4564(4)	6642(2)	7444(1)	15(1)
C(14)	2927(4)	7679(2)	7704(1)	14(1)
C(15)	675(4)	8118(2)	7254(1)	15(1)
C(16)	44(4)	7489(2)	6575(1)	14(1)
C(17)	3478(4)	8298(2)	8480(1)	14(1)
O(1)	3032(3)	1492(2)	9734(1)	12(1)
O(2)	6985(3)	1201(2)	9101(1)	17(1)
O(3)	1879(3)	9074(2)	8798(1)	18(1)
O(4)	5764(3)	7917(2)	8788(1)	20(1)
Ca(1)	0	0	10000	10(1)
C(1E)	3847(6)	9684(4)	5221(3)	47(2)
C(2E)	6363(5)	4733(5)	9855(4)	70(2)

Table 5.14: Anisotropic displacement parameters ($Å^2 \times 10^3$) for **Ca(tcpb):C_2H_6**

	U^{11}	U^{22}	U^{33}	U^{23}	U^{13}	U^{12}
C(1)	14(1)	13(1)	11(1)	-1(1)	-3(1)	-1(1)
C(2)	12(1)	16(1)	9(1)	-2(1)	-1(1)	-2(1)
C(3)	11(1)	18(1)	9(1)	-1(1)	-2(1)	-1(1)
C(4)	15(1)	12(1)	9(1)	0(1)	-6(1)	-5(1)
C(5)	18(1)	18(1)	10(1)	-3(1)	-2(1)	-1(1)
C(6)	13(1)	16(1)	15(1)	-1(1)	-4(1)	0(1)
C(7)	14(1)	12(1)	11(1)	0(1)	-5(1)	-4(1)
C(8)	14(1)	18(1)	9(1)	-1(1)	-2(1)	-4(1)
C(9)	12(1)	15(1)	13(1)	-1(1)	-5(1)	0(1)
C(10)	15(1)	12(1)	11(1)	-1(1)	-5(1)	-4(1)
C(11)	15(1)	15(1)	6(1)	2(1)	-1(1)	-4(1)
C(12)	15(1)	16(1)	11(1)	-2(1)	-1(1)	-1(1)
C(13)	13(1)	20(1)	12(1)	-1(1)	-4(1)	-4(1)
C(14)	14(1)	18(1)	9(1)	-2(1)	0(1)	-6(1)
C(15)	16(1)	16(1)	12(1)	-2(1)	-1(1)	-1(1)
C(16)	14(1)	18(1)	11(1)	0(1)	-4(1)	-3(1)
C(17)	16(1)	16(1)	10(1)	0(1)	-1(1)	-6(1)
O(1)	15(1)	14(1)	8(1)	0(1)	-4(1)	-5(1)
O(2)	13(1)	22(1)	15(1)	5(1)	-5(1)	-1(1)
O(3)	20(1)	22(1)	13(1)	-7(1)	-2(1)	-2(1)
O(4)	18(1)	32(1)	14(1)	-12(1)	-6(1)	-1(1)
Ca(1)	10(1)	13(1)	7(1)	-1(1)	-4(1)	-2(1)
C(1E)	41(3)	38(3)	60(3)	4(2)	11(2)	-11(2)
C(2E)	55(3)	41(3)	104(4)	9(3)	27(2)	-2(2)

Table 5.15: Hydrocarbon adsorption on **Ca(sdb)** and **Ca(tcpb)**, gas uptake measured with the gas isotherms, $-\Delta H$ and Q_{st} obtained through DSC vacuum-swing experiments.

	Ca(sdb)			Ca(tcpb)		
	Uptake (wt%)	**$-\Delta H$ (kJ/mol$_{MOF}$)**	**Q_{st} (kJ/mol$_{GAS}$)**	**Uptake (wt%)**	**$-\Delta H$ (kJ/mol$_{MOF}$)**	**Q_{st} (kJ/mol$_{GAS}$)**
CH_4	1.66	10(1)	28(3)	1.99	8.3(1)	18.0(2)
C_2H_2	2.96	16.2(1)	41.5(4)	7.51	55.4(4)	30.3(2)
C_2H_4	3.75	16.5(3)	35.0(5)	7.47	46.5(1)	29.2(1)
C_2H_6	3.96	15.6(3)	36.3(7)	8.33	53.5(1)	32.3(1)

Table 5.16: Comparison of calculated and experimental enthalpies and the heat of adsorption of C_2H_n in **Ca(tcpb)**

HC Gas	**$-\Delta H$ (kJ/mol$_{MOF}$)**		**Q_{st} (kJ/mol$_{GAS}$)**	
	Calculated	**Experimental**	**Calculated**	**Experimental**
CH_4	10.61	8.3(1)	23	18.0(2)
C_2H_2	53.15	55.4(4)	29	30.3(2)
C_2H_4	42.95	46.5(1)	27	29.2(1)
C_2H_6	52.88	53.5(1)	32	32.3(1)
C_3H_6	68.16	62.6(5)	43	39.5(3)
C_3H_8	69.11	62.8(3)	44	40.0(2)
C_4H_{10}	67.9	59.9(3)	50	44.1(2)

Table 5.17: Comparison of C_2H_n uptake values in **Ca(sdb)** and **Ca(tcpb)** obtained trough isotherms measurments vs. crystal structure refinement results.

	Ca(sdb)		**Ca(tcpb)**	
	Gas occupancy (mol/mol)		Gas occupancy (mol/mol)	
	isotherms	refinement	isotherms	refinement
C_2H_2	0.39	0.3(1)	1.72	1.76(1)
C_2H_4	0.46	0.32(3)	1.59	1.47(1)
C_2H_6	0.45	0.43(5)	1.65	1.58(1)

Chapter 6

Effect of the Ligand Structural Isomerism in a Formation of Calcium Metal Organic Frameworks

The content of this chapter is published in

Plonka, A. M.; Banerjee, D.; Parise, J. B. *Cryst. Growth Des.* **2012**, *12* (5), 2460-2467.

6.1 Abstract

Using different structural isomers (2,5-; 2,4-; 2;6-; 3,4-; 3,5-) of pyridinedicarboxylic acid, nine calcium-based MOFs were synthesized under solvothermal conditions and/or were produced via a solvent-driven recrystallization of the previously synthesized compounds. The MOFs reported here were characterized using single crystal X-ray diffraction and thermal methods. They show diverse structural topologies, depending on the ligand geometry and coordinated solvent molecules, with inorganic connectivity motifs ranging from isolated octahedra to infinite chains, a layer and a three dimensional dense framework. The as-synthesized and desolvated networks further show structural transformation to hydrated phases through dissolution/reformation pathways. The process is likely driven by the high hydration energy of the calcium metal center.

6.2 Introduction

Research had been recently centered on attempts to rationally design MOFs with specific structures, by using a wide range of metal centers and organic linkers.[18a, 72] Recognizable secondary-building units (SBUs) form between first row transition metals and polytypic carboxylate ligands.[73] The presence of these SBUs raises hopes of the assembly of MOFs by design.[73] Another group of functional hybrid materials, MOFs formed from s-block metals, contain members that are lightweight (Li, Mg), non-toxic and readily available in nature (Mg, Ca), offering advantages in fields ranging from gas adsorption to biomedical applications.[74] Due to the predominantly non-directional ionic metal-ligand interactions, SBUs are not as easily recognized in MOFs formed from the s-block metals, and structural topology is governed by ligand geometries and functionalities. Thus, systematic studies of the ligand geometry, as the important determinant of the network architecture, are necessary for developing successful strategies for producing novel functional s-block MOFs.

In this work, a range of structural isomers of pyridinedicarboxylic acid (H_2pdc) was used to investigate the effect of bi-functional polydentate ligand architecture on the structure and stability of calcium-based MOFs (Fig. 6.1). Various isomers of pdc were used previously to synthesize a series of MOFs with lanthanides, first row transition and s-block metals, where diverse coordination abilities were observed.[75] The pdc ligand provides variable bridging and chelating coordination modes, due to the presence of both nitrogen and oxygen-based functional groups alongside a rigid aromatic backbone. Furhter, pdc forms six different structural isomers, where a mutual orientation between the functional groups varies between the isomers, thereby

facilitating systematic studies of the relationships between the ligand geometries and the resultant MOFs' structural topologies in a relatively simple system.

Apart from the metal centers and organic linkers, external parameters such as temperature and synthesis solvents can also influence the topologies and properties of the materials produced. Solvent often influences the coordination behavior of the metal centers, which determine the connectivity and dimensionality of the network.[76] The extent of deprotonation of organic carboxylate linkers that largely decide its coordination mode can be controlled by adjusting the basicity of the solvent medium.[77] Along with the influence of synthesis solvent on the network topology, several examples of the post-synthesis solvent induced structural transformation are reported in literature.[78] The desolvation-resolvation behavior is accompanied by changes in metal coordination geometry or network topology.[79]

Here we report nine calcium based MOFs formed from different structural isomers of pdc linkers, and by varying the nature of the solvent used in solvothermal syntheses method. One of the networks was obtained by recrystallization of anhydrous solvothermally-synthesized MOF in the solvent containing water.

6.3 Experimental Section

6.3.1 Synthesis

Eight coordination networks were synthesized under solvothermal conditions. Starting materials include calcium nitrate tetrahydrate ($Ca(NO_3)_2 \cdot 4H_2O$, Acros-Organics, 99+% purity), normally anhydrous calcium chloride ($CaCl_2$, Acros-Organics, 96% purity), 2,5- (Sigma-Aldrich

98% purity), 2,4- (Sigma-Aldrich 98% purity), 2,6- (Acros-Organics 99% purity), 3,4- (Acros-Organics 99% purity), 3,5- (Acros-Organics 98% purity) pyridinedicarboxylic acid ($C_7H_6NO_4$), N,N-dimethylformamide (C_3H_7NO, DMF, Sigma-Aldrich 99% purity,) and ethanol (EtOH, Fisher-Scientific, 95% purity). These reactants were used without further purification.

Synthesis of Ca_4(2,5-pdc)$_4$(DMF), compound 6.1. In a typical synthesis of **6.1,** one mmol each of 2,5-pdc (0.167 g) and $Ca(NO_3)_2 \cdot 4H_2O$ (0.236 g) were dissolved in a DMF/EtOH mixture (5.48 g/1.15 g; molar ratio 1:1:75:25). The resultant mixture was stirred for 2 hours to achieve homogeneity and heated for 5 days at 180°C in the oven. The product was obtained as needle-shaped crystals and washed with ethanol (yield 72%; 0.161 g).

Synthesis of Ca(2,5-pdc)(H_2O), compound 6.2. Synthesis involves one mmol of 2,5-pdc (0.167 g) and one mmol of $CaCl_2$ (0.111 g) dissolved in DMF/H_2O solution (3,65 g/1.9 g; molar ratio 1:1:50:50). The resultant mixture was stirred for 2 hours to achieve homogeneity and was heated for 5 days at 180°C inside the oven. The product was obtained as needle-shaped crystals and washed with ethanol (yield 68%; 0.152 g).

Synthesis of Ca(2,5-pdc)(DMF), compound 6.3. Synthesis involves one mmol of 2,5-pdc (0.167 g) and one mmol of $CaCl_2$ (0.111 g) dissolved in 7.3 g of DMF (molar ratio 1:1:100). The resultant mixture was stirred for 2 hours to achieve homogeneity and heated for 5 days at 180°C in an oven. The product was obtained as block-shaped crystals and washed with ethanol (yield 64%; 0.178g).

Synthesis of Ca(2,4-pdc)(H_2O), compound 6.4. A typical synthesis involves one mmol of 2,4-pdc·H_2O (0.185 g) and one mmol of $CaCl_2$ (0.111 g) dissolved in DMF/H_2O solution (3.65g/1.9g; molar ratio 1:1:50:50). The resultant mixture was stirred for 2 hours to achieve

homogeneity and heated for 5 days at 180°C inside the oven. The product was obtained as needle-shaped crystals and washed with ethanol (yield 73%; 0.163 g).

Synthesis of Ca(2,4-pdc)(DMF), compound 6.5. A typical synthesis involves one mmol of 2,4-pdc·H_2O (0.185 g) and one mmol of $CaCl_2$ (0.111 g) dissolved in 7.3 g DMF [molar ratio 1:1:100]. The resultant mixture was stirred for 2 hours to achieve homogeneity and heated for 5 days at 180°C in an oven. The product was obtained as block-shaped crystals and washed with ethanol (yield 69%; 0.192g).

Synthesis of Ca (2,6-pdc), compound 6.6. Synthesis involves one mmol of 2,6-pdc (0.167 g) and one mmol of $CaCl_2$ (0.111 g) dissolved in DMF/H_2O solution (3.65g/1.9g; molar ratio 1:1:50:50). The resultant mixture was stirred for 2 hours to achieve homogeneity and heated for 5 days at 180°C inside the oven. The product was obtained as block-shaped crystals and washed with ethanol (yield 84%; 0.172 g).

Synthesis of Ca_4(3,4-pdc)$_4$(H_2O) compound 6.7. A typical synthesis involves one mmol of 3,4-pdc (0.167 g) and one mmol of $CaCl_2$ (0.111 g) dissolved in a DMF/H_2O solution (3,65g/1.9g; molar ratio 1:1:50:50). The resultant mixture was stirred for 2 hours to achieve homogeneity and heated for 5 days at 180°C inside the oven. The product was obtained as plate-shaped crystals and washed with ethanol (yield 58%; 0.129 g).

Synthesis of Ca(3,5-pdc)(DMF), compound 6.8. A typical synthesis involves one mmol of 3,5-pdc (0.167 g) and one mmol of $CaCl_2$ (0.111 g) dissolved in 7.3 g DMF (molar ratio 1:1:100). The resultant mixture was stirred for 2 hours to achieve homogeneity and heated for 5 days at 100°C in an oven. The product was obtained as block-shaped crystal and washed with ethanol (yield 76%; 0.231 g).

Synthesis of Ca(3,5-pdc)(H_2O)$_2$, compound 6.9. Compound **6.9** was made in impure form using one mmol of 3,5-pdc (0.167 g) and one mmol of $CaCl_2$ (0.111 g) dissolved in a DMF/H_2O solution (3,65g/1.9g; molar ratio: 1:1:50:50). The resultant mixture was stirred for 2 hours to achieve homogeneity and heated for 5 days at 100°C. The product was obtained as a mixture of block-shaped crystals and unidentified powder. The single-crystal data were collected from crystals of this batch. Attempts to directly synthesize pure **6.9** from solvothermal routes were not successful. For example using a variety of synthesis solvents, namely DMF/water, pure water, water/ethanol, pure ethanol, in combination with different synthesis temperatures of 22, 60, 100 and 180°C, and with or without NH_4F as a mineralizer, failed to yield compound **6.9**. However, a pure compound **6.9** was obtained from a compound **6.8** through a solvent driven structural transformation, which is discussed in details below.

6.3.2 X-ray Crystallography

Suitable crystals of each compound were selected from the bulk residue of filtration and were then mounted on glass fibers using epoxy. Reflections for compounds **6.1** and **6.3 - 6.9** were collected using a four-circle kappa Oxford Gemini diffractometer at room temperature. Reflections for compound **6.2** were collected using a Bruker four circle P4-single crystal diffractometer equipped with a SMART 1K CCD detector at room temperature (298 K) using Mo Kα radiation (λ = 0.71073 Å) with φ and ω scans.

The crystal structures of **6.1 - 6.9** were solved using direct methods (SHELXS).[49-50] Calcium and oxygen atoms were located first followed by determination of other atom positions (C, N) from Fourier difference maps. Most of the non-hydrogen atoms were refined

anisotropically (Figs. 6.2 – 6.10). Hydrogen atoms were added to the structure model using geometrical constraints. A summary of important crystallographic details and atomic coordinates for the compounds **6.1 – 6.9** can be found in Tables 6.1 – 6.27.

Bulk sample identification and determination of phase purity were done using powder X-ray diffraction. Data were collected using a Rigaku® Ultima-IV diffractometer equipped with a Cu Kα radiation within a range of $5° \leq 2\theta \leq 40°$ (scanning rate: 1°/min). The powder patterns so collected were consistent with the powder patterns simulated based on the single crystal data (Figs. 6.11 – 6.19).

6.3.3 Thermal Analysis

TGA data for compounds **6.1 – 6.8** were collected using a Netzsch 449C Jupiter instrument (see the chapter 2.2). Samples were heated from room temperature to 750°C under a N_2 atmosphere with a heating rate of 10°C/minute (Figs. 6.22 – 6.28)

6.3.4 Solubility and Solvent-Driven Transformation

Approximately 0.05 g of each compound was placed in a glass vial with 10 ml of solvents: H_2O, EtOH, MeOH, for the solubility studies. Solvents were refreshed every day for 7 days, or until the total dissolution. In the transformation study approximately 0.05 g of desolvated compounds **6.1 – 6.5** and **6.8** was placed in 10 ml of solvents: H_2O, EtOH, MeOH and DMF for 2 days without decanting. Samples were recovered by solvent evaporation.

6.4 Results and Discussions

6.4.1 Structural Description

Calcium can adopt different coordination numbers with oxygen and/or nitrogen. In compounds **6.1 - 6.9** calcium metal centers are present in combinations of 6-, 7- or 8-coordinated environments with the functional groups of the pdc linker or solvent molecules. The average metal-oxygen bond is 2.40 (± 0.09) Å, with the range of distances from 2.263(2) Å to 2.692(1) Å (Table 6.28). The metal-oxygen bond length increases with the calcium coordination number from 6 to 8, with an average of 2.32 (± 0.04) Å for 6-coordinated, 2.40 (± 0.04) Å for 7-coordinated and 2.46 (± 0.08) Å for 8-coordinated environment. Pyridyl nitrogen atoms display two different coordination behaviors – chelating calcium together with one or two carboxylate oxygen atoms from the same linker in compounds **6.1 – 6.6** – or bridging different metal centers in compounds **6.8 – 6.9**. The average Ca-N bond length is 2.56 (± 0.04) Å.

The structural motifs found in compounds **6.1 – 6.9** are illustrated in Figure 6.30. Calcium metal centers are bridged by the carboxylate groups and/or pyridyl nitrogen atoms, forming different cationic building blocks ranging from monomers (**6.8**, **6.9**), dimers (**6.8**), tetramers (**6.1**), chains (**6.2 – 6.5)**, layer (**6.7**) and a 3-D-network (**6.6**). Organic linkers show variable coordination, involving either a chelating or bridging mode, or a combination of both (Fig. 6.31).

The geometry of the pdc linker dictates the topology of the Ca-pdc networks formed. Organic linkers 2,5- and 2,4-pdc display a very similar connectivity to metal centers, where pyridyl nitrogen and one carboxylate oxygen atom are present in chelating positions with

calcium. Such connectivity leads to the formation of four networks with similar structural topologies. Except **6.1,** compounds based on 2,4- and 2,5-pdc (**6.2 – 6.5)** are constructed of infinite chains of corner- (**6.2**) or edge- (**6.3 – 6.5**) connected CaO_nN_m polyhedra, parallel to one of the unit cell axes (*b* for **6.2** and **6.4**, *a* for **6.3** and **6.5**). Those chains are further linked together by organic ligands, results in three-dimensional structures (Fig. 6.33). The asymmetric units of the resultant structures comprise one unique metal center, and one complete organic ligand plus one solvent molecule. In each material the pdc linker connects to five calcium metal centers (Fig. 6.31). The metal coordination sphere is quite similar in the compounds **6.3 – 6.5**, where calcium is coordinating to five organic linkers and one solvent molecule, with a coordination number of 7 (**6.2**) or 8 (**6.3 – 6.5**). Carboxylate groups from pdc linkers do not chelate to the metal center in the compound **6.2,** but rather bridge the adjacent metals, what results in a lower coordination number. The calculated theoretical porosity is 4%, 42%, 0% and 35% for **6.2 – 6.5,** respectively, showing that networks incorporating DMF molecules are much more open and potentially porous than the ones containing water.[67]

Compound **6.1** shows different inorganic connectivity compared to other networks of the same metal-linker system (**6.2**, **6.3**). It is composed of edge sharing tetrameric calcium polyhedra (Fig. 6.30e), connected by organic linkers, which results in a 3-D network. The asymmetric unit of **6.1** comprises four crystallographically different calcium atoms, four organic ligands and one DMF molecule coordinated to Ca3. In this compound, calcium is either 7- (Ca1, Ca2, Ca3) or 6- (Ca4) coordinated, and pdc is connecting to 5 or 6 different metal centers (Fig 6.31a-b).

In **6.6** there is only one unique 7-coordinated metal center with distorted pentagonal bipyramidal geometry, one unique 2,6-pdc ligand and no solvent molecules. The specific geometry of 2,6-pdc allows tridentate chelating mode, where the metal is surrounded by one

nitrogen and two oxygen atoms. The carboxylate groups are further turned from the aromatic plane by 31.19° and 18.49° bridging to an adjacent metal center that leads to formation of a hexagonal dense framework of inorganic connectivity. Each CaO_6N_1 polyhedron is connected to three others, sharing one edge and two corners. The pdc carboxylate groups are coordinated in a monodentate or monodentate bridging fashion, and every organic linker is connecting to five calcium ions (Fig. 6.33e).

The asymmetric unit of compound **6.7** consists of one crystallographically unique calcium metal center, one linker and a coordinated water molecule. Calcium polyhedra are joined in edge or corner sharing fashion, forming a layered inorganic connectivity. The inorganic layer is stacked between organic layers, formed by linkers. The geometry of 3,4-pdc governs the topology of the compound **6.7** as seen in the previously described compounds. The distance between the pyridyl nitrogen and the carboxylate groups is crucial, as in the compound **6.7** only the carboxylate oxygen atoms coordinate with the metal centers, forming a layered network. The linker shows diverse coordination modes, ranging from monodentate, monodentate bridging and bidendate chelating (Fig. 6.31g). In the crystal structure, extensive O-H···N hydrogen-bonding interaction between hydrogen from water and pyridyl nitrogen, lead to formation of a three-dimensional supramolecular network (Fig. 6.32).

Both the compounds **6.8** and **6.9** are formed by a combination of calcium metal centers, connected by the 3,5-pdc linker, although their structural topologies are quite different. The co-planar arrangement of carboxylate groups with the pyridine ring facilitates the formation of planar metal-ligand connectivity, as previously reported in the case of Mg-3,5-pdc (Fig. 6.34).[74h] The asymmetric unit of the compound **6.8** consists of four unique calcium metal centers, three organic linkers and four coordinated DMF molecules. One of the pdc linkers connects the planes

together to form a 3-D network. Three of the unique calcium metal centers (Ca1, Ca3, Ca4) are present in distorted octahedral coordinations, with DMF molecules either at the vertices of the octahedra (Ca1, Ca3) or occupying one of the coordination sites (Ca4). The fourth calcium center (Ca2) is present in a seven-coordinated environment, with six carboxylate oxygen atoms and one DMF molecule. One of the carboxylate groups is present in a chelating mode, while others are bridging the adjacent Ca atoms. The asymmetric unit of compound **6.9** is composed of one unique calcium center, an organic linker and two solvent water molecules. The calcium metal center is present in a pentagonal bipyramidal geometry, where apices are occupied by water molecules and four planar corners belong to two chelating carboxylate groups. The fifth planar coordination site is occupied by a pyridyl nitrogen atom. Each organic linker is connected with three calcium centers to form the layered network; terminal water molecules occupy calcium coordination sites, which might otherwise lead to the connectivity in the third dimension.

6.4.2 Variation of Synthetic Parameters

Attempts to obtain novel multidimensional MOFs require optimization of a number of parameters in the synthesis, including the nature of the metal salt, solvent type and temperature.[74h, 76a] Both solvothermal and hydrothermal reaction conditions were employed in the present case, to study the formation of the Ca(pdc) networks. A preliminary study was performed on the Ca-2,5-pdc system, in order to rationalize the choice of a limited sub-set of solvents (Table 6.29). As a result, it was found that water, when used in a combination with other solvents (DMF, methanol, and ethanol), always favors the formation of hydrated compound **6.2.** Similar results were previously observed in a Mg-3,5-pdc system, showing the overwhelming

preference to form hydrated phases.[71h] Based on these preliminary results DMF, water, ethanol, and their 1:1 molar combinations were chosen as the preferred synthesis solvents. In retrospect the choice is intuitive, as the polar synthesis solvents are expected to favor the formation of ionic calcium coordination networks. Following the preliminary study to narrow the choice of the solvents (Table 6.29), in total nine MOFs were synthesized based on five structural isomers of the pdc linker. However, after repeated synthesis attempts using (a) higher solvent ratios (b) addition of mineralizer NH_4F, we were unable to synthesize any Ca(2,3-pdc) networks. Instead, phase pure α-calcium formate is formed, when DMF is used in pure or mixture forms, as a result of thermal decomposition of DMF molecules.[80]

6.4.3 Activation and Solvent Dependent Structural Transformations

The thermal stability of the compounds **6.1-6.8** under N_2 atmosphere depends on their structural topologies and the nature of the coordinated solvents. Compound **6.6** exhibits the highest stability, up to 580°C, due to the absence of any coordinated or free solvent molecules. Compound **6.1** shows a similar one-step decomposition pathway and is stable up to 480°C. The presence of a coordinated DMF within the isolated voids rather than open channels might be the reason for the higher thermal stability of compound **6.1**, with respect to other networks possessing coordinated solvents. All other compounds show the expected two-step decomposition pathways of solvent removal, followed by decomposition. Compounds with coordinated water molecules show higher thermal stability over the ones with coordinated DMF molecules, and this is attributed to stronger Ca-water bonding.

Compounds with the theoretical porosity in their desolvated form were tested for gas-adsorption properties after activation. They were all found non-porous based on the N_2 adsorption experiments and poorly crystalline after desolvation, based on the lack of the sharp Bragg peaks in their XRD powder diffraction patterns. Further, the water solubility of as-synthesized and activated networks **6.1 – 6.8** was tested and all of the as-synthesized compounds were found to be soluble in water except for **6.3** and **6.4**.

Freshly made and activated samples of compounds **6.1 – 6.3** (Ca-2,5-pdc system) were immersed in water, methanol and ethanol to study the solvent-driver transformation (Fig. 6.35). With the exception of compound **6.1** immersed in ethanol, where the powder XRD of the recovered material shows that it transformed to unknown microcrystalline material, sample **6.2** was formed after the evaporation of the solvent. Further, exposing activated samples **6.2** and **6.3** to DMF leads to the formation of the compound **6.3**. The activated compound **6.1** reverts to its original crystalline form upon exposure to solvent DMF. Compounds **6.5** and **6.8** transform to the hydrated phases **6.4** and **6.9,** respectively, after immersing both the activated and freshly made samples in water, ethanol and methanol (Fig 6.29). The exposure of **6.4**, **6.5** and **6.8** to DMF did not lead to the formation or recovering of crystallinity of DMF-containing phases. The transformation to the hydrated phases was previously reported by Liang et al. in other calcium based MOFs.[78a] The formation of the hydrated phases from either as-synthesized or activated compounds might follow a dissolution-reformation pathway, which is driven by the high hydration energy of the calcium metal center (H_{hyd}= -1577 kJ/mol).[81]

6.5 Conclusions

Atomic arrangements in nine calcium- and pyridinedicarboxylate-based metal organic frameworks, synthesized under solvothermal conditions or by the solvent-driven transformation, are based on a variety of the inorganic structural motifs, ranging from isolated polyhedra to infinite chains, a layer or a 3-D connectivity, depending on the linker geometry and synthetic conditions. The motif formed depends on the orientation of carboxylates with respect to the pyridyl nitrogen group and the nature of the coordinated solvent. For example, Ca-3,5-pdc frameworks (**6.8 – 6.9**) consist of monomers and dimers of calcium polyhedra, while Ca-2,6-pdc (**6**.**6**) forms a three dimensional inorganic connectivity. In both cases, the mutual angles between the carboxylate groups are the same (120°), though the close proximity of a pyridyl nitrogen atom to the carboxylate groups in 2,6-pdc favors the 3-D connectivity. As-synthesized and desolvated networks show structural transformations to hydrated phases in the presence of water through dissolution/reformation pathways involving calcium coordination spheres.

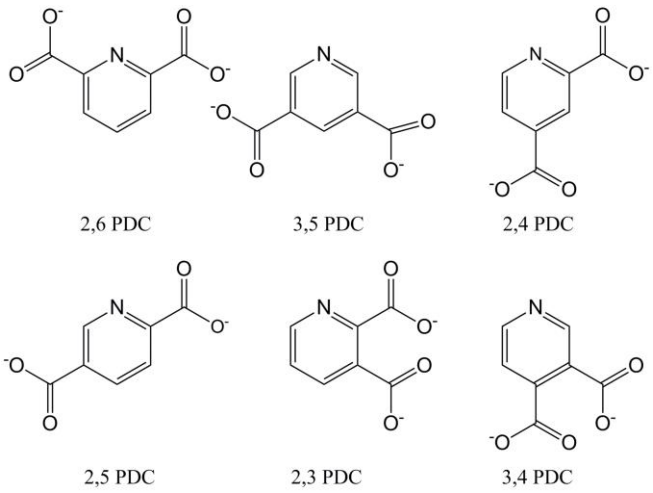

Figure 6.1 Pyridinedicarboxylate isomers investigated in this study.

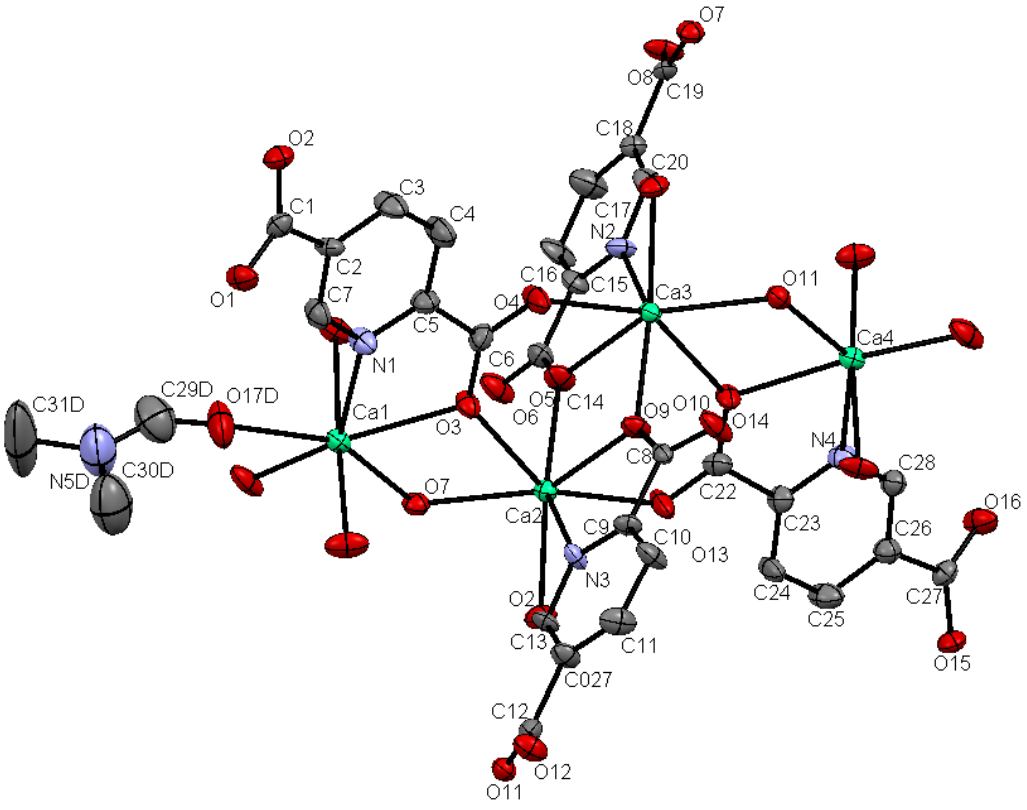

Figure 6.2 View of the local environment of calcium in **6.1**, showing the atom-numbering scheme. Displacement ellipsoids are drawn at the 50% probability level. H atoms omitted for clarity.

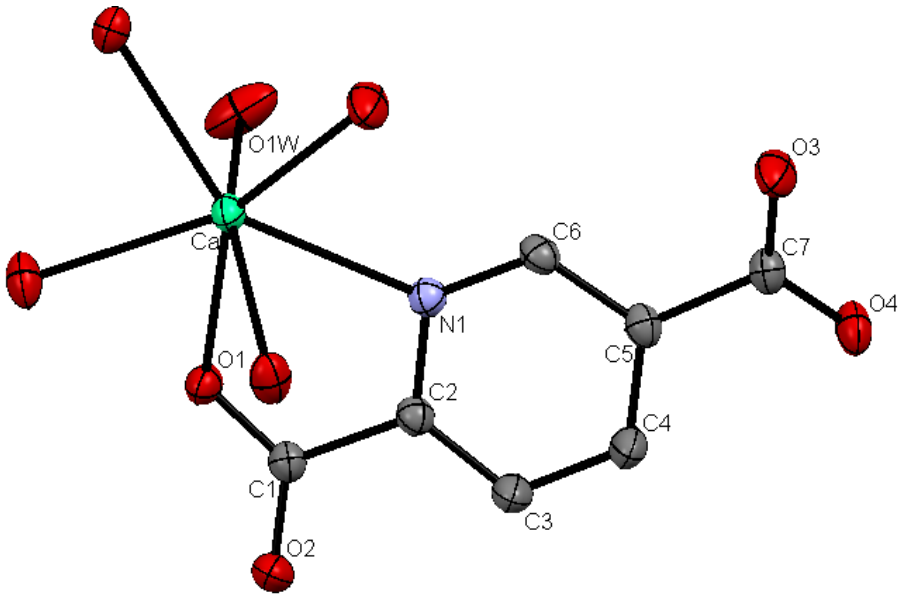

Figure 6.3 View of the local environment of calcium in **6.2**, showing the atom-numbering scheme. Displacement ellipsoids are drawn at the 50% probability level. H atoms omitted for clarity.

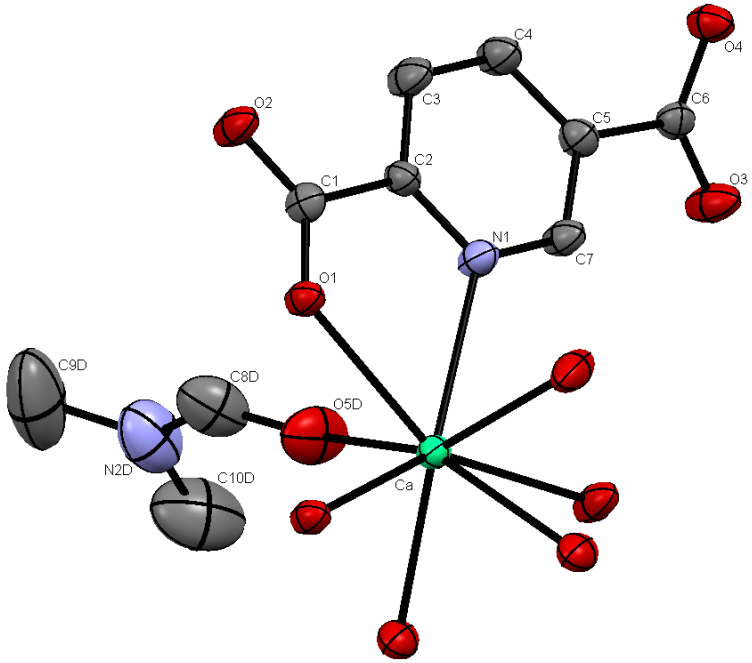

Figure 6.4 View of the local environment of calcium in **6.3**, showing the atom-numbering scheme. Displacement ellipsoids are drawn at the 50% probability level. H atoms omitted for clarity.

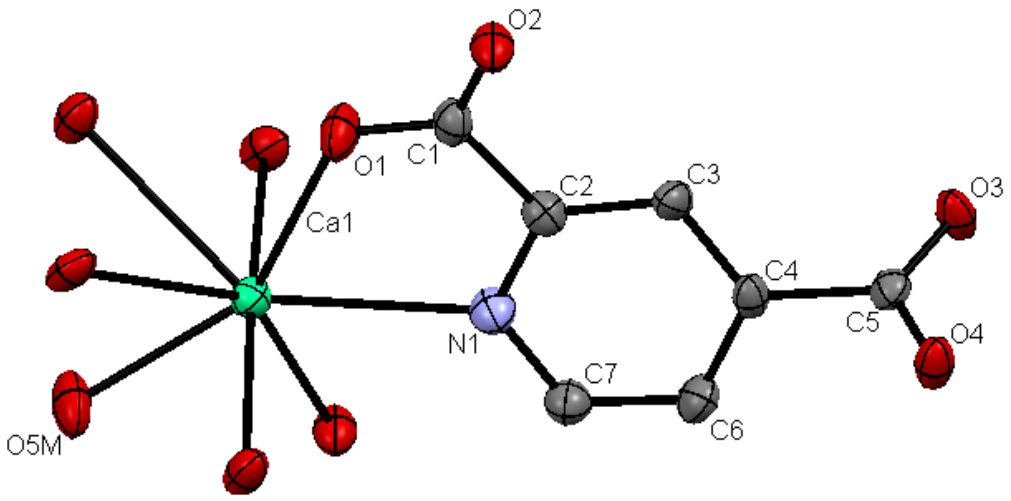

Figure 6.5 View of the local environment of calcium in **6.4**, showing the atom-numbering scheme. Displacement ellipsoids are drawn at the 50% probability level. H atoms omitted for clarity.

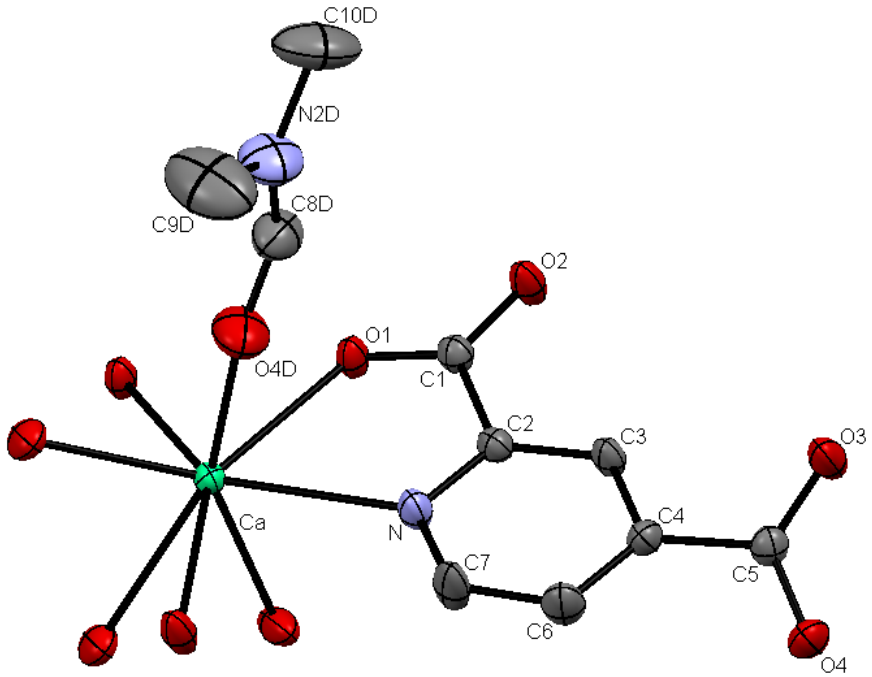

Figure 6.6 View of the local environment of calcium in **6.5**, showing the atom-numbering scheme. Displacement ellipsoids are drawn at the 50% probability level. H atoms omitted for clarity.

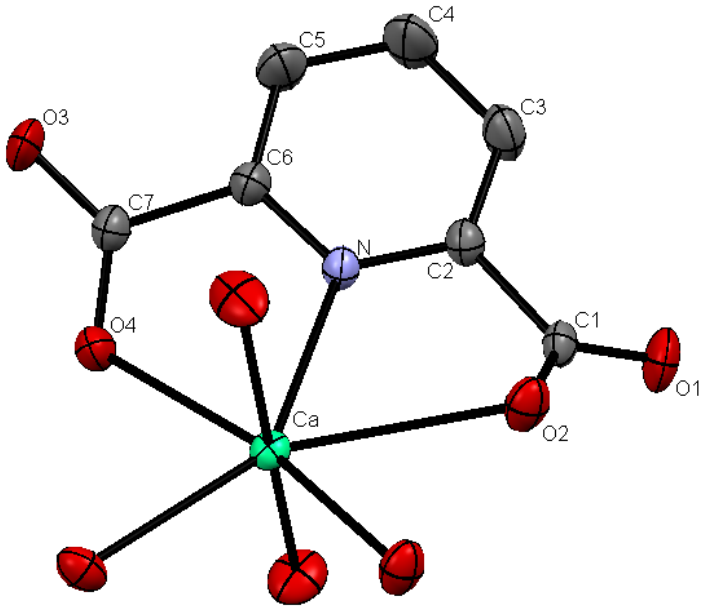

Figure 6.7 View of the local environment of calcium in **6.6**, showing the atom-numbering scheme. Displacement ellipsoids are drawn at the 50% probability level. H atoms omitted for clarity.

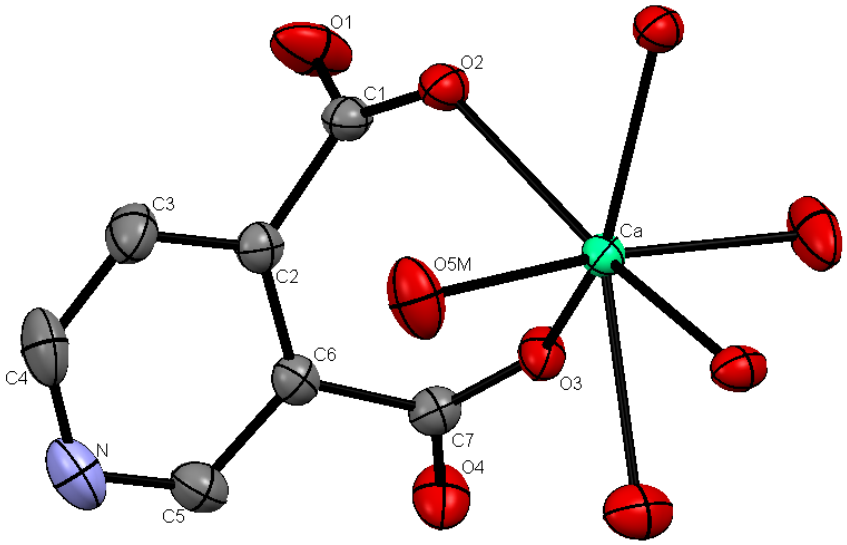

Figure 6.8 View of the local environment of calcium in **6.7**, showing the atom-numbering scheme. Displacement ellipsoids are drawn at the 50% probability level. H atoms omitted for clarity.

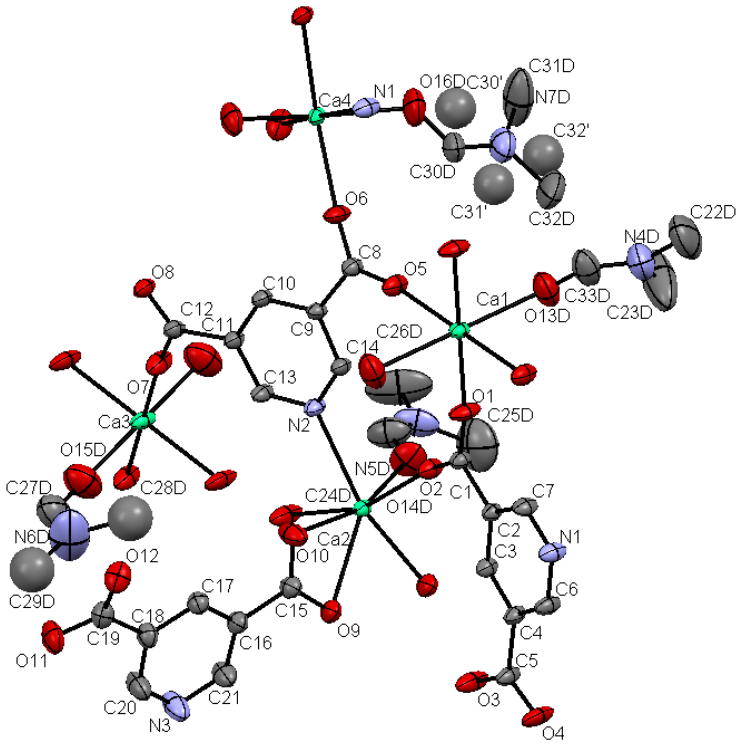

Figure 6.9 View of the local environment of calcium in **6.8**, showing the atom-numbering scheme. Displacement ellipsoids are drawn at the 50% probability level. H atoms omitted for clarity.

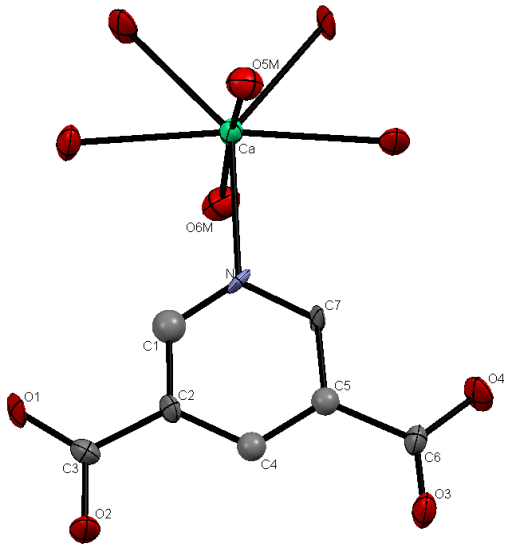

Figure 6.10 View of the local environment of calcium in **6.9**, showing the atom-numbering scheme. Displacement ellipsoids are drawn at the 50% probability level. H atoms omitted for clarity.

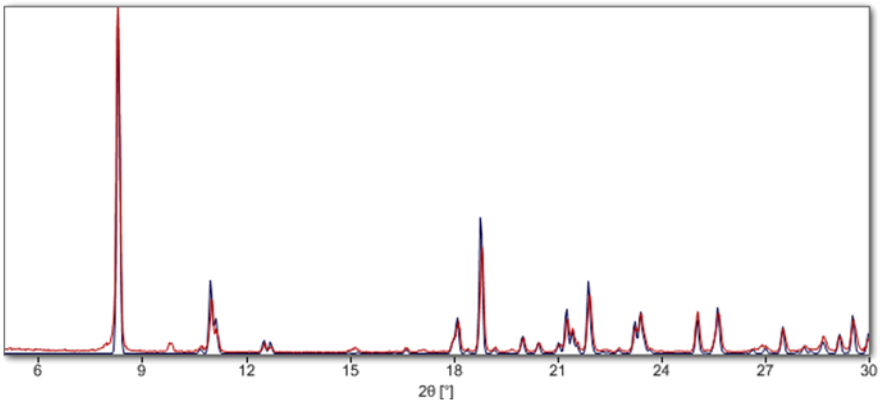

Figure 6.11 Calculated (blue) and observed (brown) powder diffraction patterns of **6.1.**

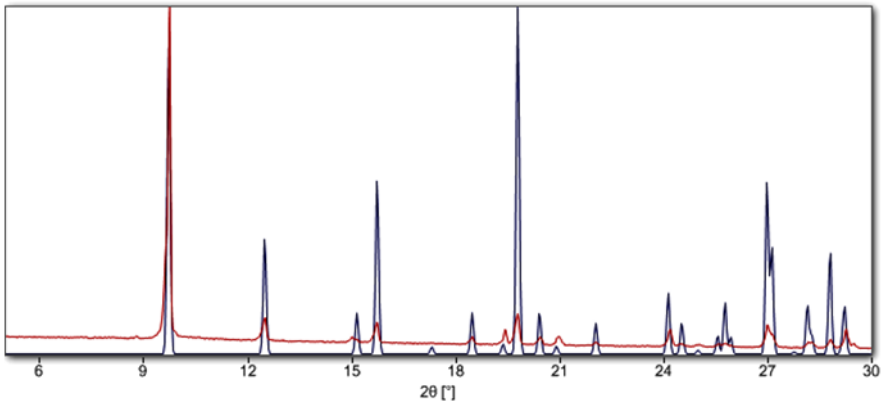

Figure 6.12 Calculated (blue) and observed (brown) powder diffraction patterns of **6.2.**

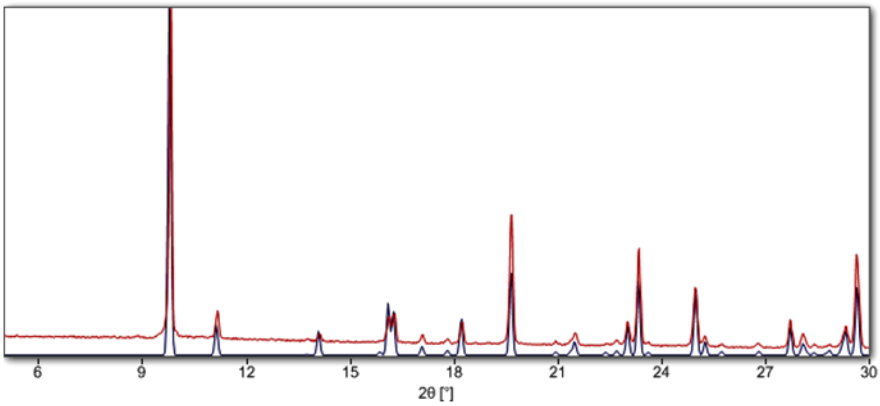

Figure 6.13 Calculated (blue) and observed (brown) powder diffraction patterns of **6.3.**

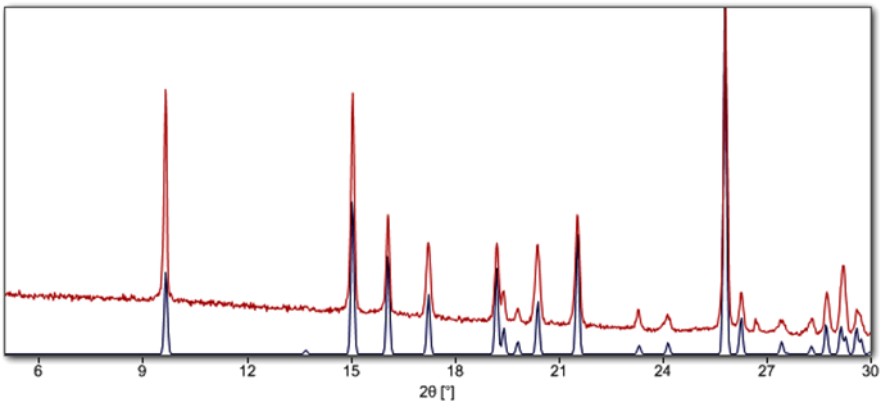

Figure 6.14 Calculated (blue) and observed (brown) powder diffraction patterns of **6.4.**

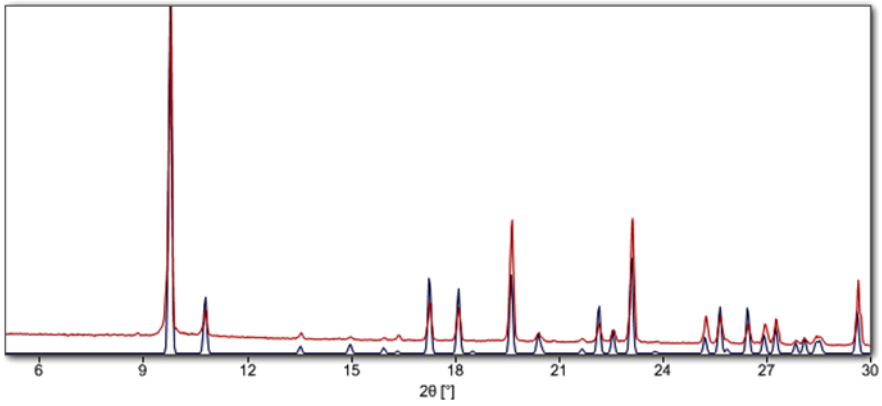

Figure 6.15 Calculated (blue) and observed (brown) powder diffraction patterns of **6.5.**

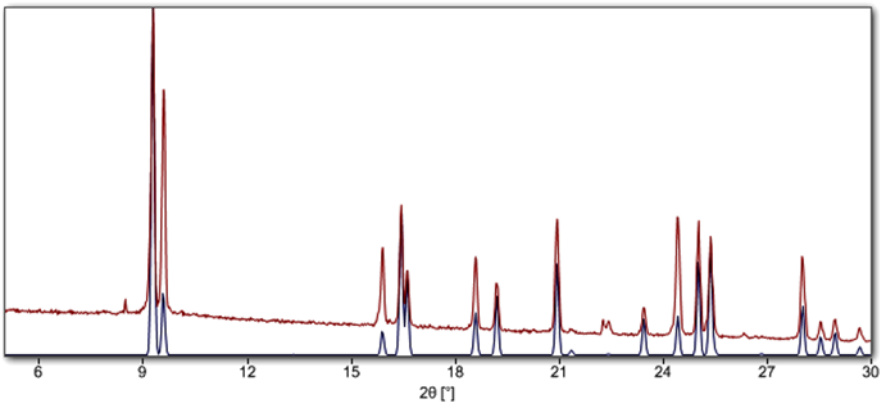

Figure 6.16 Calculated (blue) and observed (brown) powder diffraction patterns of **6.6.**

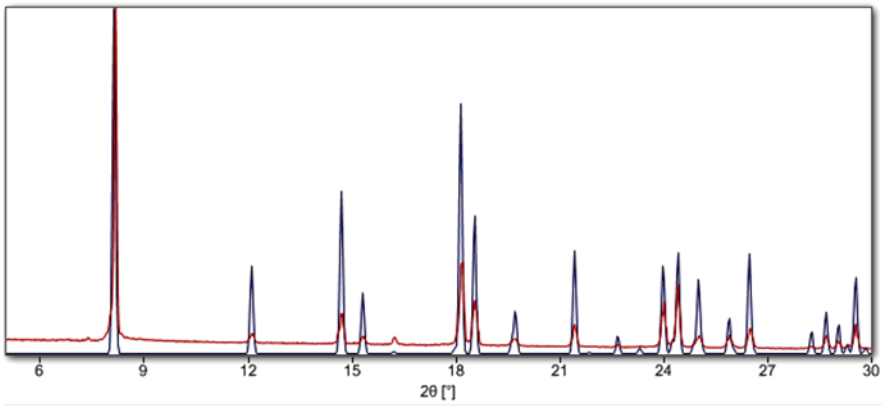

Figure 6.17 Calculated (blue) and observed (brown) powder diffraction patterns of **6.7.**

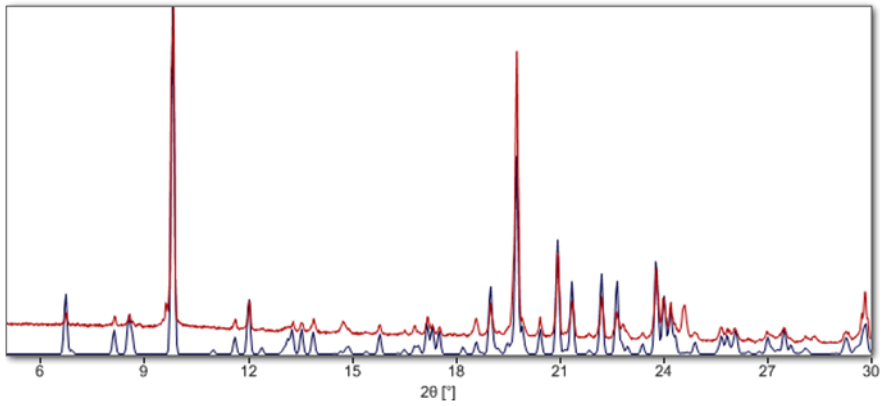

Figure 6.18 Calculated (blue) and observed (brown) powder diffraction patterns of **6.8.**

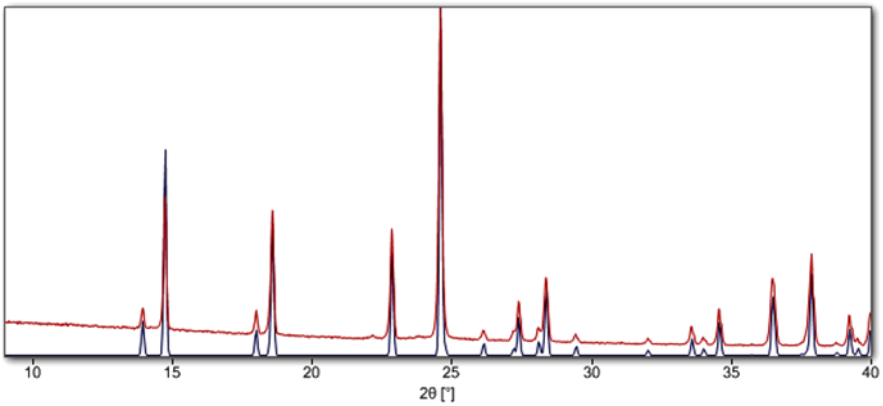

Figure 6.19 Calculated (blue) and observed (brown) powder diffraction patterns of **6.9.**

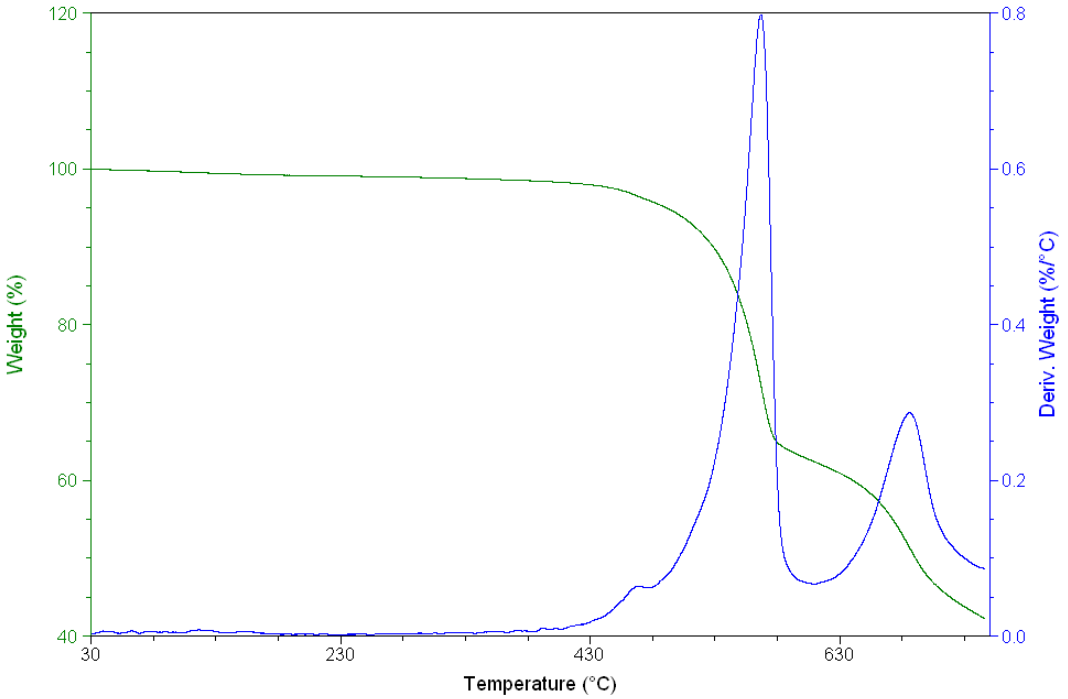

Figure 6.20 The TGA plot of the compound **6.1.**

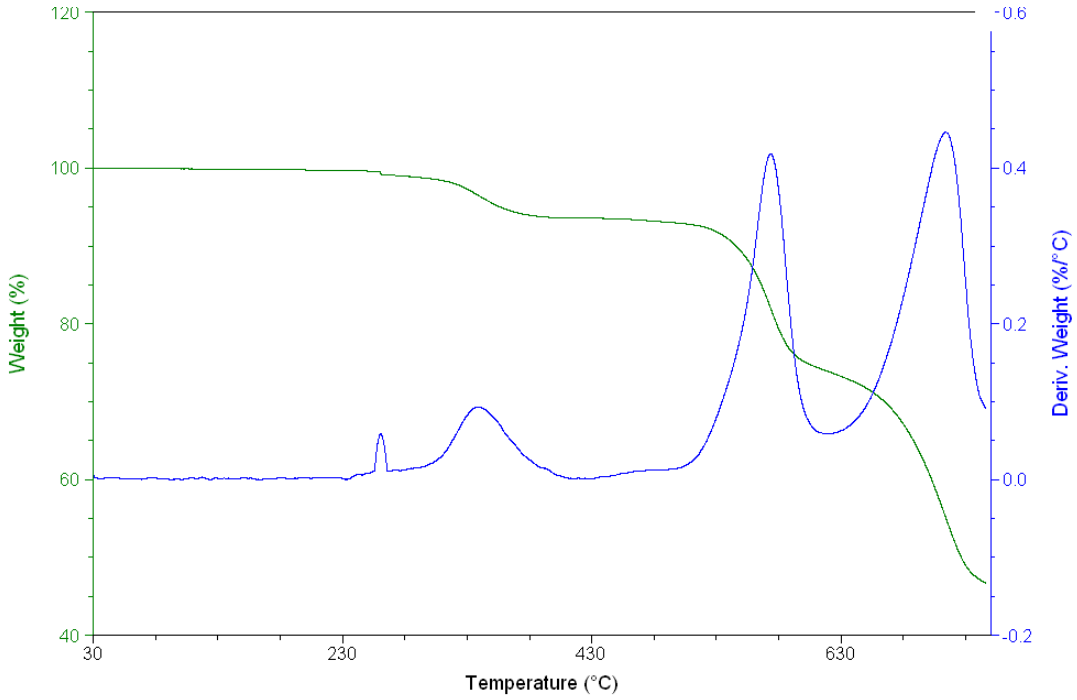

Figure 6.21 The TGA plot of the compound **6.2.**

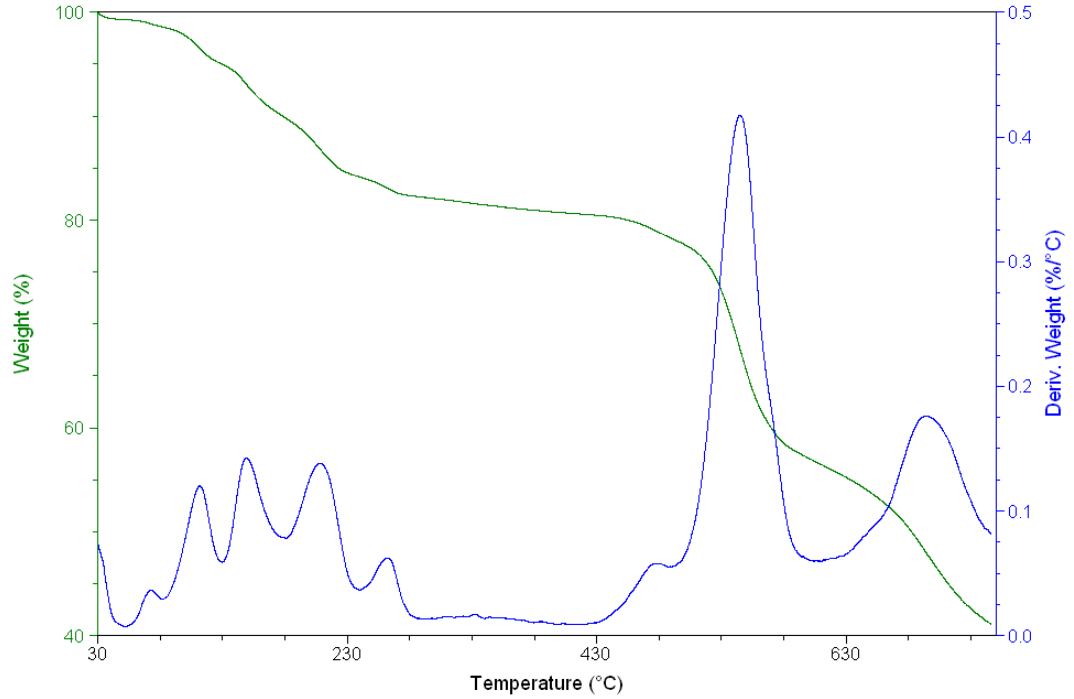

Figure 6.22 The TGA plot of the compound **6.3.**

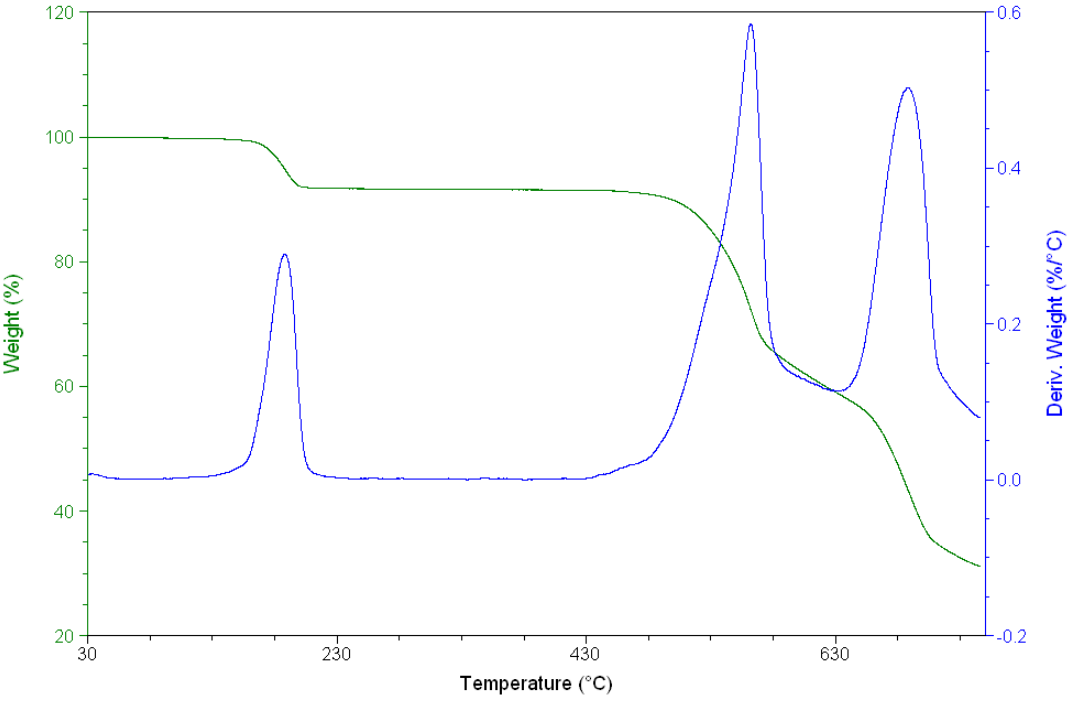

Figure 6.23 The TGA plot of the compound **6.4.**

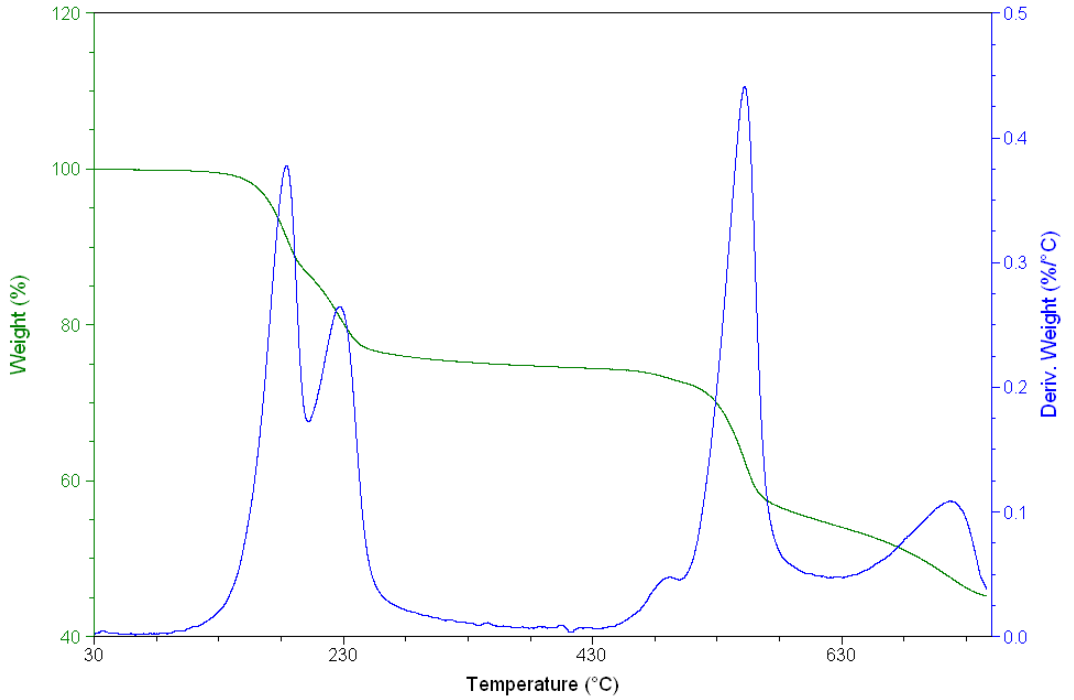

Figure 6.24 The TGA plot of the compound **6.5.**

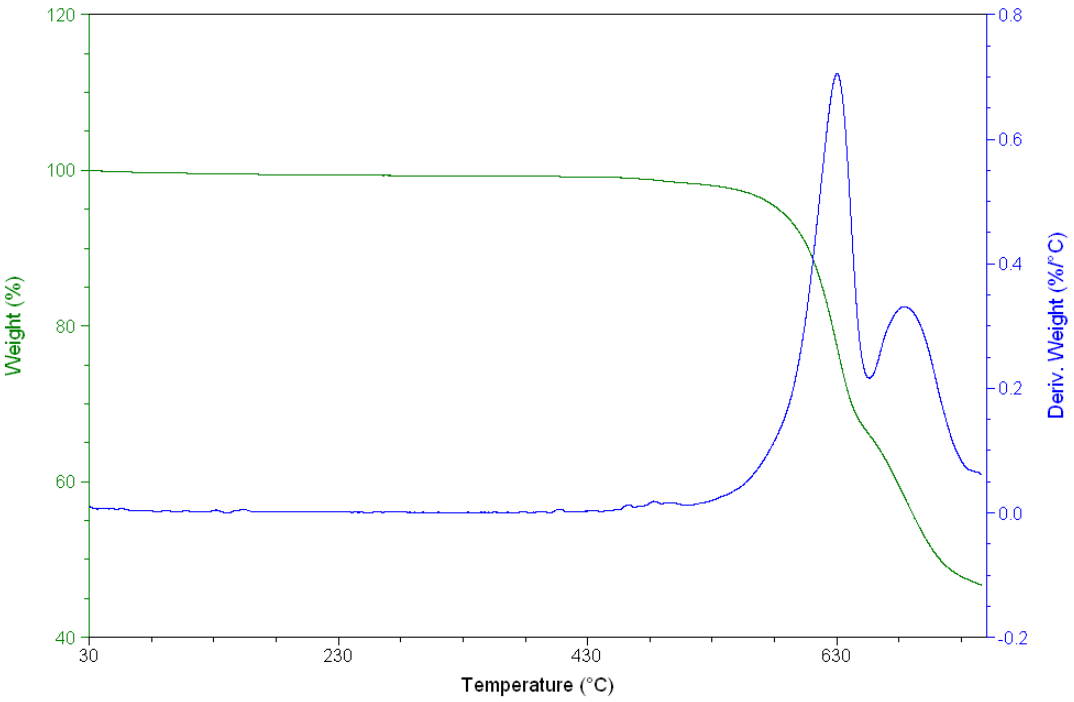

Figure 6.25 The TGA plot of the compound **6.6.**

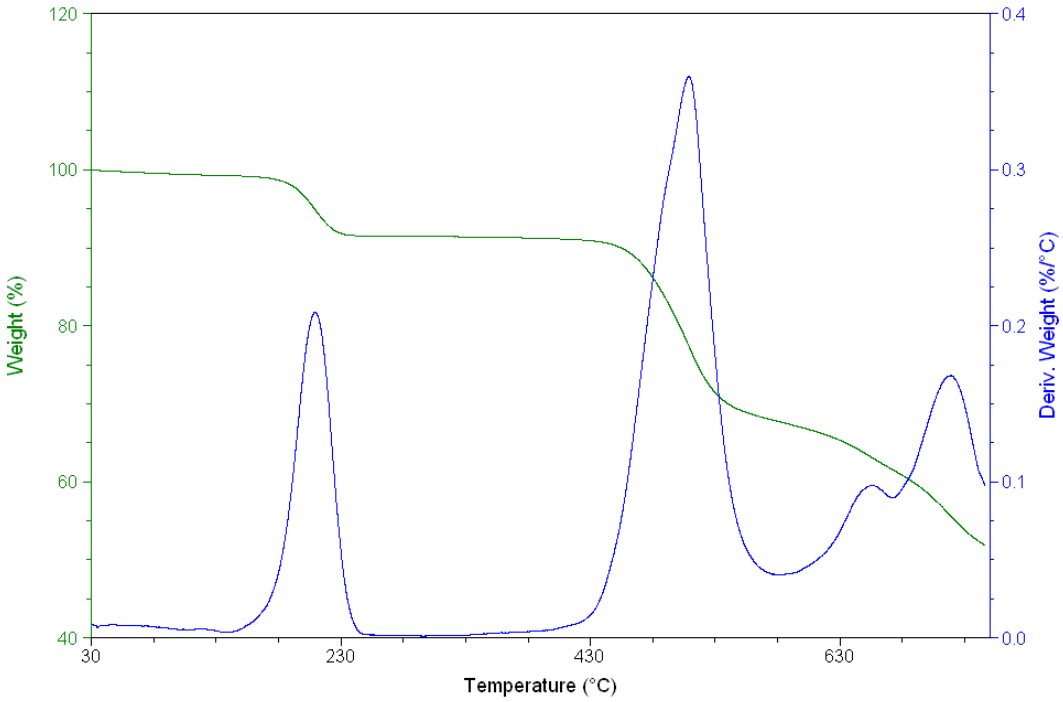

Figure 6.26 The TGA plot of the compound **6.7.**

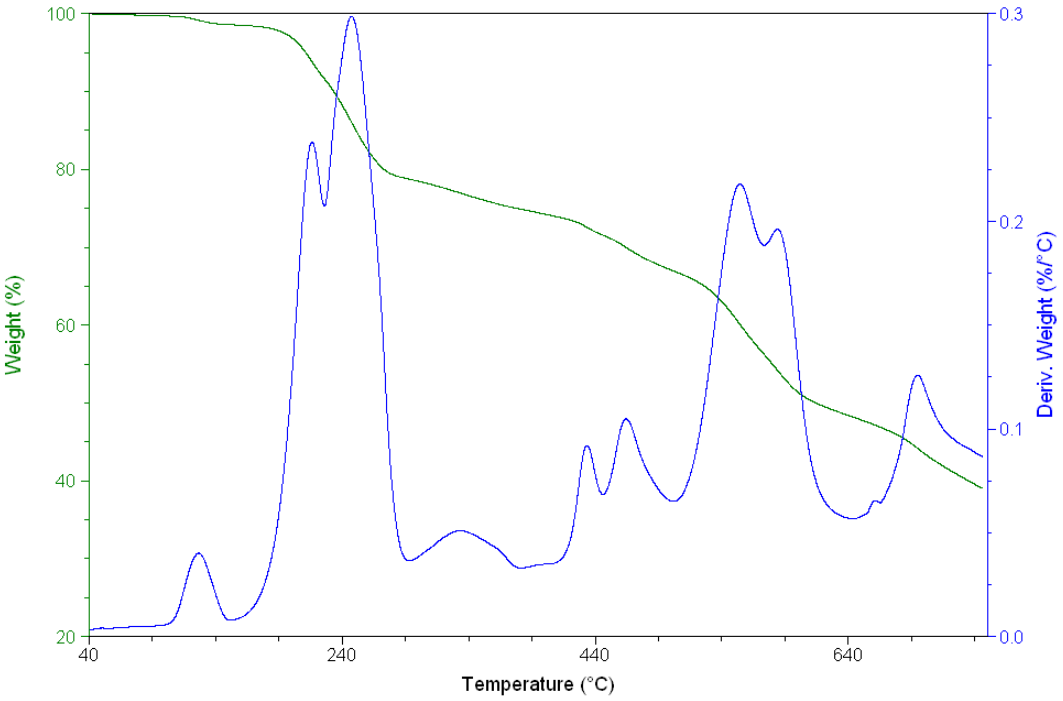

Figure 6.27 The TGA plot of the compound **6.8.**

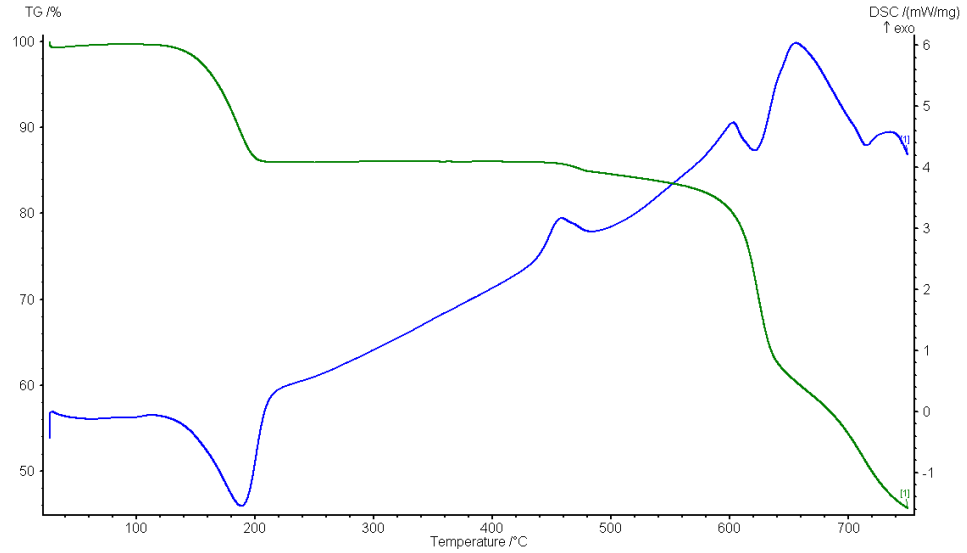

Figure 6.28 The TGA plot of the compound **6.9.**

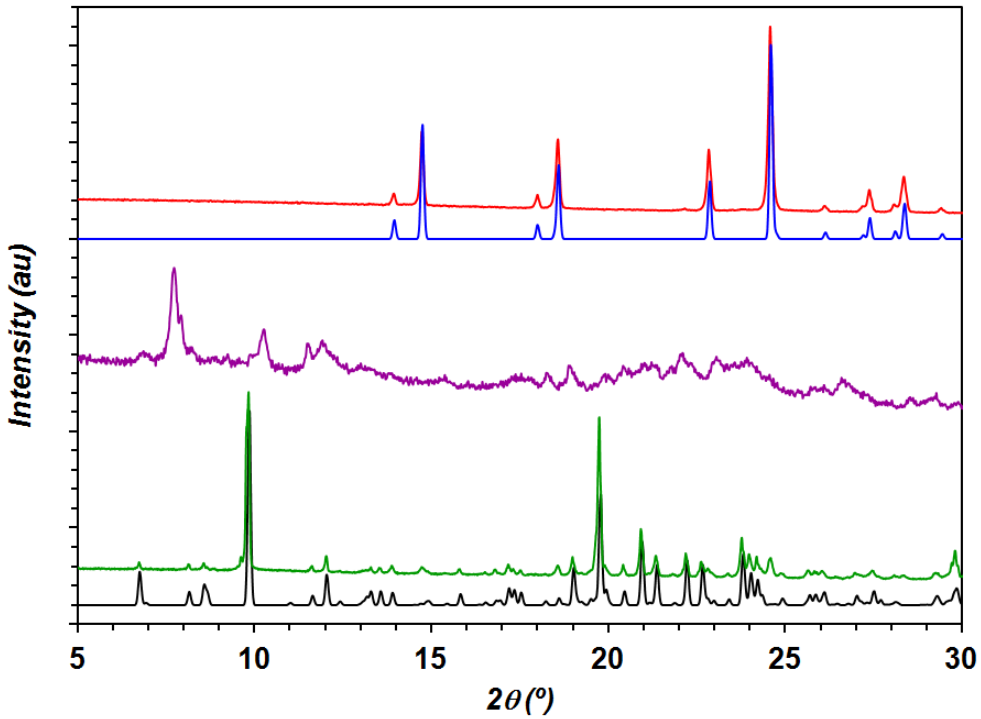

Figure 6.29 Powder diffraction patterns: bottom – compound **6.8** (black – calculated from single crystal data, green – recorded)**,** middle (purple) – activated compound **6.8**, top – compound **6.9** (blue – calculated from single crystal data, red – recorded for the material made by transformation of compound **6.8** in ethanol)

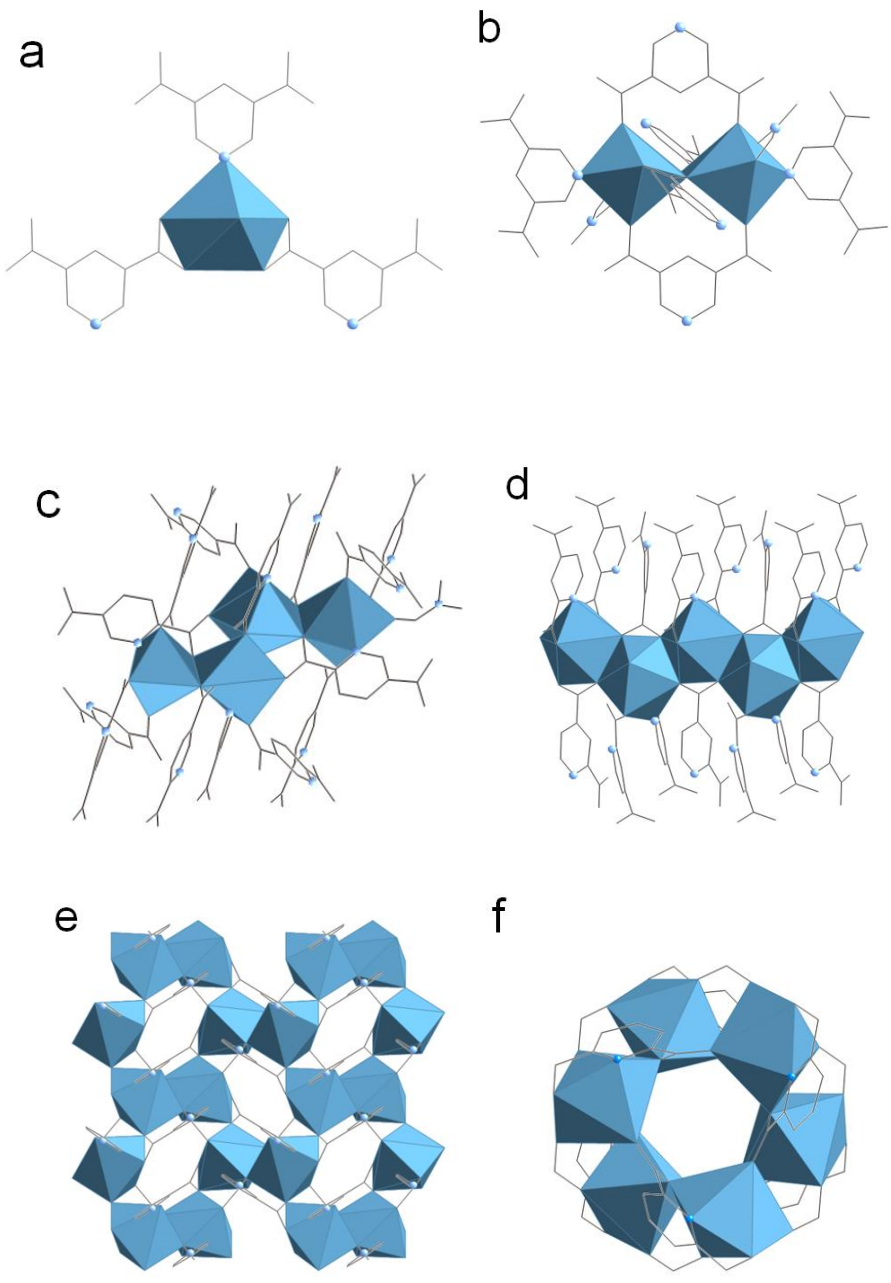

Figure 6.30 Building blocks consisting of Ca-centered polyhedra (blue) and pdc (the blue circle designates the pyridyl nitrogen position) in compounds **6.1**-**6.9**: (a) monomer found in compound **6.8** and **6.9**, (b) dimer in **6.8**, (c) tetramer in **6.1**, (d) chain in **6.4**, (e) layer in **6.7** and (f) secondary building block of the framework of **6.6**. Hydrogen atoms were omitted for clarity.

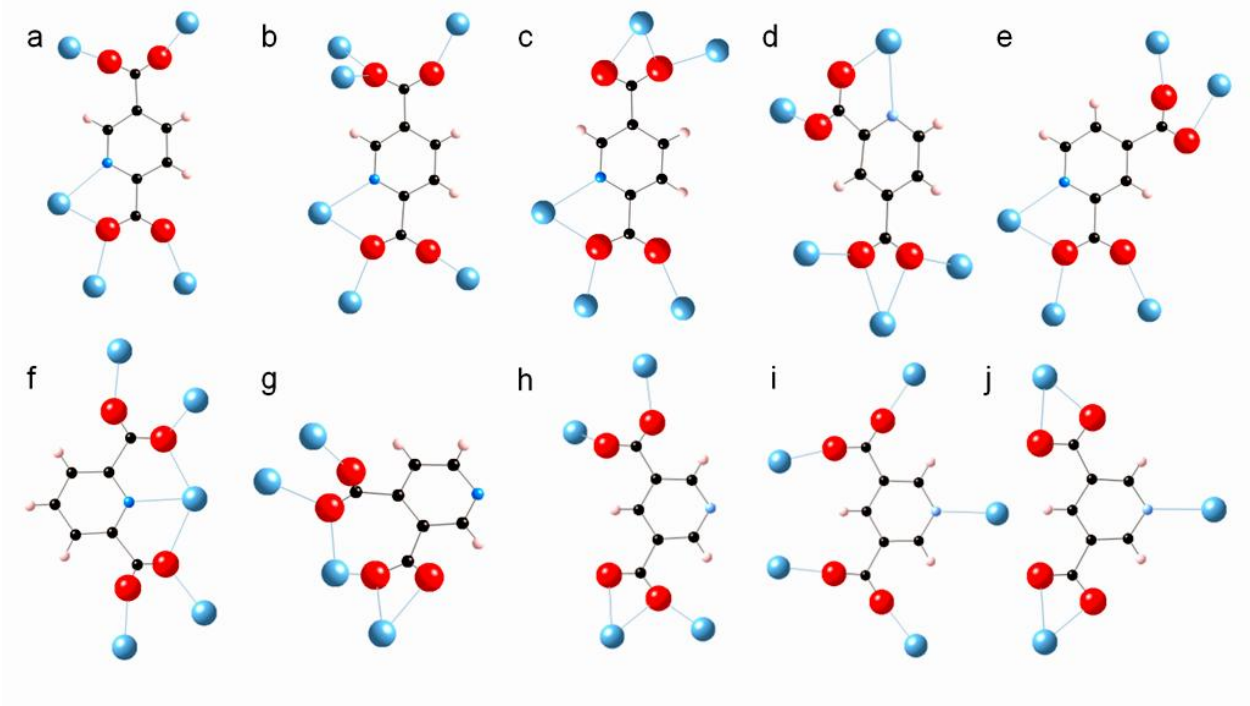

Figure 6.31 Coordination behavior of pdc linkers in **6.1** (a and b); **6.2** (a); **6.3** (c)**; 6.4** (d)**; 6.5** (e); **6.6** (f); **6.7** (g); **6.8** (h and i); **6.9** (j). Large blue spheres represent calcium, small blue spheres – nitrogen, black – carbon, red – oxygen and pink – hydrogen.

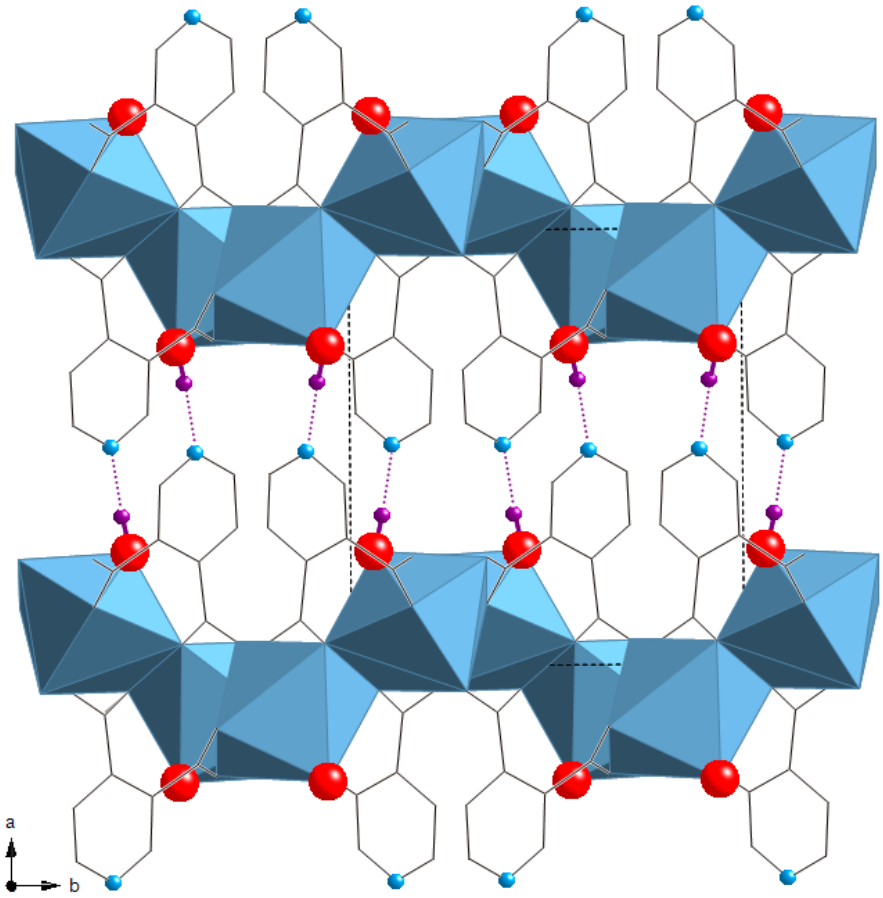

Figure **6.32** O-H···N hydrogen bonded (purple dotted line) layers in compound **6.7**, viewed along the [001] direction; carbon-carbon linkages are shown as black wireframe, calcium – centered blue polyhedra, oxygen from water molecule – red spheres, nitrogen – blue spheres, hydrogen – purple spheres. All hydrogen atoms not involved in hydrogen bonding are omitted for clarity.

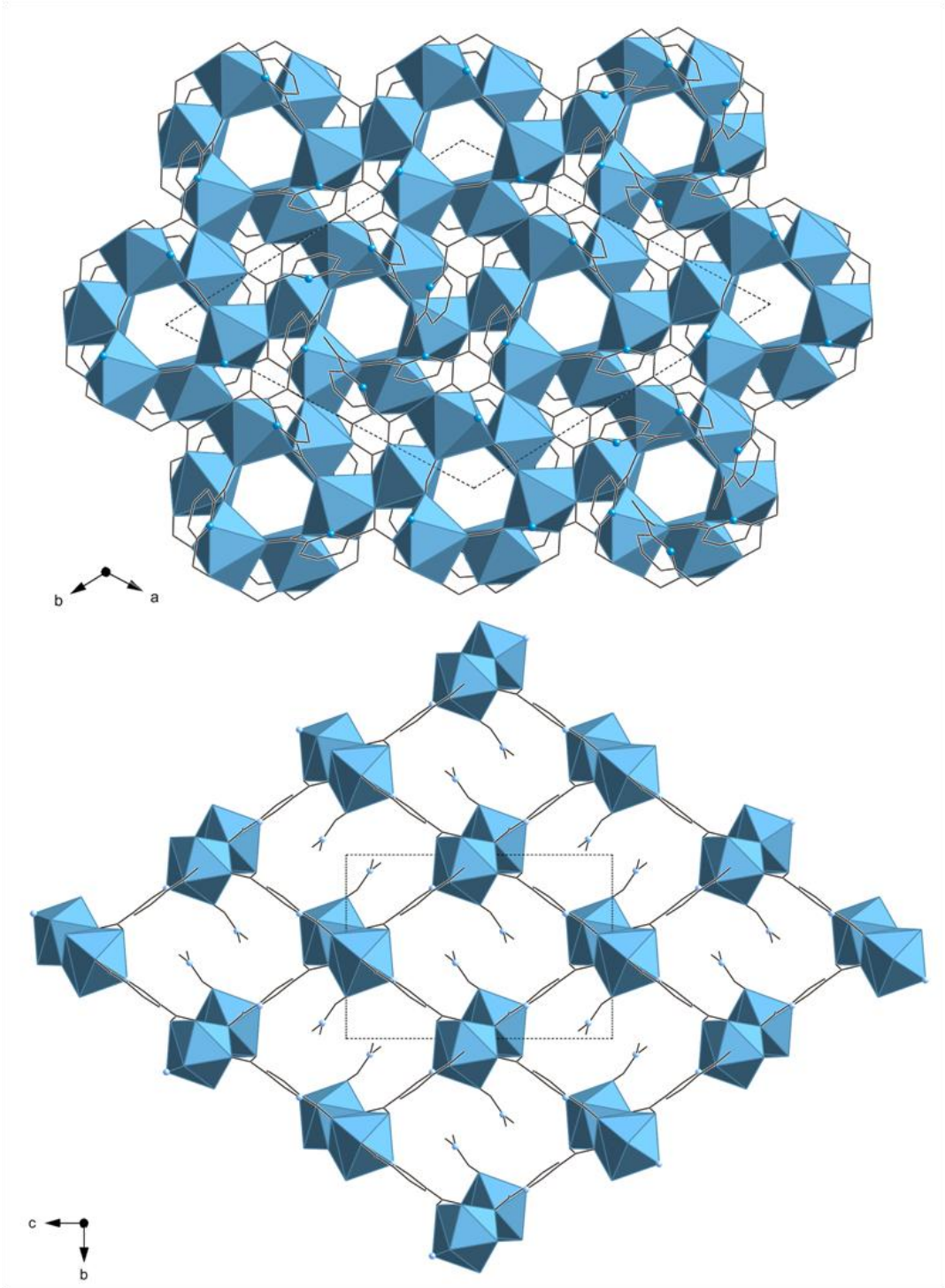

Figure 6.33 Polyhedral representation of structures in **6.6** (top) and **6.3** (bottom) in [100] and [001] direction, respectively. Hydrogen atoms are omitted for clarity.

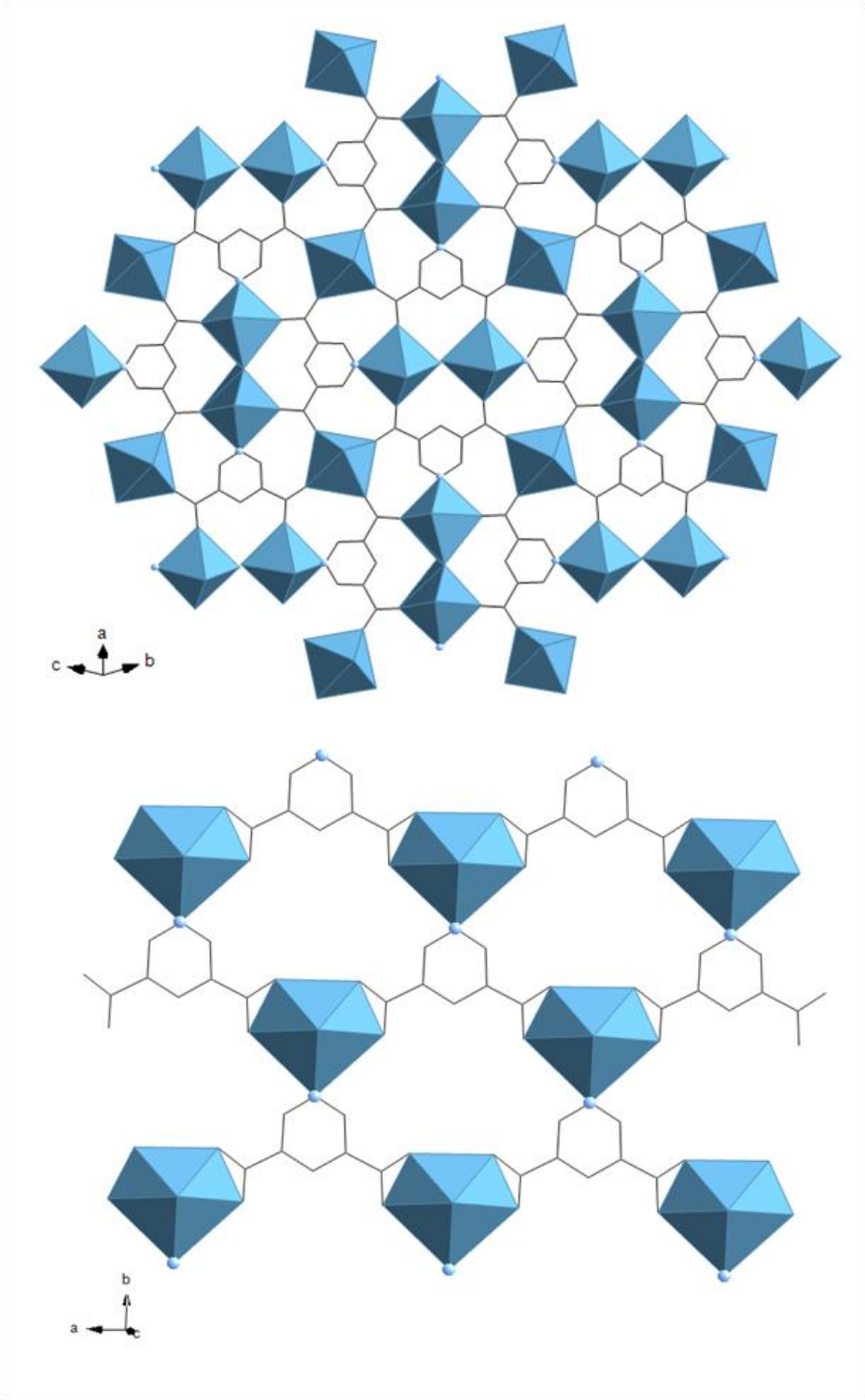

Figure 6.34 View of the single metal-linker layer in compound **6.8** (top) and **6.9** (bottom).

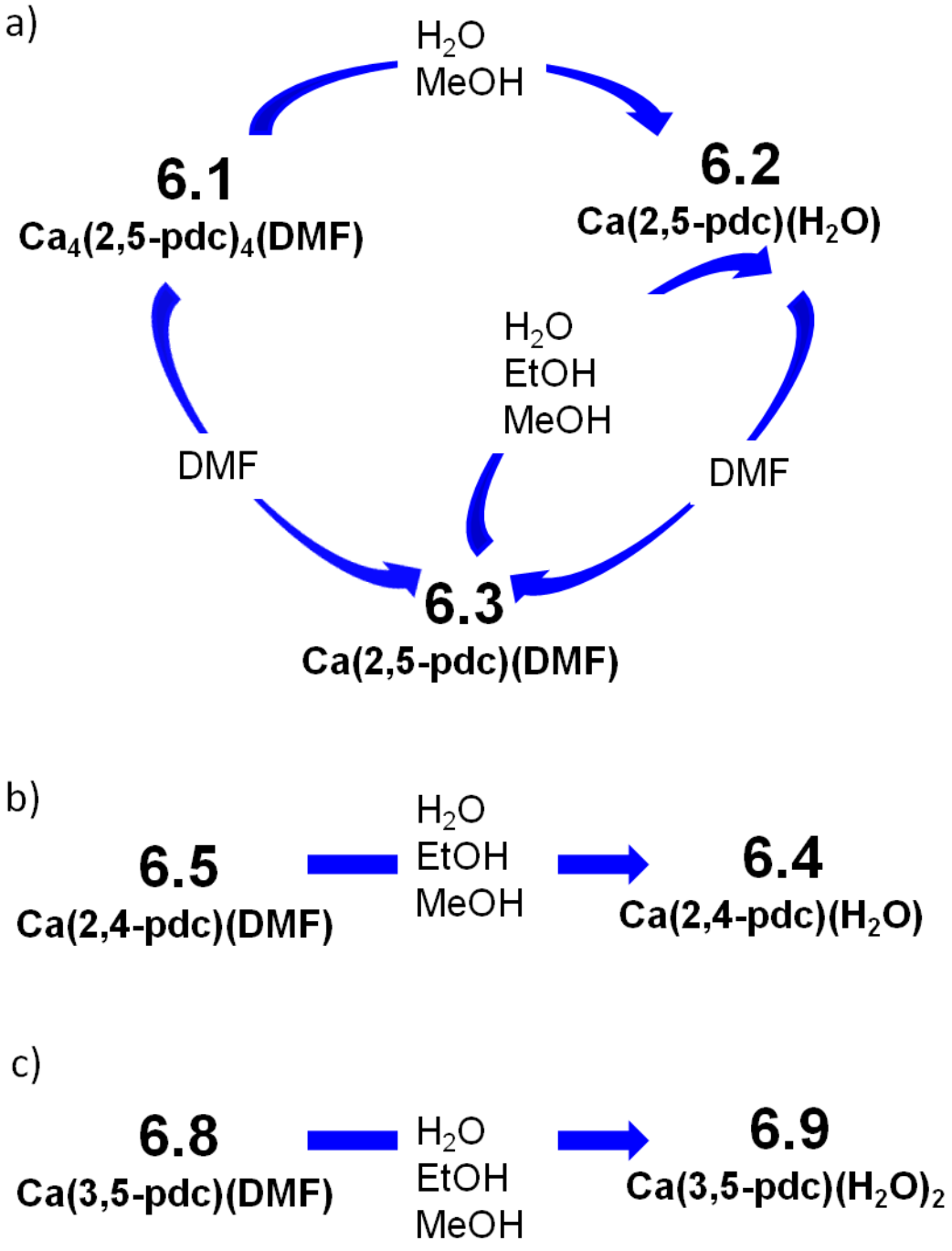

Figure 6.35 General scheme for observed transformation paths; (a) 2,5-pdc system, (b) 2,4-pdc system, (c) 3,5-pdc system

Table 6.1: Crystallographic data and structural refinement details of **Ca_4(2,5-pdc)$_4$(DMF)**, compound **6.1**.

Empirical formula	$C_{31}H_{19}Ca_4N_5O_{17}$
Formula weight	893.83
Collection Temperature (K)	293(2)
Wavelength (Å)	0.71073
Space Group	***C c***
a (Å)	17.7443(10)
b (Å)	9.0940(5)
c (Å)	22.8204(16)
β (°)	110.655(7)
Volume (Å^3)	3445.7(4)
Z	4
Calculated Density (g/cm^3)	1.723
Absorption coefficient (mm^{-1})	0.604
F(000)	1872
Crystal size (mm)	0.1 × 0.03 × 0.01
θ range of data collection (°)	3.74 to 25.03
Index range	$-21 \leq h \leq 19$,
	$-10 \leq k \leq 10$
	$-27 \leq l \leq 27$
Total reflection	14066
Independent reflection	5794
R_{int}	0.0770
Completeness to θ_{max}	99.6 %
Goodness of fit	0.821
Data/ Restraints/parameter	5794 / 2 / 514
R_1(on F_o, $I>2\sigma(I)$)	0.0429
wR_2 (on F_o^2, all data)	0.0821

Table 6.2: Crystallographic data and structural refinement details of **Ca(2,5-pdc)(H_2O)**, compound **6.2**.

Empirical formula	$C_7H_5CaNO_5$
Formula weight	223.2
Collection Temperature (K)	293(2)
Wavelength (Å)	0.71073
Space Group	P b c a
a (Å)	11.355(5)
b (Å)	7.443(3)
c (Å)	18.452(9)
Volume ($Å^3$)	1559.4(13)
Z	8
Calculated Density (g/cm^3)	1.901
Absorption coefficient (mm^{-1})	0.798
F(000)	656
Crystal size (mm)	0.2 × 0.1 × 0.1
θ range of data collection (°)	2.21 to 27.10
Index range	$-14 \leq h \leq 14$,
	$-9 \leq k \leq 9$
	$-23 \leq l \leq 22$
Total reflection	9724
Independent reflection	1702
R_{int}	0.0321
Completeness to θ_{max}	99.7 %
Goodness of fit	1.066
Data/ Restraints/parameter	1702 / 0 / 131
R_1 (on F_o, $I > 2\sigma(I)$)	0.0303
wR_2 (on F_o^2, all data)	0.0908

Table 6.3: Crystallographic data and structural refinement details of **Ca(2,5-pdc)(DMF)**, compound **6.3**.

Empirical formula	$C_{10}H_{10}CaN_2O_5$
Formula weight	278.28
Collection Temperature (K)	293(2)
Wavelength (Å)	0.71073
Space Group	***P*** $2_1/n$
a (Å)	6.4463(3)
b (Å)	10.9728(5)
c (Å)	16.0996(8)
β (°)	99.775(5)
Volume ($Å^3$)	1122.26(9)
Z	4
Calculated Density (g/cm^3)	1.647
Absorption coefficient (mm^{-1})	0.575
F(000)	575
Crystal size (mm)	0.25 × 0.2 × 0.15
θ range of data collection (°)	3.71 to 25.35
Index range	$-7 \leq h \leq 7$,
	$-13 \leq k \leq 13$
	$-19 \leq l \leq 19$
Total reflection	10504
Independent reflection	2055
R_{int}	0.0706
Completeness to θ_{max}	99.4 %
Goodness of fit	1.111
Data/ Restraints/parameter	2055 / 0 / 163
R_1 (on F_o, $I > 2\sigma(I)$)	0.0546
wR_2 (on F_o^2, all data)	0.1607

Table 6.4: Crystallographic data and structural refinement details of **Ca(2,4-pdc)(H_2O)**, compound **6.4**.

Empirical formula	$C_7H_5CaNO_5$
Formula weight	223.2
Collection Temperature (K)	293(2)
Wavelength (Å)	0.71073
Space Group	$P\ 2_1\ 2_1\ 2_1$
a (Å)	6.2110(10)
b (Å)	6.9005(9)
c (Å)	18.285(3)
Volume ($Å^3$)	783.7(2)
Z	4
Calculated Density (g/cm^3)	1.881
Absorption coefficient (mm^{-1})	0.794
F(000)	451
Crystal size (mm)	0.24 × 0.1 × 0.02
θ range of data collection (°)	3.97 to 25.67
Index range	$-7 \leq h \leq 7$,
	$-8 \leq k \leq 8$
	$-21 \leq l \leq 22$
Total reflection	6572
Independent reflection	1487
R_{int}	0.0718
Completeness to θ_{max}	99.4 %
Goodness of fit	0.810
Data/ Restraints/parameter	1487 / 0 / 133
R_1 (on F_o, $I > 2\sigma(I)$)	0.0303
wR_2 (on F_o^2, all data)	0.0556

Table 6.5: Crystallographic data and structural refinement details of **Ca(2,4-pdc)(DMF)**, compound **6.5**.

Empirical formula	$C_{10}H_{10}CaN_2O_5$
Formula weight	278.28
Collection Temperature (K)	293(2)
Wavelength (Å)	0.71073
Space Group	$\boldsymbol{P}\ 2_1/n$
a (Å)	6.4275(4)
b (Å)	16.3870(12)
c (Å)	10.9764(9)
β (°)	99.182(6)
Volume ($Å^3$)	1141.30(14)
Z	4
Calculated Density (g/cm^3)	1.620
Absorption coefficient (mm^{-1})	0.565
F(000)	362
Crystal size (mm)	0.4 × 0.03 × 0.03
θ range of data collection (°)	3.76 to 25.35
Index range	$-7 \leq h \leq 7$,
	$-19 \leq k \leq 19$
	$-13 \leq l \leq 13$
Total reflection	7941
Independent reflection	2068
R_{int}	0.0729
Completeness to θ_{max}	98.8 %
Goodness of fit	1.077
Data/ Restraints/parameter	2068 / 0 / 163
R_1 (on F_o, $I > 2\sigma(I)$)	0.0436
wR_2 (on F_o^2, all data)	0.1220

Table 6.6: Crystallographic data and structural refinement details of **Ca(2,6-pdc)**, compound **6.6**.

Empirical formula	$C_7H_3CaNO_4$
Formula weight	205.18
Collection Temperature (K)	293(2)
Wavelength (Å)	0.71073
Space Group	***R* -3**
a (Å)	18.5021(5)
c (Å)	11.9010(4)
Volume ($Å^3$)	3528.22(18)
Z	18
Calculated Density (g/cm^3)	1.738
Absorption coefficient (mm^{-1})	0.776
F(000)	362
Crystal size (mm)	0.4 × 0.2 × 0.2
θ range of data collection (°)	3.65 to 26.34
Index range	$-23 \leq h \leq 23$,
	$-23 \leq k \leq 23$
	$-14 \leq l \leq 14$
Total reflection	14627
Independent reflection	1603
R_{int}	0.0488
Completeness to θ_{max}	99.8 %
Goodness of fit	1.038
Data/ Restraints/parameter	1603 / 0 / 118
R_1 (on F_o, $I > 2\sigma(I)$)	0.0239
wR_2 (on F_o^2, all data)	0.0659

Table 6.7: Crystallographic data and structural refinement details of **Ca(3,4-pdc)(H_2O)**, compound **6.7**.

Empirical formula	$C_7H_5CaNO_5$
Formula weight	223.2
Collection Temperature (K)	293(2)
Wavelength (Å)	0.71073
Space Group	***P*** $2_1/n$
a (Å)	11.347(7)
b (Å)	9.914(4)
c (Å)	7.907(4)
β (°)	104.489(6)
Volume ($Å^3$)	861.2(8)
Z	4
Calculated Density (g/cm^3)	1.722
Absorption coefficient (mm^{-1})	0.723
F(000)	432
Crystal size (mm)	0.2 × 0.2 × 0.15
θ range of data collection (°)	3.71 to 26.37
Index range	$-14 \leq h \leq 14$,
	$-12 \leq k \leq 12$
	$-9 \leq l \leq 9$
Total reflection	10865
Independent reflection	1746
R_{int}	0.0807
Completeness to θ_{max}	99.5 %
Goodness of fit	1.084
Data/ Restraints/parameter	1746 / 0 / 128
R_1 (on F_o, $I > 2\sigma(I)$)	0.0375
wR_2 (on F_o^2, all data)	0.1013

Table 6.8: Crystallographic data and structural refinement details of **Ca(3,5-pdc)(DMF)**; **6.8**.

Empirical formula	$C_{33}H_{37}Ca_3N_7O_{16}$
Formula weight	907.94
Collection Temperature (K)	293(2)
Wavelength (Å)	0.71073
Space Group	***P*** -1
a (Å)	12.0501(3)
b (Å)	13.9638(3)
c (Å)	14.7073(3)
α (°)	98.257(2)
β (°)	111.863
γ (°)	107.785(2)
Volume ($Å^3$)	2092.18(10)
Z	4
Calculated Density (g/cm^3)	1.441
Absorption coefficient (mm^{-1})	0.471
F(000)	1008
Crystal size (mm)	0.8 × 0.5 × 0.3
θ range of data collection (°)	3.77 to 26.37
Index range	$-15 \leq h \leq 15$,
	$-17 \leq k \leq 17$
	$-18 \leq l \leq 18$
Total reflection	54549
Independent reflection	8526
R_{int}	0.0291
Completeness to θ_{max}	99.7 %
Goodness of fit	1.048
Data/ Restraints/parameter	8526 / 0 / 530
R_1 (on F_o, $I > 2\sigma(I)$)	0.0437
wR_2 (on F_o^2, all data)	0.1357

Table 6.9: Crystallographic data and structural refinement details of **Ca(3,5-pdc)(H_2O)**, compound **6.9**.

Empirical formula	$C_7H_7CaNO_6$
Formula weight	241.22
Collection Temperature (K)	293(2)
Wavelength (Å)	0.71073
Space Group	***C c***
a (Å)	10.2526(3)
b (Å)	12.6758(3)
c (Å)	7.5294(3)
β (°)	106.324(4)
Volume ($Å^3$)	939.07(5)
Z	4
Calculated Density (g/cm^3)	1.692
Absorption coefficient (mm^{-1})	0.677
F(000)	488
Crystal size (mm)	0.15 × 0.05 × 0.05
θ range of data collection (°)	3.21 to 26.72
Index range	$-12 \leq h \leq 12$,
	$-16 \leq k \leq 16$
	$-9 \leq l \leq 9$
Total reflection	5591
Independent reflection	1944
R_{int}	0.0738
Completeness to θ_{max}	99.8 %
Goodness of fit	1.081
Data/ Restraints/parameter	1944 / 2 / 121
R_1 (on F_o, $I > 2\sigma(I)$)	0.0451
wR_2 (on F_o^2, all data)	0.1228

Table 6.10: Atomic coordinates ($\times 10^4$) and equivalent isotropic displacement parameters (U_{eq}; $Å^2 \times 10^3$) for **Ca_4(2,5-pdc)$_4$(DMF)**, compound **6.1**.

	x	y	z	U_{eq}
C(1)	6855(3)	5790(7)	13393(3)	23(1)
C(2)	6424(3)	5401(7)	12726(3)	21(1)
C(3)	5816(4)	4370(7)	12536(3)	34(2)
C(4)	5506(4)	3924(7)	11922(3)	38(2)
C(5)	5802(4)	4584(7)	11497(3)	26(2)
C(6)	5550(4)	4032(6)	10839(3)	26(2)
C(7)	6646(4)	6038(6)	12260(3)	29(2)
C(8)	6311(3)	684(6)	10122(3)	18(1)
C(9)	7142(3)	1234(7)	10182(3)	20(1)
C(10)	7817(3)	369(7)	10448(3)	28(2)
C(11)	8560(4)	935(7)	10483(3)	30(2)
C(12)	9367(4)	2916(6)	10199(3)	22(1)
C(13)	7876(3)	3071(7)	9949(3)	20(1)
C(14)	3834(3)	4688(7)	9043(3)	25(2)
C(15)	3022(3)	4109(7)	9021(3)	24(2)
C(16)	2326(4)	4865(7)	8719(3)	34(2)
C(17)	1604(4)	4329(7)	8734(4)	40(2)
C(18)	1614(3)	3058(6)	9074(3)	17(1)
C(19)	855(3)	2463(6)	9126(3)	19(1)
C(20)	2346(4)	2368(7)	9353(3)	25(2)
C(22)	4624(4)	1337(6)	8433(3)	24(2)
C(23)	4384(3)	619(6)	7784(3)	24(1)
C(24)	4672(4)	1158(7)	7339(3)	30(2)
C(25)	4372(4)	601(7)	6735(3)	35(2)

C(26)	3778(3)	-471(6)	6590(3)	25(2)
C(27)	3380(4)	-1037(6)	5935(3)	22(1)
C(027)	8575(3)	2288(6)	10211(3)	24(2)
C(28)	3551(3)	-993(6)	7071(3)	24(1)
C(29D)	7030(5)	9929(10)	11720(4)	66(2)
C(30D)	8451(5)	10206(9)	12182(5)	89(3)
C(31D)	7558(8)	12310(9)	12154(8)	143(5)
N(1)	6349(3)	5674(5)	11658(2)	25(1)
N(2)	3042(3)	2848(5)	9331(3)	25(1)
N(3)	7162(3)	2565(5)	9941(2)	21(1)
N(4)	3845(3)	-487(5)	7663(2)	24(1)
N(5D)	7634(5)	10780(7)	12013(4)	76(2)
O(1)	7554(2)	6344(5)	13531(2)	30(1)
O(2)	6503(2)	5526(4)	13771(2)	29(1)
O(3)	5905(2)	4575(4)	10490(2)	24(1)
O(4)	5020(3)	3082(5)	10684(2)	36(1)
O(5)	4430(2)	3921(4)	9327(2)	29(1)
O(6)	3834(2)	5864(5)	8762(2)	37(1)
O(7)	928(2)	1520(4)	9556(2)	23(1)
O(8)	208(2)	2936(5)	8753(2)	29(1)
O(9)	5734(2)	1547(4)	9904(2)	23(1)
O(10)	6266(2)	-602(5)	10295(2)	36(1)
O(11)	9301(2)	3875(4)	9774(2)	21(1)
O(12)	10000(2)	2455(4)	10590(2)	28(1)
O(13)	5135(3)	2318(5)	8551(2)	35(1)
O(14)	4263(2)	847(4)	8784(2)	24(1)
O(15)	3758(2)	-910(4)	5565(2)	26(1)
O(16)	2693(3)	-1563(5)	5804(2)	36(1)

O(17D)	7042(3)	8642(6)	11596(2)	57(1)
Ca(1)	6362(1)	7080(1)	10679(1)	20(1)
Ca(2)	5808(1)	3890(1)	9432(1)	18(1)
Ca(3)	4380(1)	1536(1)	9844(1)	18(1)
Ca(4)	3896(1)	-1651(1)	8701(1)	20(1)

Table 6.11 Anisotropic displacement parameters ($Å^2 \times 10^3$) for **Ca_4(2,5-pdc)$_4$(DMF)**; **6.1**.

	U^{11}	U^{22}	U^{33}	U^{23}	U^{13}	U^{12}
C(1)	20(3)	25(4)	23(4)	-1(3)	8(3)	5(3)
C(2)	17(3)	30(4)	19(4)	3(3)	10(3)	-2(3)
C(3)	39(4)	44(4)	22(5)	3(3)	14(3)	-13(3)
C(4)	38(4)	45(4)	30(5)	-10(3)	11(3)	-23(3)
C(5)	29(4)	30(4)	21(4)	-1(3)	12(3)	-5(3)
C(6)	31(4)	24(4)	22(4)	-6(3)	10(3)	-1(3)
C(7)	29(4)	29(4)	25(4)	-5(3)	5(3)	-11(3)
C(8)	21(3)	20(4)	14(3)	-3(3)	8(3)	-7(3)
C(9)	11(3)	27(4)	22(4)	3(3)	5(2)	1(2)
C(10)	19(3)	22(4)	42(4)	11(3)	10(3)	-3(3)
C(11)	22(3)	34(4)	33(4)	16(3)	10(3)	10(3)
C(12)	27(4)	20(4)	24(4)	-4(3)	14(3)	-1(3)
C(13)	12(3)	25(4)	24(4)	1(3)	6(2)	-6(2)
C(14)	19(3)	26(4)	30(4)	-4(3)	9(3)	-5(3)
C(15)	25(4)	23(4)	25(4)	6(3)	11(3)	-5(3)
C(16)	28(4)	22(4)	56(5)	22(3)	19(3)	2(3)
C(17)	29(4)	40(4)	54(5)	15(4)	19(3)	2(3)
C(18)	16(3)	20(3)	15(3)	4(3)	5(2)	3(3)
C(19)	16(3)	19(4)	27(4)	-2(3)	13(3)	0(3)
C(20)	30(4)	25(4)	20(4)	10(3)	8(3)	-2(3)
C(22)	20(3)	31(4)	23(4)	1(3)	9(3)	-1(3)
C(23)	21(3)	29(4)	18(4)	-3(3)	4(3)	-3(3)
C(24)	33(4)	36(4)	24(4)	-11(3)	14(3)	-21(3)
C(25)	32(4)	50(4)	26(5)	-2(3)	15(3)	-8(3)
C(26)	27(3)	28(3)	24(4)	-1(3)	11(3)	-3(3)
C(27)	24(4)	24(3)	18(4)	-1(3)	7(3)	3(3)
C(027)	14(3)	25(4)	32(4)	4(3)	7(3)	1(3)
C(28)	23(3)	26(3)	22(4)	-2(3)	8(3)	-2(3)
C(29D)	70(5)	57(6)	63(6)	9(5)	16(4)	-7(5)
C(30D)	80(6)	56(6)	115(9)	-5(6)	13(6)	5(5)
C(31D)	84(6)	51(6)	273(15)	-66(9)	36(7)	-3(6)

N(1)	27(3)	31(3)	15(3)	1(2)	4(2)	-9(2)
N(2)	19(3)	30(3)	30(3)	4(3)	15(2)	1(2)
N(3)	15(2)	14(3)	30(3)	4(2)	5(2)	-3(2)
N(4)	25(3)	31(3)	18(3)	-2(2)	9(2)	-2(2)
N(5D)	69(4)	50(5)	101(7)	-16(4)	21(4)	-6(4)
O(1)	18(3)	47(3)	25(3)	-9(2)	6(2)	-10(2)
O(2)	32(2)	35(3)	27(3)	-2(2)	18(2)	-1(2)
O(3)	33(2)	22(2)	18(2)	1(2)	9(2)	-9(2)
O(4)	43(3)	45(3)	24(3)	-15(2)	16(2)	-28(2)
O(5)	16(2)	29(3)	41(3)	4(2)	10(2)	3(2)
O(6)	30(2)	23(2)	60(3)	16(2)	19(2)	1(2)
O(7)	25(2)	25(2)	20(3)	2(2)	11(2)	-2(2)
O(8)	10(2)	45(3)	30(3)	16(2)	6(2)	5(2)
O(9)	14(2)	23(3)	32(3)	7(2)	9(2)	3(2)
O(10)	24(2)	20(2)	63(4)	15(2)	16(2)	-1(2)
O(11)	20(2)	20(2)	24(3)	1(2)	9(2)	-2(2)
O(12)	18(2)	32(3)	31(3)	11(2)	5(2)	0(2)
O(13)	49(3)	32(3)	26(3)	-8(2)	18(2)	-25(2)
O(14)	36(2)	22(2)	17(3)	0(2)	13(2)	-8(2)
O(15)	31(2)	32(2)	22(3)	-3(2)	17(2)	-2(2)
O(16)	20(3)	58(3)	27(3)	-14(2)	8(2)	-12(2)
O(17D)	88(3)	31(3)	47(3)	-10(3)	20(3)	-20(3)
Ca(1)	19(1)	20(1)	23(1)	2(1)	7(1)	-2(1)
Ca(2)	18(1)	20(1)	18(1)	1(1)	8(1)	-1(1)
Ca(3)	17(1)	20(1)	18(1)	-1(1)	8(1)	-3(1)
Ca(4)	18(1)	22(1)	21(1)	3(1)	7(1)	0(1)

Table 6.12: Atomic coordinates ($\times 10^4$) and equivalent isotropic displacement parameters (U_{eq}; $Å^2 \times 10^3$) for **Ca(2,5-pdc)·(H$_2$O)**, compound **6.2**.

	x	y	z	U_{eq}
Ca	5295(1)	1121(1)	7079(1)	19(1)
O(1)	6090(1)	4188(2)	7247(1)	22(1)
C(6)	5362(2)	2509(2)	5205(1)	21(1)
O(3)	5029(2)	1163(2)	3772(1)	34(1)
C(2)	6535(2)	4134(2)	5983(1)	20(1)
N(1)	5636(1)	2968(2)	5889(1)	20(1)
O(2)	7681(1)	5674(2)	6866(1)	27(1)
C(7)	5592(2)	2601(2)	3836(1)	21(1)
C(1)	6798(2)	4708(2)	6760(1)	19(1)
C(5)	5955(2)	3161(2)	4594(1)	21(1)
C(3)	7189(2)	4808(3)	5411(1)	29(1)
O(1W)	3542(1)	2811(2)	6969(1)	46(1)
C(4)	6892(2)	4326(3)	4705(1)	28(1)
O(4)	5888(1)	3631(2)	3324(1)	29(1)

Table 6.13: Anisotropic displacement parameters ($Å^2 \times 10^3$) for **Ca(2,5-pdc)·(H_2O)**; **6.2**

	U^{11}	U^{22}	U^{33}	U^{23}	U^{13}	U^{12}
Ca	22(1)	19(1)	15(1)	-2(1)	1(1)	-3(1)
O(1)	26(1)	22(1)	19(1)	-2(1)	4(1)	-3(1)
C(6)	24(1)	18(1)	22(1)	-2(1)	-3(1)	-2(1)
O(3)	48(1)	31(1)	23(1)	-7(1)	3(1)	-15(1)
C(2)	23(1)	18(1)	19(1)	-1(1)	-1(1)	-1(1)
N(1)	21(1)	20(1)	19(1)	-1(1)	0(1)	0(1)
O(2)	25(1)	33(1)	23(1)	-4(1)	0(1)	-9(1)
C(7)	25(1)	21(1)	17(1)	-1(1)	-1(1)	3(1)
C(1)	21(1)	17(1)	18(1)	0(1)	0(1)	1(1)
C(5)	26(1)	18(1)	18(1)	0(1)	-2(1)	2(1)
C(3)	32(1)	32(1)	21(1)	-2(1)	0(1)	-14(1)
O(1W)	32(1)	37(1)	70(1)	21(1)	18(1)	6(1)
C(4)	35(1)	32(1)	18(1)	2(1)	2(1)	-11(1)
O(4)	46(1)	25(1)	16(1)	2(1)	-2(1)	-2(1)

Table 6.14: Atomic coordinates ($\times 10^4$) and equivalent isotropic displacement parameters (U_{eq}; $Å^2 \times 10^3$) for **Ca(2,5-pdc)·(DMF)**, compound **6.3**.

	x	y	z	U_{eq}
Ca	7570(1)	715(1)	478(1)	19(1)
O(1)	11460(4)	690(2)	574(2)	23(1)
O(2)	14614(4)	1480(3)	1120(2)	33(1)
O(3)	6918(4)	4053(3)	3392(2)	38(1)
N(1)	9663(5)	1809(3)	1759(2)	25(1)
C(5)	9881(6)	3103(4)	2974(2)	24(1)
C(2)	11714(6)	1970(4)	1770(2)	21(1)
C(3)	12908(6)	2708(4)	2361(3)	32(1)
C(7)	8783(6)	2376(4)	2350(2)	26(1)
C(4)	11999(6)	3270(4)	2971(3)	29(1)
O(5D)	8251(6)	2715(3)	-30(2)	59(1)
C(6)	8786(6)	3754(4)	3607(2)	23(1)
C(1)	12693(6)	1327(4)	1097(2)	23(1)
N(2D)	9418(9)	4128(4)	-886(3)	68(2)
C(8D)	9662(10)	3119(5)	-417(4)	58(2)
C(10D)	7356(13)	4755(7)	-1015(5)	94(3)
C(9D)	11069(15)	4576(7)	-1297(5)	105(3)
O(4)	9840(4)	3995(3)	4314(2)	28(1)

Table 6.15: Anisotropic displacement parameters ($Å^2 \times 10^3$) for **Ca(2,5-pdc)·(DMF)**; **6.3**

	U^{11}	U^{22}	U^{33}	U^{23}	U^{13}	U^{12}
Ca	16(1)	20(1)	20(1)	-2(1)	4(1)	-1(1)
O(1)	19(1)	28(2)	23(1)	-8(1)	3(1)	-1(1)
O(2)	19(1)	44(2)	37(2)	-18(1)	9(1)	-4(1)
O(3)	21(2)	51(2)	41(2)	-21(2)	1(1)	5(1)
N(1)	19(2)	28(2)	28(2)	-8(2)	4(1)	-3(1)
C(5)	25(2)	24(2)	23(2)	-5(2)	5(2)	-1(2)
C(2)	20(2)	25(2)	19(2)	-4(2)	2(2)	0(2)
C(3)	18(2)	43(3)	35(2)	-13(2)	6(2)	0(2)
C(7)	17(2)	31(2)	29(2)	-10(2)	4(2)	0(2)
C(4)	24(2)	34(2)	29(2)	-12(2)	5(2)	-2(2)
O(5D)	66(2)	40(2)	65(3)	22(2)	-6(2)	-22(2)
C(6)	22(2)	23(2)	23(2)	-5(2)	4(2)	-5(2)
C(1)	22(2)	21(2)	26(2)	-3(2)	5(2)	2(2)
N(2D)	97(4)	47(3)	59(3)	8(2)	14(3)	-12(3)
C(8D)	84(4)	33(3)	53(3)	0(3)	-3(3)	-6(3)
C(10D)	119(6)	57(4)	94(6)	24(4)	-19(5)	0(4)
C(9D)	163(9)	81(5)	85(5)	1(4)	63(6)	-38(5)
O(4)	25(2)	33(2)	25(2)	-9(1)	0(1)	2(1)

Table 6.16: Atomic coordinates ($\times 10^4$) and equivalent isotropic displacement parameters (U_{eq}; $Å^2 \times 10^3$) for **Ca(2,4-pdc)·(H$_2$O)**, compound **6.4**.

	x	y	z	U_{eq}
C(2)	8016(5)	313(5)	10480(2)	21(1)
C(3)	8946(6)	409(4)	9789(2)	23(1)
C(6)	5630(7)	-709(4)	9294(2)	27(1)
C(7)	4765(6)	-669(4)	10001(2)	26(1)
N(1)	5929(4)	-156(4)	10583(2)	26(1)
O(1)	8220(4)	796(3)	11754(1)	32(1)
O(2)	11303(4)	627(4)	11118(1)	29(1)
O(3)	9167(5)	1348(3)	8109(2)	27(1)
O(4)	9105(5)	-1825(3)	8161(1)	28(1)
O(5M)	1383(5)	-225(5)	12708(2)	38(1)
Ca(1)	4405(1)	245(1)	11915(1)	21(1)
C(1)	9304(7)	627(5)	11169(2)	23(1)
C(4)	7746(6)	-146(5)	9186(2)	21(1)
C(5)	8750(5)	-193(5)	8434(2)	22(1)

Table 6.17: Anisotropic displacement parameters ($Å^2 \times 10^3$) for **Ca(2,4-pdc)·(H$_2$O)**; **6.4**

	U^{11}	U^{22}	U^{33}	U^{23}	U^{13}	U^{12}
C(2)	19(2)	21(2)	24(2)	2(2)	0(2)	3(2)
C(3)	22(3)	24(2)	22(2)	-7(2)	4(2)	-4(2)
C(6)	31(3)	32(2)	19(2)	1(2)	-5(2)	-2(2)
C(7)	23(3)	30(2)	26(2)	-1(2)	-1(2)	-1(2)
N(1)	22(2)	32(2)	24(2)	3(2)	-3(1)	0(2)
O(1)	24(2)	52(2)	20(2)	-6(1)	3(1)	4(1)
O(2)	19(2)	46(2)	22(2)	1(1)	-1(1)	-2(1)
O(3)	38(2)	17(1)	25(2)	5(1)	10(2)	0(1)
O(4)	45(2)	20(1)	20(2)	-1(1)	6(2)	2(1)
O(5M)	31(2)	65(2)	19(2)	10(2)	1(1)	4(2)
Ca(1)	22(1)	21(1)	20(1)	0(1)	-1(1)	-1(1)
C(1)	29(3)	23(2)	18(2)	4(2)	0(2)	1(2)
C(4)	28(2)	16(2)	18(2)	0(2)	5(2)	1(2)
C(5)	21(2)	27(2)	18(2)	0(2)	-3(2)	-1(2)

Table 6.18: Atomic coordinates ($\times 10^4$) and equivalent isotropic displacement parameters (U_{eq}; $Å^2 \times 10^3$) for **Ca(2,4-pdc)·(DMF)**, compound **6.5**.

	x	y	z	U(eq)
Ca	2178(1)	421(1)	4194(1)	17(1)
O(1)	6053(3)	537(1)	4283(2)	23(1)
O(4)	5095(3)	4294(1)	1007(2)	29(1)
O(3)	7692(3)	3468(1)	759(2)	36(1)
C(2)	5485(3)	1710(2)	3000(2)	20(1)
O(2)	8761(2)	1050(1)	3460(2)	29(1)
N	3404(3)	1629(1)	2987(2)	26(1)
C(5)	6020(4)	3619(2)	1152(2)	22(1)
O(4D)	2628(4)	-163(2)	2217(2)	49(1)
C(3)	6326(3)	2348(2)	2421(2)	23(1)
C(6)	2892(4)	2864(2)	1773(3)	32(1)
C(4)	5040(4)	2943(2)	1807(2)	21(1)
C(8D)	4156(6)	-472(2)	1843(3)	42(1)
N(2D)	4051(5)	-893(2)	812(2)	50(1)
C(1)	6899(3)	1043(2)	3644(2)	21(1)
C(7)	2174(4)	2202(2)	2360(3)	37(1)
C(10D)	5936(7)	-1238(3)	436(4)	73(1)
C(9D)	2046(7)	-1075(3)	46(4)	90(2)

Table 6.19: Anisotropic displacement parameters ($Å^2 \times 10^3$) for **Ca(2,4-pdc)·(DMF)**; **6.5**

	U^{11}	U^{22}	U^{33}	U^{23}	U^{13}	U^{12}
Ca	15(1)	15(1)	20(1)	1(1)	5(1)	0(1)
O(1)	19(1)	23(1)	27(1)	11(1)	5(1)	1(1)
O(4)	31(1)	20(1)	35(1)	7(1)	8(1)	6(1)
O(3)	28(1)	31(1)	52(1)	16(1)	21(1)	8(1)
C(2)	17(1)	21(1)	23(1)	1(1)	5(1)	1(1)
O(2)	18(1)	33(1)	40(1)	16(1)	9(1)	5(1)
N	18(1)	25(1)	37(1)	9(1)	9(1)	2(1)
C(5)	20(1)	23(1)	23(1)	5(1)	1(1)	1(1)
O(4D)	60(1)	51(2)	39(1)	-12(1)	22(1)	-4(1)
C(3)	13(1)	25(1)	31(2)	7(1)	4(1)	1(1)
C(6)	21(1)	29(2)	45(2)	12(1)	6(1)	7(1)
C(4)	22(1)	18(1)	24(1)	3(1)	6(1)	2(1)
C(8D)	58(2)	37(2)	32(2)	-1(1)	15(2)	0(2)
N(2D)	64(2)	55(2)	33(2)	-10(1)	15(1)	7(1)
C(1)	17(1)	23(1)	23(1)	2(1)	3(1)	0(1)
C(7)	15(1)	33(2)	64(2)	19(2)	10(1)	4(1)
C(10D)	86(3)	83(3)	52(2)	-11(2)	21(2)	39(2)
C(9D)	76(3)	129(5)	65(3)	-48(3)	8(2)	-6(3)

Table 6.20: Atomic coordinates ($\times 10^4$) and equivalent isotropic displacement parameters (U_{eq}; $Å^2 \times 10^3$) for **Ca(2,6-pdc)**, compound **6.6**.

	x	y	z	U_{eq}
C(1)	9396(1)	6676(1)	3121(1)	19(1)
C(2)	10100(1)	7547(1)	3371(1)	21(1)
C(3)	10575(1)	7743(1)	4336(1)	32(1)
C(4)	11170(1)	8569(1)	4523(2)	44(1)
C(5)	11308(1)	9155(1)	3708(2)	38(1)
C(6)	10836(1)	8895(1)	2734(1)	23(1)
C(7)	11020(1)	9465(1)	1734(1)	22(1)
N	10225(1)	8110(1)	2585(1)	19(1)
O(1)	9459(1)	6084(1)	3498(1)	32(1)
O(2)	8809(1)	6633(1)	2545(1)	28(1)
O(3)	11459(1)	10225(1)	1904(1)	36(1)
O(4)	10727(1)	9109(1)	804(1)	24(1)
Ca	9269(1)	7819(1)	956(1)	16(1)

Table 6.21: Anisotropic displacement parameters ($Å^2 \times 10^3$) for **Ca(2,6-pdc)**; **6.6**

	U^{11}	U^{22}	U^{33}	U^{23}	U^{13}	U^{12}
C(1)	19(1)	17(1)	20(1)	5(1)	5(1)	7(1)
C(2)	19(1)	20(1)	22(1)	4(1)	1(1)	8(1)
C(3)	32(1)	30(1)	27(1)	10(1)	-4(1)	10(1)
C(4)	46(1)	38(1)	28(1)	3(1)	-16(1)	6(1)
C(5)	39(1)	25(1)	31(1)	-1(1)	-10(1)	1(1)
C(6)	25(1)	18(1)	22(1)	1(1)	-1(1)	7(1)
C(7)	21(1)	18(1)	24(1)	2(1)	2(1)	7(1)
N	19(1)	16(1)	21(1)	3(1)	0(1)	8(1)
O(1)	32(1)	19(1)	42(1)	12(1)	4(1)	11(1)
O(2)	19(1)	21(1)	36(1)	3(1)	-4(1)	6(1)
O(3)	44(1)	14(1)	32(1)	5(1)	0(1)	2(1)
O(4)	27(1)	22(1)	19(1)	2(1)	2(1)	8(1)
Ca	15(1)	17(1)	19(1)	-1(1)	0(1)	9(1)

Table 6.22: Atomic coordinates ($\times 10^4$) and equivalent isotropic displacement parameters (U_{eq}; $Å^2 \times 10^3$) for **Ca(3,4-pdc)·(H_2O)**, compound **6.7**.

	x	y	z	U_{eq}
Ca	967(1)	1592(1)	4831(1)	19(1)
O(3)	1400(2)	1549(1)	2039(2)	26(1)
O(4)	2497(2)	1549(2)	101(2)	34(1)
O(2)	544(1)	-697(1)	3857(2)	26(1)
C(1)	1075(2)	-1295(2)	2855(3)	23(1)
O(1)	591(2)	-2068(2)	1666(2)	45(1)
C(6)	2949(2)	-102(2)	2345(2)	22(1)
C(2)	2432(2)	-1132(2)	3121(2)	22(1)
O(5M)	2640(2)	604(2)	6872(2)	42(1)
N	4930(2)	-1090(2)	3368(3)	41(1)
C(7)	2228(2)	1065(2)	1421(3)	23(1)
C(5)	4190(2)	-151(2)	2485(3)	31(1)
C(4)	4429(2)	-2046(3)	4159(3)	39(1)
C(3)	3204(2)	-2108(2)	4042(3)	34(1)

Table 6.23: Anisotropic displacement parameters ($Å^2 \times 10^3$) for **Ca(3,4-pdc)·(H_2O)**; **6.7**

	U^{11}	U^{22}	U^{33}	U^{23}	U^{13}	U^{12}
Ca	20(1)	19(1)	19(1)	0(1)	7(1)	0(1)
O(3)	31(1)	25(1)	25(1)	4(1)	14(1)	6(1)
O(4)	44(1)	39(1)	28(1)	9(1)	21(1)	9(1)
O(2)	27(1)	23(1)	30(1)	-3(1)	14(1)	-2(1)
C(1)	24(1)	22(1)	25(1)	0(1)	10(1)	-3(1)
O(1)	37(1)	55(1)	48(1)	-30(1)	18(1)	-22(1)
C(6)	23(1)	24(1)	18(1)	-3(1)	6(1)	0(1)
C(2)	25(1)	22(1)	20(1)	-4(1)	8(1)	0(1)
O(5M)	37(1)	57(1)	30(1)	-5(1)	2(1)	16(1)
N	26(1)	56(1)	39(1)	-2(1)	6(1)	9(1)
C(7)	26(1)	23(1)	19(1)	-1(1)	7(1)	-2(1)
C(5)	25(1)	35(1)	33(1)	-1(1)	11(1)	-2(1)
C(4)	36(1)	45(1)	34(1)	6(1)	6(1)	20(1)
C(3)	39(1)	28(1)	37(1)	7(1)	14(1)	7(1)

Table 6.24: Atomic coordinates ($\times 10^4$) and equivalent isotropic displacement parameters (U_{eq}; $Å^2 \times 10^3$) for **Ca(3,5-pdc)·(DMF)**, compound **6.8**.

	x	y	z	U_{eq}
Ca(1)	0	0	5000	22(1)
Ca(2)	2992(1)	4196(1)	4228(1)	19(1)
Ca(3)	0	5000	0	30(1)
Ca(4)	-4618(1)	617(1)	-1377(1)	19(1)
O(8)	-2418(2)	1619(1)	-591(1)	29(1)
O(2)	2524(2)	3116(1)	5183(1)	31(1)
O(9)	5239(2)	4461(1)	4304(1)	32(1)
O(6)	-3164(2)	132(2)	2264(1)	38(1)
O(5)	-1358(2)	439(1)	3638(1)	36(1)
O(4)	8402(2)	4606(2)	8369(2)	46(1)
O(3)	7269(2)	5031(2)	7046(2)	49(1)
O(1)	1600(2)	1650(1)	5492(1)	38(1)
C(9)	-1222(2)	1384(2)	2440(2)	21(1)
N(2)	717(2)	2899(2)	2897(1)	27(1)
C(11)	-1015(2)	2252(2)	1184(2)	23(1)
C(14)	13(2)	2119(2)	3133(2)	23(1)
O(7)	-938(2)	3251(1)	23(1)	41(1)
C(4)	6147(2)	3592(2)	7439(2)	25(1)
C(3)	4959(2)	3475(2)	6696(2)	24(1)
C(2)	3852(2)	2624(2)	6492(2)	21(1)
C(13)	193(2)	2958(2)	1938(2)	27(1)
C(10)	-1729(2)	1447(2)	1444(2)	24(1)
C(1)	2554(2)	2443(2)	5658(2)	22(1)
N(1)	5129(2)	2012(2)	7774(2)	32(1)

O(12)	4417(2)	741(1)	741(1)	38(1)
O(10)	3596(2)	2986(2)	3291(2)	46(1)
C(15)	4687(2)	3666(2)	3533(2)	28(1)
O(11)	5403(2)	1680(2)	-36(2)	47(1)
C(18)	5518(2)	2577(2)	1487(2)	30(1)
C(16)	5342(2)	3565(2)	2857(2)	28(1)
C(7)	3985(2)	1908(2)	7050(2)	28(1)
C(6)	6189(2)	2849(2)	7968(2)	30(1)
C(8)	-1968(2)	584(2)	2809(2)	24(1)
O(16D)	-4599(3)	-186(2)	-2908(2)	61(1)
C(19)	5077(2)	1580(2)	667(2)	29(1)
C(5)	7373(2)	4482(2)	7642(2)	30(1)
C(12)	-1500(2)	2387(2)	119(2)	25(1)
C(17)	4933(2)	2620(2)	2137(2)	28(1)
O(13D)	-755(2)	541(2)	6180(2)	59(1)
O(14D)	1824(2)	5122(2)	4654(2)	61(1)
N(3)	6914(3)	4403(2)	2287(2)	54(1)
C(20)	6495(3)	3483(2)	1596(2)	45(1)
C(21)	6336(3)	4429(2)	2903(2)	40(1)
O(15D)	1313(3)	4489(2)	-613(2)	73(1)
N(7D)	-5604(3)	-1158(2)	-4561(2)	58(1)
C(24D)	1062(4)	5487(3)	4155(4)	71(1)
N(5D)	774(3)	6211(2)	4512(3)	67(1)
C(33D)	-1017(4)	21(3)	6744(3)	61(1)
N(4D)	-1031(4)	403(3)	7603(2)	75(1)
C(27D)	1983(4)	4180(4)	-895(3)	72(1)
N(6D)	2673(5)	3690(5)	-471(4)	117(2)
C(26D)	-179(5)	6586(4)	3993(6)	123(2)

C(22D)	-1323(6)	-259(5)	8231(4)	107(2)
C(23D)	-748(9)	1524(5)	7963(5)	168(4)
C(25D)	1430(7)	6712(5)	5641(5)	113(2)
C(28D)	2562(6)	3386(5)	457(5)	113
C(29D)	3429(6)	3315(5)	-870(5)	113
C(31D)	-4497(10)	-1360(8)	-4523(5)	113(3)
C(30D)	-5596(5)	-590(4)	-3790(3)	50(1)
C(32D)	-6744(7)	-1542(6)	-5612(4)	93(3)
C(32')	-5810(17)	-2011(13)	-5249(13)	93
C(30')	-4637(17)	-836(13)	-3572(13)	93
C(31')	-6583	-676	-4673	93

Table 6.25: Anisotropic displacement parameters ($Å^2 \times 10^3$) for **Ca(3,5-pdc)·(DMF)**; **6.8**

	U^{11}	U^{22}	U^{33}	U^{23}	U^{13}	U^{12}
Ca(1)	16(1)	21(1)	21(1)	10(1)	5(1)	1(1)
Ca(2)	17(1)	18(1)	18(1)	8(1)	5(1)	4(1)
Ca(3)	18(1)	29(1)	28(1)	18(1)	0(1)	-1(1)
Ca(4)	18(1)	17(1)	16(1)	6(1)	5(1)	3(1)
O(8)	21(1)	31(1)	22(1)	10(1)	2(1)	1(1)
O(2)	23(1)	31(1)	30(1)	20(1)	3(1)	3(1)
O(9)	29(1)	31(1)	26(1)	-2(1)	11(1)	6(1)
O(6)	18(1)	44(1)	35(1)	22(1)	3(1)	-3(1)
O(5)	25(1)	39(1)	30(1)	24(1)	3(1)	2(1)
O(4)	22(1)	45(1)	40(1)	27(1)	-8(1)	-7(1)
O(3)	26(1)	49(1)	44(1)	36(1)	-3(1)	-8(1)
O(1)	20(1)	29(1)	44(1)	21(1)	1(1)	-4(1)
C(9)	16(1)	22(1)	23(1)	10(1)	6(1)	3(1)
N(2)	20(1)	26(1)	22(1)	10(1)	3(1)	-2(1)
C(11)	19(1)	23(1)	21(1)	10(1)	5(1)	3(1)
C(14)	17(1)	25(1)	21(1)	10(1)	4(1)	2(1)
O(7)	37(1)	32(1)	30(1)	19(1)	2(1)	-6(1)
C(4)	20(1)	22(1)	22(1)	10(1)	3(1)	1(1)
C(3)	21(1)	21(1)	23(1)	12(1)	5(1)	4(1)
C(2)	18(1)	20(1)	21(1)	8(1)	5(1)	4(1)
C(13)	20(1)	26(1)	25(1)	14(1)	5(1)	-1(1)
C(10)	16(1)	23(1)	22(1)	9(1)	3(1)	2(1)
C(1)	19(1)	20(1)	22(1)	8(1)	6(1)	2(1)
N(1)	22(1)	28(1)	34(1)	20(1)	4(1)	2(1)
O(12)	54(1)	22(1)	37(1)	11(1)	16(1)	16(1)
O(10)	37(1)	34(1)	56(1)	-7(1)	29(1)	-2(1)
C(15)	28(1)	24(1)	28(1)	3(1)	13(1)	8(1)
O(11)	67(1)	39(1)	38(1)	4(1)	34(1)	17(1)
C(18)	36(1)	26(1)	28(1)	7(1)	16(1)	12(1)
C(16)	29(1)	26(1)	27(1)	3(1)	13(1)	8(1)
C(7)	20(1)	23(1)	31(1)	15(1)	6(1)	1(1)

C(6)	20(1)	29(1)	30(1)	17(1)	1(1)	2(1)
C(8)	20(1)	23(1)	23(1)	11(1)	6(1)	2(1)
O(16D)	83(2)	67(2)	37(1)	5(1)	34(1)	29(1)
C(19)	37(1)	27(1)	27(1)	8(1)	13(1)	18(1)
C(5)	20(1)	29(1)	25(1)	15(1)	1(1)	-1(1)
C(12)	18(1)	27(1)	24(1)	13(1)	5(1)	4(1)
C(17)	30(1)	24(1)	28(1)	6(1)	14(1)	8(1)
O(13D)	69(2)	79(2)	54(1)	28(1)	42(1)	39(1)
O(14D)	59(1)	64(2)	70(2)	14(1)	25(1)	46(1)
N(3)	63(2)	35(1)	56(2)	-3(1)	43(1)	-4(1)
C(20)	56(2)	35(1)	47(2)	5(1)	38(2)	7(1)
C(21)	45(2)	26(1)	40(1)	-2(1)	25(1)	0(1)
O(15D)	66(2)	90(2)	91(2)	42(2)	47(2)	43(2)
N(7D)	71(2)	54(2)	43(2)	1(1)	28(1)	17(1)
C(24D)	50(2)	59(2)	98(3)	13(2)	25(2)	27(2)
N(5D)	48(2)	57(2)	115(3)	33(2)	42(2)	34(1)
C(33D)	70(2)	85(3)	59(2)	31(2)	41(2)	50(2)
N(4D)	77(2)	98(3)	51(2)	21(2)	39(2)	24(2)
C(27D)	67(2)	90(3)	72(3)	42(2)	37(2)	32(2)
N(6D)	124(4)	188(5)	93(3)	54(3)	50(3)	123(4)
C(26D)	64(3)	75(3)	219(7)	43(4)	35(4)	48(3)
C(22D)	114(4)	159(5)	84(3)	67(4)	68(3)	56(4)
C(23D)	253(10)	87(4)	119(5)	-24(4)	132(6)	-30(5)
C(25D)	153(6)	108(4)	114(5)	23(3)	75(4)	80(4)
C(31D)	156(8)	174(9)	59(4)	29(5)	48(5)	129(8)
C(30D)	51(3)	61(3)	34(2)	3(2)	24(2)	15(2)
C(32D)	87(5)	99(5)	43(3)	-10(3)	23(3)	-5(4)

Table 6.26: Atomic coordinates ($\times 10^4$) and equivalent isotropic displacement parameters (U_{eq}; $Å^2 \times 10^3$) for **Ca(3,5-pdc)·(H_2O)**, compound **6.9**.

	x	y	z	U(eq)
C(1)	-502(6)	4095(6)	6024(9)	29(1)
C(2)	-578(6)	5199(5)	5956(10)	22(1)
C(3)	-1878(6)	5720(4)	6007(9)	23(2)
C(4)	577(8)	5760(2)	5832(12)	21(1)
C(5)	1714(7)	5203(5)	5791(9)	20(1)
C(6)	3031(6)	5757(5)	5772(9)	22(2)
C(7)	1662(5)	4121(5)	5773(9)	22(1)
N	555(7)	3556(2)	5907(13)	25(1)
O(1)	-2898(3)	5173(4)	5902(8)	33(1)
O(2)	-1926(5)	6719(4)	6124(7)	31(1)
O(3)	3063(5)	6717(5)	5658(7)	30(1)
O(4)	4038(4)	5151(4)	5857(8)	33(1)
O(5M)	-20(5)	1734(4)	2670(8)	31(1)
O(6M)	1193(6)	1743(4)	9100(9)	34(1)
Ca	572(2)	1581(1)	5888(4)	21(1)

Table 6.27: Anisotropic displacement parameters ($Å^2 \times 10^3$) for **Ca(3,5-pdc)·(H_2O)**; **6.9**

	U^{11}	U^{22}	U^{33}	U^{23}	U^{13}	U^{12}
C(2)	11(2)	18(2)	37(2)	-2(1)	8(1)	3(1)
C(3)	22(3)	17(4)	32(3)	-5(3)	10(2)	3(3)
C(6)	13(2)	22(4)	33(3)	-1(3)	8(2)	-3(3)
C(7)	6(1)	10(2)	51(2)	3(1)	10(1)	4(1)
N	15(1)	17(1)	45(1)	-11(3)	11(1)	-13(2)
O(1)	10(2)	23(2)	69(4)	-1(2)	15(2)	8(2)
O(2)	24(3)	11(2)	60(4)	0(3)	15(3)	1(2)
O(3)	15(3)	23(2)	54(3)	6(3)	12(3)	0(2)
O(4)	25(3)	16(2)	62(4)	11(2)	21(3)	11(2)
O(5M)	36(2)	26(2)	32(3)	-1(3)	12(2)	0(2)
O(6M)	33(2)	26(2)	38(3)	1(3)	4(2)	-4(2)
Ca	15(1)	14(1)	34(1)	2(1)	9(1)	0(1)

Table 6.28: Selected inter-atomic distances (Å) for compounds **6.1-6.9**

Compound	Calcium Coordination Number	Ca – N bond length	Ca – O bond length		
			Shortest	Longest	Average
6.1 (Ca1)	7	2.581(5)	2.266(4)	2.464(5)	2.38 (8)
6.1 (Ca2)	7	2.569(4)	2.322(4)	2.440(4)	2.40(4)
6.1 (Ca3)	7	2.543(5)	2.325(4)	2.486(4)	2.40(6)
6.1 (Ca4)	6	2.566(5)	2.269(4)	2.352(4)	2.32(3)
6.2	7	2.620(2)	2.343(1)	2.474(1)	2.40 (6)
6.3	8	2.563(3)	2.364(3)	2.557(3)	2.462(6)
6.4	8	2.628(3)	2.356(2)	2.689(3)	2.46(13)
6.5	8	2.574(2)	2.344(2)	2.612(2)	2.46 (8)
6.6	7	2.493(1)	2.273(1)	2.691(1)	2.44(16)
6.7	7	-	2.290(2)	2.503(2)	2.41(8)
6.8 (Ca1)	6	-	2.305(2)	2.373(2)	2.35(4)
6.8 (Ca2)	7	2.564(2)	2.263(2)	2.574(2)	2.39(12)
6.8 (Ca3)	6	-	2.302(2)	2.368(2)	2.33(3)
6.8 (Ca4)	6	2.494(2)	2.270(2)	2.378(2)	2.30(4)
6.9	7	2.503(2)	2.331(6)	2.535(5)	2.41(9)

Table 6.29: Solvent dependent formation of calcium MOFs (Ca-2,5-pdc system)

Solvent System	Composition of the solvent	Ca-salt used in synthesis	
		$CaCl_2$	$Ca(NO_3)_2 \cdot 4H_2O$
		Resulting compound	
DMF	Pure	**6.3**	**6.3**
Ethanol	Pure	**6.2**	**6.2**
Water	Pure	**6.2**	**-**
Methanol	Pure	**-**	**-**
DMF/water	1:1	**6.2**	**6.2**
DMF/Ethanol	1:1	**6.3**	**6.1**
DMF/Methanol	1:1	**6.2**	**6.2**
Methanol/Ethanol	1:1	**6.2**	**6.2**
DMF/ethanol/water	2:1:1	**6.2**	**6.2**
DMF/methanol/water	2:1:1	**6.2**	**6.2**
DMF/methanol/ethanol	1:1:1	**6.2**	**6.2**
Methanol/Ethanol/Water	1:1:1	**6.2**	**6.2**

Chapter 7

Conclusions

In conclusion, we used multiple analytical tools to understand, at the molecular level, the mechanism of gas adsorption on three metal organic frameworks. For the study we focused on MOFs with no open metal sites, and found that organic linkers provide strong adsorption sites for gases such as CO_2 or small hydrocarbons. Further, we discovered that MOFs with no open metal sites are active for the CO_2/N_2 separation in the presence of water. Finally, we observed that small pores and multiple adsorption sites lead to selective adsorption of C_2 hydrocarbons over methane. These results will guide further efforts in a design of gas-selective porous solids.

The purpose of this project was to gain a deeper understanding of the mechanism of gas adsorption in metal organic frameworks (MOFs). MOFs, a new class of porous materials, are advantageous over currently used alakolamine solutions or zeolites for CO_2 sequestration or hydrocarbon separation. Ca-based MOFs, which were a primary target of this research, present advantages such as Earth abundance of Ca metal, leading to low cost of MOFs production, low toxicity and ease of synthesis.

Herein we focused on structural studies of gas binding sites within a MOF pore space. Crystallographic determination of mechanisms of gas adsorption in crystalline MOFs contribute to our understanding of specific interactions responsible for the enhanced adsorption and selectivity, and can assist with identifying new synthetic targets for various gas separation processes. It requires high quality XRD data to precisely identify sorption sites, and to augment a still limited number of structural reports of gases adsorbed on porous MOFs. Identifying the connection between the geometry and selectivity will also open up new streams of research.

Our observations suggest that a new structural feature - a "π-pocket" - formed by specific geometrical organization of the organic linker, provides structural advantages for improving the efficiency of the gas separation. CO_2 adsorption on the "π-pocket" was discovered in a Ca-based MOF – **Ca(sdb)**. **Ca(sdb)** is a novel, porous MOF, which does not contain open metal sites or additional functionalities. **Ca(sdb)** adsorbs CO_2 with high binding energy and is selective for CO_2 over N_2 (45). We postulate that CO_2-π interactions are responsible for the high CO_2/N_2 sorption selectivity, even in the presence of water in the gas stream. A better understanding of interactions between adsorbed gases and the "π-pockets" will be applicable to a wide range of materials proposed for carbon capture.

To confirm the discovered mechanism of the gas adsorption on the "π-pocket", as well as to characterize how metal node influences CO_2 affinity, CO_2/N_2 selectivity and adsorption mechanism, we synthesized the Cd-based analogue and studied its' CO_2 adsorption performance. We found that different topology of the network of **Cd(sdb)** leads to lower surface area, CO_2 uptake and CO_2/N_2 selectivity than in the case of **Ca(sdb)**. However, as **Cd(sdb)**, similarly to **Ca(sdb)**, do not contain open metal sites, it is active for the CO_2 adsorption in the presence of water. We postulate that CO_2 adsorbs on the "π-pockets" inside the channels of **Cd(sdb)** as suggested by *in situ* XRD results. Further, the energy of CO_2 adsorption on both **Ca(sdb)** and **Cd(sdb)** has similar values (31 vs. 27 kJ/mol), which supports the hypothesis of adsorption on the "π-pockets".

We further characterized adsorption mechanisms of ethane, ethylene and acetylene (C_2H_n) on **Ca(sdb)** and a new, porous Ca-based MOF: **Ca(tcpb)**. We found that both materials are selective towards C_2H_n hydrocarbons over methane with the maximum C_2/C_1 selectivity of 74 for C_2H_6/CH_4 in **Ca(sdb)**. We used single crystal X-ray diffraction to study crystal structures

of C_2H_n-loaded **Ca(sdb)** and **Ca(tcpb)** and found that small pore sizes (~5-6 Å) lead to a strong ordering of gas molecules. The **Ca(sdb)** framework behaves like a trap towards the C_2 hydrocarbons providing strong adsorption sites, through C-H$^{\cdots}\pi$ interactions with four phenyl rings. Adsorbate-adsorbent interactions in **Ca(tcpb)** appear to be similar to the **Ca(sdb)** case, except in channels where additional polarizing -OH groups and oxygen atoms serve as strong adsorption sites for C_2H_n, through a C-H$^{\cdots}$O interaction. Those single crystal data are confirmed by the experimental gas adsorption and XRD-DSC studies.

Additionally to structural gas adsorption studies we performed an exploratory solvothermal synthesis of new Ca-based MOFs based on 5 different pyridinediacrboxylate isomers. Pyridinediacrboxylic acid forms six different structural isomers, where a mutual orientation between functional groups varies between the isomers, thereby facilitating systematic studies of the relationships between ligand geometries and resultant MOFs' structural topologies in a relatively simple system. Synthesized MOFs show diverse structural topologies, depending on the ligand geometry and coordinated solvent molecules, with inorganic connectivity motifs ranging from isolated octahedra to infinite chains, a layer and a three dimensional dense framework. We found out that the motif formed depends on the orientation of the carboxylates with respect to the pyridyl nitrogen group and the nature of the coordinated solvent. Finally, as-synthesized and desolvated networks show structural transformations to hydrated phases in the presence of water through dissolution/reformation pathways involving calcium coordination spheres.

References

1. Earth System Research Laboratory. **2012.** http://www.esrl.noaa.gov

2. IPCC, Mitigation of Climate Change. Contribution of Working Group III to the Fifth Assessment Report of the Intergovernmental Panel on Climate Change. Cambridge, United Kingdom and New York, USA **2014**.

3. U.S. Energy Information Administration. **2015.** http://www.eia.gov/electricity

4. Metz, B. D.; de Connick, H.; Loos, M.; Meyer, L., Intergovernmental Panel on Climate Change. Special Report on Carbon Dioxide Capture and Storage, Cambridge University Press, Cambridge, **2005.**

5. Sumida, K.; Rogow, D. L.; Mason, J. A.; McDonald, T. M.; Bloch, E. D.; Herm, Z. R.; Bae, T.-H.; Long, J. R., Carbon Dioxide Capture in Metal-Organic Frameworks. *Chem. Rev.* **2011,** *112* (2), 724-781.

6. Li, J. R.; Ma, Y. G.; McCarthy, M. C.; Sculley, J.; Yu, J. M.; Jeong, H. K.; Balbuena, P. B.; Zhou, H. C., Carbon dioxide capture-related gas adsorption and separation in metal-organic frameworks. *Coord. Chem. Rev.* **2011,** *255* (15-16), 1791-1823.

7. Figueroa, J. D.; Fout, T.; Plasynski, S.; McIlvried, H.; Srivastava, R. D., Advances in CO_2 capture technology - The U.S. Department of Energy's Carbon Sequestration Program. *Int. J. of Greenh. Gas Control* **2008,** *2* (1), 9-20.

8. (a) Kusakabe, K.; Kuroda, T.; Murata, A.; Morooka, S., Formation of a Y-Type Zeolite Membrane on a Porous α-Alumina Tube for Gas Separation. *Ind. Eng. Chem. Res.* **1997,** *36* (3), 649-655;

(b) Cavenati, S.; Grande, C. A.; Rodrigues, A. E., Adsorption Equilibrium of Methane, Carbon Dioxide, and Nitrogen on Zeolite 13X at High Pressures. *J. Chem. Eng. Data* **2004,** *49* (4), 1095-1101;

(c) Himeno, S.; Tomita, T.; Suzuki, K.; Yoshida, S., Characterization and selectivity for methane and carbon dioxide adsorption on the all-silica DD3R zeolite. *Microporous Mesoporous Mater.* **2007,** *98* (1–3), 62-69;

(d) Choi, S.; Drese, J. H.; Jones, C. W., Adsorbent Materials for Carbon Dioxide Capture from Large Anthropogenic Point Sources. *ChemSusChem* **2009,** *2* (9), 796-854.

9. (a) Li, G.; Xiao, P.; Webley, P.; Zhang, J.; Singh, R.; Marshall, M., Capture of CO_2 from high humidity flue gas by vacuum swing adsorption with zeolite 13X. *Adsorption* **2008,** *14* (2-3), 415-422;

(b) Li, G.; Xiao, P.; Webley, P. A.; Zhang, J.; Singh, R., Competition of CO_2/H_2O in adsorption based CO_2 capture. *Energy Procedia* **2009,** *1* (1), 1123-1130.

10. Cao, C.; Chung, T.-S.; Liu, Y.; Wang, R.; Pramoda, K., Chemical cross-linking modification of 6FDA-2, 6-DAT hollow fiber membranes for natural gas separation. *J. Membr. Sci.* **2003,** *216* (1), 257-268.

11. Duan, X.; Zhang, Q.; Cai, J.; Cui, Y.; Wu, C.; Yang, Y.; Qian, G., A new microporous metal-organic framework with potential for highly selective separation methane from acetylene, ethylene and ethane at room temperature. *Microporous Mesoporous Mater.* **2014,** *190*, 32-37.

12. Magnowski, N.; Avila, A.; Lin, C.; Shi, M.; Kuznicki, S., Extraction of ethane from natural gas by adsorption on modified ETS-10. *Chem. Eng. Sci.* **2011,** *66* (8), 1697-1701.

13. Banerjee, D.; Liu, J.; Thallapally, P. K., Separation of C_2 Hydrocarbons by Porous Materials: Metal Organic Frameworks as Platform. *Comments Inorg. Chem.* **2014,** (ahead-of-print), 1-21.

14. Herm, Z. R.; Bloch, E. D.; Long, J. R., Hydrocarbon Separations in Metal-Organic Frameworks. *Chem. Mater.* **2013,** *26* (1), 323-338.

15. Jarvelin, H.; Fair, J. R., Adsorptive separation of propylene-propane mixtures. *Ind. Eng. Chem. Res.* **1993,** *32* (10), 2201-2207.

16. Matsufuji, T.; Nishiyama, N.; Matsukata, M.; Ueyama, K., Separation of butane and xylene isomers with MFI-type zeolitic membrane synthesized by a vapor-phase transport method. *J. Membr. Sci.* **2000,** *178* (1), 25-34.

17. Li, B.; Zhang, Y.; Krishna, R.; Yao, K.; Han, Y.; Wu, Z.; Ma, D.; Shi, Z.; Pham, T.; Space, B.; Liu, J.; Thallapally, P. K.; Liu, J.; Chrzanowski, M.; Ma, S., Introduction of π-Complexation into Porous Aromatic Framework for Highly Selective Adsorption of Ethylene over Ethane. *J. Amer. Chem. Soc.* **2014,** *136* (24), 8654-8660.

18. (a) James, S. L., Metal-organic frameworks. *Chem. Soc. Rev.* **2003,** *32* (5), 276-288;

(b) Zhou, H.-C.; Long, J. R.; Yaghi, O. M., Introduction to Metal-Organic Frameworks. *Chem. Rev.* **2012,** *112* (2), 673-674.

19. Miller, S. R.; Wright, P. A.; Devic, T.; Serre, C.; Ferey, G.; Llewellyn, P. L.; Denoyel, R.; Gaberova, L.; Filinchuk, Y., Single Crystal X-ray Diffraction Studies of Carbon Dioxide and Fuel-Related Gases Adsorbed on the Small Pore Scandium Terephthalate Metal Organic Framework. *Langmuir* **2009,** *25* (6), 3618-3626.

20. (a) Cohen, S. M., Postsynthetic Methods for the Functionalization of Metal-Organic Frameworks. *Chem. Rev.* **2011,** *112* (2), 970-1000;

(b) Stock, N.; Biswas, S., Synthesis of Metal-Organic Frameworks (MOFs): Routes to Various MOF Topologies, Morphologies, and Composites. *Chem. Rev.* **2011,** *112* (2), 933-969.

21. (a) Suh, M. P.; Park, H. J.; Prasad, T. K.; Lim, D.-W., Hydrogen storage in metal-organic frameworks. *Chem. Rev.* **2011,** *112* (2), 782-835;

(b) Kreno, L. E.; Leong, K.; Farha, O. K.; Allendorf, M.; Van Duyne, R. P.; Hupp, J. T., Metal-organic framework materials as chemical sensors. *Chem. Rev.* **2011,** *112* (2), 1105-1125;

(c) He, Y.; Zhou, W.; Qian, G.; Chen, B., Methane storage in metal-organic frameworks. *Chem. Soc. Rev.* **2014,** *43* (16), 5657-5678;

(d) Lee, J.; Farha, O. K.; Roberts, J.; Scheidt, K. A.; Nguyen, S. T.; Hupp, J. T., Metal-organic framework materials as catalysts. *Chem. Soc. Rev.* **2009,** *38* (5), 1450-1459;

(e) Ramaswamy, P.; Wong, N. E.; Shimizu, G. K. H., MOFs as proton conductors - challenges and opportunities. *Chem. Soc. Rev.* **2014,** *43* (16), 5913-5932;

(f) Zhang, T.; Lin, W., Metal-organic frameworks for artificial photosynthesis and photocatalysis. *Chem. Soc. Rev.* **2014,** *43* (16), 5982-5993.

22. Li, J.-R.; Sculley, J.; Zhou, H.-C., Metal-Organic Frameworks for Separations. *Chem. Rev.* **2012,** *112* (2), 869-932.

23. (a) Deria, P.; Mondloch, J. E.; Karagiaridi, O.; Bury, W.; Hupp, J. T.; Farha, O. K., Beyond post-synthesis modification: evolution of metal-organic frameworks via building block replacement. *Chem. Soc. Rev.* **2014,** *43* (16), 5896-5912;

(b) Evans, J. D.; Sumby, C. J.; Doonan, C. J., Post-synthetic metalation of metal-organic frameworks. *Chem. Soc. Rev.* **2014,** *43* (16), 5933-5951.

24. Noro, S.-i.; Mizutani, J.; Hijikata, Y.; Matsuda, R.; Sato, H.; Kitagawa, S.; Sugimoto, K.; Inubushi, Y.; Kubo, K.; Nakamura, T., Porous coordination polymers with ubiquitous and biocompatible metals and a neutral bridging ligand. *Nat Commun* **2015,** *6*.

25. Johnson, J. A.; Chen, S.; Reeson, T. C.; Chen, Y.-S.; Zeng, X. C.; Zhang, J., Direct X-ray Observation of Trapped CO_2 in a Predesigned Porphyrinic Metal-Organic Framework. *Chem. Eur. J.* **2014,** *20* (25), 7632-7637.

26. Krishna, R.; van Baten, J. M., A comparison of the CO_2 capture characteristics of zeolites and metal–organic frameworks. *Sep. Purif. Technol.* **2012,** *87* (0), 120-126.

27. (a) Kizzie, A. C.; Wong-Foy, A. G.; Matzger, A. J., Effect of Humidity on the Performance of Microporous Coordination Polymers as Adsorbents for CO_2 Capture. *Langmuir* **2011,** *27* (10), 6368-6373;

(b) Liu, J.; Wang, Y.; Benin, A. I.; Jakubczak, P.; Willis, R. R.; LeVan, M. D., CO_2/H_2O Adsorption Equilibrium and Rates on Metal-Organic Frameworks: HKUST-1 and Ni/DOBDC. *Langmuir* **2010,** *26* (17), 14301-14307.

28. Fracaroli, A. M.; Furukawa, H.; Suzuki, M.; Dodd, M.; Okajima, S.; Gándara, F.; Reimer, J. A.; Yaghi, O. M., Metal-Organic Frameworks with Precisely Designed Interior for Carbon Dioxide Capture in the Presence of Water. *J. Amer. Chem. Soc.* **2014,** *136* (25), 8863-8866.

29. Wright, P. A.; Thomas, J. M.; Cheetham, A. K.; Nowak, A. K., Localizing active sites in zeolitic catalysts: neutron powder profile analysis and computer simulation of deuteropyridine bound to gallozeolite-L. *Nature* **1985,** *318* (6047), 611-614.

30. (a) Dietzel, P. D. C.; Johnsen, R. E.; Fjellvag, H.; Bordiga, S.; Groppo, E.; Chavan, S.; Blom, R., Adsorption properties and structure of CO_2 adsorbed on open coordination sites of metal-organic framework Ni_2(dhtp) from gas adsorption, IR spectroscopy and X-ray diffraction. *Chem. Commun.* **2008,** (41);

(b) Lin, J. B.; Xue, W.; Zhang, J. P.; Chen, X. M., An ionic porous coordination framework exhibiting high CO_2 affinity and CO_2/CH_4 selectivity. *Chem. Commun.* **2011,** *47* (3), 926-928;

(c) Stavitski, E.; Pidko, E. A.; Couck, S.; Remy, T.; Hensen, E. J. M.; Weckhuysen, B. M.; Denayer, J.; Gascon, J.; Kapteijn, F., Complexity behind CO_2 Capture on NH_2-MIL-53(Al). *Langmuir* **2011,** *27* (7), 3970-3976;

(d) Carrington, E. J.; Vitorica-Yrezabal, I. J.; Brammer, L., Crystallographic studies of gas sorption in metal-organic frameworks. *Acta Crystallogr., Sect. B: Struct. Sci.* **2014,** *70* (3), 0-0;

(e) Vaidhyanathan, R.; Iremonger, S. S.; Shimizu, G. K. H.; Boyd, P. G.; Alavi, S.; Woo, T. K., Direct Observation and Quantification of CO_2 Binding Within an Amine-Functionalized Nanoporous Solid. *Science* **2010,** *330* (6004), 650-653.

31. Serre, C.; Bourrelly, S.; Vimont, A.; Ramsahye, N. A.; Maurin, G.; Llewellyn, P. L.; Daturi, M.; Filinchuk, Y.; Leynaud, O.; Barnes, P.; Ferey, G., An explanation for the very large breathing effect of a metal-organic framework during CO_2 adsorption. *Adv. Mater.* **2007,** *19* (17), 2246.

32. (a) Nijem, N.; Wu, H.; Canepa, P.; Marti, A.; Balkus Jr, K. J.; Thonhauser, T.; Li, J.; Chabal, Y. J., Tuning the gate opening pressure of metal-organic frameworks (MOFs) for the selective separation of hydrocarbons. *J. Amer. Chem. Soc.* **2012,** *134* (37), 15201-15204;

(b) Gücüyener, C.; van den Bergh, J.; Gascon, J.; Kapteijn, F., Ethane/Ethene Separation Turned on Its Head: Selective Ethane Adsorption on the Metal-Organic Framework ZIF-7 through a Gate-Opening Mechanism. *J. Amer. Chem. Soc.* **2010,** *132* (50), 17704-17706.

33. (a) Farrusseng, D.; Daniel, C.; Gaudillère, C.; Ravon, U.; Schuurman, Y.; Mirodatos, C.; Dubbeldam, D.; Frost, H.; Snurr, R. Q., Heats of Adsorption for Seven Gases in Three Metal−Organic Frameworks: Systematic Comparison of Experiment and Simulation. *Langmuir* **2009,** *25* (13), 7383-7388;

(b) Jiang, J.; Sandler, S. I., Monte Carlo simulation for the adsorption and separation of linear and branched alkanes in IRMOF-1. *Langmuir* **2006,** *22* (13), 5702-5707.

34. Munch, A. S.; Mertens, F. O. R. L., HKUST-1 as an open metal site gas chromatographic stationary phase-capillary preparation, separation of small hydrocarbons and electron donating compounds, determination of thermodynamic data. *J. Mater. Chem.* **2012,** *22* (20), 10228-10234.

35. Bloch, E. D.; Queen, W. L.; Krishna, R.; Zadrozny, J. M.; Brown, C. M.; Long, J. R., Hydrocarbon Separations in a Metal-Organic Framework with Open Iron(II) Coordination Sites. *Science* **2012,** *335* (6076), 1606-1610.

36. Matsuda, R.; Kitaura, R.; Kitagawa, S.; Kubota, Y.; Belosludov, R. V.; Kobayashi, T. C.; Sakamoto, H.; Chiba, T.; Takata, M.; Kawazoe, Y., Highly controlled acetylene accommodation in a metal-organic microporous material. *Nature* **2005,** *436* (7048), 238-241.

37. Alaerts, L.; Kirschhock, C. E. A.; Maes, M.; van der Veen, M. A.; Finsy, V.; Depla, A.; Martens, J. A.; Baron, G. V.; Jacobs, P. A.; Denayer, J. F. M.; De Vos, D. E., Selective Adsorption and Separation of Xylene Isomers and Ethylbenzene with the Microporous Vanadium(IV) Terephthalate MIL-47. *Angew. Chem. Int. Ed.* **2007,** *46* (23), 4293-4297.

38. (a) Samsonenko , D. G.; Kim, H.; Sun, Y.; Kim, G.-H.; Lee, H.-S.; Kim, K., Microporous Magnesium and Manganese Formates for Acetylene Storage and Separation. *Chemistry – An Asian Journal* **2007,** *2* (4), 484-488;

(b) Kim, H.; Samsonenko, D. G.; Das, S.; Kim, G.-H.; Lee, H.-S.; Dybtsev, D. N.; Berdonosova, E. A.; Kim, K., Methane Sorption and Structural Characterization of the Sorption Sites in $Zn_2(bdc)_2(dabco)$ by Single Crystal X-ray Crystallography. *Chem. Asian J.* **2009,** *4* (6), 886-891.

39. Zhang, J.-P.; Chen, X.-M., Optimized Acetylene/Carbon Dioxide Sorption in a Dynamic Porous Crystal. *J. Amer. Chem. Soc.* **2009,** *131* (15), 5516-5521.

40. Banerjee, D.; Parise, J. B., Recent Advances in s-Block Metal Carboxylate Networks. *Cryst. Growth Des.* **2011,** *11* (10), 4704-4720.

41. Pungor, E.; Horvai, G., A practical guide to instrumental analysis. CRC press: **1994**.

42. Lowell, S., Characterization of porous solids and powders: surface area, pore size and density. Springer Science & Business Media: **2004**; Vol. 16.

43. Brunauer, S.; Emmet, P.; Teller, F., Surface area measurements of activated carbons, silica gel and other adsorbents. *J. Am. Chem. Soc.* **1938,** *60*, 309-319.

44. Sing, K. S. W., Adsorption methods for the characterization of porous materials. *Adv. Colloid Interface Sci.* **1998,** *76–77* (0), 3-11.

45. Myers, A. L.; Prausnitz, J. M., Thermodynamics of mixed-gas adsorption. *AIChE Journal* **1965,** *11* (1), 121-127.

46. Cessford, N. F.; Seaton, N. A.; Düren, T., Evaluation of Ideal Adsorbed Solution Theory as a Tool for the Design of Metal–Organic Framework Materials. *Ind. Eng. Chem. Res.* **2012,** *51* (13), 4911-4921.

47. (a) Babarao, R.; Hu, Z.; Jiang, J.; Chempath, S.; Sandler, S. I., Storage and separation of CO_2 and CH_4 in silicalite, C168 schwarzite, and IRMOF-1: a comparative study from Monte Carlo simulation. *Langmuir* **2007,** *23* (2), 659-666;

(b) Bae, Y.-S.; Mulfort, K. L.; Frost, H.; Ryan, P.; Punnathanam, S.; Broadbelt, L. J.; Hupp, J. T.; Snurr, R. Q., Separation of CO_2 from CH_4 using mixed-ligand metal-organic frameworks. *Langmuir* **2008,** *24* (16), 8592-8598;

(c) Bae, Y.-S.; Farha, O. K.; Spokoyny, A. M.; Mirkin, C. A.; Hupp, J. T.; Snurr, R. Q., Carborane-based metal-organic frameworks as highly selective sorbents for CO_2 over methane. *Chem. Commun.* **2008,** (35), 4135-4137;

(d) Zhang, Z.; Li, Z.; Li, J., Computational study of adsorption and separation of CO_2, CH_4, and N_2 by an rht-Type metal-organic framework. *Langmuir* **2012,** *28* (33), 12122-12133.

48. Plonka, A. M.; Banerjee, D.; Woerner, W. R.; Zhang, Z.; Nijem, N.; Chabal, Y. J.; Li, J.; Parise, J. B., Mechanism of Carbon Dioxide Adsorption in a Highly Selective Coordination Network Supported by Direct Structural Evidence. *Angew. Chem. Int. Ed.* **2013,** *52* (6), 1692-1695.

49. Sheldrick, G., shelxs 97, Program for the Solution of Crystal Structure. University of Göttingen, Germany: **1997**.

50. Sheldrick, G., SHELXTL, Structure Determination Software Programs. Bruker Analytical X-ray System Inc., Madison, WI, USA **1997**.

51. Farrugia, L. J., WinGX and ORTEP for Windows: an update. *Appl. Cryst.* **2012,** *45* (4), 849-854.

52. Greenwood, N. N.; Earnshaw, A., Chemistry of the Elements. Elsevier: **2012**.

53. Oxfrod Diffraction, CrysAlis Pro and CrysAlis RED. Oxford Diffraction Ltd, Abingdon, England: 2007.

54. APEX, I., Software Package. *Bruker AXS Inc* **2005,** *5465*, 5317.

55. Banerjee, D.; Zhang, Z.; Plonka, A. M.; Li, J.; Parise, J. B., A Calcium Coordination Framework Having Permanent Porosity and High CO_2/N_2 Selectivity. *Cryst. Growth Des.* **2012,** *12* (5), 2162-2165.

56. (a) Martin, M. G.; Siepmann, J. I., Transferable potentials for phase equilibria. 1. United-atom description of n-alkanes. *J. Physic. Chem. B* **1998,** *102* (14), 2569-2577;

(b) Martin, M. G.; Siepmann, J. I., Novel configurational-bias Monte Carlo method for branched molecules. Transferable potentials for phase equilibria. 2. United-atom description of branched alkanes. *J. Phys. Chem. B* **1999,** *103* (21), 4508-4517.

57. Allen, M.; Frenkel, D.; Talbot, J., Molecular dynamics simulation using hard particles. *Computer physics reports* **1989,** *9* (6), 301-353.

58. Breneman, C. M.; Wiberg, K. B., Determining atom-centered monopoles from molecular electrostatic potentials. The need for high sampling density in formamide conformational analysis. *J. Comput. Chem.* **1990,** *11* (3), 361-373.

59. Gaussian09, R. A., 1, MJ Frisch, GW Trucks, HB Schlegel, GE Scuseria, MA Robb, JR Cheeseman, G. Scalmani, V. Barone, B. Mennucci, GA Petersson et al., Gaussian. *Inc., Wallingford CT* **2009**.

60. Hariharan, P.; Pople, J. A., The effect of d-functions on molecular orbital energies for hydrocarbons. *Chem. Phys. Lett.* **1972,** *16* (2), 217-219.

61. Torrisi, A.; Mellot-Draznieks, C.; Bell, R. G., Impact of ligands on CO_2 adsorption in metal-organic frameworks: First principles study of the interaction of CO_2 with functionalized benzenes. I. Inductive effects on the aromatic ring. *J. Chem. Phys.* **2009,** *130* (19).

62. (a) Nijem, N.; Thissen, P.; Yao, Y.; Longo, R. C.; Roodenko, K.; Wu, H.; Zhao, Y.; Cho, K.; Li, J.; Langreth, D. C., Understanding the preferential adsorption of CO_2 over N_2 in a flexible metal-organic framework. *J. Amer. Chem. Soc.* **2011,** *133* (32), 12849-12857;

(b) Zhao, Y.; Wu, H.; Emge, T. J.; Gong, Q.; Nijem, N.; Chabal, Y. J.; Kong, L.; Langreth, D. C.; Liu, H.; Zeng, H., Enhancing gas adsorption and separation capacity through ligand functionalization of microporous metal-organic framework structures. *Chem. Eur. J.* **2011,** *17* (18), 5101-5109.

63. Yao, Y.; Nijem, N.; Li, J.; Chabal, Y. J.; Langreth, D. C.; Thonhauser, T., Analyzing the frequency shift of physiadsorbed CO_2 in metal organic framework materials. *Phys. Rev. B* **2012,** *85* (6), 064302.

64. (a) Tan, C.; Yang, S.; Champness, N. R.; Lin, X.; Blake, A. J.; Lewis, W.; Schröder, M., High capacity gas storage by a 4, 8-connected metal–organic polyhedral framework. *Chem. Commun.* **2011,** *47* (15), 4487-4489;

(b) Lin, J.-B.; Zhang, J.-P.; Chen, X.-M., Nonclassical active site for enhanced gas sorption in porous coordination polymer. *J. Amer. Chem. Soc.* **2010,** *132* (19), 6654-6656;

(c) Britt, D.; Furukawa, H.; Wang, B.; Glover, T. G.; Yaghi, O. M., Highly efficient separation of carbon dioxide by a metal-organic framework replete with open metal sites. *PNAS* **2009,** *106* (49), 20637-20640.

65. Wu, H.; Reali, R. S.; Smith, D. A.; Trachtenberg, M. C.; Li, J., Highly selective CO_2 capture by a flexible microporous metal-organic framework (MMOF) material. *Chem. Eur. J.* **2010,** *16* (47), 13951-13954.

66. Chen, X.; Plonka, A. M.; Banerjee, D.; Krishna, R.; Schaef, H. T.; Ghose, S.; Thallapally, P. K.; Parise, J. B., Direct Observation of Xe and Kr Adsorption in a Xe-selective Microporous Metal Organic Framework. *J. Am. Chem. Soc.* **2015**. (in review)

67. Spek, A., Single-crystal structure validation with the program PLATON. *J. Appl. Cryst.* **2003,** *36* (1), 7-13.

68. Fairen-Jimenez, D.; Galvelis, R.; Torrisi, A.; Gellan, A. D.; Wharmby, M. T.; Wright, P. A.; Mellot-Draznieks, C.; Dueren, T., Flexibility and swing effect on the adsorption of energy-related gases on ZIF-8: combined experimental and simulation study. *Dalton Trans.* **2012,** *41* (35), 10752-10762.

69. (a) Tsuzuki, S.; Fujii, A., Nature and physical origin of CH/π interaction: significant difference from conventional hydrogen bonds. *Phys. Chem. Chem. Phys.* **2008,** *10* (19), 2584-2594;

(b) Melandri, S., "Union is strength": how weak hydrogen bonds become stronger. *Phys. Chem. Chem. Phys.***2011,** *13* (31), 13901-13911.

70. Düren, T.; Snurr, R. Q., Assessment of isoreticular metal-organic frameworks for adsorption separations: a molecular simulation study of methane/n-butane mixtures. *J. Phys. Chem. B* **2004,** *108* (40), 15703-15708.

71. Nishio, M.; Umezawa, Y.; Honda, K.; Tsuboyama, S.; Suezawa, H., CH/π hydrogen bonds in organic and organometallic chemistry. *CrystEngComm* **2009,** *11* (9), 1757-1788.

72. Tranchemontagne, D. J.; Mendoza-Cortés, J. L.; O'Keeffe, M.; Yaghi, O. M., Secondary building units, nets and bonding in the chemistry of metal–organic frameworks. *Chem. Soc. Rev.* **2009,** *38* (5), 1257-1283.

73. Makal, T. A.; Yuan, D.; Zhao, D.; Zhou, H.-C., Metal-organic frameworks. *Chem. Nanostr. Mat.* **2011,** *2*, 37-64.

74. (a) Abrahams, B. F.; Grannas, M. J.; Hudson, T. A.; Robson, R., A Simple Lithium (I) Salt with a Microporous Structure and Its Gas Sorption Properties. *Angew. Chem. Inter. Ed.* **2010,** *49* (6), 1087-1089;

(b) Banerjee, D.; Borkowski, L. A.; Kim, S. J.; Parise, J. B., Synthesis and Structural Characterization of Lithium-Based Metal-Organic Frameworks. *Crys. Growth Des.* **2009,** *9* (11), 4922-4926;

(c) Sumida, K.; Hill, M. R.; Horike, S.; Dailly, A.; Long, J. R., Synthesis and hydrogen storage properties of $Be_{12}(OH)_{12}$(1, 3, 5-benzenetribenzoate)$_4$. *J. Amer. Chem. Soc.* **2009,** *131* (42), 15120-15121;

(d) Porter, W. W.; Wong-Foy, A.; Dailly, A.; Matzger, A. J., Beryllium benzene dicarboxylate: the first beryllium microporous coordination polymer. *J. Mat. Chem.* **2009,** *19* (36), 6489-6491;

(e) Dinca, M.; Long, J. R., Strong H_2 binding and selective gas adsorption within the microporous coordination solid $Mg_3(O_2C\text{-}C_{10}H_6\text{-}CO_2)_3$. *J. Amer. Chem. Soc.* **2005,** *127* (26), 9376-9377;

(f) Dietzel, P. D.; Johnsen, R. E.; Fjellvåg, H.; Bordiga, S.; Groppo, E.; Chavan, S.; Blom, R., Adsorption properties and structure of CO_2 adsorbed on open coordination sites of metal–organic framework Ni_2(dhtp) from gas adsorption, IR spectroscopy and X-ray diffraction. *Chem. Commun.* **2008,** (41), 5125-5127;

(g) Mallick, A.; Saha, S.; Pachfule, P.; Roy, S.; Banerjee, R., Selective CO_2 and H_2 adsorption in a chiral magnesium-based metal organic framework (Mg-MOF) with open metal sites. *J. Mat. Chem.* **2010,** *20* (41), 9073-9080;

(h) Banerjee, D.; Finkelstein, J.; Smirnov, A.; Forster, P. M.; Borkowski, L. A.; Teat, S. J.; Parise, J. B., Synthesis and structural characterization of magnesium based coordination networks in different solvents. *Cryst. Growth Des.* **2011,** *11* (6), 2572-2579;

(i) Imaz, I.; Rubio-Martínez, M.; An, J.; Sole-Font, I.; Rosi, N. L.; Maspoch, D., Metal–biomolecule frameworks (MBioFs). *Chem. Commun.* **2011,** *47* (26), 7287-7302.

75. (a) Ghosh, S. K.; Bharadwaj, P. K., Self-assembly of lanthanide helicate coordination polymers into 3D metal-organic framework structures. *Inorg. Chem.* **2004,** *43* (7), 2293-2298;

(b) Frisch, M.; Cahill, C. L., Synthesis, structure and fluorescent studies of novel uranium coordination polymers in the pyridinedicarboxylic acid system. *Dalton Trans.* **2006,** (39), 4679-4690;

(c) Ghosh, S. K.; Bharadwaj, P. K., Coordination polymers of La(III) as bunched infinite nanotubes and their conversion into an open-framework structure. *Inorg. Chem.* **2005,** *44* (9), 3156-3161.

76. (a) Forster, P. M.; Burbank, A. R.; Livage, C.; Férey, G.; Cheetham, A. K., The role of temperature in the synthesis of hybrid inorganic-organic materials: the example of cobalt succinates. *Chem. Commun.* **2004,** (4), 368-369;

(b) Chen, S.-C.; Zhang, Z.-H.; Huang, K.-L.; Chen, Q.; He, M.-Y.; Cui, A.-J.; Li, C.; Liu, Q.; Du, M., Solvent-controlled assembly of manganese (II) tetrachloroterephthalates with 1D chain, 2D layer, and 3D coordination architectures. *Cryst. Growth Des.* **2008,** *8* (9), 3437-3445;

(c) Huang, X.-C.; Li, D.; Chen, X.-M., Solvent-induced supramolecular isomerism in silver (I) 2-methylimidazolate. *CrystEngComm* **2006,** *8* (4), 351-355;

(d) Pedireddi, V.; Varughese, S., Solvent-dependent coordination polymers: Cobalt complexes of 3, 5-dinitrobenzoic acid and 3, 5-dinitro-4-methylbenzoic acid with 4, 4'-bipyrdine. *Inorg. Chem.* **2004,** *43* (2), 450-457;

(e) Wang, F.-K.; Yang, S.-Y.; Huang, R.-B.; Zheng, L.-S.; Batten, S. R., Control of the topologies and packing modes of three 2D coordination polymers through variation of the solvent ratio of a binary solvent mixture. *CrystEngComm* **2008,** *10* (9), 1211-1215.

77. Pan, L.; Frydel, T.; Sander, M. B.; Huang, X.; Li, J., The effect of pH on the dimensionality of coordination polymers. *Inorg. Chem.* **2001,** *40* (6), 1271-1283.

78. (a) Liang, P.-C.; Liu, H.-K.; Yeh, C.-T.; Lin, C.-H.; Zima, V. t. z., Supramolecular Assembly of Calcium Metal-Organic Frameworks with Structural Transformations. *Cryst. Growth Des.* **2011,** *11* (3), 699-708;

(b) Li, C.-P.; Du, M., Role of solvents in coordination supramolecular systems. *Chem. Commun.* **2011,** *47* (21), 5958-5972;

(c) Nagarathinam, M.; Vittal, J. J., Anisotropic Movements of Coordination Polymers upon Desolvation: Solid-State Transformation of a Linear 1D Coordination Polymer to a Ladderlike Structure. *Angew. Chem. Int. Ed.* **2006,** *45* (26), 4337-4341;

(d) Xue, D.-X.; Zhang, W.-X.; Chen, X.-M.; Wang, H.-Z., Single-crystal-to-single-crystal transformation involving release of bridging water molecules and conversion of chain helicity in a chiral three-dimensional metal-organic framework. *Chem. Commun.* **2008,** (13), 1551-1553.

79. (a) Kitagawa, S.; Uemura, K., Dynamic porous properties of coordination polymers inspired by hydrogen bonds. *Chem. Soc. Rev.* **2005,** *34* (2), 109-119;

(b) Banerjee, D.; Kim, S. J.; Li, W.; Wu, H.; Li, J.; Borkowski, L. A.; Philips, B. L.; Parise, J. B., Synthesis and Structural Characterization of a 3-D Lithium Based Metal-Organic Framework Showing Dynamic Structural Behavior. *Cryst. Growth Des.* **2010,** *10* (6), 2801-2805.

80. Watanabe, T.; Matsui, M., A redetermination of the crystal structures of α-calcium formate, α-strontium formate and barium formate by X-ray analyses. *Acta Crystallogr. Sect. B: Struct. Cryst. Cryst. Chem.* **1978,** *34* (9), 2731-2736.

81. Lee, J. D., Concise inorganic chemistry. John Wiley & Sons: **2008**.